UAB
Universitat Autònoma de Barcelona

Electrolyte-Gated Organic Field-Effect Transistors for (Bio)-Sensing Applications

Sara Ruiz Molina

Electrolyte-Gated Organic Field-Effect Transistors for (Bio)-Sensing Applications

Sara Ruiz Molina

Doctoral Thesis

Chemistry Department

Universidad Autónoma de Barcelona

PhD Programme in Chemistry

Supervisora: Marta Mas Torrent

Molecular Materials for Electronic Devices (eMolMat)

Molecular Nanoscience and Organic Materials (NANOMOL)

Institut de Ciéncia de Materials de Barcelona (ICMAB-CSIC)

04/11/2024

Memòria presentada per aspirar al Grau de Doctor per

Sara Ruiz Molina

Visit i plau:

Prof. Marta Mas Torrent

04/11/2024

MARTA MAS TORRENT, Research Professor of the Spanish Council of Research (CSIC), at the Materials Science Institute of Barcelona (ICMAB)

CERTIFIES

That Sara Ruiz Molina has performed, under her supervision, the research work entitled "Electrolyte-Gated Organic Field-Effect Transistors for (bio)sensing applications". This work has been carried out under the framework of the Chemistry PhD Programme of the Chemistry Department of the Autonomous University of Barcelona.

And in witness whereof this is signed by

Director:
Prof. Marta Mas-Torrent

04/11/2024

A mi familia y amigos, si es que no sois lo mismo.

ACKNOWLEDGMENTS

Me gustaría dedicar un buen rato para agradecer una por una a todas las personas que he conocido y me han aportado tantos buenos momentos durante estos años, pero este apartado se haría eterno…Empezamos.

Cuando estás en secundaria y tus profesores te encaminan hacia la temida SELECTIVIDAD, aún es pronto y no sabes qué hacer con tu vida. Yo tuve la suerte de tener un profesor de química, Juan María García, el cual despertó mi curiosidad hacia la química y, sobre todo, hacia la docencia. Ya en el Grado en Química conocí al ahora Doctor Julio García, quien hasta hoy sigue siendo uno de mis grandes apoyos en todos los aspectos de mi vida, y también lo fue durante toda mi etapa universitaria, que no ha sido corta. Pero no habría llegado a hacer el doctorado sino hubiera coincidido a Loli Eliche, una gran profesora e investigadora. Por capricho del destino, en lugar de realizar mi tesis en Jaén, donde llevaba toda mi vida, el grupo de Nanomol me estaba esperando en: ¡Barcelona!

Ahora que esta etapa llega a su fin, quiero agradecer a Marta Mas, por darme la oportunidad de entrar en este grupo, aunque para mí siempre ha sido y será parte de mi familia. Gracias Marta, por guiarme durante este tiempo y ofrecer tu apoyo tanto en lo profesional como en lo personal cuando ha sido necesario. También quiero agradecer a Dr. Simona Ricci y Dr. Adrián Tamayo, por su amistad y su gran ayuda durante mis primeros meses en este grupo. De manera especial también doy las GRACIAS, en mayúscula, a Dr. Tommaso Salzillo, el cual se convirtió en un gran compañero de piso y sobre todo gran amigo, sin su apoyo y su paciencia para escuchar mis lamentaciones y problemas no hubiera llevado los primeros años de mis tesis de la misma forma, ni hubiera existido esa camiseta que aún guardo con tanto cariño. (ATPC TEAM!)

The work carried out in this thesis would not have been possible without collaborations with other research groups. I would like to thank all the collaborator which have contributed to the research done in this thesis. I would like to thank, Dr. Stefano Casalini, Dr. Andrea Cester and, especially Dr. Nicolò Lago from University of Padova, for receive me in their group during my stay in Italy. I would like to thank Dr. Gabriel Gomila, Dr. Adrika Kyndiah and Dr. Shubham Tanwar, for collaboration with them in IBEC.

Thank you all the members of the e-MolMat group, I have spent most of the time with you talking and working in the lab. Thanks to Dr. Jinghai Li, Dr. Carme Martínez, Dr. Ángel Campos, José Catalán, Betty Giglio, María Jesús Ortíz, Lluis y Mayla. También tengo que

agradecer a todos los compañeros de NANOMOL y fuera de este grupo también, por hacer que desconecte cuando hacía falta y siempre ofrecerse para hablar en los momentos de crisis, y por seguir siendo una gran familia que guarda las tradiciones de tesis aún con el paso del tiempo. Muchas gracias a Edu, Marc, David, Guillem, Júlia P., Laia, Giovanni, Miquel, Rubén, Nerea, Alejandro, Judit T., Elba, Sol, Allan, Marta Alcaina, Carla Castellar, Albert Revuelta, Francesc.

Y un gracias enorme a las grandes amistades que he hecho en este centro durante estos años. A Xavier Rodríguez por haber sido y por seguir siendo un gran compañero, y por haberse convertido en un amigo único e irremplazable. *Pels bons moments que hem passat i els que vindran. Per aguantar els meus problemes amb la tesi i els drames personals, et estaré sempre molt agraïda, Xavi. T'estimo molt.* También, gracias a Francesca Merlina y Adrián Rodríguez por ser un grupo de 3 grandes amigos, por siempre apoyarme y animarme en los peores momentos y por estar siempre para ese vermutín en el Flanders, que siempre se acaba convirtiendo en más de uno. Gracias también al genial grupo de Bingo Musical, Sara Garrido y Nùria Pujol, por ser unas personas muy importantes y especiales para mi… y muy graciosas, por cierto (sois las mejores). A Betta, por la amistad que forjamos en ese viaje express a Andalucía sin conocernos de nada y que no olvidaré nunca. A Mario Villa por convertirte en un buen amigo en tan poco tiempo, por las conversaciones profundas de fiesta y las celebraciones que aún nos quedan. Gracias también a Alejandro Sabater por haber compartido conmigo estos años en Barcelona y haberse convertido en parte de mi familia para siempre.

Gracias a mi querido coro del ICMAB, siempre recordaré nuestros momentos de desconexión en los ensayos, y a nuestros dos grande directores: Raúl y Laia. Y a mis compis del cole, por darme ánimos durante la recta final de la escritura, intentando combinar clases y tesis, y por calmarme siempre con una sonrisa cuando entro a la sala de profes decaída. Gracias Olga G., Mònica R., María R., Roser, F., Nùria T. y al profe James.

Por último, y lo más importante siempre, gracias a mi GRAN familia Ruiz-Molina por su apoyo durante esta etapa de mi vida. Porque desde el momento en que decidí dar este cambio e irme a vivir a muchísimos kilómetros de mi sitio de toda la vida, ellos siempre me han apoyado y entendido, y han hecho que me sienta cerca de ellos.

ABSTRACT

This doctoral thesis focused on the development and application of Electrolyte-Gated Organic Field-Effect Transistors (EGOFETs) and Hydrogel-Gated Organic Field-Effect Transistors (HYGOFETs) for bioelectronic purposes. Devices were fabricated by depositing small molecules of organic semiconductors (OSC) blended with an insulating polymer from solution, employing the Bar-Assisted Meniscus-Shearing technique (BAMS). The work involved designing flexible, low-power biosensors for detecting biomolecule aggregation and cellular activity, particularly amyloid peptides, which are relevant for neurodegenerative diseases like Alzheimer's and Parkinson's. The ability of EGOFETs to detect proteins without the need for makers highlighted their potential in systematic studies of protein aggregation and drug testing. In addition, HYGOFETs, utilizing agarose hydrogel, demonstrated improved stability in biosensing environments. The thesis also explored the potential of EGOFETs as strain sensors and their application in flexible electronics, identifying key electrical changes under mechanical stress. The research introduced innovative solutions for addressing voltage drift in EGOFETs and showed their capacity to record and stimulate cellular activity, specifically single-cell membrane potentials. Overall, the findings emphasized the promising future of EGOFETs and HYGOFETs in bioelectronic applications, enhancing the understanding of these devices while paving the way for advanced flexible biosensors.

ARTICLES INCLUDED IN THIS THESIS

[1] Electrolyte-Gated Organic Field-Effect Transistor for Monitoring Amyloid Aggregation. Sara Ruiz-Molina, Carme Martínez-Domingo, Simona Ricci, Stefano Casalini and Marta Mas-Torrent. (Accepted)

[2] Influence of Mechanical Stress on Flexible Electrolyte-Gated Organic Field-Effect Transistors. Sara Ruiz-Molina, Simona Ricci, Carme Martínez-Domingo, María Jesús Ortiz-Aguayo, Raphael Pfattner, G. Schweicher, Y. H. Geerts, Tommaso Salzillo and Marta Mas-Torrent. (Submitted)

[3] Real-Time Threshold Voltage Compensation on Dual-Gate Electrolyte-Gated Organic Field-Effect Transistors. Nicolò Lago, Marco Buonomo, Sara Ruiz-Molina, Andrea Pollesel, Rafael Cintra Hensel, Francesco Sedona, Mauro Sambi, Marta Mas-Torrent, Stefano Casalini and Andrea Cester. *Organic Electronics,* 2022, 106, 106531.

[4] Single-Cell Membrane Potential Stimulation and Recording by an Electrolyte-Gated Organic Field-Effect Transistor. Nicolò Lago, Alessandra Galli, Sarah Tonello, Sara Ruiz-Molina, Saralea Marino, Stefano Casalini, Marco Buonomo, Simona Pisu, Marta Mas-Torrent, Giada Giorgi, Morten Gram Pedersen, Mario Bortolozzi and Andrea Cester. *Advanced Electronic Materials,* 2024, 2400134.

PUBLICATIONS NOT INCLUDED IN THIS THESIS

[5] Nanoscale Operando Characterization of Electrolyte-Gated Organic Field-Effect Transistors Reveals Charge Transport Bottlenecks. Shubham Tanwar, Ruben Millan-Solsona, Sara Ruiz-Molina, Marta Mas-Torrent, Adrica Kyndiah and Gabriel Gomila. *Advanced Materials,* 2024, 36, 2309767.

[6] Automated Scanning Dielectric Microscopy Toolbox for Operando Nanoscale Electrical Characterization of Electrolyte-Gated Organic Transistors. Shubham Tanwar, Ruben Millan-Solsona, Sara Ruiz-Molina, Marta Mas-Torrent, Adrica Kyndiah and Gabriel Gomila. *Advanced Electronic Materials,* 2024, 2400222.

CONFERENCE CONTRIBUTIONS

[i] JPhD2021 poster presentation.

[ii] DocFam Summer School. Poster presentation. 2022

[iii] Orbitaly2022. Poster presentation.

[iv] Doctoral workshop PhD programme in Chemistry. Poster and Oral presentation. 2022

[v] ACTIVE workshop 2022. Oral presentation.

[vi] Electrolyte-Gated Organic Field-Effect Transistors for sensing an Alzheimer's Disease Hallmark. Sara Ruiz-Molina, Carme Martínez-Domingo, Simona Ricci, Stefano Casalini and Marta Mas-Torrent. E-MRS Spring Meeting, Strasburg (France), oral presentation (2023)

LIST OF ABBREVIATIONS AND SYMBOLS

ABBREVIATIONS

A11 Ab	A11 anti-oligomer antibodies
Ab	Antibody
ABP	Beta-amyloid plaques
AD	Alzheimer's disease
ADAs	Anti-drug antibodies
AFM	Atomic force microscopy
Ag	Antigen
APP	Amyloid precursor protein
BAMS	Bar-assisted meniscus shearing
BGBC	Bottom-gate bottom-contact
BGTC	Bottom-gate top-contact
BO	Benign oligomers
C_8O-BTBT-OC_8	2,7- dioctyloxy[1]benzothieno[3,2,b]benzothiophene
CG	Coplanar gate
ChemFET	Chemically-sensitive field-effect transistor
CSF	Cerebrospinal fluid
CV	Cyclic voltammetry
Cys-PG	Cysteine-tagged Protein G
D	Drain electrode
diF-TES-ADT	2,8-difluoro-5,11-bis(triethylsilylethynyl)anthradithiophene
DLS	Dynamic light scattering
DPV	Differential pulse voltammetry
EDL	Electrical double layer
EGFET	Electrolyte-gated field-effect transistor
EGOFET	Electrolyte-Gated Organic Field-Effect Transistor
EGT	Electrolyte-gated transistor
EIS	Electrochemical impedance spectroscopy
G	Gate electrode
GCS	Gouy-Chapman-Stern
hMSCs	Human mesenchymal stem cells
HOMO	Highest occupied molecular orbital
hPSCs-CMs	Human pluripotent stem cell-derived cardiomyocyte cells

HYGOFET	Hydrogel-based organic field-effect transistor
IHL	Inner Helmholtz layer
IP	Ionization potential
ISFET	Ion-sensitive field-effect transistor
LOD	Limit of detection
LUMO	Lowest unoccupied molecular orbital
MCH	6-Mercapto-1-Hexanol
MOSFET	Metal-oxide-semiconductor field-effect transistor
MTR	Multiple trapping and release
OECT	Organic electrochemical transistor
OFET	Organic field-effect transistor
OHL	Outer Helmholtz layer
OLED	Organic light-emitting diode
OPV	Organic Photovoltaic
OSC	Organic semiconductor
P3HT	Poly-3-hexylthiophene
PBS	Phosphate buffer saline
PDMS	Poly(dimethylsiloxane)
PFBT	2,3,4,5,6-Pentafluorothiophenol
PG	Recombinant protein G
PMMA	Polymethylmethacrylate
POC	Point-of-care
PS	Polystyrene
R2R	Roll-to-roll
S	Source electrode
SAM	Self-assembled monolayer
SHE	Standardized Hydrogen Electrode
SiO_2	Silicon oxide
TEM	Transmission electron microscopy
TG	Top gate
TGBC	Top-gate bottom-contact
TGTC	Top-gate top-contact
ThT	Thioflavin t
TO	Toxic oligomers

SYMBOLS

μ_{FE}	Field-effect mobility
C	Capacitance
C_0	Ionic strength
C_{dl}	Double-layer capacitance
C_{eff}	Effective capacitance
C_{Gouy}	Capacitance of the diffuse layer
C_{Stern}	Capacitance of the Stern layer
D	Drain
e	Elementary charge
E_F	Fermi level
E_g	Band gap
G	Gate
g_m	Transconductance
I_{Off}	Off-current
I_{On}	On-current
$I_{On/Off}$	On/off current ratio
I_{SD}	Source-drain current
I_{SG}	Gate-source current
k	Gauge factor
k_b	Boltzmann constant
L	Channel length
M_w	Molecular weight
N_A	Avogadro number
N_T	Density of charge carrier traps
$ø_{WF}$	Work-function
pI	Isoelectric point
Q	Charge
R_{ct}	Charge transfer resistance
S	Source
SS	Sub-threshold swing

T	Temperature
$V_{CG,S}$	Coplanar gate-source voltage
V_{FB}	Flat-band voltage
V_{GS}	Source-drain voltage
V_{ON}	On voltage
$V_{TG,S}$	Top gate-source voltage
V_{th}	Threshold voltage
W	Channel width
λ	Reorganization energy
ε	Strain

CONTENTS

CHAPTER 1

GENERAL INTRODUCTION

1. Introduction to organic electronics

In modern electronics, inorganic materials like silicon are predominant, primarily because of their electrical properties and the well-established production techniques. Silicon transistors are known for their high mobility, which makes them ideal for manufacturing high-speed devices. However, they come with significant limitations, such as high production costs and limited scalability. This makes it essential to explore alternatives to silicon-based electronics that are more cost-effective.

Organic electronics allows for the creation of organic devices at a lower cost using roll-to-roll (R2R) processing methods. Organic materials are biocompatible and can be deposited at low temperatures, making them compatible with flexible substrates. The field of organic electronics emerged in the 1970s following the discovery of the first small molecule organic metal, tetrathiafulvalene-tetracyanoquinodimethane (TTF-TCNQ),[1] and the development of chemically doped polyacetylene, the first conductive conjugated polymer.[2] These breakthroughs generated significant scientific interest and paved the way for advancing new organic conductive and semiconductor materials.

Organic semiconductors (OSCs) consist primarily of carbon (C), and hydrogen (H) atoms. Still, they can also contain heteroatoms like nitrogen (N), phosphorous (P), oxygen (O), sulfur (S), halogens, and even some transition metals. These materials are valued for their mechanical, optical, and electrical properties, making them suitable for a range of applications. Unlike inorganic semiconductors, OSCs offer benefits such as lower manufacturing costs due to solution processing, reduced energy consumption, lighter weight, compatibility with flexible substrates, and the ability to tailor their chemical structures.[3,4] However, they also have drawbacks, such as lower stability in ambient conditions and reduced electrical efficiency.

OSCs are employed in a wide range of electronic devices (**Figure 1.1**), including organic light-emitting diodes (OLEDs),[5,6] organic solar cells or photovoltaic devices (OPVs),[7,8] and organic field-effect transistors (OFETs).[9–11]

OLEDs are devices that convert electrical energy into light. They are composed of two layers of OSCs. The first is an n-type OSC layer, responsible for transporting electrons, while the second is a p-type OSC, which carries holes. When electrons and holes meet at the interface, they recombine to form excitons, which emit light as they return to their ground state. The wavelength of the emitted light, whether ultraviolet (UV), visible (VIS), or infrared (IR), can be controlled by selecting the right combination of OSCs.[12] A key advantage of OLEDs over traditional LEDs is their lower energy consumption and the simplicity of switching them off. **OPVs**,[13] on the other hand, they are devices that convert sunlight into electrical energy. In contrast to OLEDs, the OSCs in OPVs absorb sunlight rather than emitting it. When light is absorbed, excitons form at the interface of the p-type and n-type OSC layers. These excitons then split into free electrons and holes, which move toward the electrodes, generating an electric current. OPVs are attractive because of their low production costs and the potential to create tandem solar cells that improve solar radiation absorption. However, their primary drawback is their limited stability. Lastly, **OFETs** control the current flowing through an OSC connected between two electrodes using an electric field created with a third electrode (the gate). The gate is separated from the other electrodes by an insulating layer, often made from a metal oxide or polymer, which acts as a dielectric.[11] In 1987, Koezuka et al.,[14], and Tsumura et al.,[15] they reported the first OFETs. They used polythiophene as OSC, which exhibited a mobility of 10^{-5} $cm^2 \cdot V^{-1} \cdot s^{-1}$. Today, OSCs show mobility values of the same order or even superior to amorphous silicon transistors, typically 1 $cm^2 \cdot V^{-1} \cdot s^{-1}$, making them a promising option for consumer electronics.

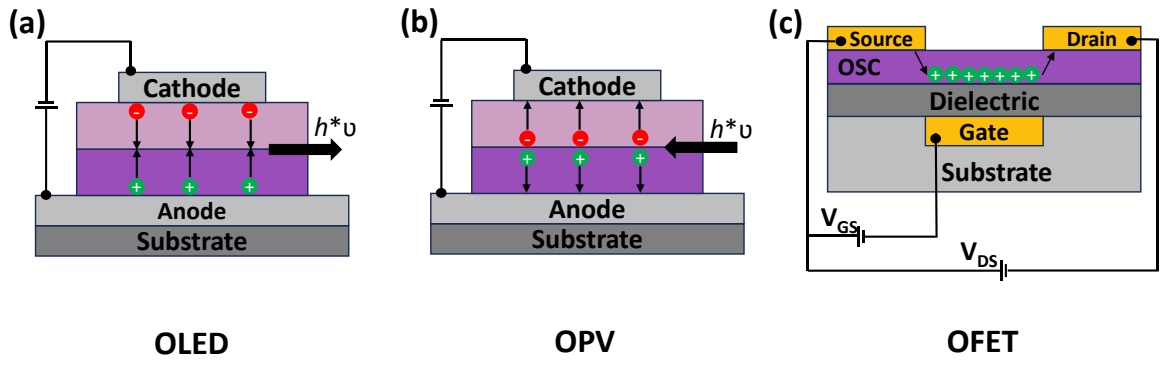

Figure 1.1. Schematic representation of a typical **(a)** OLED, **(b)** OPV, and **(c)** p-type OFET structure, including their operation principle.

2. Organic semiconductors

2.1. Organic semiconductor materials

Materials can be divided into three main categories based on their electrical properties: insulators, semiconductors, and metals. Inorganic semiconductors, such as silicon (Si), germanium (Ge), and gallium arsenide (GaAs), are composed of atoms connected by covalent bonds. Thanks to the strong interatomic interactions, long-rage, delocalized electron bands throughout the material are formed. In these semiconductors, the valence band represents the ground state where electrons reside, while the conduction band remains empty. The energy required to transition electrons from the valence band to the conduction band is called the band gap (Eg), which is a characteristic feature of a semiconductor, representing an energy range where no electron states exist. The conductivity of inorganic semiconductors typically falls between that of metals (around 10^{6} S·m^{-1}) and insulators (around 10^{-6} S·m^{-1}).[16] Organic conductors and semiconductors, in contrast, are held together by weak van der Waals forces, which generally result in materials with higher resistance.

Organic semiconductors (OSCs) are composed of carbon-based small molecules or polymers with conjugated structures, characterized by having delocalized π-orbitals along their molecular backbone. The electrical behavior of these materials is influenced by various intermolecular interactions, such as π-π stacking, van der Waals forces, or hydrogen bonding, depending on their molecular and supramolecular architecture.[17] Unlike inorganic semiconductors, OSCs do not exhibit long-range electron delocalization. Instead, when two sp2 hybridized carbon atoms align along the same axis, they form

delocalized molecular π-orbitals (Figure 1.2). The interaction between the π-orbitals in semiconductor molecules results in the formation of distinct energy levels, specifically the highest occupied molecular orbital (HOMO) and the lowest unoccupied molecular orbital (LUMO). Ath the ground state, electrons fill the energy levels below the HOMO, while the energy levels above the LUMO remain vacant. The energy gap between the HOMO and LUMO typically ranges from 1 to 4 eV, and this gap is what determines the optoelectronic properties of the OSCs.[18]

Organic semiconductors, OSCs, can be categorized into organic polymers and small molecules, and further classified as n-type, p-type, or ambipolar based on the type of charge carrier they transport. N-type OSCs predominantly conduct electrons. These materials, often organic molecules or polymers, tend to accept electrons and are easily reduced. P-type OSCs, on the other hand, primarily transport holes, meaning they are composed of electron-donating organic molecules or polymers that are prone to oxidation. Ambipolar OSCs are capable of acting as both electron donors and acceptors, allowing them to transport either holes or electrons depending on the electric field applied. The ability of OSCs to undergo oxidation or reduction is determined by the energy levels of their HOMO (highest occupied molecular orbital) and LUMO (lowest unoccupied molecular orbital) orbitals. These energy levels also provide insights into the material's environmental stability and its resistance to external factors like water and oxygen. P-type OSCs tend to have relatively high HOMO energy levels, typically around -5.0 eV, which contributes to their greater stability under ambient conditions. In contrast, n-type OSCs have lower LUMO energy levels, around -4.0 eV, making them more susceptible to degradation by water, oxygen, and light.[18]

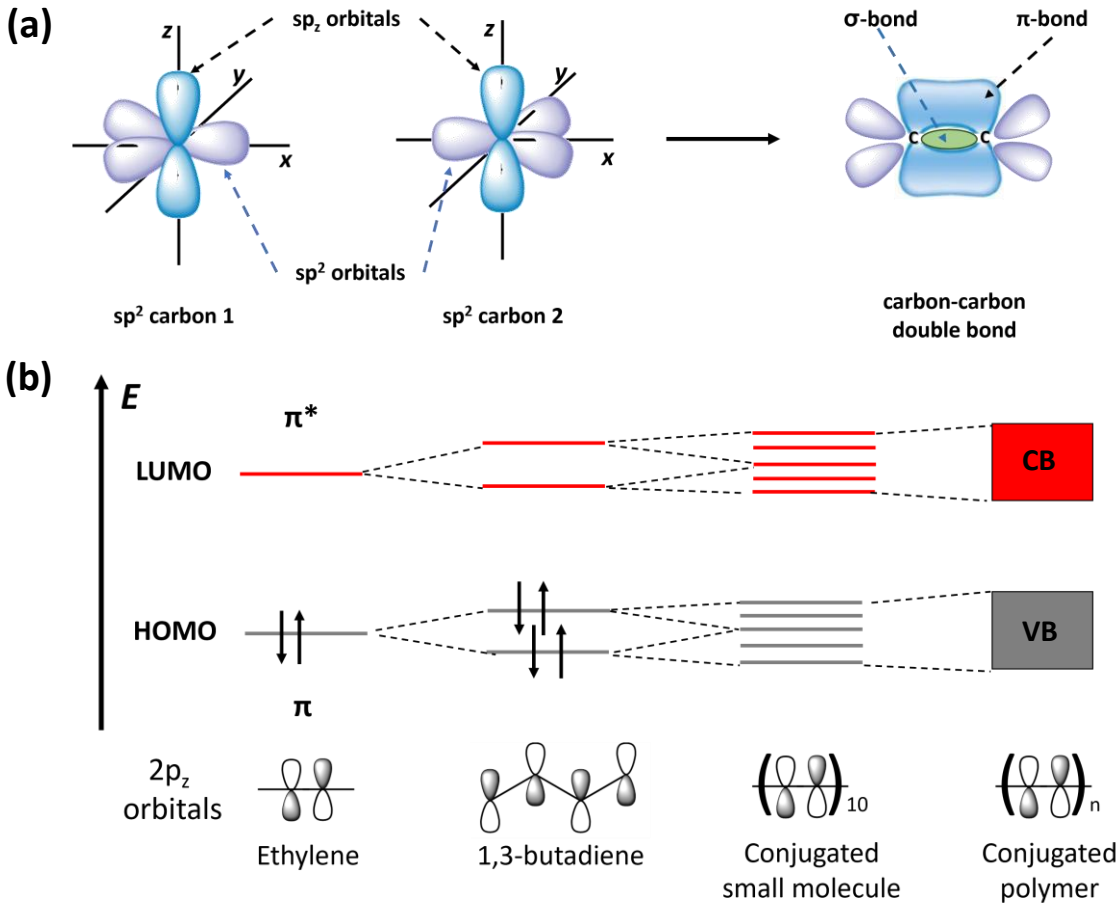

Figure 1.2. (a) Schematic illustration of hybridized sp^2 and unhybridized 2pz orbitals forming a σ-bond and a π-bond in a carbon-carbon double bond. **(b)** Extension of molecular orbitals into long conjugated oligomers and polymers, illustrating the formation of band structures (**VB**, valence band; **CB**, conduction band) in organic semiconductors. Adapted from ref [19].

Conjugated polymer semiconductors (**Figure 1.3**) are well-suited for solution-based processing methods such as spin-coating, dip-coating, and bar-coating, which will be discussed in later sections. This is largely due to their good solubility in organic solvents, and their excellent film-forming capabilities. However, when polymeric OSCs are processed from solution, they often result in thin films that are either amorphous or have low crystallinity, with small microcrystalline domains dispersed within an amorphous matrix. While the reduced crystallinity of these films can lower the mobility of charge carriers, their ease of processing in solution has made them attractive for low-cost applications.

Poly(3-hexylthiophene), or **P3HT,** is one of the most widely used polymer semiconductors, offering a mobility of around 0.1 $cm^2 \cdot V^{-1} \cdot s^{-1}$.[20] The mobility is made possible by the semicrystalline lamellar microstructures formed through head-to-tail connections of the hexyl side chains. However, P3HT has limited environmental stability due to its low oxidation potential. Another highly semicrystalline polymer is poly(2,5-bis(3-alkylthiophen2-yl)thieno(3,2-b)thiophene), or **PBTTT**, which exhibits higher mobility of 1 $cm^2 \cdot V^{-1} \cdot s^{-1}$.[21] In PBTTT, the ordered structure is achieved through better interdigitation of the side chains within the thiophene-thienothiophene units, which also improves its stability by increasing the ionization potential.[22] Recently, high-performance donor-acceptor copolymers have gained attention, through large-scale production of these highly pure materials remains a challenge. Doped organic semiconducting polymers have also been extensively studied for their conductive properties. One well-researched material is Poly(3,4-ethylenedioxythiophene) (**Figure 1.3**) doped with polystyrene sulfonate (**PEDOT:PSS**), known for its high conductivity, reaching up to 4600 $S \cdot cm^{-1}$, and its stability.[23] PEDOT has shown great potential for use in applications such as energy conversion and storage devices, including organic solar cells, dye-sensitized solar cells, supercapacitors, and fuel cells, as well as in thermoelectric and stretchable devices.[24]

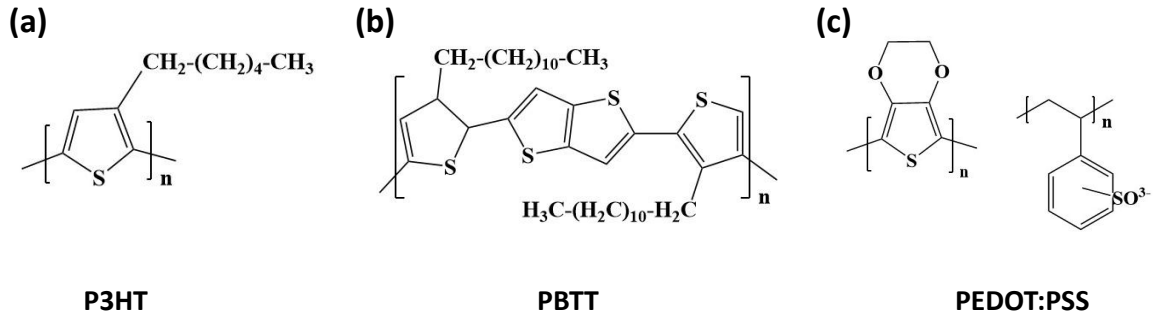

Figure 1.3. Molecular structure of **(a,b)** two organic semiconducting polymers, and **(c)** a conducting doped polymer.

Small molecule OSCs (**Figure 1.4**) are generally more challenging to process from solution due to their lower solubility in common organic solvents.[11] However, they tend to form highly crystalline thin films because of their ability to create ordered molecular structures. This higher degree of crystallinity enhances charge transport, making small molecule OSCs appealing for organic electronics. Two of the most widely studied classes of small molecule OSCs are acenes and thiophenes. To improve the crystal structure and

morphology of their thin films and facilitate solution processing, alkyl chains or electron-donating groups are often incorporated into the aromatic core. An example is bis(triisopropylsilylethynyl)pentacene (**TIPS-PEN**), a derivative of pentacene, which was developed to increase its solubility. When pentacene is deposited through physical vapor deposition, it forms a herring-bone-shaped crystal that enables charge carrier mobility of 1 $cm^2 \cdot V^{-1} \cdot s^{-1}$ in OFETs.[25] In contrast, TIPS-PEN processed from solution forms a two-dimensional "bricklayer" arrangement with significant π-π stacking, resulting in improved charge carrier mobility of around 1.5 $cm^2 \cdot V^{-1} \cdot s^{-1}$ in OFETs.[26,27] Among thiophenes, one of the most studied is [1]benzothieno[3,2-b][1]benzothiophene (**BTBT**), known for its highly delocalized electronic structure and low-lying HOMO level. However, BTBT is extremely insoluble in organic solvents, which has led to the development of various derivatives to improve its solubility. For instance, alkyl chains have been added at positions 2 and 7 of the aromatic rings. One of the most frequently used and highly performing derivative is 2,7-dioctyl BTBT (**C_8-BTBT-C_8**).[28,29] Another compound that has served as a benchmark material for OFET active layers is 2,8-difluoro-5,11-bis(triethylsilylethynyl)anthradithiophene (**diF-TES-ADT**), which has achieved mobilities exceeding 1 $cm^2 \cdot V^{-1} \cdot s^{-1}$ when processed using solution-based methods.[30,31]

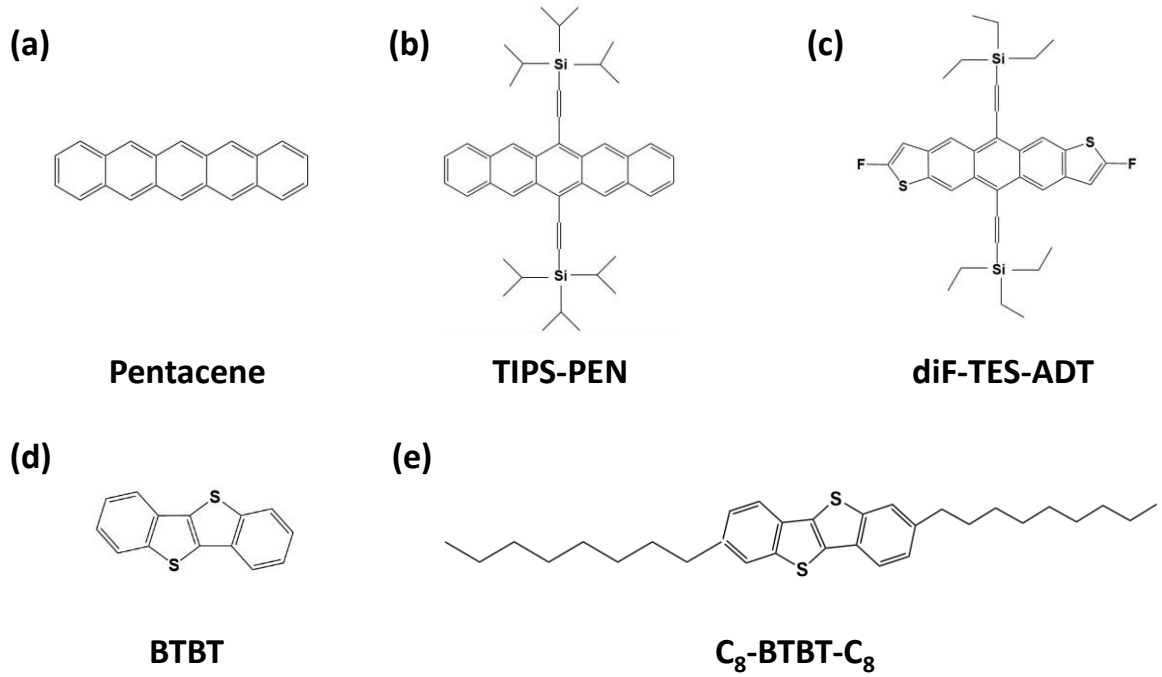

Figure 1.4. Molecular structures of p-type small molecule OSCs. **(a)** Pentacene, **(b)** TIPS-PEN, **(c)** diF-TES-ADT, **(d)** BTBT, and **(e)** C_8-BTBT-C_8.

One approach to enhance the solubility of small molecules in solution is to blend them with **insulating polymers** like polystyrene (**PS**) or polymethylmethacrylate (**PMMA**).[32] This helps mitigate surface dewetting, which often occurs due to the low viscosity of OSC solutions, leading to inconsistent coatings with limited reproducibility across devices. By incorporating insulating polymers, the viscosity of the solution is increased, resulting in the formation of more uniform thin films. When blends of OSCs and insulating polymers are deposited, vertical phase separation frequently occurs, promoting the crystallization of the OSC. This technique typically results in bilayer structures (polymer:OSC), and sometimes trilayer structures (polymer:OSC:polymer).[32] The phase separation mechanism is affected by several factors, including the type of substrate, solvent boiling point, processing conditions, and particularly, the characteristics of the polymer binder and OSC. In these layered configurations, the insulating polymer interfaces with the gate dielectric, serving as a passivation layer that reduces the density of charge carrier traps at the dielectric/OSC interface. This is accomplished by minimizing the exposure of the polar hydroxyl (OH) groups present in oxide-binding polymers tend to yield more crystalline films that exhibit greater environmental stability, which is especially crucial for liquid-gated transistors. Several benchmark OSCs, such as TIPS-PEN,[30,33] C_8-BTBT-C_8,[30] and diF-TES-ADT,[30,34] blended with PS have demonstrated this bilayer phase separation effect.

Combining organic semiconductor molecules with insulating polymers effectively addresses the common processing challenges associated with small-molecule OSCs. This approach not only enhances the crystallinity of the thin films but also improves device reproducibility by facilitating the formation of uniform and homogeneous coatings. Additionally, it reduces the quantity of OSC needed, leading to enhanced device performance and stability.[32,35,36]

2.2. Charge transport in organic semiconductors

Charge transport in organic semiconductor materials differs from that in inorganic semiconductors due to the structure of organic crystals. In inorganic semiconductors, charge carriers can easily move between delocalized energy levels, also known as band transport.[37] In contrast, charge transport in OSCs is often achieved by thermally induced hopping between neighboring molecules,[38,39] although band-like transport has been observed in a few highly ordered OSCs.[40,41] Indeed, transport mechanisms for organic materials have been proposed based on their structural order, which varies from amorphous films to single crystals. The most commonly used models to describe transport in organic semiconductors are band-like transport, multiple trapping and release model, and hopping.[42–44]

- Band transport

High-quality organic single-crystal films with low charge trap density exhibit band-like transport. In such structured crystal lattices, the valence band is formed by the interaction of neighboring molecules' highest occupied molecular orbitals (HOMO), while the conduction band is formed by the lowest unoccupied molecular orbital (LUMO), allowing for an extended wave function over many molecular units. Charge carrier mobility increases at lower temperatures, like inorganic semiconductors. Higher temperatures increase lattice phonon dispersion, promoting electron scattering and leading to a decrease in the charge carrier mobility.[45]

- Multiple trapping and release model

The multiple trapping and release model (MTR) was presented for polycrystalline OSCs with crystallites separated by grain boundaries. The model is based on the concept that charge carriers move in narrow, delocalized bands, but their motion is disrupted by the material's high concentration of traps, which are localized states inside the energy gap. These traps can be caused by chemical impurities, crystal structural flaws, grain boundaries, and other factors. The trapping and releasing processes hinder the mobility of the pure and ordered material, which is consistent with the behavior found in most OSCs. Additionally, this model can describe the gate voltage dependence of the charge carrier mobility, which is often observed.

- Hopping transport

Hopping transport is the predominant mechanism of charge transfer in amorphous or highly disordered OSCs. In this type of mechanism, the charge carriers are highly localized and move from an occupied site to an adjacent vacant site. The process is often described using Marcus' model from 1956, originally developed to explain the oxidation-reduction reactions between charged and neutral molecules in solution. In molecular crystals, the charge carriers interact strongly with the molecular structure, leading to the formation of polarons. Furthermore, the presence of charged molecules can affect neighboring molecules, causing intermolecular displacements and polarization effects that influence the crystalline structure. Consequently, transport occurs via polaron hopping between sites and is determined by two key parameters: **(i)** the electronic coupling or transfer integral (*t*), representing the interaction between two adjacent molecules' HOMOs or LUMOs, and **(ii)** the reorganization energy (λ), accounting for the molecular conformational changes upon change acceptance or release. The hopping rate is calculated based on these factors:

$$k = \frac{2\pi}{\hbar} t^2 \left(\frac{1}{\sqrt{4\pi\lambda K_B T}} \right) e^{\frac{\lambda}{4K_B T}} \qquad \boldsymbol{Eq.1.1}$$

where *t* is the transfer integral and K_B is the Boltzmann constant.

For effective charge transport, a high electronic coupling between neighboring molecules is required, which would result in a high transfer integral. On the contrary, the organization's energy should remain low to reduce energy loss associated with conformational changes during electron transfer. These factors are affected by the distance, orientation, and molecular structure of the OSC molecules. Moreover, the relationship between mobility and temperature varies compared to the band transfer mechanism. In this scenario, lattice vibrations facilitate charge carrier mobility by supplying the energy needed to surmount energetic barriers. As a result, hopping transport is a phonon-assisted process that is thermally activated.

2.3. Organic semiconductors processing techniques

The deposition of organic semiconductors is a crucial phase in the fabrication of organic electrical devices. The processing techniques can be broadly into two main types: Vapor-phase and solution-based deposition methods.

- Vapour-phase deposition techniques

Vapor phase deposition involves thermally evaporating materials within a high-vacuum chamber (10^{-6}–10^{-8} mbar) at elevated temperatures.[46] The materials begin to evaporate when the vapor pressure of the heated material surpasses that of the chamber and condenses on the target substrates (**Figure 1.5**). This technique often produces high-quality OSC films and provides advantages in terms of film thickness control and repeatability. The technique also enables the deposition of multilayer structures and the co-deposition of different materials. Despite these benefits, vapor phase deposition requires costly equipment and is less suited for large-scale manufacturing. This thesis discusses field-effect transistors that are based on solution-processed OSCs.

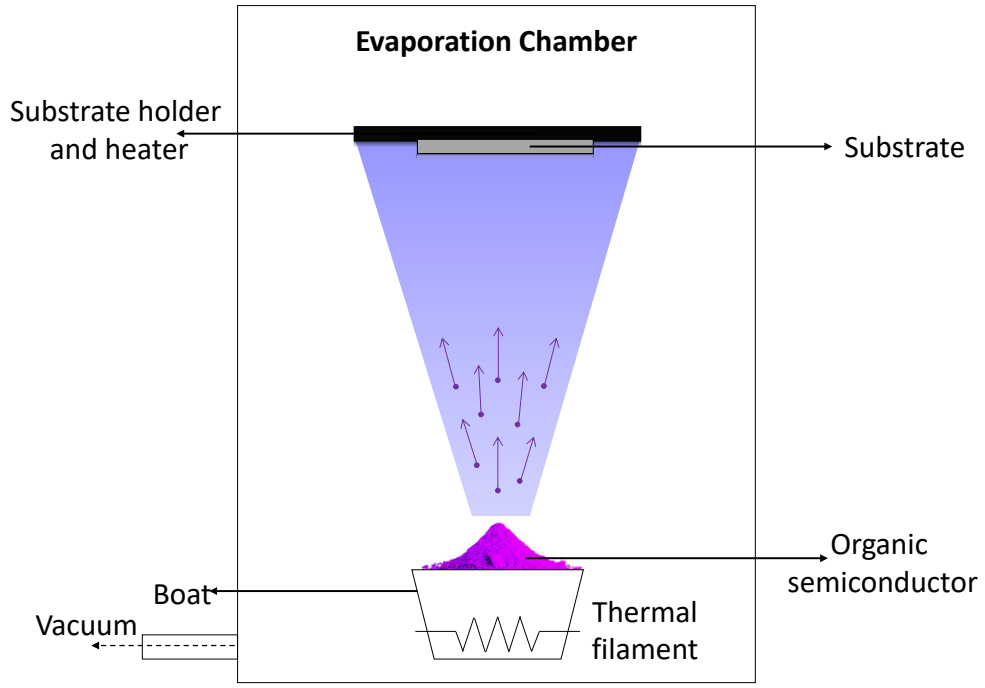

Figure 1.5. Schematic representation of a thermal evaporation system.

- Solution-based deposition techniques

Solution processing techniques are widely used for depositing thin films of organic semiconductors (OSCs) due to their cost-effectiveness and suitability for large-scale production.[47,48] This method involves dissolving the OSC material in an appropriate organic solvent before applying it to a target substrate. The most commonly employed solution-based deposition methods include drop-casting, spin-coating, dip-coating, spray-coating, zone-casting, blade-coating, and bar-assisted meniscus shearing.

- Drop-casting

Drop-casting is a straightforward method for depositing OSCs (Figure 1.6). In the process, an OSC solution is applied onto a substrate, where the solvent evaporates, leaving behind OSC crystals on the substrate surface.[49] This method is commonly used to manufacture single-crystal OSCs, but its use as a thin film deposition method is limited due to several drawbacks. Drop-casting typically generates non-uniform films with varying thickness and shape, which depend significantly on the OSC concentration and solvent evaporation rate.

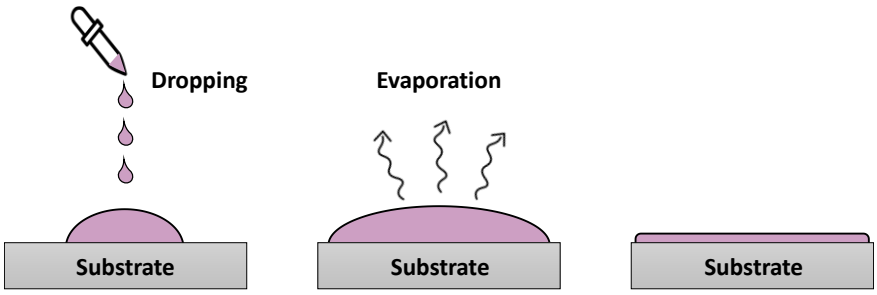

Figure 1.6. Schematic representation of the drop-casting technique.

- Spin-coating

Spin coating is a widely used method for producing OSC thin films on a laboratory scale. In this method, drops of the OSC solution are cast onto the substrate, which is rapidly spun to evenly distribute the solution across the surface (Figure 1.7). As the solvent evaporates, a thin film of OSC is formed. However, due to the quick drying time and the unidirectional centrifugal force, the molecules typically lack sufficient time to organize into a highly crystalline structure. Sometimes the films exhibit high alignment along the centrifugal force direction. To achieve high-performance devices, post-thermal treatments may be necessary to enhance the crystallinity of the OSC film.[50] The thickness of the film is determined by the solution concentration, its viscosity, and the spin coater's

working parameters. However, this technique consumes a lot of solvent and is unsuitable for large-scale manufacturing.

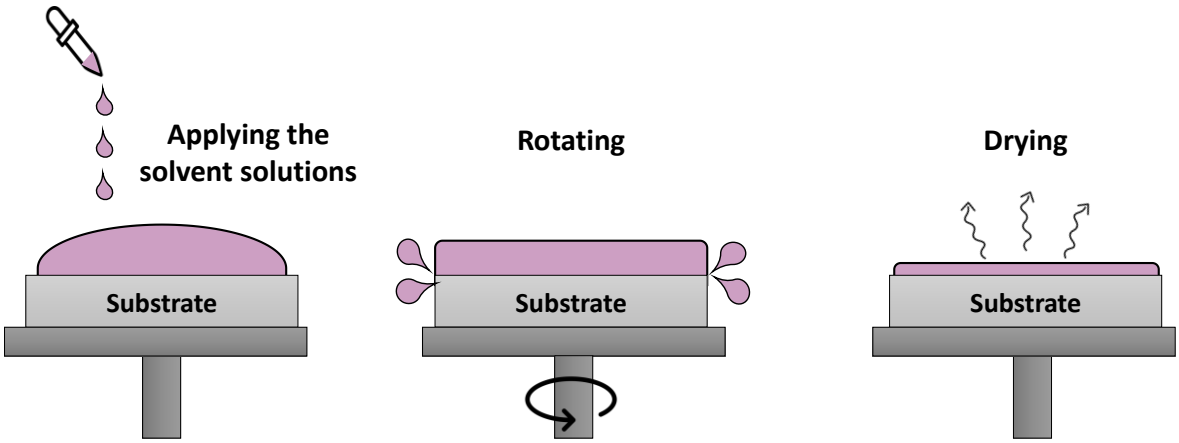

Figure 1.7. Schematic representation of the spin-coating technique.

- Spray coating

Spray coating involves vaporizing an OSC solution using a high-pressure gas carrier, often N_2 (**Figure 1.8**). This method is a widely used industrial technique for coating target materials such as glass, metal, and plastic.[51] The thickness and morphology of the layer produced by this method are affected by several factors, such as air pressure, solution viscosity, solvent characteristics, gun tip geometry, and distance between the nozzle and the substrate. This procedure can be used to cover large areas, but it often results in rougher and thinner sheets than spin coating.

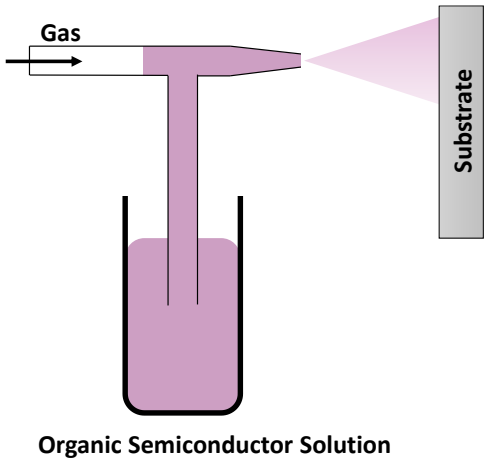

Figure 1.8. Schematic representation of the spray coating technique.

- Inkjet printing

Inkjet printing operates by creating droplets of an OSC solution through fluid surface tension. These droplets are then propelled from a jet nozzle to cover the required surface area of the substrate (**Figure 1.9**). Inkjet printing enables the deposition of a wide range of materials and the construction of multilayered and patterned structures.[52,53] However, controlling droplets through formulation can be quite challenging.

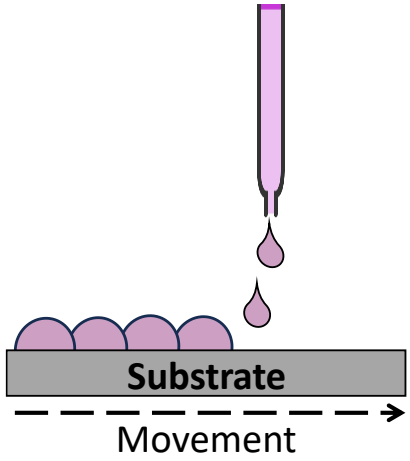

Figure 1.9. Schematic representation of inkjet printing.

- Meniscus-guided printing techniques

Meniscus-guided methods are used to induce the creation of a thin layer by translating a solution meniscus over a substrate. The overconcentration of semiconductor material in the solution is caused by OSC ink displacement and solvent evaporation. Once the supersaturation point is reached, the OSC precipitates and starts to crystallize along the evaporation line front.[54–56] There are several approaches based on how the meniscus is created and restricted. The following methods are commonly used for meniscus-guided coating: dip-coating, zone-casting, blade coating, and bar-assisted meniscus shearing (**BAMS**). A brief review of each method is provided below.

- Dip coating

Dip coating is a laboratory-scale procedure that involves dipping the substrate in an OSC solution and gently removing it to produce a thin, organized layer (**Figure 1.10**). The substrate is then raised, pushing the OSC and creating a homogenous layer on the substrate's surface.[57,58] The solvent evaporation rate and crystallization can be controlled

by adjusting the solvent, concentration, solution bath temperature, and withdrawal speed. Although dip coating is suitable for covering large sample areas and often results in homogeneous thin films, it can be relatively expensive due to the need for a significant volume of the OSC solution.

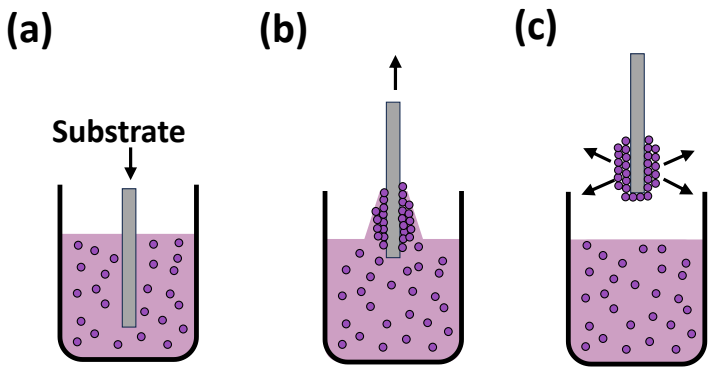

Figure 1.10. Schematic representation of the dip-coating technique: **(a)** Dipping, **(b)** withdrawal, and **(c)** evaporation.

- Zone-casting

Zone casting is the process that involves continuously depositing an OSC solution on a moving substrate using a flat nozzle (**Figure 1.11**).[59] The solvent evaporation from the meniscus zone may be regulated by altering the substrate temperature. At the same time, the solution's supply rate, concentration, and substrate speed all influence the film's eventual thickness and crystallinity. Although this approach is appropriate for large-scale manufacturing, it has significant drawbacks, such as a slow deposition speed (< 1 mm·s^{-1}), and the production of extremely anisotropic films.

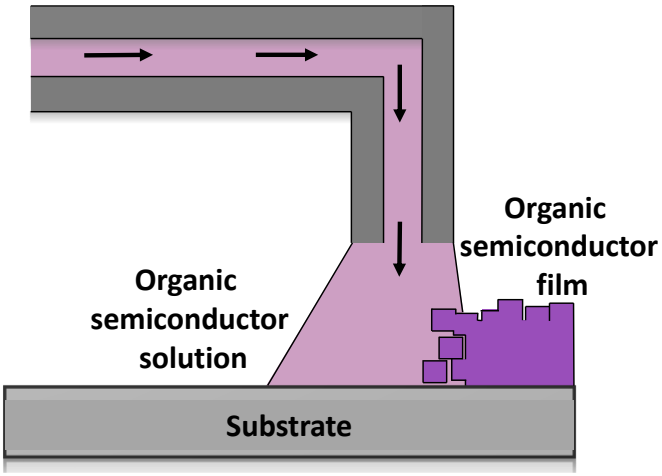

Figure 1.11. Schematic representation of the zone casting deposition technique.

- Blade coating

Blade coating is a process that involves spreading an OSC solution meniscus with a blade. A homogeneous coating is created by the movement of either the blade or the substrate, and heating the substrate can aid in solvent evaporation (Figure 1.12). The thickness of the coating is determined by the distance between the substrate and the blade. This technique can operate at high speeds (e.g., several meters per minute). Precision temperature control allows for rapid solvent evaporation once the film has formed.[60]

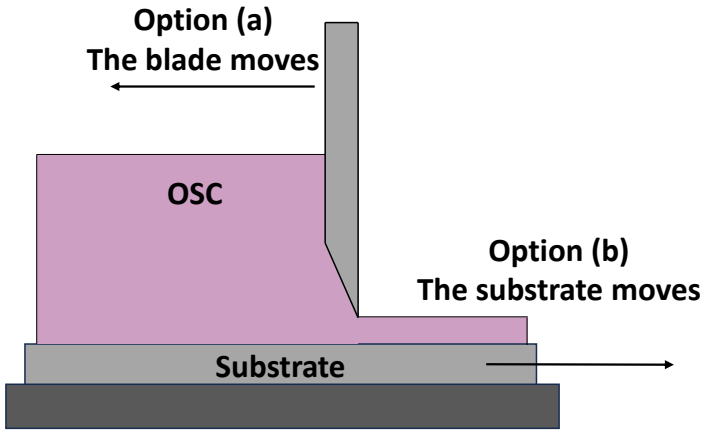

Figure 1.12. Schematic representation of the blade coating deposition technique.

- Bar-Assisted Meniscus Shearing technique

The Bar-Assisted Meniscus Shearing technique (BAMS) was developed by our research group as a variation of the blade-coating approach. This technique distinguishes itself from conventional blade coating methods by forming a liquid meniscus between the substrate and a rounded bar. The solution is progressively introduced between the bar and the substrate, allowing a liquid meniscus to develop. Horizontal movement of the bar or the substrate is then used to create a uniform thin layer (Figure 1.13). Depending on the solvent used and the crystallization regime desired, the hot plate temperature is selected. The thickness of the resulting film is influenced by several factors, including the speed of the bar relative to the substrate, the temperature, the distance between the bar and the substrate, the viscosity of the OSC solution, and the surface tension of the solution. This method has been successfully exploited using a wide range of OSCs and OSC blends containing insulating polymers. Its simplicity and the fact that post-coating treatments are not required, make it a promising approach for processing OSC thin films

with high crystallinity over large regions. A typical example of a thin film coated by BAMS is given in Figure 1.14.

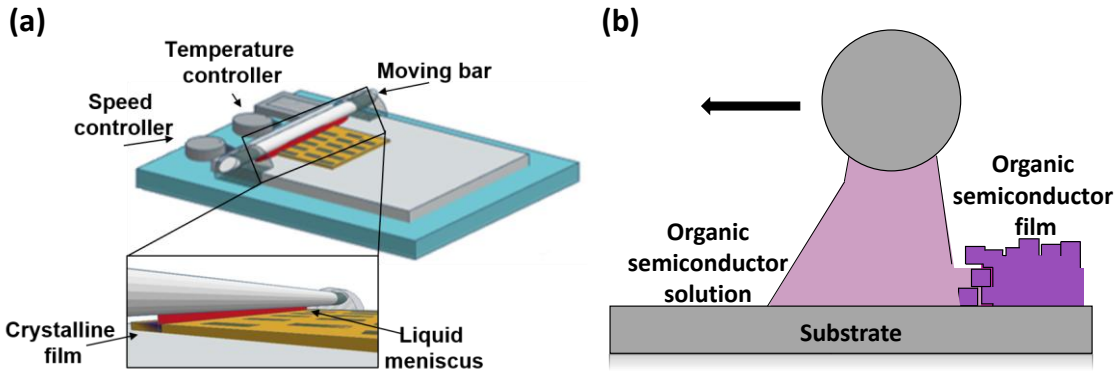

Figure 1.13. Schematic representation of BAMS technique.

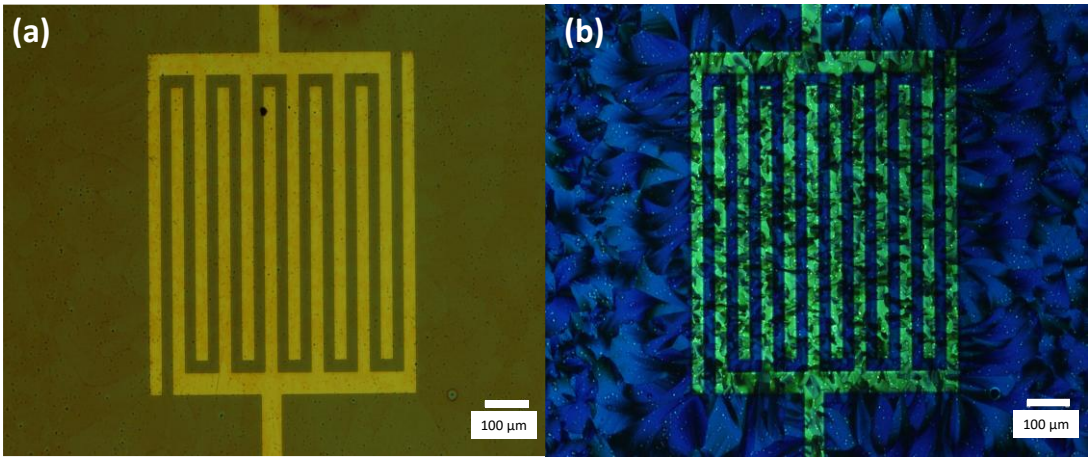

Figure 14. Polarised optical microscope images of a typical thin film coated by BAMS based on a diF-TES-ADT:PS blend. **(a)** polarized/analyzer= 0° and **(b)** polarizer/analyzer= 90°. The scale bar corresponds to 100 µm.

3. Organic transistors: operating principles and characterization

Transistors are primarily valued for their capacity to amplify and control input signals. Among the various types of transistors, field-effect transistors (**FETs**) are the most prevalent due to their responsiveness to changes in surface potential. The metal oxide semiconductor field-effect transistors (**MOSFETs**) are the most widely employed configuration in both digital and analog circuits. A MOSFET (**Figure 1.15**) consists of two electrodes, known as the source (S) and drain (D), which are separated by a semiconductor material, typically silicon. The current flowing between the source and drain can be controlled by applying a voltage to the oxide-insulated gate electrode. The threshold voltage necessary to turn on the transistor is determined by the specific metal and semiconductor materials used in its construction.

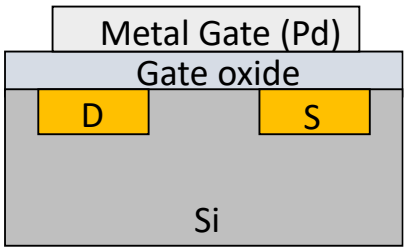

Figure 1.15. Schematic representation of a MOSFET.

Likewise, organic field-effect transistors (OFETs) are devices with three terminals: source, drain, and gate. Likewise, organic field-effect transistors (OFETs) are devices with three terminals: source, drain, and gate. The active layer in these transistors is composed of an OSC, which can be a conjugated polymer or a small molecule. A dielectric layer separates the gate from the OSC. When a voltage is applied to the gate electrode, it generates an electric field that induces a thin layer of mobile charge carriers at the interface of the OSC and the dielectric. Consequently, the gate terminal effectively regulates the charge density within the semiconductor channel, influencing its electrical conductivity. By applying a voltage between the drain and source terminals, charge carriers can move through the semiconductor channel.[46,61,62]

Figure 1.16 presents the energy band diagrams for ideal p-type and n-type OFET. The Fermi level (E_F) represents the energy level at which there is a 50% probability of electron occupancy, according to the Fermi-Dirac distribution. The work function ($ø_{WF}$) of metals is defined as the energy required to remove an electron from the Fermi level to

the vacuum level, while the ionization potential (IP) of an OSC indicates the energy needed to extract an electron from the highest occupied molecular orbital (HOMO) to the vacuum level.[61] In an ideal p-type OSC, when no voltage is applied to the gate terminal there are no mobile charges, and, consequently, charge transport does not occur, even when a potential is applied between the source and drain. However, when a negative voltage is applied between the source and gate (V_{GS}), the HOMO level bends upward in energy to align with the E_F of the source electrode, and then holes begin to accumulate at the semiconductor-insulator interface. At this stage, applying a negative potential between the source and drain (V_{DS}) allows the holes to flow toward the drain terminal.[61,62] For an n-type OSC, similar phenomena occur but involving the lowest unoccupied molecular orbital (LUMO) level, and the application of positive voltages are required.

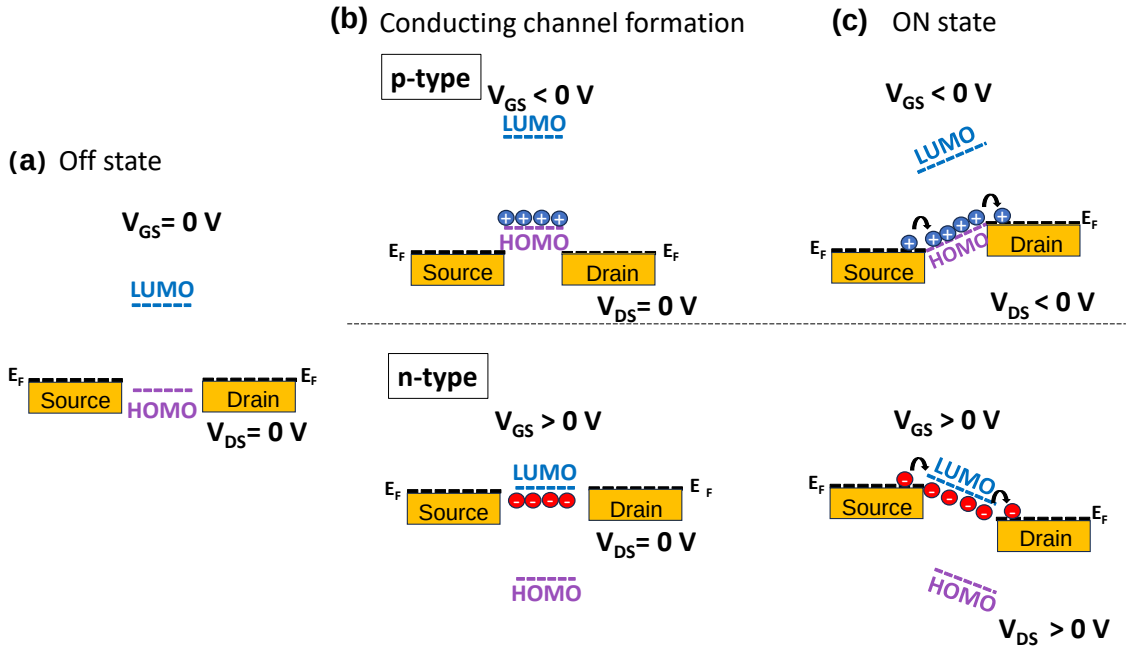

Figure 1.16. Illustration of the operational principles of an OFET. **(a)** The device in off-state, when no V_{DS} and V_{GS} are applied, **(b)** charge accumulation of charges within in the semiconductor channel upon the application of a gate-source voltage, and **(c)** drain current flowing through the transistor channel after applying a drain-source voltage.

3.1. OFET devices geometry

An OFET typically consists of three components: a thin layer of an OSC, a gate dielectric, and three electrodes. These components can be arranged in four distinct configurations, the nomenclature of which specifies the location of the three electrodes (source, drain, and gate) with respect the OSC: **(a)** bottom-gate bottom-contact (BGBC), **(b)** bottom-gate top-contact (BGTC), **(c)** top-gate bottom-contact (TGBC), and **(d)** top-gate top-contact (TGTC) (**Figure 1.17**).[61]

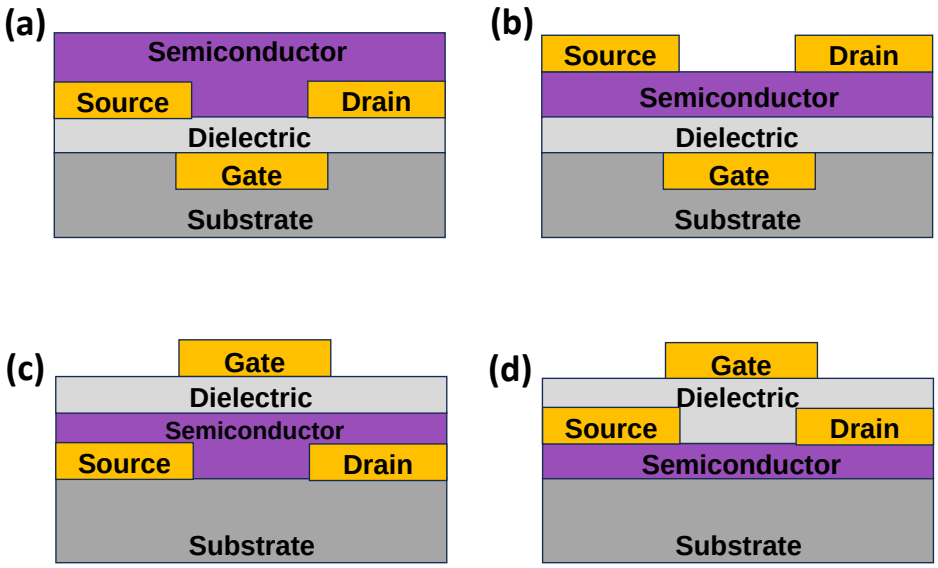

Figure 1.17. (a) Bottom-gate bottom-contact (**BGBC**), **(b)** bottom-gate top-contact (**BGTC**), **(c)** top-gate bottom-contact (**TGBC**), and **(d)** top-gate top-contact (**TGTC**) OFET geometries.

Device configuration can have an impact on OFET performance. For instance, devices with BGBC and TGTC architecture may experience increased contact resistance because the contact area between the organic semiconductor channel and the source injection electrode is limited. In TC configurations, metal electrodes are generally deposited using a shadow mask as the last step of the fabrication process. This technique often leads to a reduction in contact resistance since it increases the total interface area between the metal and the OSC, enhancing charge injection efficiency. Additionally, TG designs encapsulate the device, providing improved protection for the OSC against detrimental environmental factors.[63,64] The BGBC design is the most preferred choice for easy and speedy testing of OSCs.

3.2. Main device electrical characteristics

Horowitz et al.[65] developed a mathematical model to describe the current-voltage characteristics of OFETs, based on the principles of MOSFETs. However, this model relies on several assumptions that may not always align perfectly with the behavior of OFETs. Firstly, it presumes that charge carrier mobility (μ) remains constant throughout the operation of the device. In reality, OFETs often exhibit gate-bias-dependent mobility, likely due to the charge transport mechanism present in organic materials.[66] Secondly, the model assumes that the electric field along the channel, governed by the source-drain voltage, is negligible compared to the electric field across the channel, which is determined by the source-gate voltage. This is known as the gradual channel approximation. This assumption holds when the channel length (L) is significantly greater than the thickness of the insulator. Lastly, the model assumes that the contact between the metal electrodes and the OSC is purely Ohmic, overlooking any parasitic contact resistances that may be present.[62]

OFETs can operate in two modes based on the distribution of charge carriers within the channel. When a small drain voltage ($V_{DS}<<V_{GS}-V_{th}$) is applied, the density of charge carriers becomes proportional to both the I_{DS} current and V_{DS}. This leads to the transistors functioning in a **linear mode**, as explained in the following details:

$$I_{DS,lin} = \frac{W\mu C_i}{L}(V_{GS} - V_{th})V_{DS} \quad \text{if } (V_{DS} \ll V_{GS} - V_{th}) \qquad \textbf{Eq. 1.2}$$

where $I_{DS,lin}$ represents the drain-source current in the linear region. The variables W and L refer to the width and length of the channel, respectively, μ denotes the field-effect mobility and C_i is the gate capacitance per unit area. The parameters V_{GS}, V_{DS}, and V_{th} correspond to the gate-source voltage, drain-source voltage, and threshold voltage, respectively.

As V_{DS} increases, the concentration of charge carriers near the drain electrode decreases. When the condition $V_{DS}=(V_{GS}-V_{th})$ is achieved, the charge density at the drain electrode becomes zero, causing the channel to enter a state known as “pinch-off” (P). This pinch-off point signifies the maximum value of I_{DS}, as it remains constant even with a further increase in the drain voltage V_{DS}. At this point, the transistor enters in the

saturation regime. The saturation current ($I_{DS,sat}$) can be expressed using the following equation:

$$I_{DS,sat} = \frac{W\mu C_i}{2L}(V_{GS} - V_{th}) \quad \text{if} \quad (V_{DS} > V_{GS} - V_{th}) \qquad \textbf{Eq. 1.3}$$

The current-voltage relationship described by these two equations is effectively illustrated through the two primary measurements conducted in OFETs: **(a)** the **output** characteristics, where V_{DS} is varied while maintaining a constant V_{GS}, and **(b) the transfer** characteristics, where V_{GS} is altered while keeping V_{DS} constant (**Figure 1.18**).

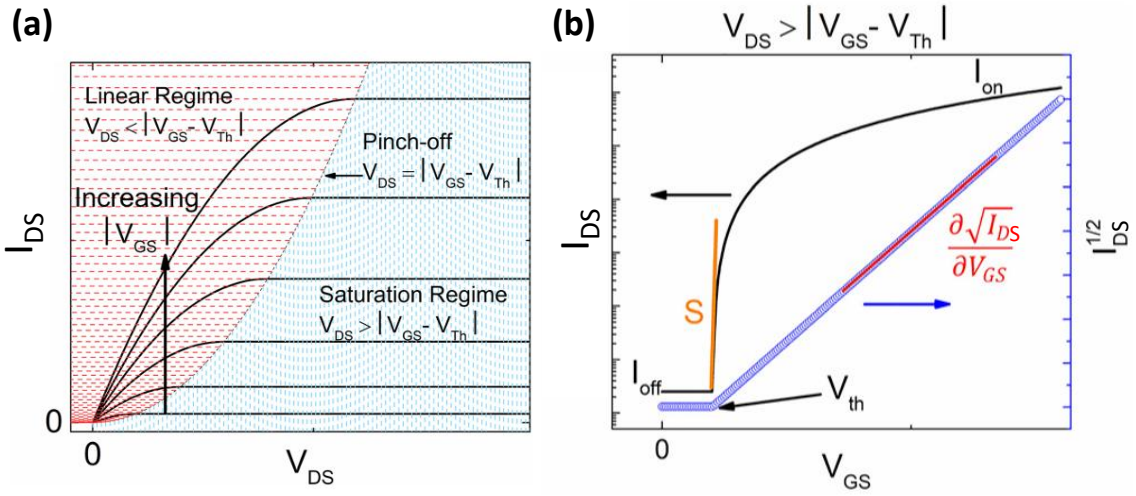

Figure 1.18. (a) The output characteristics and **(b)** the transfer characteristics in the saturation regime of an ideal OFET.[67]

3.3. OFET parameters and device performance

The electrical performance of an OFET, a multi-parameter device, can be described by several figures of merit, the parameters of which are usually analyzed to better understand the quality and performance of the device. Parameters include field effect mobility, threshold voltage, turn-on voltage, on/off ratio, subthreshold swing, and hysteresis.

- Field-effect mobility

The field-effect mobility, denoted as μ_{FE}, is the key parameter that defines the performance of OFETs. Charge mobility is essential for effective charge transport, as it indicates the extent to which the movement of charge carriers (such as electrons or holes) is affected by an applied electric field.[68] When a weak electric field is applied in a semiconductor, each charge carrier experiences a force of *-qE* (where *q* represents the elementary charge and *E* is the electric field), leading to acceleration along the direction of the field. This acceleration results in a velocity known as drift velocity, ν, which should be distinguished from the thermal motion of electrons.[18,68] The relationship between mobility and the applied electric field can be expressed as follows:

$$\mu = \frac{|\upsilon|}{|E|} \qquad \mathbf{Eq.\,1.4}$$

where υ represents the average drift velocity of charge carriers, while *E* denotes the applied electric field. Consequently, the unit of mobility is expressed as $cm^2 \cdot V^{-1} \cdot s^{-1}$. However, when the electric field exceeds 10^5 $V \cdot cm^{-1}$, the linear correlation between drift velocity and the applied electric field ceases to hold, leading to non-linear behavior.

In an OFET device, the mobility value should be close to the intrinsic mobility of the OSC material. However, real devices often have lower values due to flaws and parasitic resistances. Therefore, significant changes in mobility are common when measurements are taken under non-ideal conditions. Field-effect mobility is assessed using equations in the linear and saturation regimes, respectively, and μ can be extracted at each specific V_{GS} as follows:

$$\mu_{FE,lin} = \frac{L}{WC_i|V_{DS}|}\left(\frac{\partial I_{DS,lin}}{\partial V_{GS}}\right)V_{DS} = const \quad \textbf{Eq. 1. 5}$$

$$\mu_{FE,sat} = \frac{2L}{WC_i}\left(\frac{\partial\sqrt{I_{DS,sat}}}{\partial V_{GS}}\right)^2 V_{DS} = const \quad \textbf{Eq. 1. 6}$$

for linear (**Eq. 1.5**) and saturation (**Eq. 1.6**) regimes, respectively. An alternative way is to calculate the device mobility from the slope of the linear section of the I_{DS} versus V_{GS} plot (or $(I_{DS})^{1/2}$ versus V_{GS} in the saturation regime), which provides a fair approximation but lacks information regarding μ_{FE}'s reliance on V_{GS}.

- Threshold voltage and switch-on voltage

In OFETs, the threshold voltage is defined as the minimum gate-source voltage required to produce a significant drain current. The threshold voltage can be extracted from the transfer characteristics by a rearrangement of equations (**Eq. 1.5**) and (**Eq. 1.6**), as shown for the field-effect mobility calculation.

On the other hand, the switch-on voltage (V_{ON}) is defined as the V_{GS} at which the conductive channel starts to develop and can be calculated using the log(I_{DS})-V_{GS} plot. I_{DS} does not depend on the gate voltage below $|V_{ON}|$, but it suddenly increases for V_{GS} values above V_{ON}. In an ideal OFET, $V_{th,}$ and V_{ON} should have the same value, and both parameters should be zero.

- On/Off ratio

The ratio of the off-current (the current measured when the device is inactive), I_{off}, and the on-current (the highest source-drain current), I_{on}, is an important parameter for assessing the performance of OFETs. A high-performance OFET should have a high $I_{On/Off}$ ratio, ideally falling within the range of 10^6-10^7. This ratio is critical as it indicates the device's current amplification characteristics and its ability to switch between on and off states effectively.[61]

- Subthreshold swing, SS

The subthreshold region refers to the response of I_{DS}/V_{GS} at gate voltages that fall below the threshold voltage. This region is crucial as it provides insights into the effectiveness of charge accumulation once a gate voltage is applied. It serves as an indicator of how quickly the device transitions to an 'on' state in response to the gate voltage. Specifically, it is defined as the voltage necessary to increase the source-drain current by one order of magnitude, as shown in the following equation:

$$SS = \frac{\partial V_{GS}}{\partial(\log I_{DS})} \qquad \textbf{Eq. 1. 7}$$

A small value of SS would allow the device to switch with small voltage changes, reducing the gadget's power usage. Furthermore, SS is a reliable indication of trap density at the OSC/dielectric interface.[61]

- Hysteresis effect

Hysteresis is a comparison of the difference in I_{DS} values for the same V_{GS} between forward and reverse scans of the transfer characteristics. This parameter is considered a negative consequence of the OFET characteristics. The direction of hysteresis, whether it is 'clockwise' or 'anti-clockwise', depends on whether the backward scan has a higher or lower current than the forward scan. Hysteresis is heavily influenced by measurement parameters such as sweep rate, step width, and delay time. Furthermore, the electrical response may exhibit hysteresis due to various physical processes. These include charge trapping at the interfaces of the OSC/dielectric and OSC/electrode, as well as the slow reaction of mobile charge carriers.

Device performance is generally optimized in terms of all of the factors discussed above, taking into account OSC crystallization, dielectric and electrode material selection, and contact with the semiconductor layer. However, if this optimization is not fully completed, various unwanted consequences in OFET characteristics might be noticed, mostly related to charge trapping and charge injection difficulties.

4. Bioelectronics

Organic bioelectronics has arisen as a novel and intriguing topic in which the distinguishing properties of organic semiconductors are investigated and used at the interface with biological systems. Devices that include electrolytes in their structure have been demonstrated to be effective vehicles for researching mixed electronic/ionic conduction and interacting with a biological medium, bacteria, mammalian cells, animals, and plants. Many multidisciplinary groups are currently investigating the potential applications of these organic electronic devices in biosensors, neuronal interfaces, drug delivery devices, and tissue engineering structures.[69] Different transistor-like organic devices have been employed for bioelectronics applications, such as ion-sensitive and chemically field-effect transistors and electrolyte-gated field-effect transistors.

4.1. Ion-sensitive and chemically-sensitive field-effect transistors

The development of effective technologies for identifying and quantifying chemical and biological compounds for process control and environmental monitoring is becoming increasingly important. Ion-sensitive field-effect transistors (**ISFET, Figure 1.19 (a)**)[70] have been developed since the 1970s. In essence, an ISFET is a metal-oxide field-effect transistor (MOSFET) with a reference electrode that separates the gate connection from the silicon substrate. On the other hand, organic ISFETs (**ISOFETs**, **Figure 1.19 (b)**) have a lower production cost and other benefits such as compatibility with mechanical flexible substrates.[71]

The ion-sensitive FET (ISFET) detects ion concentration in a solution by measuring changes in output current. Its operational principles rely on an ion-selective membrane placed atop the gate dielectric, an electrolyte solution, and a reference electrode immersed in the solution, which acts as the gate electrode. This membrane selectively allows certain ions with a low energy barrier to pass through the membrane-solution interface while effectively blocking other ions that have a high energy barrier.[62,72] When the concentration of the target ions varies, these ions diffuse across the membrane following the concentration gradient, while other ions remain restricted. Consequently, this diffusion leads to changes in the interfacial potential at the source-gate junction, resulting in modifications to the conductivity of the ISFET channel.

A device variation of an ISFET is the so-called chemically sensitive FET (**ChemFET, Figure 1.19 (c)**), which is sensitive to substances other than ions. A ChemFET is used as a sensor to assess chemical concentrations in solution.[73,74] The current through the transistor varies in proportion to the concentration of the target analyte. The analyte solution separates the source and the gate (or reference) electrodes.[75] A semipermeable membrane on the FET's surface contains receptor moieties that preferentially bind to the target analyte, resulting in a concentration gradient between the solution and the gate electrode. This concentration gradient generates a chemical potential between the source and gate, which is detected by the FET.

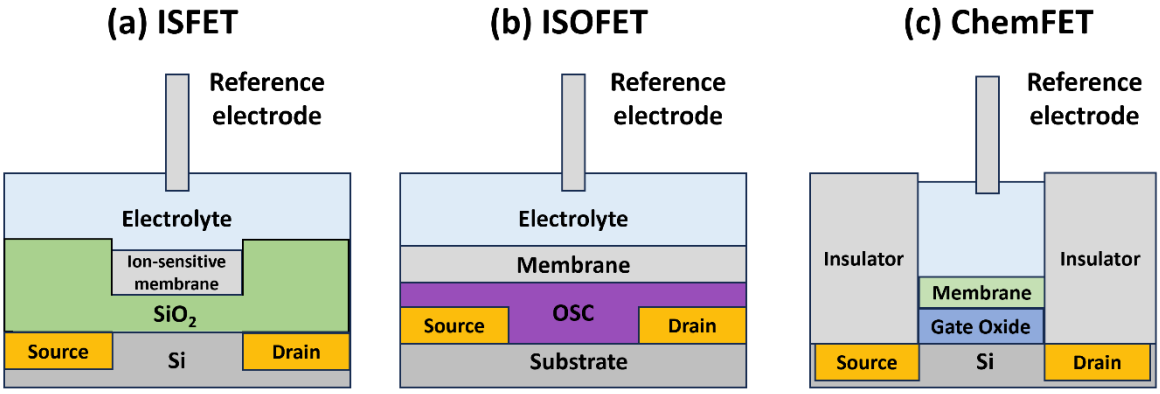

Figure 1.19. Schematic representation of an **(a)** ISFET, **(b)** ISOFET, and **(c)** ChemFET.

The previously mentioned ISFETs and ChemFETs were originally based on inorganic materials, specifically silicon semiconductors, but organic versions (ISOFETs) have been produced in recent years.[76,77] So far, the majority of research in this field has focused on devices that combine an organic semiconductor with an inorganic gate dielectric, such as Si_2N_4 or Ta_2O_5, to offer hydrogen ion selectivity.[78]

4.2. Electrolyte-gated transistors

As previously mentioned, a field effect transistor (**FET**) is a device with three terminals, where the current flowing between the source and drain electrodes, referred to as the channel, is regulated by a third terminal known as the gate electrode. The channel's conductivity is influenced by the capacitively coupling of the gate electrode to the channel and generating an electric field through an insulator. Alternatively, the dielectric can be replaced by an electrolyte, through which the gate electrode is capacitively coupled to the device channel, leading to an **electrolyte-gated field effect transistor (EGFT)**. In 1984, Wrighton and colleagues,[79] developed electrolyte-gated transistors, **EGTs**, using polypyrrole, an organic semiconductor that allows ion permeability. Unlike ion-sensitive field-effect transistors,[80] which include an insulating layer between the semiconductor and the electrolyte, EGTs facilitate direct contact between the electrolyte and the semiconductor. The design allows for direct interaction between ions and electrical charges present in the channel material.

EGFETs are capable of working with both inorganic and organic materials, such as amorphous oxides,[81] transition metal dichalcogenides,[82] graphene,[83] nanotubes,[84] organic small molecules, and polymers.[85] However, for ion-permeable semiconductors, the ionic-electronic interaction takes place across the three-dimensional volume of the material channel. The devices operating in this operational mode are addressed as electrochemical transistors.[86,87] Ion-permeable channels are now based on organic mixed ionic-electronic conductors, which are typically polymers capable of solvating and transporting ions.[88,89]

Organic bioelectronic sensors are widely recognized in increasing popularity because they can combine high-performance sensing with cheap manufacturing on large-area flexible substrates, allowing for low-cost health monitoring and diagnosis. In biological recognition, **electrolyte-gated organic field-effect transistors** (**EGOFETs**) and **organic electrochemical transistors** (**OECTs**) stand out because of their ease of fabrication and operation. Both EGOFETs and OECTs are being studied for biosensing applications. EGOFETs were recently demonstrated to be capable of performing label-free single-molecule detections, even in serum.[90] The main appealing characteristics of these devices are **(a)** low-cost processability, **(b)** the ability to employ biocompatible and flexible

materials for implantable and wearable devices, **(c)** intrinsic signal amplification, **(d)** low working voltages, and **(e)** label-free and fast response.

The EGFTs architecture for the fabrication of biosensors varies depending on the application, but they always share at least two characteristics:[90] the first one is that devices operate in electrolytes or in even body fluids. To guarantee that the devices perform well under these conditions, the devices' materials and structures must be strategically designed. And, secondly, EGFTs include a layer of biological recognition components through a biofunctionalization process that selectively binds to the analyte of interest. It might be, for example, a biomarker that is useful in diagnostic or prognostic applications.

The gate contact in EGTs does not need to be positioned directly in front of the channel because charge modulation occurs due to the accumulation or depletion of ions within the electrolyte. Consequently, in EGTs, the gate can be placed laterally, that is in the same plane as the source and drain electrodes, significantly simplifying the fabrication process.[91] EGTs can be constructed in various device architectures, depending on the gate electrode's location relative to the semiconductor channel, as follows:

- In the top-gated configuration, the gate is situated directly above the channel (**Figure 1.20 (a)**). The electrolyte can consist of a biological fluid, allowing for the direct assessment of its chemical, biological, or ionic characteristics through the EGT. This layout is employed in applications such as electrophysiology,[92,93] ion detection,[94,95] and neuromorphic [96,97] computing.
- A variation of the top-gated EGT features a bio-layer integrated into the gate electrode (**Figure 1.20 (b)**). This configuration is frequently used to create highly sensitive label-free biosensors, where protein probes like antibodies, peptides, and enzymes, or genomic probes composed of DNA or RNA molecules,[98,99] are attached to the gate to selectively bind and detect the target biomarker.
- A top-gated EGT with a biolayer placed on the top of the channel (**Figure 1.20 (c)**), is commonly employed for cell monitoring[100,101] and biosensors, where the biofunctionalization of the semiconducting channel is deemed more preferred.
- A design where the bio-layer is in the electrolyte rather than the gate or semiconductor surface (**Figure 1.20 (d)**) can monitor cell membrane tight junctions[102,103] and selectively detect and monitor ions.[104,105]

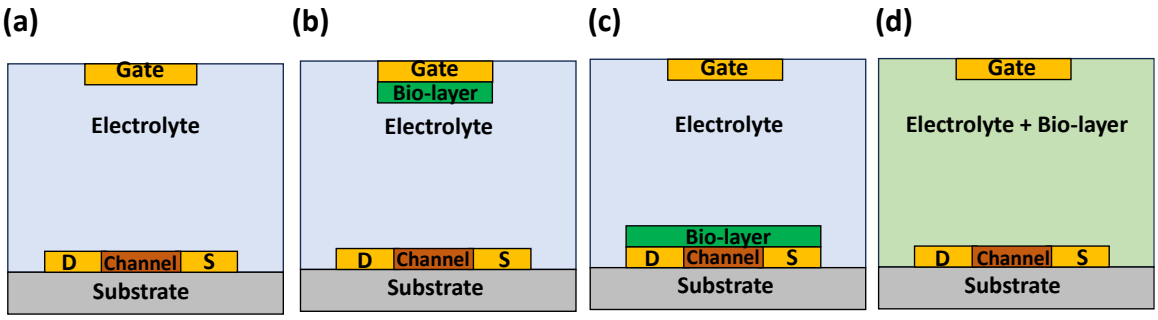

Figure 1.20. Basic architectures of an Electrolyte-Gated Transistor (EGT). **(a)** top-gated architecture, **(b)** top-gated EGT with a bio-layer on the gate electrode, **(c)** top-gated EGT with a bio-layer on the transistor channel, **(d)** top-gated EGT with a bio-layer included in the electrolyte. Adapted from ref[106].

- In the less common bottom-gate construction, an ion-conducting membrane (a solid electrolyte) separates the metallic gate from the semiconductor channel[107] (**Figure 1.21 (a)**). This design may be used in physiological recording when a bio-compatible semiconductor channel (PEDOT: PSS) is brought into close contact with human tissue, as for when monitoring neurological activity.[108]
- A side-gated arrangement places the gate in the same plane as the semiconductor channel[109,110] (**Figure 1.21 (b)**). This design is often used for neuromorphic applications or biosensing applications when a bioreceptor is incorporated.[111,112] In this case, the side gate can function as a global gate, biassing many adjacent semiconductor channels.
- The extended gate (or floating gate) design (**Figure 1.21 (c)**) features two distinct electrolyte compartments (I and II) linked by a gold electrode with two pads. In this setup, the floating gate is capacitively coupled to both the semiconductor channel and the control gate through the electrolyte.[113] This floating gate configuration is primarily employed for biological or chemical sensing, although it has also been applied for other purposes, such as transducing cell electroactivity.[116] In the context of biological sensing, capture molecules are immobilized on the arm of the floating gate located in electrolyte compartment II. When target molecules are introduced into compartment II, they bind to the functionalized pad, generating a signal in the EGT. The separation of the two compartments prevents direct contact between the target molecules and the semiconductor channel in compartment I, thereby reducing the risk of non-specific adsorption on the semiconductor.

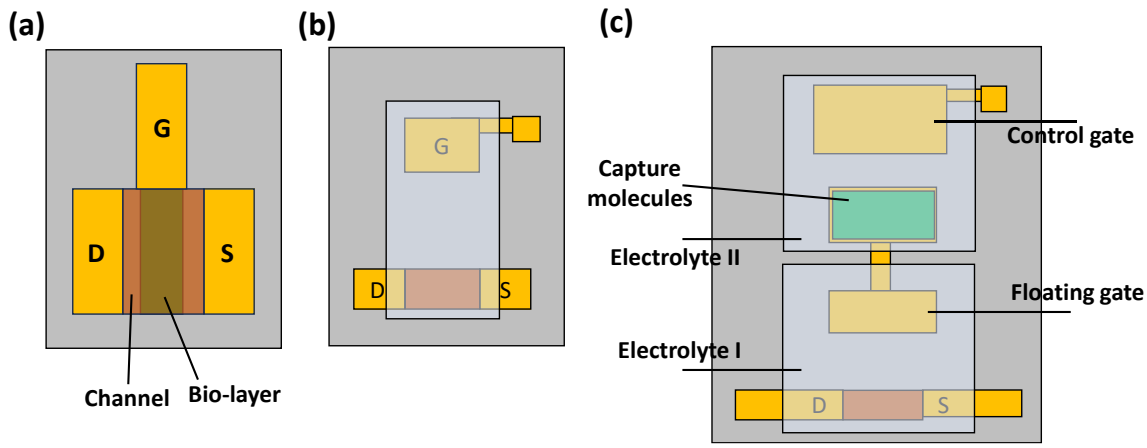

Figure 1.21. Bottom-gated EGT architecture **(a)**, side-gated EGT architecture **(b)**, and extended gate (or floating gate) EGT architecture **(c)**. Adapted from ref[106].

If the EGT is to be employed for selective biomolecule detection, the gate or floating gate must be chemically functionalized with capture molecules (i.e., bio-receptors). The electrode can be functionalized by immersing it in the receptor solution,[117,118] or by exposing the electrode to the receptor solution using a PDMS well or a microfluidic cell.[115,119]

4.2.1. Organic electrochemical transistors (OECTs)

Electrolyte-Gated Transistors based on organic mixed ionic-electronic conductors are called Organic Electrochemical Transistors (**OECTs**). These are three-terminal devices with a conducting polymer connecting the source and drain electrodes. The gate electrode and the polymer are separated by an electrolyte (**Figure 1.22**). Their functioning relies on the doping and dedoping processes of the polymer, which result in variations in conductivity. Initially, these devices were fabricated by electropolymerizing the polymer onto microelectrodes, but nowadays it is more common the print of conducting polymers such as polypyrrole,[79] polyaniline,[120] and polythiophene.[121] However, the most predominant material semiconductor used in OECTs is poly(3,4-ehtylenedioxythiophene) doped with poly(styrenesulfonate) (**PEDOT: PSS**), thanks to its high ionic and electrical conductivity.[122]

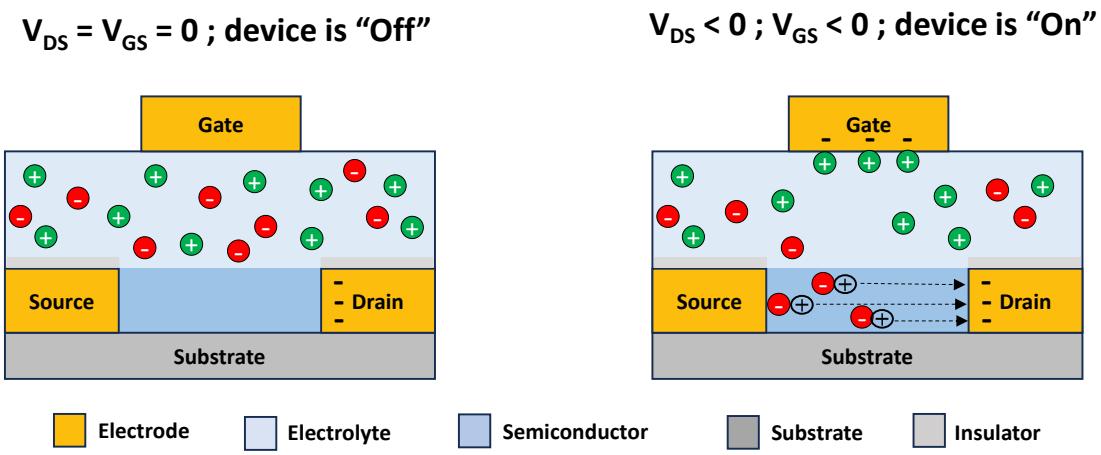

Figure 1.22. Operating principle of a p-type organic electrochemical transistor (OECT) operating in accumulation mode, highlighting the formation of an electrical double layer across the bulk of the organic semiconductor channel. Adapted from ref[123].

In contrast to Wrighton et al. initial study,[124–126] PEDOT:PSS OECTs are frequently 'on', which means that the presence of PSS causes PEDOT to conduct even when no gate voltage is applied and the device operates in the depletion mode. Hence, a gate bias induces cations from the electrolyte to enter the polymer bulk and neutralize the negatively charged sulfonate moieties on the PSS backbone. This reduces hole's density, resulting in reduced polymer conductivity and current across the channel. As a result, an OECT can transform an ionic current into an electrical current, making it an excellent instrument for monitoring biological processes. Furthermore, one of the key benefits of

OECTs is their capacity to function at extremely low voltages (less than 1 V), making them ideal for biosensing in aqueous conditions. This is because low voltages are required to avoid unwanted redox reactions of water or biomolecules.

4.2.2. Electrolyte-gated organic field-effect transistors (EGOFETs)

Electrolyte-Gated Organic Field-Effect Transistors (**EGOFETs**) were first reported in 2010 by Kergoat et al.[127] Since then they have subsequently garnered a great deal of attention and their development has progressed a lot in a relatively short period. These devices represent a sub-class of organic field-effect transistors (OFETs), where the dielectric materials are substituted with a liquid electrolyte, where the gate electrode is directly immersed in it. They function in accumulation mode, benefiting from the capacitive coupling between the gate electrode and the OSC layer through the electrolyte.

EGOFETs are ideal for biosensing applications where analyte molecules may be identified in liquid environments due to their high electrical double-layer capacitance (EDLC) that allows sub-voltage operation (< 0.5 V). Thus, EGOFET devices are capable of detecting biomolecules of interest in aqueous media such as saliva, blood serum, mucus, drinkable water, and so on, both in vivo and ex vivo. Such low operating window potential also makes EGOFET ideal for developing low-power devices.

The operational principle of an EGOFET is depicted in **Figure 1.23.** When a voltage is applied to the gate electrode, either cations or anions migrate toward the gate surface, forming an electrical double layer at the electrolyte/gate interface, depending on the voltage's polarity. Simultaneously, a second electrical double layer forms at the OSC/electrolyte interface due to the accumulation of charges in the OSC, which are opposite to the applied gate voltage. This setup allows for the flow of mobile charges through the OSC layer when a voltage is applied between the source and drain terminals.[62]

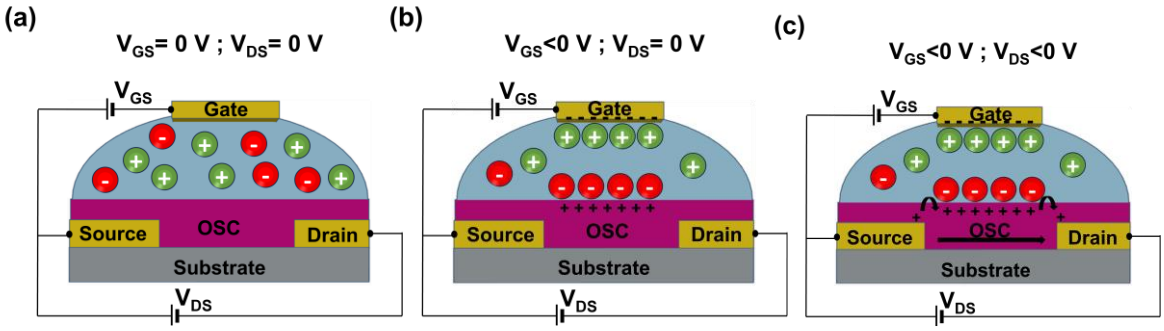

Figure 1.23. Schematic illustration of a p-type EGOFET device demonstrating the formation of electrical double layers. **(a)** No source-gate or source-drain voltage is applied to the device, **(b)** a negative potential at the gate terminal leads to the development of an electrical double layer at both the gate/electrolyte interface and the OSC/electrolyte interface, causing holes to accumulate at the OSC interface, and **(c)** a negative source-drain voltage enables the flow of the mobile holes along the active layer. Adapted from ref[62]

The capacitance of the electrical double-layer is crucial for understanding the low operating voltages of these devices. studies have indicated that the contact between an electrode and solution behaves analogously to a capacitor.[128] A capacitor consists of two conductive plates separated by a dielectric material, capable of storing electrical charge at the surface of the plates in contact with the dielectric when a potential is applied. The amount of charge stored is directly proportional to the applied voltage, governed by a proportionality constant known as capacitance, measured in Farads, as represented by the following equation:

$$C = \frac{Q}{V} \qquad \textbf{Eq. 1.8}$$

where *C* represents the capacitance, *Q* denotes the electrical charge, and *E* indicates the potential.

At a given potential, there exists a specific quantity of charge present both on the metal surface and within the solution, such that:

$$q^M = -q^S \quad \textbf{Eq. 1. 9}$$

where q^M represents the charge in the metal surface and q^S is the charge into the solution.

The separation of the charges results in the formation of an electrical double-layer, which is distinguished by a double-layer capacitance, C_{dl}.[128]

The Gouy-Chapman-Stern (GCS) model outlines the structure of the electrical double layer, which consists of several distinct regions on the solution side: (i) the inner layer, (ii) the outer layer, and (iii) the diffuse layer, illustrated in Figure 1.24. The inner Helmholtz layer (IHL) marks the distance x_1 from the metallic surface, where ions are adsorbed, preventing solvated ions from approaching this layer. The outer Helmholtz layer (OHL) is situated at a distance x_2 from the metal surface, representing the area where solvated ions can access but are non-specifically adsorbed. In this zone, the interaction between the charged plate and solvated ions is dictated solely by long-range electrostatic forces, remaining independent of the types of ions present. Together, the IHL and OHL form the Stern layer. The diffuse layer, also referred to as the Gouy layer, extends from the OHL into the bulk of the solution, where solvated ions diffuse due to thermal agitation.[129]

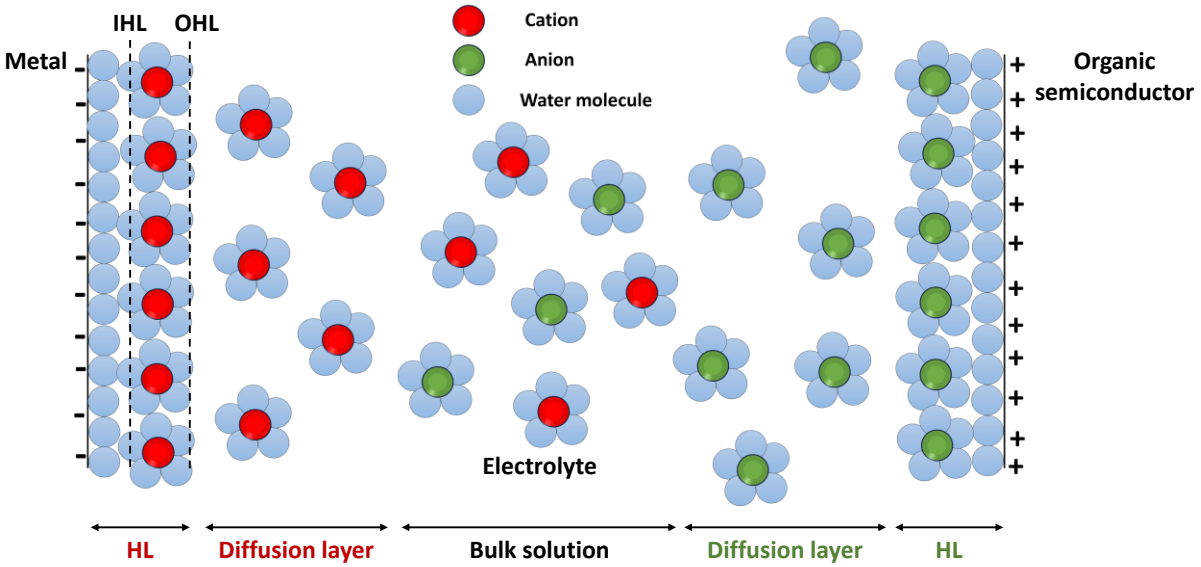

Figure 1.24. Illustration of the ion distribution within the Helmholtz layer (HL), the diffuse layer, and the bulk solution/electrolyte. Adapted from ref[130].

According to the GCS model, the capacitance of a single EDL consists of two contributions in series, as described in the following relation:

$$\frac{1}{C_{dl}} = \frac{1}{C_{Stern}} + \frac{1}{C_{Gouy}} \qquad \textbf{Eq. 1. 10}$$

where C_{Stern} is the capacitance of the Stern layer and C_{Gouy} is the capacitance of the diffuse layer.

The thickness of the diffuse layer is affected by the ionic strength of the solution. When the concentration of the solution exceeds 10^{-2} M, the diffuse layer thickness is generally less than 100 Å. The distance from the charged metal surface to the edge of the diffuse layer is known as the Debye length, which represents the distance required for ions in the solution to effectively neutralize the charge of the electrode. The Debye length is inversely proportional to the ionic strength of the solution, which can be expressed by the following relationship:

$$\lambda_D = \sqrt{\frac{\varepsilon_0 \varepsilon_r K_B T}{2 C_0 N_A e^2}} \qquad \textbf{Eq. 1. 11}$$

where ε_0 and ε_r denote the vacuum and the relative permittivity, respectively. K_B represents the Boltzmann constant, T is the absolute temperature, C_0 indicates the ionic strength of the solution, N_A is Avogadro's number and e is the elementary charge.

The inverse connection between the Debye length and the C_{dl} is as follows:

$$C_{dl} \sim \frac{1}{\lambda_D} \quad \textbf{Eq. 1. 12}$$

An increase in ionic strength results in a reduction of the Debye length and an increase in the C_{dl}. Typical values for electrical double-layer capacitance range from 10-40 $\mu F \cdot cm^{-2}$, which is significantly higher -by three orders of magnitude- than the capacitance of common dielectrics used in OFETs, such as SiO_2 and polymeric dielectrics, which typically fall within the $nF \cdot cm^{-2}$ range. The thickness of the electrical double layer enables liquid-gated transistors to function efficiently with very low source-gate and source-drain voltages, typically ranging from 1 V and -1 V.

The maximum voltage that can be applied in an EGOFET is primarily constricted by the electrolysis of the solution, particularly in the case of water-gated transistors is expressed as:[62,131]

$$H_20 \rightarrow 2H^+ + \frac{1}{2}0_2 + 2e^- \qquad E^0 = 0.57\ V \qquad \textbf{Eq. 1. 13}$$

$$2H_2O + 2e^- \rightarrow H_2 + 20H^- \qquad E^0 = -0.66\ V \qquad \textbf{Eq. 1. 14}$$

where the E^0 is the one concerning the Standardized Hydrogen Electrode (SHE).

EGOFETs have lower field-effect mobility than OFETs, with best-reported mobilities of 0.1-0.2 $cm^2 \cdot V^{-1} \cdot s^{-1}$.[132,133] For instance, the mobility of the EGOFET based on the OSC diF-TES-ADT blended with PS thin film, measured in water media has been reported to be 0.18 $cm^2 \cdot V^{-1} \cdot s^{-1}$.[132] Furthermore, because it is challenging to extract the double-layer capacitance values and their dependency on the applied voltage, it is more typical for EGOFET devices to report the product of mobility and effective double-layer

capacitance ($C_{eff}\cdot\mu_{FE}$), which can be directly extracted from the slope of the transfer curves. The $I_{On/Off}$ ratio in EGOFET devices ranges from 10^2 to 10^3.

The appealing features of EGOFETs, including their low operating voltages, inherent amplification capabilities, compatibility with biocompatible and flexible materials, and suitability for low-cost fabrication techniques, position them favorably for bioelectronics applications. Specifically, the use of EGOFETs as biosensors for detecting various biomarkers is gaining momentum due to their label-free operation, exceptional sensitivity, and high specificity. Numerous efforts have been directed toward creating innovative architectures for electronic biosensors and developing unique materials that facilitate the incorporation of active receptors into the devices while maintaining outstanding performance.[134,135]

4.3. Applications of electrolyte-gated organic field-effect transistors

In recent times, electrolyte-gated transistor (EGT) devices have gained traction as promising biosensing technologies.[106,136] They are being actively investigated for applications in clinical diagnostics and drug development.[106,137] The typical architecture of these detection devices features a gate electrode that is functionalized with biorecognition elements such as antibodies, aptamers, or enzymes, tailored to the specific target analyte.[106,138] Most detection experiments utilizing EGTs employ multiparametric steady-state analysis of transfer curves concerning the concentration of the target analyte.[139,140] By examining the change in one or more parameters against analyte concentration, a dose-response curve can be established. For instance, the relative change in current at a fixed gate voltage, referred to as the signal, can be plotted against analyte concentration, allowing the construction of isotherms and the extraction of thermodynamic properties. The simplicity of this approach lies on the fact that the EGT sensor is operated in thermochemical equilibrium with the electrolyte solution, making the measured signal proportional to the availability of recognition sites.

Integrating biomolecules into an electrical device is an important stage in the biosensor production process. Several variables influence the immobilization approach used, including the qualities of the biosystem and support material, the type of

transducer employed, and, most crucially, the application for which the sensor is intended. To ensure the vitality and functioning of the biomolecules, experimental variables such as temperature, ionic strength, and pH must be carefully controlled throughout immobilization and operation. Furthermore, effective immobilization is defined as anchoring in the optimal orientation to establish a high affinity for the target ligand and limiting non-specific adsorption.[141] Strategies that can lead to highly oriented structures and homogeneous covering of the surface, and that can provide well-exposed active sites for direct coupling with the target component are discussed below:[142]

- Physical absorption:

Biomolecules can be physically adsorbed onto various surfaces through hydrophobic, ionic, and van der Waals interactions. This adsorption process is straightforward and cost-effective for immobilizing biomolecules. For instance, proteins like antibodies can be directly adsorbed into noble metals such as gold, silver, and platinum, as well as on carbon materials like glassy carbon, carbon paste, and nanotubes, along with metal oxides and conductive or semiconductive substances.[141–143] the immobilization process involves exposing the support material to a protein solution under appropriate conditions, leading to an attractive interaction between the solid surface and the protein, resulting in surface coverage. While the simplicity of adsorption is an advantage, the ease of desorption can also be a drawback in some cases. However, this characteristic can be beneficial, as the ability to easily remove proteins from the substrate allows for effective regeneration of the system.

- Covalent binding:

A common method of protein immobilization involves establishing a covalent bond between the protein and the substrate. This technique typically utilizes functional groups such as carboxylic -COOH, hydroxyl -OH, amino -NH_2, and thiol -SH groups, to facilitate the covalent attachment of biomolecules to a solid support. The functional groups present on the surface of the material interact with corresponding groups on the exterior of the biomolecules, forming stable connections.[142,144]

- Affinity coupling:

Affinity binding methods provide enhanced control over both the orientation and density of biomolecules immobilized on a surface. One notable example is the avidin-biotin interaction, a robust non-covalent bond widely used for biofunctionalizing various

surfaces in bio-electronic detection systems. This strong interaction is particularly advantageous for improving the specificity and sensitivity of detection in biosensors.[142,145] For example, biotinylated molecules bind to avidin-modified surfaces, with streptavidin and neutravidin as common alternatives. Biotin can covalently link to various biomolecules (e.g., antibodies, peptides, DNA) and react with specific functional groups. Histidine-based methods (His Tag) enable site-specific immobilization, while Protein A/G systems bind antibodies but may reduce surface density.[141]

- Self-Assembled Monolayer (SAM):

Self-assembled monolayers (SAMs) are another commonly used way of immobilizing biomolecules. Self-assembly refers to the orderly organization of molecules on a surface. SAMs are generated by self-aligning certain molecules in two dimensions on surfaces, resulting in a quasi-crystalline structure. SAMs of alkanethiols on gold surfaces are among the most commonly utilized and well-established ones.[147] SAMs are used to either prevent or enhance protein immobilization.[146] The molecules used for the development of SAMs for biosensing feature two distinct functional groups: one that binds to the sensor's surface and another one that serves to anchor biomolecules. To modify gate electrodes with SAMs, the substrate is typically immersed in a dilute solution containing the SAM precursor molecules, which spontaneously interact with the surface forming a structured layer on the electrode. This approach allows for tailored surface properties and enhances the functionality of biosensors.[142]

Each of these methods offers distinct advantages and can be chosen based on the specific requirements of the bioelectronic application.

As mentioned before, OECTs and EGOFETs can be applied in biosensing. OECTs have been widely utilized to detect redox species including glucose,[148] gallic acid,[149] dopamine,[150] and uric acid.[151] This arrangement provides good sensitivity and selectivity, particularly in ion detection.[152] OECTs may operate as both amperometric and potentiometric sensors, making them extremely versatile in a variety of detecting applications. In contrast, EGOFETs use ion non-permeable electronic channel materials and, unlike OECTs, have only been suggested as potentiometric sensors.[90] This property makes them especially suitable in applications requiring the detection of analytes that do not engage in redox processes. Besides, EGOFETs have shown potential for pH

sensing[153,154] and biosensing of small toxic organic molecules,[139,155] proteins like interleukins,[156] and TNF-α, an inflammatory biomarker.[157]

The adoption of EGOFETs as biosensors for the detection of various biomarkers is rapidly increasing, primarily because of their label-free operational mode, exceptional sensitivity, and high specificity. In EGOFET biosensors, a recognition element, such as an antibody or an aptamer, needs to be immobilized at one of the critical interfaces, specifically either the gate/electrolyte or the semiconductor/electrolyte interface.[142] When binding occurs, the capacitive coupling facilitates the amplification of subtle electrostatic potentials, allowing even minor changes to be translated into significant variations in the transistor's performance metrics, such as drain current and threshold voltage.[90]

The initial efforts to integrate biomolecules into EGOFETs were primarily centered on the biofunctionalization of the OSC.[158–161] However, this approach was largely abandoned because most OSCs are inherently hydrophobic, making them unsuitable for hosting hydrophilic biomolecules, and prone to deterioration. Consequently, recent examples of EGOFET biosensors now focus on linking recognition moieties directly to the gate terminal, which is typically a gold electrode.[133,134,142,162,163]

For instance, Burtscher et al.[164] presented an overview of cytokine biosensing, emphasizing the benefits of organic electrical systems for monitoring inflammatory indicators. These indicators can be detected at ultralow concentrations under physiological settings, demonstrating the sensitivity and promise of EGOFETs in advanced biosensing applications. Another example is the work of Sensi et al.[165], who reported the first label-free EGOFET immunosensor that integrates a biological drug, named Nivolumab (Opdivo ©), as a specific recognition moiety to quantitatively and selectively detect anti-drug antibodies (ADAs) against the drug, being the theoretical limit of detection as low as 100 fM (Figure 1.25). This study suggests the potential for developing dose ADAs with a sensing platform that is portable, easily scalable, and customizable to meet clinicians' requirements. Additionally, it can function as a Point-of-Care (POC) test, requiring no specialized training for personnel to operate.

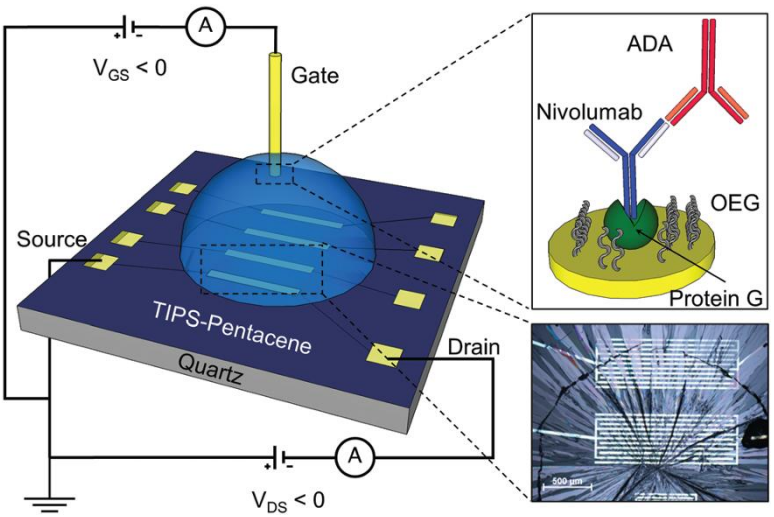

Figure 1.25. EGOFET and the gate functionalization scheme. The gate, as shown in the top inset, is functionalized with protein G and oligo(ethylene glycol) (OEG) monolayers to passivate the non-covered gold surface. The Fc region of Nivolumab antibodies binds the protein G, ensuring an effective orientation. Extracted from ref[165].

In the following table (**Table 1.1**) are reported different examples of EGOFETs developed for biosensing applications, where different materials have been used and, in the vast majority of studies, the gate electrode has been used to incorporate the biorecognition site:

Table 1.1. EGOFET devices used for biosensing applications. Extracted from ref[77]

Analyte	Channel material	Biorecognition site	Detection limit	Ref
IgG	P3HT	Gate	Single-molecule in 0.1 mL	[117]
Gluten	P3HT	Extended gate	20 ppM	[115]
Plum pox virus	Pentacene	Gate	180 pg mL^{-1}	[166]
Tryptophan	DB-TTF/PS blend	Gate	1 pM	[167]
C-reactive protein	P3HT	Gate	210 zM (13±4 molecules in 100 µL)	[163]
α-synuclein	DiF-TES-ADT/PS blend	Gate	0.25 pM	[168]
HIV-1 p24 capsid protein	P3HT	Gate	30 zM (2± 1 molecules in 100 mL)	[169]
α-fetoprotein	PDBT-co-TT	Channel	0.15 ng mL^{-1}	[170]
Anti-nivolumab antibody	TIPS-pentacene	Gate	100 fM	[165]
miRNA-21	TIPS-pentacene	Gate	35 pM	[171]
Streptavidin	C8-BTBT-C8	Channel	6 µg mL^{-1}	[172]
Neurofilament light chain	TIPS-pentacene	Gate	30 fM	[173]
Xylella fastidiosa	P3HT	Gate	2± 1 bacteria in 0.1 mL	[174]

EGOFET potential is not restricted to biosensing; it has been demonstrated that these devices may also be used as transducers in other applications such as in cell monitoring, neuromorphic applications, and electrophysiological activity:

- Cell monitoring and neuromorphic applications:

EGOFETs have not been frequently employed for cell monitoring, most likely due to their recent development and less frequent description when compared to OECTs, which have lately received significant attention for these types of applications.[175] EGOFETs have been commonly reported with top-gate configurations rather than side-gates, which may have restricted their application in cell monitoring. However, EGOFETs have recently emerged as highly effective technological platforms for sensing and stimulating living cells and organisms—for example, Zhang et al.[176] present a liquid-liquid dual-gate organic transistor designed for enhanced cell sensing capabilities, achieving

maximum transconductance (i.e. maximum amplification). In their device architecture, the threshold voltage of the top liquid-gated conduction channel is regulated by a bottom gate, which is insulated from the semiconductor with an Al_2O_3/SiO_2 bilayer gate dielectric. They have demonstrated that the dual-gate structure enables a much better sensor response to the detachment of human mesenchymal stem cells (hMSCs) (**Figure 1.26**).

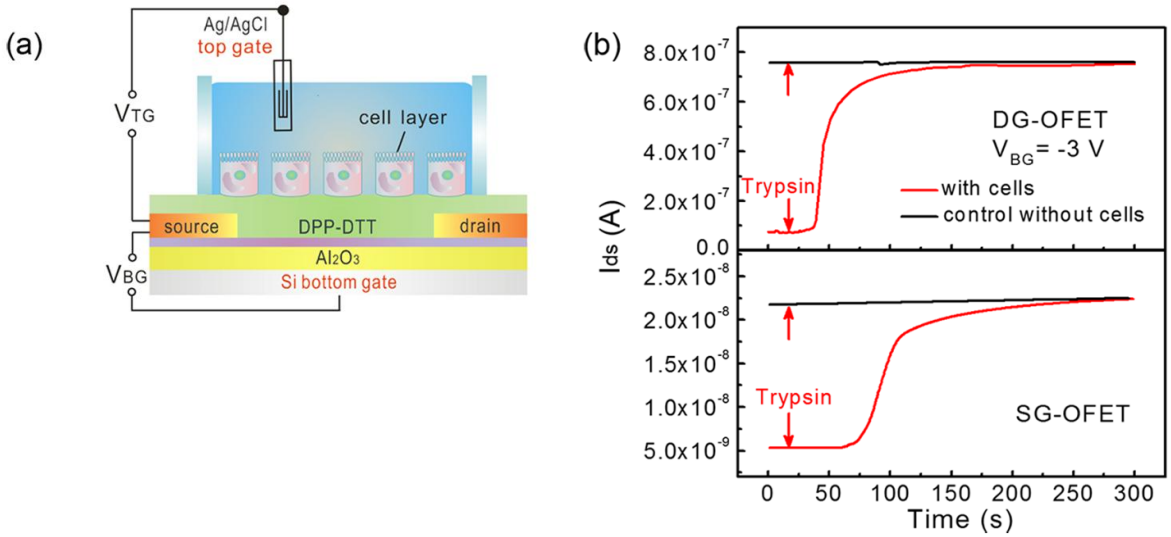

Figure 1.26. **(a)** Schematic diagram of the cell-sensing platform, **(b)** in situ responses of the DG-OFET (top) and SG-OFET (bottom) with (red line) and without (black line) hMSCs upon trypsin treatment. Extracted from ref[176].

EGOFETs with high capacitance present a promising substrate for neuromorphic circuits.[97] Cramer et al.[177] described the application of EGOFETs to stimulate and record signals from neural networks derived from murine stem cells. In their study, cell, cultures were grown and differentiated on specially constructed EGOFET, as illustrated in **Figure 1.27**. To control cell growth, a polystyrene pool was attached to the top of the pentacene film, with platinum wire functioning as the gate electrode. The design included four interdigitated source-drain electrodes on a single substrate; two were designated for signal recording, while the other two were used for stimulating the cell culture. Cramer et al.[177] found that once a population of neurons was established, the interconnected neural network could be activated, allowing for the aggregation of bioelectric signals to be recorded. This observation indicates that the device responds specifically to signals induced by neurons rather than undifferentiated stem cells. Such functionality is not only advantageous for interfacing or implanting neural signal transducers and electrical stimulation but also holds potential for stem cell-based treatments for spinal cord

injuries. Consequently, EGOFETs utilizing ultrathin pentacene films could emerge as promising transducers for neural activity.

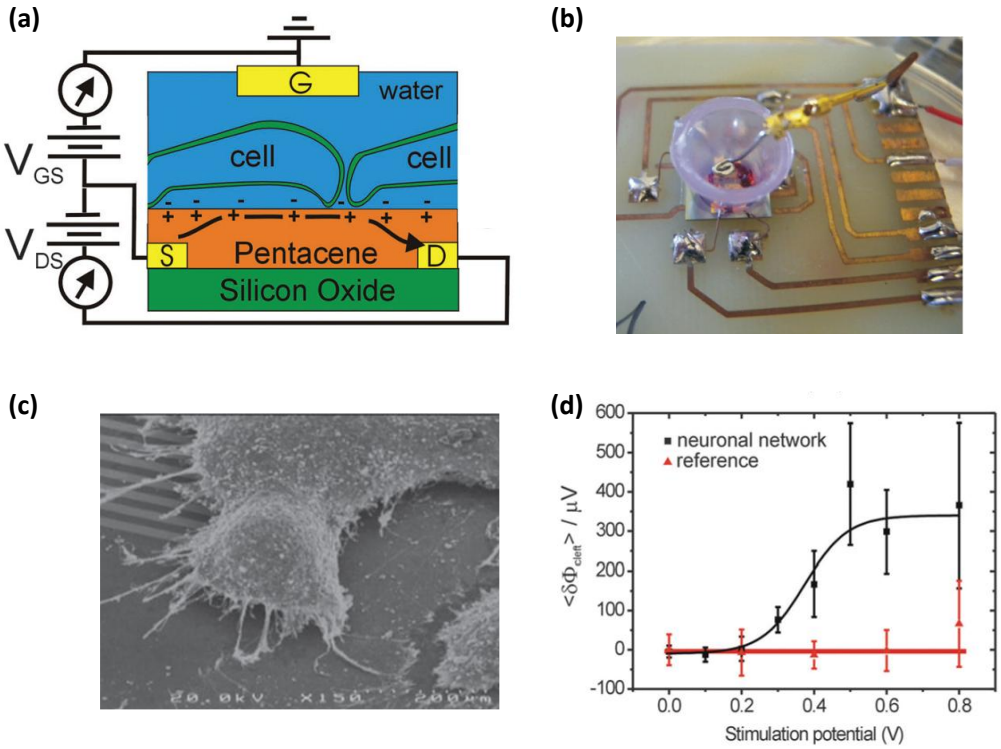

Figure 1.27. Liquid-gated pentacene transistor designed for neural interfacing. **(a)** schematic illustration showing the working principle and electrical connections of the device; **(b)** a photo of the assembled device highlighting the wiring of the four transistors on a printed circuit board, along with the cell culture pool and the platinum gate electrode; **(c)** SEM micrograph; details of neurons on the active devices, and **(d)** average maximum change in the cleft potential following stimulation. Adapted from ref[177].

- **Electrophysical activity:**

Organic electronic materials have unexplored promise as revolutionary instruments for non-invasive electrophysiological recording and stimulation systems.[106] In this field, Kyndiah et al.[93] demonstrated that EGOFETs constructed from a blend of soluble organic semiconductors and an insulating polymer exhibit remarkable sensitivity and long-term stability for electrophysical applications. Their devices successfully recorded the extracellular potential of human pluripotent stem cell-derived cardiomyocyte cells (hPSCs-CMs) over several weeks, as illustrated in **Figure 1.28**. This research highlights that EGOFETs utilizing organic blends serve as excellent bioelectronic transducers for extracellular electrical recording of excitable cells and tissues, offering a compelling alternative to traditional electrochemical transistors.

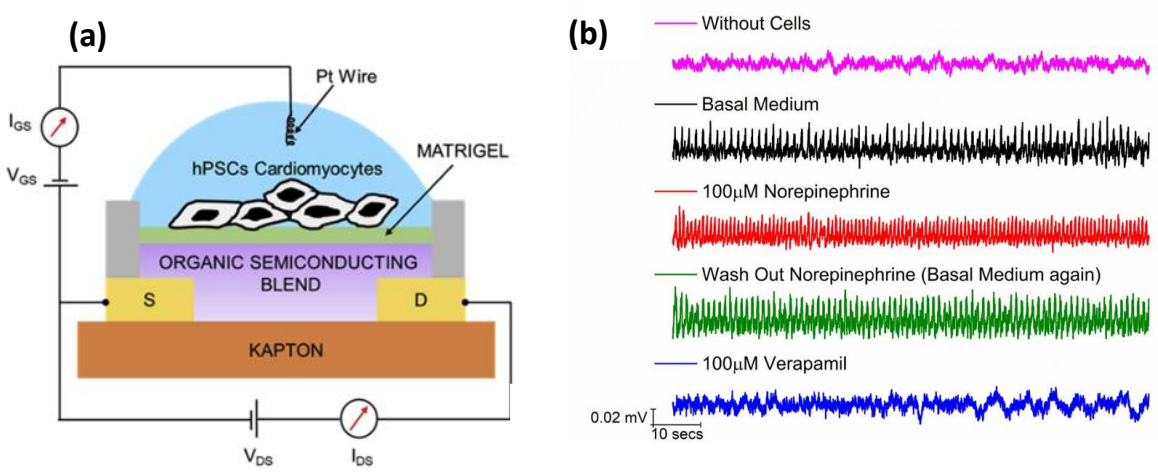

Figure 1.28. **(a)** Schematic diagram of the EGOFET coupled to hPSCs-CMs grown as a cluster of cells, and **(b)** transistor IV curves recorded throughout the study, with day 1 representing the initial seeding of the cells on the device and day 10 when the drug was introduced into the cell medium. Adapted from ref[93].

5. General objectives

This thesis focuses on the manufacture of high-performance Electrolyte-Gated Organic Field-Effect Transistors (EGOFETs) using blends of p-type small molecule semiconductors combined with polystyrene as a binding polymer. Thin films of these blends have been coated using a solution-based technique called Bar-Assisted Meniscus Shearing (BAMS). The main objectives of this thesis are the development of EGOFETs as transducers to study the aggregation of biomolecules and cell activity, as well as the development of flexible EGOFETs. Specifically, the thesis focuses on the following objectives:

- Development of an EGOFET-based transducer for monitoring amyloid peptide aggregation by immobilizing specific oligomer autoantibodies on the gold gate electrode surface.
- Assessment of the electrical performance under the mechanical strain of flexible EGOFETs based on blends of diF-TES-ADT:PS and C_8O-BTBT-OC_8:PS.
- Development of a Hydrogel-Based Organic Field-Effect Transistor (HYGOFET) employing agarose gel as a solid electrolyte. Study of its potential application as a pH sensor or in bio-sensing by using bio-modified hydrogels.
- Exploration of the use of the fabricated EGOFETs as transducers for cell activity recording employing a double-gate structure to improve electrical control during long-term measurements.

6. References

[1] Anderson, P. W., Lee, P. A. & Saitoh, M. Remarks on giant conductivity in TTF-TCNQ. *Solid State Commun.* 1973, 13, 595–598.

[2] Shirakawa, H., Louis, E. J., MacDiarmid, A. G., Chiang, C. K. & Heeger, A. J. Synthesis of electrically conducting organic polymers: halogen derivatives of polyacetylene, (CH)x. *J. Chem. Soc. Chem. Commun.* 1977, 16, 578–580.

[3] Choi, M.-C., Kim, Y. & Ha, C.-S. Polymers for flexible displays: From material selection to device applications. *Prog. Polym. Sci.* 2008, 33, 581–630.

[4] Zhan, Y., Mei, Y. & Zheng, L. Materials capability and device performance in flexible electronics for the Internet of Things. *J. Mater. Chem. C.* 2014, 2, 1220–1232.

[5] Bernius, M., Inbasekaran, M., Brien, J. & Wu, W. Progress with light-emitting polymers. *Adv. Mater.* 2000, 12, 1737-1750.

[6] Friend, R. H., Gymer, R. W., Holmes, A. B., Burroughes, J. H., Marks, R. N., Taliani, C., Bradley, D. D. C., Dos Santos, D. A., Brédas, J. L., Lögdlund, M. & Salaneck, W. R. Electroluminescence in conjugated polymers. *Nature.* 1999, 397, 121–128.

[7] Grätzel, M. Photoelectrochemical cells. *Nature.* 2001, 414, 338–344.

[8] Meng, L., Zhang, Y., Wan, X., Li, C., Zhang, X., Wang, Y., Ke, X., Xiao, Z., Ding, L., Xia, R., Yip, H.-L., Cao, Y. & Chen, Y. Organic and solution-processed tandem solar cells with 17.3% efficiency. *Science*. 2018, 361, 1094-1098.

[9] Heilmeier, G. H. & Zanoni, L. A. Surface studies of α-copper phthalocyanine films. *J. Phys. Chem. Solids.* 1964, 25, 603–611.

[10] Horowitz, G., Fichou, D., Peng, X., Xu, Z. & Garnier, F. A field-effect transistor based on conjugated alpha-sexithienyl. *Solid State Commun.* 1989, 72, 381–384.

[11] Mas-Torrent, M. & Rovira, C. Novel small molecules for organic field-effect transistors: towards processability and high performance. *Chem. Soc. Rev.* 2008, 37, 827–838.

[12] Geffroy, B., Le Roy, P. & Prat, C. Organic light-emitting diode (OLED) technology: materials, devices and display technologies. *Polymer International*. 2006, 55, 572-582.

[13] Ameri, T., Dennler, G., Lungenschmied, C. & Brabec, C. J. Organic tandem solar cells: A review. *Energy Environ. Sci.* 2009, 2, 347–363.

[14] Koezuka, H., Tsumura, A. & Ando, T. Field-effect transistor with polythiophene thin film. *Synth. Met.* 1987, 8, 699–704.

[15] Tsumura, A., Koezuka, H. & Ando, T. Macromolecular electronic device: Field-effect transistor with a polythiophene thin film. *Appl. Phys. Lett.* 1986, 49, 1210–1212.

[16] Grundmann, M. (2016) The Physics of semiconductors: An introduction including nanophysics and applications, Springer.

[17] MacGillivray, L. R. On substituents, steering, and stacking to control properties of the organic solid state. *CrystEngComm.* 2004, 6, 77–78.

[18] Tamayo Serra, A. (2022) Printing of organic semiconductors: morphology, crystal structure and interfaces. Doctoral thesis. UAB.

[19] Griffith, M. J., Cottam, S., Stamenkovic, J., Posar, J. A. & Petasecca, M. Printable organic semiconductors for radiation detection: from fundamentals to fabrication and functionality. *Front. Phys.* 2020, 8, 22.

[20] Sirringhaus, H., Brown, P. J., Friend, R. H., Nielsem, M. M., Bechgaard, K., Langeveld-Voss, B. M. W., Spiering, A. J. H., Janssen, R. A. J., Meijer, E. W., Herwig, P. & de Leeuw, D. M. Two-dimensional charge transport in self-organized, high-mobility conjugated polymers. *Nature.* 1999, 401, 685–688.

[21] McCulloch, I., Henney, M., Bailey, C., Genevicius, K., Macdonald, I., Shkunov, M., Sparrowe, D., Tierney, S., Wagner, R., Zhang, W., Chabinyc, M. L., Kline, R. J., McGehee, M. D. & Toney, M. F. Liquid-crystalline semiconducting polymers with high charge-carrier mobility. *Nat. Mater.* 2006, 5, 328–333.

[22] Sirringhaus, H. 25th Anniversary Article: Organic field-effect transistors: the path beyond amorphous silicon. *Adv. Mater.* 2014, 26, 1319–1335.

[23] Groenendaal, L., Jonas, F., Freitag, D., Pielartzik, H. & Reynolds, J. R. Poly(3,4-eh3tylenedioxythiophene) and its derivatives: past, present, and future. *Advanced Materials.* 2000, 12, 481-494.

[24] Sun, K., Zhang, S., Li, P., Xia, Y., Zhanf, X., Du, D., Isikgor, F. H. & Ouyang, J. Review on application of PEDOTs and PEDOT:PSS in energy conversion and storage devices. *J. Mater. Sci. Mater. Electron.* 2015, 26, 4438–4462.

[25] Stadlober, B., Zirkl, M., Beutl, M., Leising, G., Bauer.Gogonea, S. & Bauer, S. High-mobility pentacene organic field-effect transistors with a high-dielectric-constant fluorinated polymer film gate dielectric. *Appl. Phys. Lett.* 2005, 86, 242902.

[26] Park, S. K., Kuo, C. C., Anthony, J. E. & Jackson, T. N. High mobility solution-processed OTFTs: IEEE International Electron Devices Meeting, 2005 IEDM. *IEEE Int. Electron Devices Meet. 2005 IEDM - Tech. Dig.* 2005.

[27] Giri, G., Park, S., Vosgueritchian, M., Shulaker, M. M. & Bao, Z. High-mobility, aligned crystalline domains of TIPS-Pentacene with metastable polymorphs through lateral confinement of crystal growth. Advanced Materials. 2013, 26, 487-493.

[28] Ruzié, C., Karpinska, J., Laurent, A., Sanguinet, L., Hunter, S., Anthopoulos, T. D., Lemaur, V., Cornil, J., Kennedy, A. R., Fenwick, O., Samorì, P., Schweicher, G., Chattopadhyay, B. & Geerts, Y. H. Design, synthesis, chemical stability, packing, cyclic voltammetry, ionisation potential, and charge transport of [1]benzothieno[3,2-: B] [1]benzothiophene derivatives. *J. Mater. Chem. C.* 2016, 4, 4863–4879.

[29] Niebel, C., Kim, Y., Ruzié, C., Karpinska, J., Chattopadhyay, B., Schweicher, G., Richard, A., Lemaur, V., Olivier, Y., Cornil, J., Kennedy, A. R., Diao, Y., Lee, W.-Y., Mannsfeld, S., Bao, Z. & Geerts, Y. H. Thienoacene dimers based on the thieno[3,2-b]thiophene moiety: synthesis, characterization and electronic properties. *J. Mater. Chem. C.* 2014, 3, 674–685.

[30] Temiño, I., Del Pozo, F. G., Ajayakumar, M. R., Galindo, S., Puigdollers, J. & Mas-Torrent, M. A rapid, low-cost, and scalable technique for printing state-of-the-art organic field-effect transistors. *Adv. Mater. Technol.* 2016, 1, 1600090.

[31] Pitsalidis, C., Pappa, A. M., Hunter, S., Laskarakis, A., Kaimakamis, T., Payne, M. M., Anthony, J. E., Anthopoulos, T. D. & Logothetidis, S. High mobility transistors based on electrospray-printed small-molecule/polymer semiconducting blends. *J. Mater. Chem. C.* 2016, 4, 3499–3507.

[32] Riera-Galindo, S., Leonardi, F., Pfattner, R. & Mas-Torrent, M. Organic semiconductor/polymer blend films for organic field-effect transistors. *Advanced Materials Technologies*. 2019, 4, 1900104.

[33] Da Rocha, C. T., Haase, K., Zheng, Y., Löffler, M., Hambsch, M. & Mannsfel, S. C. B. Solution coating of small molecule/polymer blends enabling ultralow voltage and high-mobility organic transistors. *Advanced Electronic Materials*. 2018, 4, 1800141.

[34] Niazi, M. R., Li, R., Li, E. Q., Kirmani, A. R., Abdelsamie, M., Wang, Q., Pan, W., Payne, M. M., Anthony, J. E., Smilgies, D.-M., Thoroddsen, S. T., Giannelis, E. P. &

Amassian, A. Solution-printed organic semiconductor blends exhibiting transport properties on par with single crystals. *Nat. Commun.* 2015, 6, 8598.

[35] Riera-Galindo, S., Tamayo, A. & Mas-Torrent, M. Role of polymorphism and thin-film morphology in organic semiconductors processed by solution shearing. *ACS Omega*. 2018, 3, 2329–2339.

[36] Paterson, A. F., Singh, S., Fallon, K. J., Hodsden, T., Han, Y., Schroeder, B. C., Bronstein, H., Heeney, M., McCulloch, I. & Anthopoulos, T. D. Recent progress in high-mobility organic transistors: a reality check. *Advanced Materials*. 2018, 30, 1801079.

[37] Bhattacharya P, Fornari R, Kamimura H. (2011) Comprehensive Semiconductor Science and Technology - 1st Edition

[38] Marcus, R. A. On the theory of oxidation-reduction reactions involving electron transfer. I. *J. Chem. Phys.* 2004, 24, 966–978.

[39] Ela, A. H. A. E. & Afifi, H. H. Hopping transport in organic semiconductor system. *J. Phys. Chem. Solids.* 1979, 40, 257–259.

[40] Cho, J. & Mori, T. Low-temperature band transport and impact of contact resistance in organic field-effect transistors based on single-crystal films of Ph-BTBT-C10. *Phys. Rev. Appl.* 2016, 5, 064017 (2016).

[41] Uemura, T., Nakayama, K., Hirose, Y., Soeda, J., Uno, M., Li, W., Yamagishi, M., Okada, Y. & Takeya, J. Band-like transport in solution-crystallized organic transistors. *Curr. Appl. Phys.* 2012, 12, S87–S91.

[42] Kôhler A, Bässler H. (2015) Electronic Processes in Organic Semiconductors: An Introduction. Wiley.

[43] Coropceanu, V., Cornil, J., Filho, D. A. S., Olivier, Y., Silbey, R. & Brédas, J.-L. Charge transport in organic semiconductors. *Chemical Reviews*. 2007, 107, 926-952.

[44] Liu, C., Huang, K., Park, W.-T., Li, M., Yang, T., Liu, X., Liang, L., Minari, T. & Noh, Y.-Y. A unified understanding of charge transport in organic semiconductors: the importance of attenuated delocalization for the carriers. *Mater. Horiz.* 2017, 4, 608–618.

[46] Kymissis, I. (2009) Organic Field Effect Transistors: Theory, Fabrication and Characterization. Springer.

[47] Diao, Y., Shaw, L., Bao, Z. & Mannsfeld, S. C. B. Morphology control strategies for solution-processed organic semiconductor thin films. *Energy Environ. Sci.* 2014, 7, 2145–2159.

[48] Xu, Y., Liu, C., Khim, D. & Noh, Y.-Y. Development of high-performance printed organic field-effect transistors and integrated circuits. *Phys. Chem. Chem. Phys.* 2015, 17, 26553–26574.

[49] Kim, C. S., Lee, S., Gomez, E. D., Anthony, J. E. & Loo, Y. L. Solvent-dependent electrical characteristics and stability of organic thin-film transistors with drop cast bis(triisopropylsilylethynyl) pentacene. *Appl. Phys. Lett.* 2008, 93, 103302.

[50] Aegerter M A, Menning M. (2004) Sol-Gel Technologies for Glass Producers and Users. Springer.

[51] Georgakopoulos, S., Pérez-Rodríguez, A., Campos, A., Temiño, I., Galindo, S., Barrena, E., Ocal, C. & Mas-Torrent, M. Spray-coated contacts from an organic charge transfer complex solution for organic field-effect transistors. *Org. Electron.* 2017, 48, 365–370.

[52] Kjellander, B. K. C., Smaal, W. T. T., Anthony, J. E. & Gelinck, G. H. Inkjet printing of TIPS-PEN on soluble polymer insulating films: A route to high-performance thin-film transistors. *Adv. Mater.* 2010, 22, 4612–4616.

[53] Mitra, K. Y., Polomoshnov, M., Martínez-Domingo, C., Mitra, D., Ramon, E. and Baumann, R. R. Fully inkjet-printed thin-film transistor array manufactured on paper substrate for cheap electronic applications. *Advanced Electronic Materials.* 2017, 3, 1700275.

[54] Del Pozo, F., Fabiano, S., Pfattner, R., Georgakopoulos, S., Galindo, S., Liu, X., Braun, S., Fahlman, M., Veciana, J., Rovira, C., Crispin, X., Berggren, M. and Mas-Torrent, M. Single crystal-like performance in solution-coated thin-film organic field-effect transistors. *Adv. Funct. Mater.* 2016, 26, 2379–2386.

[55] Niazi, M. R., Li, R., Abdelsamie, M., Zhao, K., Anjum, D. H., Payne, M. M., Anthony, J., Smilgies, D. M. and Amassian, A. Contact-induced nucleation in high-performance bottom-contact organic thin film transistors manufactured by large-area compatible solution processing. *Adv. Funct. Mater.* 2016, 26, 2371–2378.

[56] Bucella, S. G., Luzio, A., Gann, E., Thomsen, L., McNeill, C. R., Pace, G., Perinot, A., Chen, Z., Facchetti, A. and Caironi, M. Macroscopic and high-throughput printing of aligned nanostructured polymer semiconductors for MHz large-area electronics. *Nat. Commun.* 2015, 6, 8394.

[57] Jang, J., Nam, S., Im, K., Hur, J., Cha, S. N., Kim, J., Son, H. B., Suh, H., Loth, M. A., Anthony, J. E., Park, J.-J., Park, C. E., Kim, J. M. and Kim. K. Highly crystalline soluble acene crystal arrays for organic transistors: Mechanism of crystal growth during dip-coating. *Adv. Funct. Mater.* 2012, 22, 1005–1014.

[58] Li, L., Gao, P., Schuermann, K. C., Ostendorp, S., Wang, W., Du, C., Lei, Y., Fuchs, H., De Cola, L., Müllen, K. and Chi, L. Controllable growth and field-effect property of monolayer to multiplayer microstripes of an organic semiconductor. *Journal of the American Chemical Society.* 2010, 132, 8807-8809.

[59] Tracz, A., Pakula, T. and Jeszka, J. Zone casting - A universal method of preparing oriented anisotropic layers of organic materials. *Mater. Sci.* 2005, 22, 415–421.

[60] Chang, Y.-H., Tseng, H.-R., Chen, C.-Y., Meng, H.-F., Chen, E.-C., Horng, S.-F. and Hsu, C.-S. Polymer solar cell by blade coating. *Org. Electron.* 2009, 10, 741–746.

[61] Klauk, H. Organic thin-film transistors. *Chem. Soc. Rev.* 2010, 39, 2643–2666.

[62] Ricci, S. (2020) Liquid-Gated Transistors for Biosensing Applications. Doctoral thesis. UAB

[63] Hwang, D. K., Fuentes-Hernandez, C., Kim, J., Postcavage Jr, W. J., Kim, S.-J. and Kippelen, B. Top-gate organic field-effect transistors with high environmental and operational stability. *Adv. Mater.* 2011, 23, 1293–1298.

[64] Ahmed, R., Kadashchuk, A., Simbrunner, C., Schwabegger, G., Baig, M. A. and Sitter, H. Gemetrical structure and interface dependence of bias stress induced threshold voltage shift in C60-based OFETs. *ACS Applied Materials & Interfaces*. 2014, 6, 15148-15153.

[65] Horowitz, G. Organic Field-Effect Transistors. *Adv. Mater.* 1998, 10, 365–377.

[66] Horowitz, G., Hajlaoui, R., Bouchriha, H., Bourguiga, R. & Hajlaoui, M. The concept of “threshold voltage” in organic field-effect transistors. *Adv. Mater.* 1998, 10, 923–927.

[67] Lamport, Z. A., Haneef, H. F., Anand, S., Waldrip, M. and Jurchescu, O. D. Tutorial: Organic field-effect transistors: Materials, structure and operation. *API Journal of Applied Physics.* 2018, 124, 071101.

[68] Sze, S. M., Lee, M.-K., Lee, M. K. (2012) Semiconductor Devices, Physics and Technology. Wiley.

[69] Malliaras, G. and McCulloch, I. Introduction: Organic Bboelectronics. *Chem. Rev.* 2022, 122, 4323–4324.

[70] Bergveld, P. Development of an ion-sensitive solid-state device for neurophysiological measurements. *IEEE Trans. Biomed. Eng.* 1970, 17, 70–71.

[71] Ritjareonwattu, S., Yun, Y., Pearson, C. and Petty, M. C. Enhanced sensitivity of an organic field-effect transistor pH sensor using a fatty acid Langmuir–Blodgett film. *Org. Electron.* 2010, 11, 1792–1795.

[72] Angizi, S., Huang, X., Hong, L., Akbar, M. A., Selvaganapathy, P. R. and Kruse, P. Defect density-dependent pH response of graphene derivatives: Towards the development of pH-sensitive graphene oxide devices. *Nanomaterials*. 2022, 12, 1801.

[73] Turner, A., Karube, I. and Wilson, G. (1987) Biosensor Fundamentals and Applications. Oxford Science Publications.

[74] Reinhoudt, D. N. Application of supramolecular chemistry in the development of ion-selective CHEMFETs. *Sens. Actuators B Chem.* 1992, 6, 179–185.

[75] Banning, D. H., Kuhl, G. M., Howell, M. M. and Johnson, D. W. Evaluating impacts of bambusuril pocket size and sterics on anion binding trends using ChemFET sensors. *Org. Biomol. Chem.* 2024, 22, 269–273.

[76] Janata, J. Thirty years of CHEMFETs—a personal view. *Electroanalysis.* 2004, 16, 1831–1835.

[77] Li, Q., Zhao, J., Huang, Y., Tang, W., Peng, S., Qiu, S., Zhang, Q. and Guo, X. Integrated low voltage ion Sensing organic field effect transistor system on plastic. *IEEE Electron Device Lett.* 2018, 39, 591–594 (2018).

[78] Zhang, Z., Pu, Z., Su, X., Li, C., Zheng, H. and Li, D. Flexible organic field-effect transistors-based biosensors: progress and perspectives. Analytical and Bioanalytical Chemistry. 2023, 415, 1607-1625.

[79] White, H. S., Kittlesen, G. P. and Wrighton, M. S. Chemical derivatization of an array of three gold microelectrodes with polypyrrole: fabrication of a molecule-based transistor. *J. Am. Chem. Soc.* 1984, 106, 5375–5377.

[80] Bergveld, P. Development, operation, and application of the ion-sensitive field-effect transistor as a tool for electrophysiology. *IEEE Trans. Biomed. Eng.* 1972, 19, 342–351.

[81] Woo Son, H., Park, J. H., Chae, M.-S., Kim, B.-H. and Kim, T. G. Bilayer indium gallium zinc oxide electrolyte-gated field-effect transistor for biosensor platform with high reliability. *Sens. Actuators B Chem.* 2020, 312, 127955.

[82] Song, J., Chu, Y., Liu, Z. and Xu, H. Fabrication of solution-processed ambipolar electrolyte-gated field effect transistors from a MoS2–polymer hybrid for multifunctional optoelectronics. *J. Mater. Chem. C.* 2021, 9, 1701–1708.

[83] Furlan de Oliveira, R., Livio, P. A., Montes-García, V., Ippolito, S., Eredia, M., Fanjul-Bolado, P., González-García, M. B., Casalini, S. and Samorì, P. Liquid-gated transistors based on reduced graphene oxide for flexible and wearable electronics. *Adv. Funct. Mater.* 2019, 29, 1905375.

[84] Lu, S. and Franklin, A. D. Printed carbon nanotube thin-film transistors: progress on printable materials and the path to applications. *Nanoscale.* 2020, 12, 23371–23390.

[85] Leonardi, F., Casalini, S., Zhang, Q., Galindo, S., Gutiérrez, D. and Mas-Torrent, M. Electrolyte-gated organic field-effect transistor based on a solution sheared organic semiconductor blend. *Adv. Mater.* 2016, 28, 10311–10316.

[86] Volkov, A. V., Wijeratne, K., Mitraka, E., Ail, U., Zhao, D., Tybrandt, K., Andreasen, J. W., Berggren, M., Crispin, X. and Zozoulenko, I. V. Understanding the capacitance of PEDOT:PSS. *Adv. Funct. Mater.* 2017, 27, 1700329.

[87] Romele, P., Ghittorelli, M., Kovács-Vajna, Z. M. and Torricelli, F. Ion buffering and interface charge enable high performance electronics with organic electrochemical transistors. *Nat. Commun.* 2019, 10, 3044.

[88] Moser, M., Ponder Jr, J. F., Wadsworth, A., Giovannitti, A. and Mc Culloch, I. Materials in organic electrochemical transistors for bioelectronic applications: Past, present, and future. *Advanced Functional Materials.* 2019, 29, 1807033.

[89] Paulsen, B. D., Tybrandt, K., Stavrinidou, E. and Rivnay, J. Organic mixed ionic–electronic conductors. *Nat. Mater.* 2020, 19, 13–26.

[90] Picca, R. A., Manoli, K., Macchia, E., Sarcina, L., Di Franco, C., Cioffi, N., Blasi, D., Österbacka, R., Torricelli, F., Scamarcio, G. and Torsi, L. Ultimately sensitive organic bioelectronic transistor sensors by materials and device structure design. *Adv. Funct. Mater.* 2020, 30, 1904513.

[91] Rivnay, J., Inal, S., Salleo, A., Owens, R. M., Berggren, M. and Malliaras, G. G. Organic electrochemical transistors. *Nat. Rev. Mater.* 2018, 3, 1–14.

[92] Bai, L., Elósegui, C. G., Li, W., Yu, P., Fei, J. and Mao, L. Biological applications of organic electrochemical transistors: Electrochemical biosensors and electrophysiology recording. *Front. Chem.* 2019, 7, 313.

[93] Kyndiah, A., Leonardi, F., Tarantino, C., Cramer, T., Millan-Solsona, R., Garreta, E., Montserrat, N., Mas-Torrent, M. and Gomila, G. Bioelectronic recordings of cardiomyocytes with accumulation mode electrolyte gated organic field effect transistors. *Biosens. Bioelectron.* 2020, 150, 111844.

[94] Melzer, K., Münzer, A. M., Jaworska, E., Maksymiuk, K., Michalska, A. and Scarpa, G. Selective ion-sensing with membrane-functionalized electrolyte-gated carbon nanotube field-effect transistors. *Analyst.* 2014, 139, 4947–4954.

[95] Sessolo, M., Rivnay, J., Bandiello, E., Malliaras, G. G. and Bolink, H. J. Ion-selective organic electrochemical transistors. *Adv. Mater. Deerfield Beach Fla.* 2014, 26, 4803-4807.

[96] Keene, S. T., Lubrano, C., Kazemzadef, S., Melianas, A., Tuchman, Y., Polino, G., Scognamiglio, P., Cinà, L., Salleo, A., van de Burgt, Y. and Santoro, F. A biohybrid synapse with neurotransmitter-mediated plasticity. *Nat. Mater.* 2020, 19, 969–973.

[97] Ling, H., Koutsouras, D. A., Kazemzadeh, S., van de Burgt, Y., Yan, F. and Gkoupidenis, P. Electrolyte-gated transistors for synaptic electronics, neuromorphic computing, and adaptable biointerfacing. *Appl. Phys. Rev.* 2020, 7, 011307.

[98] Campos, R., Borme, J., Guerreiro, J. R., Machado Jr, G., Cerqueira, M. F., Petrovykh, D. Y. and Alpuim, P. Attomolar Label-free detection of DNA hybridization with electrolyte-gated graphene field-effect transistors. *ACS Sens.* 2019, 4, 286–293.

[99] Hwang, M. T., Heiranian, M., Kim, Y., You, S., Leem, J., Taqieddin, A., Faramarzi, V., Jing, Y., Park, I., van der Zande, A. M., Nam, S., Aluru, N. R. and Bashir, R. Ultrasensitive detection of nucleic acids using deformed graphene channel field effect biosensors. *Nat. Commun.* 2020, 11, 1543.

[100] Zhang, Z., Zheng, T. and Zhu, R. Long-term and label-free monitoring for osteogenic differentiation of mesenchymal stem cells using force sensor and impedance measurement. *J. Mater. Chem. B.* 2020, 8, 9913–9920.

[101] Decataldo, F., Barbalinardo, M., Gentili, D., Tessarolo, M., Calienni, M., Cavallini, M. and Fraboni, B. Organic electrochemical transistors for real-time monitoring of in vitro silver nanoparticle toxicity. *Adv. Biosyst.* 2020, 4, 1900204.

[102] Ferro, M. P., Leclerc, L., Sleiman, M., Marchiori, B., Pourchez, J., Owens, R. M. and Ramuz M. Effect of e cigarette emissions on tracheal cells monitored at the air-liquid interface using an organic electrochemical transistor. *Adv. Biosyst.* 2019, 3, 1800249.

[103] Lingstedt, L. V., Ghittorelli, M., Brückner, M., Reinholz, J., Craciun, N. I., Torricelli, F., Mailämder, V., Gkoupidenis, P. and Blom, P. W. M. Monitoring of cell layer integrity with a current-driven organic electrochemical transistor. *Adv. Healthc. Mater.* 2019, 8, 1900128.

[104] Demuru, S., Paul, B. and Briand, D. Real-time multi-ion detection in the sweat concentration range enabled by flexible, printed, and microfluidics-integrated organic transistor arrays. *Adv. Mater. Technol.* 2020, 5, 2000328.

[105] Romele, P., Gkoupidenis, P., Koutsouras, D. A., Lieberth, K., Kovács-Vajna, Z., Blom, P. W. M. and Torricelli, F. Multiscale real time and high sensitivity ion detection with complementary organic electrochemical transistors amplifier. *Nat. Commun.* 2020, 11, 3743.

[106] Torricelli, F., Adrahtas, D. Z., Bao, Z., Berggren, M., Biscarini, F., Bonfiglio, A., Bortolotti, C. A., Frisbie, C. D., Macchia, E., Malliaras, G. G., McCulloch, I., Moser, M., Nguyen, T.-Q., Owens, R. M., Salleo, A., Spanu, A. and Torsi, L. Electrolyte-gated transistors for enhanced performance bioelectronics. *Nat. Rev. Methods Primer.* 2021, 1, 66.

[107] Spyropoulos, G. D., Gelinas, J. N. and Khodagholy. Internal ion-gated organic electrochemical transistor: A building block for integrated bioelectronics. *Science Advances.* 2019, 5, eaau7378.

[108] Cea, C., Spyropoulos, G. D., Jastrzebska-Perfect, P., Ferrero, J. J., Gelinas, J. N. and Khodagholy, D. Enhancement-mode ion-based transistor as a comprehensive interface and real-time processing unit for in vivo electrophysiology. *Nat. Mater.* 2020, 19, 679–686.

[109] Gualandi, I., Marzocchi, M., Achilli, A., Cavedale, D., Bonfiglio, A. and Fraboni, B. Textile organic electrochemical transistors as a platform for wearable biosensors. *Sci. Rep.* 2016, 6, 33637.

[110] Sensi, M., Berto, M., Candini, A., Liscio, A., Cossarizza, A., Beni, V., Biscarini, F. and Bortolotti, C. A. Modulating the faradic operation of all-printed organic electrochemical transistors by facile in situ modification of the gate electrode. *ACS Omega.* 2019, 4, 5374–5381.

[111] Gkoupidenis, P., Koutsouras, D. A. and Malliaras, G. G. Neuromorphic device architectures with global connectivity through electrolyte gating. *Nat. Commun.* 2017, 8, 15448.

[112] Koutsouras, D., Prodromakis, T., Malliaras, G., Blom, P. and Gkoupidenis, P. Functional connectivity of organic neuromorphic devices by global voltage oscillations devices by global voltage oscillations. *Adv. Intell. Syst.* 2019, 1, 1900013.

[113] White, S., Dorfman, K. and Frisbie, C. Operating and sensing mechanism of electrolyte-gated transistors with floating gates: Building a platform for amplified biodetection. *J. Phys. Chem. C.* 2015, 120, 108-117.

[114] White, S. P., Dorfman, K. D. and Frisbie, C. D. Label-free DNA sensing platform with low-voltage electrolyte-gated transistors. *Anal. Chem.* 2015, 87, 1861–1866.

[115] White, S. P., Frisbie, C. D. and Dorfman, K. D. Detection and sourcing of gluten in grain with multiple floating-gate transistor biosensors. *ACS Sens.* 2018, 3, 395–402.

[116] Spanu, A., Lai, S., Cosseddu, P., Tedesco, M., Martinoia, S. and Bonfiglio, A. An organic transistor-based system for reference-less electrophysiological monitoring of excitable cells. *Sci. Rep.* 2015, 5, 8807.

[117] Macchia, E., Manoli, K., Holzer, B., Di Franco, C., Ghittorelli, M., Torricelli, F., Alberga, D., Mangiatordi, G. F., Palazzo, G., Scamarcio, G. and Torsi, L. Single-molecule detection with a millimetre-sized transistor. *Nat. Commun.* 2018, 9, 3223.

[118] Holzer, B., Manoli, K., Ditaranto, N., Macchia, E., Tiwari, A., Di Franco, C., Scamarcio, G., Palazzo, G. and Torsi. Characterization of covalently bound anti-human immunoglobulins on self-assembled monolayer modified gold electrodes. *Adv. Biosyst.* 2017, 1, 1700055.

[119] Dorfman, K. D., Adrahtas, D. Z., Thomas, M. S. and Frisbie, C. D. Microfluidic opportunities in printed electrolyte-gated transistor biosensors. *Biomicrofluidics.* 2020, 14, 011301.

[120] Paul, E. W., Ricco, A. J. and Wrighton, M. S. Resistance of polyaniline films as a function of electrochemical potential and the fabrication of polyaniline-based microelectronic devices. *J. Phys. Chem.* 1985, 89, 1441–1447.

[121] Thackeray, J. W. and Wrighton, M. S. Chemically responsive microelectrochemical devices based on platinized poly(3-methylthiophene): Variation in conductivity with

variation in hydrogen, oxygen, or pH in aqueous solution. *Massachusetts Inst of Tech.* 1986, 36.

[122] Kirchmeyer, S. and Reuter, K. Scientific importance, properties and growing applications of poly(3,4-ethylenedioxythiophene). *J. Mater. Chem.* 2005, 15, 2077–2088 (2005).

[123] Marks, A., Griggs, S., Gasparini, N. and Moser, M. Organic electrochemical transistors: An emerging technology for biosensing. *Adv. Mater. Interfaces.* 2022, 9, 2102039.

[124] Paul, E. W., Ricco, A. J. and Wrighton, M. S. Resistance of polyaniline films as a function of electrochemical potential and the fabrication of polyaniline-based microelectronic devices. *J. Phys. Chem.* 1985, 89, 1441–1447.

[125] Chao, S. and Wrighton, M. S. Characterization of a solid-state polyaniline-based transistor: water vapor dependent characteristics of a device employing a poly(vinyl alcohol)/phosphoric acid solid-state electrolyte. *J. Am. Chem. Soc.* 1987, 109, 6627–6631.

[126] Thackeray, J. W., White, H. S. and Wrighton, M. S. Poly-3-methylthiophene coated electrodes. Optical and electrical properties as a function of redox potential and amplification of electrical and chemical signals using poly-3-methylthiophene-based microelectrochemical transistors. *The Journal of Physical Chemistry.* 1985, 89, 5133-5140.

[127] Kergoat, L., Herlogsson, L., Braga, D., Piro, B., Pham, M.-C., Crispin, X., Berggren, M. and Horowitz, G. A water-gate organic field-effect transistor. *Adv. Mater.* 2010, 22, 2565–2569.

[128] Bard, A. J. and Faulkner, L. R. (2000) Electrochemical Methods: Fundamentals and Applications. 2nd Edition. Wiley.

[129] Du, H., Lin, X., Xu, Z. and Chu, D. Electric double-layer transistors: a review of recent progress. *J. Mater. Sci.* 2015, 50, 5641–5673.

[130] Wanf, J., Ye, D., Meng, Q., Di, C.-A., and Zhu, D. Advances in organic transistor-based biosensors. *Advanced Materials Technologies.* 2020, 5, 2000218.

[131] Cramer, T., Campana, A., Leonardi, F., Casalini, S., Kyndiah, A., Murgia, M. and Biscarini, F. Water-gated organic field effect transistors – opportunities for biochemical sensing and extracellular signal transduction. *J. Mater. Chem. B.* 2013, 1, 3728–3741.

[133] Zhang, Q., Leonardi, F., Casalini, S., Temiño, I. and Mas-Torrent, M. High performing solution-coated electrolyte-gated organic field-effect transistors for aqueous media operation. *Sci. Rep.* 2016, 6, 39623.

[133] Mulla, M. Y., Tuccori, E., Magliulo, M., Lattanzi, G., Palazzo, G., Persaud, K. and Torsi, L. Capacitance-modulated transistor detects odorant binding protein chiral interactions. *Nat. Commun.* 2015, 6, 6010.

[134] Casalini, S., Leonardi, F., Cramer, T. and Biscarini, F. Organic field-effect transistor for label-free dopamine sensing. *Org. Electron.* 2013, 14, 156–163.

[135] Manco Urbina, P. A., Paradisi, A., Hasler, R., Sensi, M., Berto, M., Saygin, G. D., Dostalek, J., Pinti, M., Greco, P., Borsari, M., Jnoll, W., Bortolotti, C. A. and Biscarini, F. Dynamic studies of antibody-antigen interactions with an electrolyte-gated organic transistor. *Cell Rep. Phys. Sci.* 2014, 5, 101919.

[136] Pappa, A.-M., Parlak, O., Scheiblin, G., Mailley, P., Salleo, A. and Owens, R. Organic electronics for point-of-care metabolite monitoring. *Trends Biotechnol.* 2018, 36, 45–59.

[137] Scarano, S., Mascini, M., Turner, A. P. F. and Minunni, M. Surface plasmon resonance imaging for affinity-based biosensors. *Biosens. Bioelectron.* 2010, 25, 957–966.

[138] Sarcina, L., Torsi, L., Picca, R. A., Manoli, K. and Macchia, E. Assessment of gold bio-functionalization for wide-interface biosensing platforms. *Sensors.* 2020, 20, 3678.

[139] Piro, B., Wang, D., Benaoudia, D., Tibaldi, A., Anquetin, G., Noël, V., Reisberg, S., Mattana, G. and Jackson, B. Versatile transduction scheme based on electrolyte-gated organic field-effect transistor used as immunoassay readout system. *Biosens. Bioelectron.* 2017, 92, 215–220.

[140] Macchia, E., Manoli, K., Di Franco, C., Picca, R. A., Österbacka, R., Palazzo, G., Torricelli, F., Scamarcio, G. and Torsi, L. Organic field-effect transistor platform for label-free, single-molecule detection of genomic biomarkers. *ACS Sens.* 2020, 5, 1822–1830.

[141] Pavlickova, P., Schneider, E. M. and Hug, H. Advances in recombinant antibody microarrays. *Clin. Chim. Acta Int. J. Clin. Chem.* 2004, 343, 17–35.

[142] Mulla, M. Y., Torsi, L. and Manoli, K. Chapter Seventeen - Electronic biosensors based on EGOFETs. *Methods in Enzymology*. 2020, 642, 403–433.

[143] Seshadri, P., Manoli, K., Schneiderhan-Marra, N., Anthes, U., Wierzchowiec, P., Bonrad, K., Di Franco, C. and Torsi, L. Low-picomolar, label-free procalcitonin analytical

detection with an electrolyte-gated organic field-effect transistor based electronic immunosensor. *Biosens. Bioelectron.* 2018, 104, 113–119.

[144] Rusmini, F., Zhong, Z. and Feijen, J. Protein immobilization strategies for protein biochips. *Biomacromolecules.* 2007, 8, 1775–1789.

[145] Green, N. M. Avidin. *Adv. Protein Chem.* 1975, 29, 85–133.

[146] Ulman, A. Formation and structure of self-assembled monolayers. *Chemical Reviews.* 1996, 96, 1533-1554.

[147] Xia, Y. and Whitesides, G. M. Soft Lithography. *Angew. Chem. Int. Ed.* 1998, 37, 550–575.

[148] Tang, H., Yan, F., Lin, P., Xu, J. and Chan, H. L. Highly sensitive glucose biosensors based on organic electrochemical transistors using platinum gate electrodes modified with enzyme and nanomaterials. *Advanced Functional Materials.* 2011, 21, 2264-2272.

[149] Zhang, L., Li, Q., Li, Z., Du, Z., Hong, X. and Qiu, L. An enzyme biosensor based on organic transistors for recognizing α-amino acid enantiomers. *J. Electrochem. Soc.* 2020, 167, 067517.

[150] Gualandi, I., Tonelli, D., Mariani, F., Scavetta, R., Marzocchi, M. and Fraboni, B. Selective detection of dopamine with an all PEDOT:PSS Organic electrochemical transistor. *Sci. Rep.* 2016, 6, 35419.

[151] Galliani, M., Diacci, C., Berto, M., Sensi, M., Beni, V., Berggren, M., Borsari, M., Simon, D. T., Biscarini, F., Bortolotti, C. A. Flexible printed organic electrochemical transistors for the detection of uric acid in artificial wound exudate. *Adv. Mater. Interfaces*. 2020, 7, 2001218.

[152] Lin, P., Yan, F. abd Chan, H. L. W. Ion-sensitive properties of organic electrochemical transistors. *ACS Appl. Mater. Interfaces.* 2010, 2, 1637–1641.

[153] Di Lauro, M., Casalini, S., Berto, M., Campana, A., Cramer, T., Murgia, M., Geoghegan, M., Bortolotti, C. A. and Biscarini, F. The substrate is a pH-controlled second gate of electrolyte-gated organic field-effect transistor. *ACS Appl. Mater. Interfaces.* 2016, 8, 31783–31790.

[154] Fillaud, L., Petenzi, T., Pallu, J., Piro, B., Mattana, G., and Noel, V. Switchable hydrogel-gated organic field-effect transistors. *Langmuir.* 2018, 34, 3686–3693.

[155] Nguyen, T. T. K., Nguyen, T. N., Anquetin, G., Reisberg, S., Noël, V., Mattana, G., Touzeau, J., Barbault, F., Pham, M. C. and Piro, B. Triggering the electrolyte-gated organic

field-effect transistor output characteristics through gate functionalization using diazonium chemistry: Application to biodetection of 2,4-dichlorophenoxyacetic acid. *Biosens. Bioelectron.* **2018,** 113, 32–38.

[156] Diacci, C., Berto, M., Di Lauro, M., Bianchini, E., Pinti, M., Simon, D. T., Biscarini, F. and Bortolotti, C. A. Label-free detection of interleukin-6 using electrolyte gated organic field effect transistors. *Biointerphases.* **2017,** 12, 05F401.

[157] Berto, M., Diacci, C., D'Agata, R., Pinti, M., Bianchini, E., Di Lauro, M.m Casalini, S., Cossarizza, A., Berggren, M., Simon, D., Spoto, G., Biscarini, F. and Bortolotti, C. A. EGOFET peptide aptasensor for label-free detection of inflammatory cytokines in complex fluids. *Adv. Biosyst.* **2018,** 2, 1700072.

[158] Buth, F., Donner, A., Sachsenhauser, M., Stutzmann, M. and Garrido, J. A. Biofunctional electrolyte-gated organic field-effect transistors. *Adv. Mater.* **2012,** 24, 4511–4517.

[159] Kergoat, L., Piro, B., Berggren, M., Pham, M. C., Yassar, A. and Horowitz, G. DNA detection with a water-gated organic field-effect transistor. *Org. Electron.* **2012,** 13, 1–6.

[160] Magliulo, M., Mallardi, A., Mulla, M. Y., Cotrone, S., Pistillo, B. R., Favia, P., Vikholm-Lundin, I., Palazzo, G. and Torsi, L. Electrolyte-gated organic field-effect transistor sensors based on supported biotinylated phospholipid bilayer. *Adv. Mater.* **2013,** 25, 2090–2094.

[161] Mulla, M. Y., Seshadri, P., Torsi, L., Manoli, K., Mallardi, A., Ditaranto, N., Santacroce, M. V., Di Franco, C., Scamarcio, G. and Magliulo, M. UV crosslinked poly(acrylic acid): a simple method to bio-functionalize electrolyte-gated OFET biosensors. *J. Mater. Chem. B.* **2015,** 3, 5049–5057.

[162] Macchia, E., Romele, P., Manoli, K., Ghittorelli, M., Magliulo, M., Kovács-Vajna, Z. M., Torricelli, F. and Torsi, L. Ultra-sensitive protein detection with organic electrochemical transistors printed on plastic substrates. *Flex. Print. Electron.* **2018,** 3, 034002.

[163] Macchia, E., Manoli, K., Holzer, B., Di Franco, C., Picca, R. A., Cioffi, N., Scamarcio, G., Palazzo, G. and Torsi, L. Selective single-molecule analytical detection of C-reactive protein in saliva with an organic transistor. *Anal. Bioanal. Chem.* **2019,** 411, 4899–4908.

[164] Burtscher, B., Maco Urbina, P. A., Diacci, C., Borghi, S., Pinti, M., Cossarizza, A., Salvarani, C., Berggren, M., Biscarini, F., Simon, D. T. and Bortolotti, C. A. Sensing

inflammation biomarkers with electrolyte-gated organic electronic transistors. *Adv. Healthc. Mater.* 2021, 10, 2100955.

[165] Sensi, M., Berto, M., Gentile, S., Pinti, M., Conti, A., Pellacani, G., Salvarani, C., Cossarizza, A., Bortolotti, C. A. and Biscarini, F. Anti-drug antibody detection with label-free electrolyte-gated organic field-effect transistors. *Chem. Commun.* 2021, 57, 367–370.

[166] Berto, M., Vecchi, E., Baiamonte, L., Condò, C., Sensi, M., Di Lauro, M., Sola, M., De Stradis, A., Biscarini, F., Minafra, A. and Bortolotti, C. A. Label free detection of plant viruses with organic transistor biosensors. *Sens. Actuators B Chem.* 2019, 281, 150–156.

[167] Muñoz, J., Leonardi, F., Özmen, T., Riba-Moliner, M., González-Campo, A., Baeza, M. and Mas-Torrent, M. Carbon-paste nanocomposites as unconventional gate electrodes for electrolyte-gated organic field-effect transistors: electrical modulation and bio-sensing. *J. Mater. Chem. C.* 2019, 7, 14993–14998.

[168] Ricci, S., Casalini, S., Parkula, V., Selvaraj, M., Saygin, G. D., Greco, P., Biscarini, F. and Mas-Torrent, M. Label-free immunodetection of α-synuclein by using a microfluidics coplanar electrolyte-gated organic field-effect transistor. *Biosens. Bioelectron.* 2020, 167, 112433.

[169] Macchia, E., Sarcina, L., Picca, R. A., Manoli, K., Di Franco, C., Scamarcio, G. and Torsi, L. Ultra-low HIV-1 p24 detection limits with a bioelectronic sensor. *Anal. Bioanal. Chem.* 2020, 412, 811–818.

[170] Sun, C., Wang, Y.-X., Sun, M., Zou, Y., Zhang, C., Cheng, S. and Hu, W. Facile and cost-effective liver cancer diagnosis by water-gated organic field-effect transistors. *Biosens. Bioelectron.* 2020, 164, 112251.

[171] Selvaraj, M., Greco, P., Sensi, M., Saygin, G. D., Bellassai, N., D'Agata, R., Spoto, G. and Biscarini, F. Label free detection of miRNA-21 with electrolyte gated organic field effect transistors (EGOFETs). *Biosens. Bioelectron.* 2021, 182, 113144.

[172] Poimanova, E. Yu., Shaposhnik, P. A., Karaman, P. N., Anisimov, D. S., Skorotetcky, M. S., Polinskaya, M. S., Borshchev, O. V., Agini, E. V. and Ponomarenko, S. A. Electrolyte-gated organic field-effect transistors based on 2,6-dioctyltetrathienoacene as a convenient platform for fabrication of liquid biosensors. *Russ. Chem. Bull.* 2022, 71, 2116–2122.

[173] Solodka, K., Berto, M., Ferraro, D., Menozzi, C., Borsari, M., Bortolotti, C. A., Biscarini, F. and Pinti, M. Detection of neurofilament light chain with label-free electrolyte-gated organic field-effect transistors. *Adv. Mater. Interfaces.* 2022, 9, 2102341.

[174] Sarcina, L., Macchia, E., Loconsole, G., D'Attoma, G., Bollella, P., Catacchio, M., Leonetti, F., Di Franco, C., Elicio, V., Scamarcio, G., Palazzo, G., Boscia, D., Saldarelli, P. and Torsi, L. Fast and reliable electronic assay of a xylella fastidiosa single bacterium in infected plants Sap. *Adv. Sci.* 2022, 9, 2203900.

[175] Piro, B., Mattana, G. and Reisberg, S. Transistors for chemical monitoring of living cells. *Biosensors.* 2018, 8, 65.

[176] Zhang, Y., Li, J., Li, R., Sbircea, D.-T., Giovannitti, A., Xu, J., Xu, H., Zhou, G., Bian, L., McCulloch, I. and Zhao, N. Liquid–solid dual-gate organic transistors with tunable threshold voltage for cell sensing. *ACS Appl. Mater. Interfaces.* 2017, 9, 38687–38694.

[177] Cramer, T., Chelli, B., Murgia, M., Barbalinardo, M., Bystrenova, E., de Leeuw, D. and Biscarini, F. Organic ultra-thin film transistors with a liquid gate for extracellular stimulation and recording of electric activity of stem cell-derived neuronal networks. *Phys. Chem. Chem. Phys.* 2013, 15, 3897–390

CHAPTER 2

Electrolyte-Gated Organic Field-Effect Transistors for Monitoring Amyloid Aggregation

Electrolyte-gated organic field-effect transistors (EGOFETs) are being widely investigated in label-free high-sensitivity biosensors, and are attracting a lot of interest for their application in diagnostic applications. This chapter shows that EGOFETs also show great potential as electrical transducers for analyzing protein aggregation processes due to their inexpensive cost, short testing duration, high sensitivity, and electrical readout. In particular, EGOFETs have been utilized here as a transducer platform to monitor amyloid aggregation kinetics, a relevant biomarker of neurodegenerative illnesses such as Alzheimer's disease.

1. Introduction

Neurodegenerative disorders are a group of conditions marked by the progressive deterioration of neurons under specific circumstances.[1] These disorders impair critical functions associated with a healthy nervous system, including movement, memory, breathing, and speech.[2] Examples of neurodegenerative diseases include Alzheimer's, Huntington's, and Parkinson's disease. Research indicates that many of these disorders are caused by protein misfolding, which results in the aggregation of misfolded proteins in the brain.

The misfolding and abnormal clustering of proteins into amyloid aggregates are linked to over 50 human diseases, including the prevalent neurodegenerative disorders Alzheimer's and Parkinson's, as well as type II diabetes.[3,4] Alzheimer's Disease (AD) is caused primarily by the aggregation of proteins in the brains of the patients. Amyloid-beta and tau are two distinct proteins found in two separate sites that have been identified as the primary causes of Alzheimer's disease. Although the primary etiology of Alzheimer's disease is not fully known, two elements have been identified as key contributors to the illness: amyloid beta plaques and tau tangles.[5]

These protein aggregates are characterized by a common β-sheet-rich conformation, referred to as a cross-β structure. This structure has a strong affinity for dyes like Congo Red and thioflavin T (ThT), which are frequently used to detect amyloid aggregates both in vitro and in vivo. Furthermore, amyloid-beta aggregates form beta-amyloid plaques (ABP), which are harmful to neurons. ABPs can accumulate between healthy neurons, interfering with the communication and signaling mechanism between them.[7] When neurons fail to deliver impulses, the brain suffers major damage and loses some capabilities, including memory (Figure 2.1).

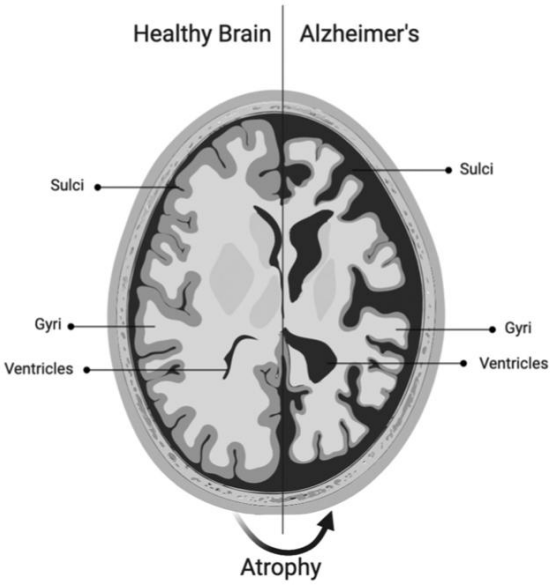

Figure 2.1. Atrophy phenomenon that happens in the brain during Alzheimer's disease. Extracted from ref[1].

Amyloid-beta peptides **$A\beta_{1-40}$** and **$A\beta_{1-42}$** are two types of amyloids that accumulate abnormally in the brain.[8] $A\beta_{1-42}$ is more important in Alzheimer's disease pathogenesis than $A\beta_{1-40}$ due to its quicker aggregation rate and propensity to create free radicals, which induce neuronal damage. Aβ can exist as monomers or they can aggregate as dimers, oligomers, protofibrils, and amyloid plaques. These species exist in a dynamic equilibrium, where one form can transform into another in both directions. They are distinguished by factors such as aggregate size, conformational state, and solubility, with fibrils and amyloid plaques being insoluble.[9] The fibrillization process follows a nucleation-dependent polymerization mechanism, where protein monomers self-assemble into oligomers of varying sizes with increasing β-sheet structure. During this process, once a critical mass of aggregates forms the cross-β structure, the rate of elongation surpasses the rate of disaggregation, leading to an exponential increase in the size and number of aggregates. This results in the majority of monomeric proteins being consumed in the assembly reaction. The kinetics of this nucleation-polymerization process exhibit a sigmoidal growth profile. The initial lag phase is characterized by the difficulty of forming new oligomers directly from monomers, while monomer addition to pre-existing aggregates occurs more easily. During this phase, soluble protein monomers self-assemble to form benign oligomers (BO), which are disordered. These oligomers then transform into toxic oligomers (TO) with a partial β-sheet-structured, marking the onset of toxicity and contributing to neurodegenerative disease progression.

The sigmoidal growth profile of amyloid aggregation reflects the easier addition of protein monomers to preformed, stable aggregated, while the nucleation step remains the rate-limiting factor. As the fibrillization process continues, a plateau phase is eventually reached due to the depletion of available monomers (**Figure 2.2**).[4] In some cases, mechanisms beyond primary nucleation and elongation, such as fibril fragmentation and fibril-based secondary nucleation, can also affect the kinetics of amyloid aggregation. These additional processes contribute to the complexity of the system by further accelerating aggregate formation and growth, often enhancing the spread of amyloid fibrils.

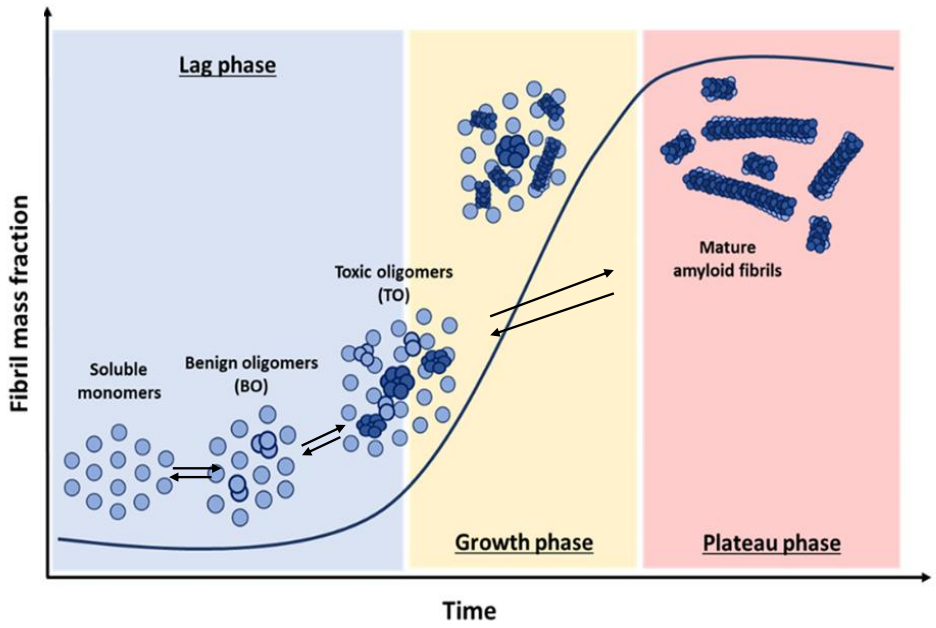

Figure 2.2. Schematic representation of amyloid formation process according to the nucleation-conversion-polymerization model. Extracted from ref[4].

Amyloid plaques in Alzheimer's disease brains are made up of these fibrils, but the soluble oligomers are currently thought to be the primary source of neurotoxicity and synaptic dysfunction.[10] These oligomers disrupt synaptic connections, cause brain inflammation, and change neuronal function, resulting in cognitive impairment. With an aging population, AD prevalence is anticipated to more than triple over the next 50 years, emphasizing the critical need for a better understanding of amyloid aggregation and the development of disease-modifying drugs.

Several techniques are used for studying and determining aggregated species including their morphology structure,[11–13] size and molecular weight,[14–16] aggregation

kinetics,[17,18] and quantification studies.[19–21] In particular, in situ amyloid oligomer detection and quantification[22] may be achieved using complex NMR methods,[23,24] fluorescence correlation spectroscopy in Thioflavin T (ThT) fluorescence assays,[25] or using oligomer-specific probes.[26] The combination of different techniques is also often necessary. For instance, Bartolini et al.[27] report a multimethodological study that included atomic force microscopy (AFM), transmission electron microscopy (TEM), fluorescence microscopy, mass spectrometry techniques (such as MALDI-TOF and ESI-QTOF) and direct thioflavin T (ThT) fluorescence spectroscopy. This approach aimed to establish a reliable and highly reproducible experimental protocol for characterizing the morphology and dimensions of $A\beta_{1-42}$ aggregates along the self-assembly pathway. Hence, studying amyloid aggregation is not straightforward and requires the use of expensive benchtop equipment and often the biomolecule label, enhancing the study's cost and complexity.

Knowing the different parameters that impact peptide aggregation (e.g., pH, concentration, temperature)[28] and examining the effect of drugs on aggregation can be extremely valuable in understanding this condition and its treatment. As a result, the capability to do systematic research to screen the effect of different parameters on the aggregation process is essential.

Electrolyte-Gated Organic Field-Effect Transistors (**EGOFETs**) are becoming appealing transducers in bio-sensing because of their low cost, ease of electrical reading, and inherent amplification capabilities.[29,30] Additionally, EGOFETs have also been employed for studying a variety of dynamic processes. For instance, EGOFETs have been exploited to investigate the formation of self-assembled monolayers of surfactants on metal surfaces. Due to the high EGOFET sensitivity, the adsorption process of cationic and anionic surfactants on the gate surface was successfully monitored.[31] The surface adsorption caused a shift in the device threshold voltage, which permitted to determine the surfactant critical monolayer concentration.

Fillaud et al.[32] also investigated a dynamic process with an EGOFET based on the study of a stimuli-responsive hydrogel that can reversibly adjust its morphological and physicochemical properties. The authors grafted an ultrathin poly(acrylic acid) hydrogel film onto the gate of a p-type EGOFET and established a correlation between the

hydrogel's swelling state at different pH and the transistor output characteristics (**Figure 2.3**). The hydrogel-related swelling process in the basic medium generates a rise in the threshold voltage as the negative charge density on the gate electrode increases abruptly and intensely. The fluctuation in drain current during the in situ pH electrolyte adjustment enabled a quantitative measurement of the hydrogel switching kinetics.

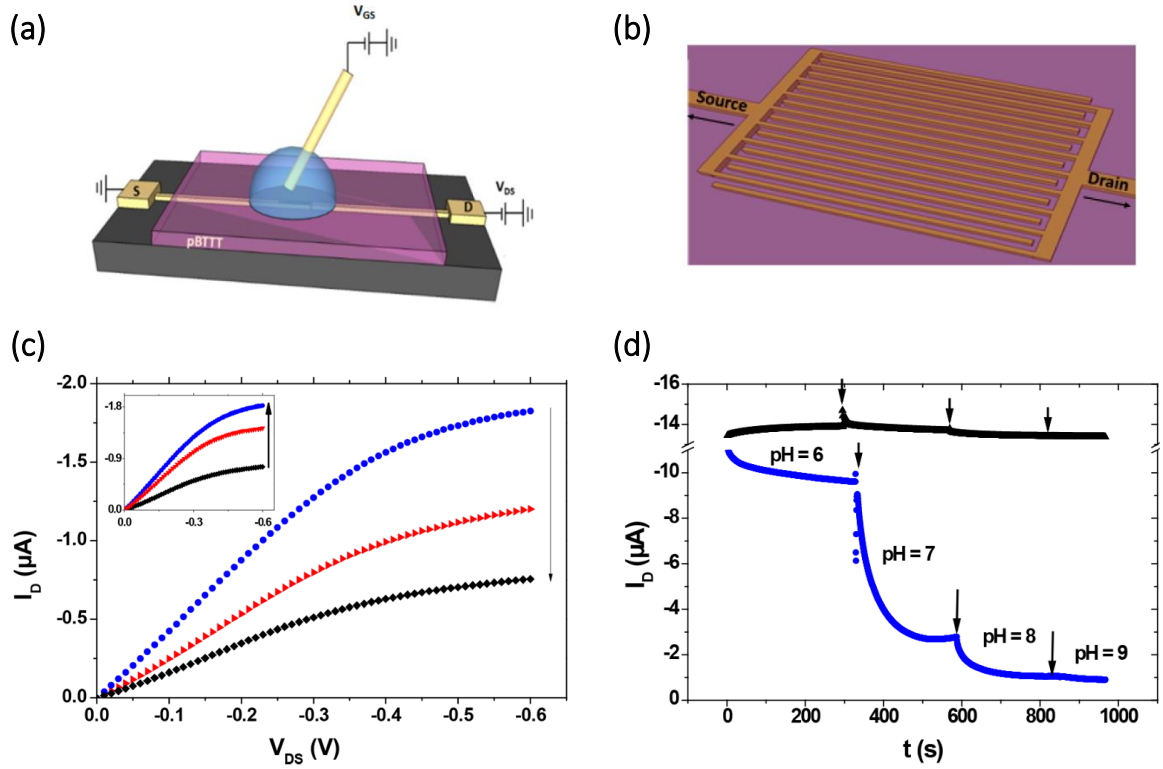

Figure 2.3. Scheme of the EGOFET structure: **(a)** The complete structure of the EGOFET and **(b)** interdigitated source and drain electrodes with dimensions of L= 10 µm and W= 30000 µm. **(c)** Output characteristics (V_{GS}= -0.6 V) of the functionalized EGOFET measured at different pH levels (pH 4 in blue, pH 7 in red, and pH 9 in black). The arrow indicates the chronological sequence in which the curves were recorded. Inset: the same experiment repeated inverting the pH sequence. **(d)** Plots of I_D versus time (V_{GS}= V_{DS}= -0.4 V) during a dynamic experiment performed using the bare gate electrode (black line) and the functionalized gate (blue line) e for successive pH jumps. Each arrow represents an injection of NaOH. Adapted from ref[32] .

Furthermore, Tamayo et al.[33] created a robust EGOFET that can respond to pH values ranging from 1-10. This was accomplished by using the pH-sensitive supramolecular host-guest complex formed by imidazole/beta-cyclodextrin (β-CD). Their sensing method involved incubating magnetic nanoparticles that were functionalized with β-CD in imidazole solutions across different pH levels by trapping these nanoparticles in a magnetic carbon electrode. Such electrode was subsequently used as

gate contact in the EGOFET. Higher pH promoted complexation, resulting in a negative shift of the device transfer characteristics (**Figure 2.4**).

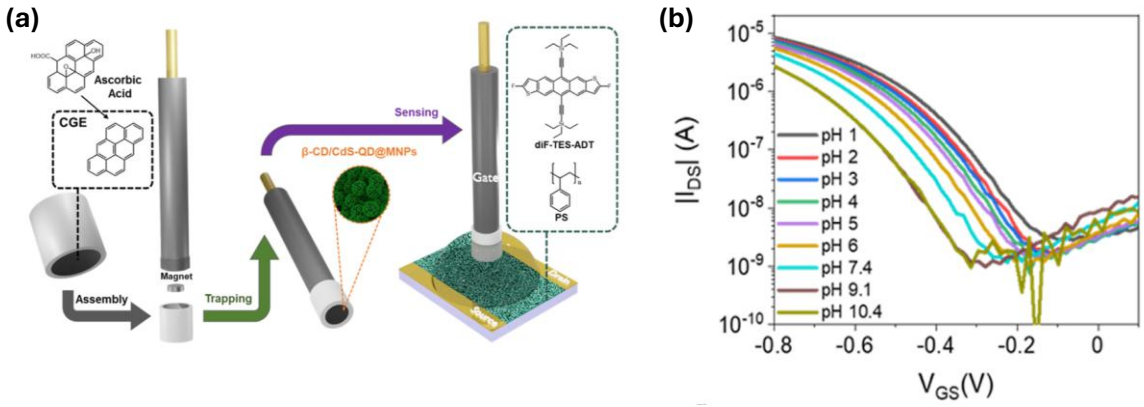

Figure 2.4. (a) Schematic representation of the EGOFET device showing the implementation of a CGE as a novel approach to sense supramolecular interaction between imidazole and β-CD/CdS-QD@MNPs. **(b)** Transfer characteristics of the EGOFET (V_{DS}= -0.4 V) using a CGE with collected β-CD(CdS-QD@MNPs that had previously been incubated in PBS with [$C_3H_4N_2$]= 6.7 mM at pH values ranging from 1 to 10.4. Adapted from ref[33].

In this chapter, EGOFET devices have been used for investigating dynamic biological processes. In particular, we used an EGOFET platform to study the amyloid aggregation process before fibril precipitation, taking $A\beta_{1\text{-}40}$ as a model system.

2. Summary of the results

EGOFETs were fabricated using as active organic semiconductor layer a thin film diF-TES-ADT blended with polystyrene. The films were prepared on Kapton substrates with a coplanar gate (**CG**) electrode serving as a reference, whereas for the aggregation monitoring measurements, a top gate (**TG**) was employed (**Figure 2.5a**).

The TG consisted of a gold disk electrode modified with A11 anti-oligomer antibodies which can specifically interact with $A\beta_{1-40}$ oligomers. This was realised by the formation of a monolayer of recombinant Protein G cysteine-tagged (cys-PG) on the gold surface. The electrodes were then treated with 6-Mercapto-1-Hexanol (MCH) to passivate the non-covered Au regions and prevent biomolecule adsorption. Finally, the electrodes were incubated with an A11 anti-oligomer antibodies (A11 Ab) solution so they could interact with the Protein G layer. Cyclic Voltammetry (CV) and Electrochemical Impedance Spectroscopy (EIS) were used to investigate the electrode changes during its functionalization. Results showed a decrease in the peak current intensity and separation of the reduction and oxidation peaks with each functionalization stage, indicating that molecular layers impede electron transport between the redox probe in the solution and the electrode. The transfer characteristics of the EGOFET with both bare and bio-modified Au disks were also studied. Modifying the electrode with cys-PG and MCH resulted in a gradual shift of the transfer curve to negative gate voltages. In contrast, introducing A11 Ab pushed the curve towards positive gate voltages. These changes can be ascribed to potentiometric effects caused by the dipole or charges of the molecules grafted on the electrode gate surface.

Two methodologies were employed to better understand the $A\beta_{1-40}$ aggregation mechanism: In **approach I**, the study involved incubating at 37°C a solution of $A\beta_{1-40}$ and immersing one A11 Ab-modified electrode at different aging times. In contrast, in **approach II** the study used a freshly modified A11 Ab-modified electrode for each incubation time.

The results obtained by EIS and EGOFET followed a similar tendency in both approaches. The data was analysed by plotting in the case of EIS the evolution with time of the relative charge transfer resistance (R_{ct}) changes with respect to the initial A11 Ab-

modified electrode ($\Delta R'_{ct} = (R_{ct,t} - R_{ct,Ab})/R_{ct,Ab}$, where $R_{ct,t}$ is the charge transfer resistance found for the Ab-coated electrode incubated in the $A\beta_{1-40}$ solution aged for a specific time period and $R_{ct,Ab}$ is the charge transfer resistance of the initial A11 Ab-coated electrode). Similarly, in the EGOFETs we explored the time evolution of the device source-drain current changes as: $\Delta I'_{DS} = (I_{DS,t} - I_{DS,Ab})/I_{DS,Ab}$ (at $V_{TG,S}$ = -0.1 V), where $I_{DS,t}$ corresponds to the source-drain current using as top-gate the A11 Ab-coated electrode immersed in the $A\beta_{1-40}$ solution aged for a specific time period and $I_{DS,Ab}$ is the current of the reference A11 Ab-coated electrode.

In approach I by EIS an increase of the electrode charge transfer resistance is observed with time until reaching saturation at 45-60 minutes. The EGOFET results showed also an increase in the device's current intensity with time during this time range until saturation (**Figure 2.5b,c**). On the other hand, in the conditions employed in approach II, both EIS and EGOFET data showed the maximum concentration of amyloid oligomers in the solution, that is the maximum electrode response, after aging the solutions for 60 minutes (**Figure 2.5d,e**). After this time, the electrode response diminished, which could be attributed to the formation of fibrils.

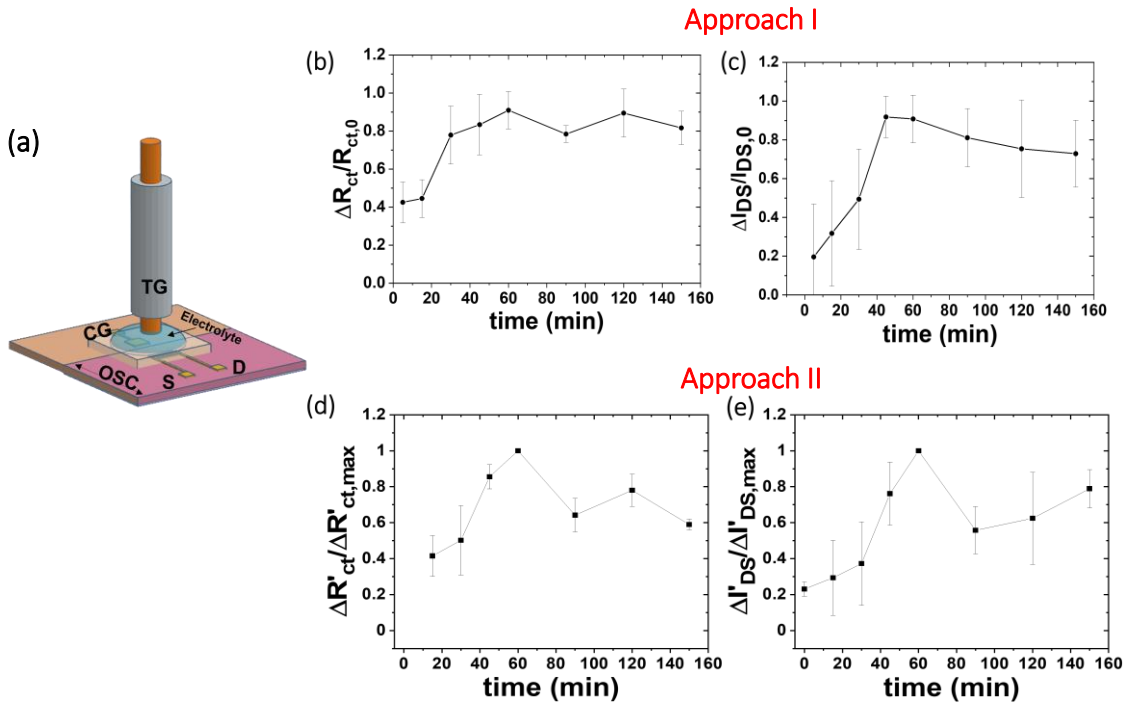

Figure 2.5. (a) Schematic representation of the device configuration (CG: coplanar gate, TG: top gate, S: source, D: drain and OSC: organic semiconductor). Electrical response in Approach I: **(b)** Evolution of the relative $\Delta R'_{ct}/\Delta R'_{ct,max}$ with the aging time of the $A\beta_{1-40}$ solution extracted from the EIS measurements. **(c)** Relative $\Delta I'_{DS}/\Delta I'_{DS,max}$ (at $V_{TG,S}$ = -0.1 V) extracted from the EGOFET characteristics at different aging times of the $A\beta_{1-40}$ solution. Electrical response in Approach II: evolution with time of **(d)** $\Delta R'_{ct}/\Delta R'_{ct,max}$ and **(e)** $\Delta I'_{DS}/\Delta I'_{DS,max}$ (at $V_{TG,S}$ = -0.1 V). In this approach each electrode has its own reference. The data in (d) and (e) are averaged from three different series of measurements and normalized to the maximum response, which takes place in all the cases at 60 min. The data reported corresponds to the values extracted from three different experiments.

Dynamic Light Scattering (DLS) experiments were also performed to corroborate our data. Remarkably, large particles with a diameter of a few hundred nanometers were detected after incubating the solutions for 60 minutes, indicating the presence of oligomeric species. However, at 90 minutes of incubation, the particle size distribution was centered at around 1000 nm, in agreement with the formation of fibrils.

3. Conclusions

An EGOFET-based platform for monitoring the formation of $A\beta_{1-40}$ low-weight oligomeric species, crucial in neurodegenerative diseases like Alzheimer's and Parkinson's, has been demonstrated. While both approaches employed yield comparable results, the first one is prone to electrode saturation and does not track the reduction in oligomeric species once fibrils form. Our study found that the maximum $A\beta_{1-40}$ oligomer concentration in the studied conditions occurs after 1 hour, which was validated by EIS, DLS, and literature data.[13] In conclusion, it has been demonstrated that EGOFETs hold great promise as label-free electrical transducers for studying protein aggregation processes due to advantages such as low cost, fast testing times, high sensitivity, and electrical readout.

4. References

[1] Ashrafian, H., Zadeh, E. H. & Khan, R. H. Review on Alzheimer's disease: Inhibition of amyloid beta and tau tangle formation. *Int. J. Biol. Macromol.* 2021, 167, 382–394.

[2] Fox, L. M. & Yamamoto, A. (2015) Chapter 7 - Macroautophagy of Aggregation-Prone Proteins in Neurodegenerative Disease. In Autophagy: Cancer, Other Pathologies, Inflammation, Immunity, Infection, and Aging. Academic Press.

[3] Cummings, J. L. & Cole, G. Alzheimer disease. *JAMA.* 2002, 287, 2335–2338.

[4] Polanco, D., Carrancho, A., Gracia, P. and & Cremade, N. Characterization of amyloid aggregation and inhibition by diffusion-based single-molecule fluorescence techniques. *Biophysica*. 2002, 2, 506-524.

[5] Hung, A. S. M., Liang, Y., Chow, T. C. H., Tang, H. C., Wu, S. L. Y., Wai, M. S. M. and Yew, D. T. Mutated tau, amyloid, and neuroinflammation in Alzheimer disease-A brief review. *Prog. Histochem. Cytochem.* 2016, 51, 1–8.

[6] Sipe, J. D., Benson, M. D., Buxbaum, J. N., Ikeda, S.-I., Merlini, G., Saraiva, M. J. and Westermark, P. Amyloid fibril proteins and amyloidosis: chemical identification and clinical classification International Society of Amyloidosis 2016 Nomenclature Guidelines. *Amyloid Int. J. Exp. Clin. Investig. Off. J. Int. Soc. Amyloidosis.* 2016, 23.

[7] Salehi, A., Delcroix, J.-D. & Swaab, D. F. Alzheimer's disease and NGF signaling. *J. Neural Transm. Vienna Austria.* 2004, 111, 323–345.

[8] Chen, G.-F., Xu, T.-H., Yan, Y., Zhou, Y.-R., Jiang, Y., Melcher, K. and Xu, H. E. Amyloid beta: structure, biology and structure-based therapeutic development. *Acta Pharmacol. Sin.* 2017, 38, 1205–1235.

[9] Hampel, H., Hardy, J., Blennow, K., Chen, C., Perry, G., Kim, S. H., Villemagne, V. L., Aisen, P., Vendruscolo, M., Iwatsubo, T., Masters, C. L., Cho, M., Lannfelt, L., Cummings, J. L. and Vergallo, A. The amyloid-β pathway in Alzheimer's Disease. *Mol. Psychiatry*. 2021, 26, 5481–5503.

[10] Kalita, S., Kalita, S., Paul, A., Sarkar, A. & Mandal, B. Peptidomimetics prepared by tail-to-side chain one component peptide stapling inhibit Alzheimer's amyloid-β fibrillogenesis. *Chem. Sci.* 2020, 11, 4171–4179.

[11] Anderson, V. L. & Webb, W. W. Transmission electron microscopy characterization of fluorescently labelled amyloid β 1-40 and α-synuclein aggregates. *BMC Biotechnol.* 2022, 11, 125.

[12] Antzutkin, O. N. Amyloidosis of Alzheimer's Abeta peptides: solid-state nuclear magnetic resonance, electron paramagnetic resonance, transmission electron microscopy, scanning transmission electron microscopy and atomic force microscopy studies. *Magn. Reson. Chem. MRC.* 2004, 42, 231–246.

[13] Stine, W. B., Dahlgren, K. N., Krafft, G. A. & LaDu, M. J. In vitro characterization of conditions for amyloid-beta peptide oligomerization and fibrillogenesis. *J. Biol. Chem.* 2003, 278, 11612–11622.

[14] Heppler, R. W., Grim, K. M., Nahas, D. D., Breese, R., Dodson, E. C., Acton, P., Keller, P. M., Yeager, M., Wang, H., Shughrue, P., Kinney, G. and Joyce, J. G. Solution state characterization of amyloid beta-derived diffusible ligands. *Biochemistry*. 2006, 45, 15157–15167.

[15] Bitan, G., Fradinger, E. A., Spring, S. M. & Teplow, D. B. Neurotoxic protein oligomers--what you see is not always what you get. *Amyloid Int. J. Exp. Clin. Investig. Off. J. Int. Soc. Amyloidosis*. 2005, 12, 88–95.

[16] Carrotta, R., Manno, M., Bulone, D., Martorana, V. & San Biagio, P. L. Protofibril formation of amyloid beta-protein at low pH via a non-cooperative elongation mechanism. *J. Biol. Chem.* 2005, 280, 30001–30008.

[17] Santa-María, I., Hernández, F., Moreno, F. J. & Avila, J. Taurine, an inducer for tau polymerization and a weak inhibitor for amyloid-beta-peptide aggregation. *Neurosci. Lett.* 2007, 429, 91–94.

[18] Klaver, A. C., Patrias, L. M., Finke, J. M. & Loeffler, D. A. Specificity and sensitivity of the Abeta oligomer ELISA. *J. Neurosci. Methods*. 2011, 195, 249–254.

[19] Klaver, A. C., Patrias, L. M., Finke, J. M. & Loeffler, D. A. Specificity and sensitivity of the Abeta oligomer ELISA. *J. Neurosci. Methods.* 2011, 195, 249–254.

[20] Georganopoulou, D. G., Chang, L., Nam, J.-M., Thaxton, C. S., Mufson, E. J., Klein, W. L. and Mirkin, C. A. Nanoparticle-based detection in cerebral spinal fluid of a soluble pathogenic biomarker for Alzheimer's disease. *Proc. Natl. Acad. Sci. U. S. A.* 2005, 102, 2273–2276.

[21] Ruiz-Arias, A., Jurado Palomares, R., Fueyo González, F., Herranz, R., Gálvez Rodríguez, N., González Vera, J. A. & Orte Gutiérrez, A. A FRET pair for quantitative and superresolution imaging of amyloid fibril formation. *Sens. Actuators B Chem.* 2022, 350, 130882.

[22] Linse, S. Toward the equilibrium and kinetics of amyloid peptide self-assembly. *Curr. Opin. Struct. Biol.* 2021, 70, 87–98.

[23] Nguyen, T. T., Siang, S. and Roche, J. High-Pressure NMR Experiments for Detecting Protein Low-Lying Conformational States. *JoVe Journal, Biochemistry*. 2021, 172, e62701.

[24] Cawood, E. E., Karamanos, T. K., Wilson, A. J. & Radford, S. E. Visualizing and trapping transient oligomers in amyloid assembly pathways. *Biophys. Chem.* 2021, 268, 106505.

[25] Tiiman, A., Jarvet, J., Gräslund, A. & Vukojevic, V. Heterogeneity and turnover of intermediates during amyloid-β (Aβ) peptide aggregation studied by fluorescence correlation spectroscopy. *Biochemistry*. 2015, 54, 7203-7211.

[26] Åslund, A., Sigurdson, C. J., Klingstedt, T., Grathwohl, S., Bolmont, T., Dickstein, D. L., Glimsdal, E., Prokop, S., Lindgren, M., Konradsson, P., Holtzmann, D. M., Hof, P. R., Heppner, F. L., Gandy, S., Jucker, M., Aguzzi, A., Hammarström, P. & Nilsson, K. P. R. Novel pentameric thiophene derivatives for in vitro and in vivo optical imaging of a plethora of protein aggregates in cerebral amyloidoses. *ACS Chem. Biol.* 2009, 4, 673–684.

[27] Bartolini, M., Naldi, M., Fiori, J., Valle, F., Biscarini, F., Nicolau, D. V. & Andrisano, V. Kinetic characterization of amyloid-beta 1-42 aggregation with a multimethodological approach. *Anal. Biochem.* 2011, 414, 215–225.

[28] Bruggink, K. A., Müller, M., Kuiperij, H. B. & Verbeek, M. M. Methods for analysis of amyloid-β aggregates. *J. Alzheimers Dis. JAD.* 2012,28, 735–758.

[29] Magliulo, M., De Tullio, D., Vikholm-Lundin, I., Albers, W. M., Munter, T., Manoli, K., Palazzo, G. & Torsi, L. Label-free C-reactive protein electronic detection with an electrolyte-gated organic field-effect transistor-based immunosensor. *Anal. Bioanal. Chem.* 2016, 408, 3943–3952.

[30] Sensi, M., Berto, M., Gentile, S., Pinti, M., Conti, A., Pellacani, G., Salvarani, C., Cossarizza, A., Bortolotti, C. A. & Biscarini, F. Anti-drug antibody detection with label-free electrolyte-gated organic field-effect transistors. *Chem. Commun.* 2021, 57, 367–370.

[31] Zhang, Q., Tamayo, A., Leonardi, F. & Mas-Torrent, M. Interplay between electrolyte-gated organic field-effect transistors and surfactants: A surface aggregation tool and protecting semiconducting layer. *ACS Appl. Mater. Interfaces* 2021, 13, 30902–30909.

[32] Fillaud, L., Petenzi, T., Pallu, J., Piro, B., Mattana, G. & Noel, V. Switchable hydrogel-gated organic field-effect transistors. *Langmuir* 2018, 34, 3686–3693.

[33] Tamayo, A., Campos-Lendinez, A., Muñoz, J., Crivillers, N. & Mas-Torrent, M. pH sensor based on supramolecular host-guest interactions and an organic field-effect transistors with a magnetic carbon gate electrode. Chemistry of Materials. 2023, 35, 9257-9263

Article 1

Electrolyte-Gated Organic Field-Effect Transistor for Monitoring Amyloid Aggregation

Sara Ruiz-Molina, Carme Martínez-Domingo, Simona Ricci, Stefano Casalini, Marta Mas-Torrent

*Accepted

Electrolyte-Gated Organic Field-Effect Transistor for monitoring amyloid aggregation

*Sara Ruiz-Molina, Carme Martinez-Domingo, Simona Ricci, Stefano Casalini, Marta Mas-Torrent**

S. Ruiz-Molina, C. Martinez-Domingo, S. Ricci, S. Casalini, M. Mas-Torrent:
Institut de Ciència de Materials de Barcelona (ICMAB-CSIC), Campus UAB, 08193 Bellaterra, Spain.
E-mail: mmas@icmab.es

Current address S. Casalini:
Department of Chemical Sciences, University of Padua, via Francesco Marzolo 1, 35131, Padova, Italy.

Keywords: electrolyte-gated organic field-effect transistor, protein aggregation, β-amyloid oligomers, Alzheimer's disease

Amyloid-beta peptide aggregation is a crucial process in neurological disorders such as Alzheimer's and Parkinson's Diseases. Amyloids tend to assemble first into oligomers and, subsequently, into larger fibrils. The oligomer species are regarded as the primary cause of neurological dysfunction and, hence, they are key biomarkers for diagnosis and therapy. However, this aggregation process is complex to study, typically requiring the use of a combination of techniques and labelling of the biomolecules. Here, we demonstrate that the Electrolyte-Gated Organic Field-Effect Transistor (EGOFET) device is a promising low-cost transducer that can be used to monitor amyloids aggregation using an electrical readout and without the need of labelling. For this purpose, the gold surface of the gate contact was modified with an amyloid-beta 1-40 ($A\beta_{1-40}$) oligomer-specific antibody using a biofunctionalization method that incorporated Cysteine-Protein G (cys-PG). The bio-engineered Au electrode was implemented as a recognition element to

monitor the aggregation kinetics of $A\beta_{1-40}$ employing two complementary detection measurements: EGOFET and Electrochemical Impedance Spectroscopy (EIS). The maximum concentration of oligomer species was detected after 1 hour of incubation. Additionally, Dynamic Light Scattering (DLS) data corroborated these results. More broadly, this work elucidates the potential of EGOFETs as a label-free platform for studying in-vitro the parameters affecting protein aggregation or for the development of medical treatments that target the reduction of such aggregation.

1. Introduction

Alzheimer's Disease (AD) is a degenerative neurological condition that primarily affects the elderly and involves memory loss, cognitive decline, and behavioural changes. It is characterized by the accumulation of abnormal protein aggregates in the brain, such as amyloid-beta (Aβ) peptides. $A\beta_{1-40}$ and $A\beta_{1-42}$ are two of the several forms of Aβ that play a role in the pathogenesis of AD, which are derived from amyloid precursor protein (APP) fragments.[1] The $A\beta_{1-40}$ has a higher abundance than $A\beta_{1-42}$, although the latter has been recognized as the most critical in AD pathology since its aggregation rate is faster and generates free radical species that provoke neuronal damage. Aβ peptides undergo a slow transformation from the native monomer peptide to soluble Aβ oligomers and, eventually, to insoluble protofibrils and fibrillar aggregates. The typical amyloid plaques found in the brains of AD patients are composed of large, insoluble fibrils that form from these protofibrils and further assemble into them. However, it is now widely accepted that the soluble oligomeric species of Aβ peptides, rather than mature fibrils, are the primary cause of neurotoxicity and synaptic dysfunction in AD patients.[2] These oligomers have the potential to disrupt synaptic connections, promote brain inflammation, and alter neuronal function, leading to cognitive damage.[3] Because of the ageing population, the prevalence of AD is expected to more than treble over the next 50 years. Hence, it is key

to gain a better understanding of amyloid aggregation processes and to urgently develop novel disease-modifying medications that can target such processes. [4,5]

Various factors, including concentration, pH, and temperature, influence amyloid peptide aggregation.[6] The study and determination of the aggregation species is a complex task and has been the focus of attention over the last few years. A large variety of techniques have been used to determine their morphology and conformational structure (e.g., Electron Microscopy (EM),[7] Atomic Force Microscopy (AFM)[8,9] and Circular Dichroism (CD)[10–12]), the species size and molecular weight (e.g. mass spectrometry, chromatography, electrophoresis and Dynamic Light Scattering (DLS)),[13–17] their aggregation kinetics (e.g., turbidity and fluorescence assays)[18–21] and their quantification (e.g., immunology-based quantification techniques,[22,23] surface-immobilized bio-barcodeassay[24] and Fluorescence Resonance Energy Transfer (FRET)).[25,26] A comparative table of the different techniques employed to study amyloid peptides and their aggregation species can be found in **Table S1**. Undoubtedly, the study of amyloid aggregation is challenging and often requires the use of a combination of complicated and expensive techniques to achieve reliable and reproducible results.[27,28]

Because of their low cost, easy electrical readout, and intrinsic amplification features, electrolyte-gated organic field-effect transistors (EGOFETs) are particularly appealing transducers. EGOFET's operation relies on the formation of two electrical double layers (EDLs) at the organic semiconductor-electrolyte and electrolyte-gate interfaces upon the application of a gate voltage, which modulates the transport flowing along the organic semiconductor. Hence, these devices are highly sensitive to changes happening at such interfaces, which have been widely exploited to fabricate bio-transducers for sensing.[29,30,31,32] However, EGOFETs potential is not limited to bio-sensing[33–35] since it has been shown that these devices can also be exploited as

transducers in other applications such as in electroceuticals,[36] bioelectric signal recording,[37] neuromorphic,[38] and to study dynamic processes.[39,40]

This paper reports on the use of an EGOFET for investigating the amyloid aggregation process before fibril precipitation, taking $A\beta_{1-40}$ as a model system. This was realized by functionalizing the gate electrode with an anti-oligomer polyclonal antibody specific to solely soluble $A\beta_{1-40}$ oligomeric species. Then, the electrode was incubated in an $A\beta_{1-40}$ solution and aged during different periods. The maximum electrical response and, hence, the maximum amount of oligomers, was found after one hour. This study was further validated using electrochemical techniques, such as Cyclic Voltammetry (CV) and Electrochemical Impedance Spectroscopy (EIS), as well as Dynamic Light Scattering (DLS) experiments. Thus, this work expands the potential uses of EGOFETs for investigating dynamic biological processes. In particular, EGOFETs can be applied as novel low-cost label-free tools to investigate amyloid aggregation, using simply an electrical signal as readout.

2. Results and discussion

2.1. EGOFET devices characterization

A thin film of a 2,8-Difluoro-5,11-bis(triethylsilylethynyl)anthradithiophene (diF-TES-ADT) and polystyrene (PS) blend (**Figure 1a**) was selected as active organic semiconductor (OSC) layer of the EGOFET. The films were prepared on top of Kapton substrates with pre-patterned source (S), drain (D), and coplanar gate (CG) electrodes using the Bar-Assisted Meniscus Shearing (BAMS) technique, as formerly reported (**Figure S1**).[41,42] The CG was used as reference gate contact, while the subsequent described aggregation monitoring experiments were carried out using a top gate (TG). Previously it was demonstrated that the presence of the insulating binding polymer is

critical for improving the material processability and achieving enhanced device performance and stability.[43,44] Cross-polarized optical microscopy images show that the semiconducting films are highly homogenous and crystalline (Figure 1a).

The as-prepared devices were electrically characterized using Milli-Q water as an electrolyte and the CG electrode. **Figure 1b** shows the transfer characteristics of the diF-TES-ADT:PS-based EGOFETs, where, as expected, a clear p-type behavior is observed.[44] The transfer characteristics, depicted in Figure 1b, reveal low hysteresis and good source-drain current (I_{DS}) modulation. In the case of liquid-gated transistors, the product of mobility (μ) and double-layer capacitance (C_{dl}) is commonly reported as the main figure of merit. A $C_{dl} \cdot \mu = 0.11(\pm 0.02)\ \mu S \cdot V^{-1}$ (in the saturation regime) was achieved for diF-TES-ADT:PS EGOFETs, which is in line with state-of-the-art liquid-gated organic transistors found in the literature.[45] In addition, the $I_{on/off}$ ratio was found to be around 10^2-10^3, while the coplanar gate-source leakage current ($I_{CG,S}$) was around 3 orders below I_{DS} and no current peaks were observed, ensuring that the device operation mechanism is via field effect and no redox processes are taking place. The corresponding output characteristics of these devices are displayed in **Figure S2a**.

In EGOFET-based transducers typically an initial device stabilization step is carried out to ensure achieving a stable device response. Thus, the devices were tested in Milli-Q water for over 80 minutes, applying a fixed coplanar gate-source ($V_{CG,S}$) and drain-source voltages (V_{DS}) of -0.2 V, whilst measuring I_{DS} (Figure 1b). It can be observed that the I_{DS} diminishes until it reaches a quasi-steady state after approximately 60 minutes, when it reaches almost 70% of the maximum current.[44] In **Figure S2b and S2c**, the device output and transfer characteristics after the stabilization step are reported. Hence, these conditions were used to stabilize the devices before performing the aggregation monitoring studies described below. It should be noted that, as mentioned, in

the following experiments, this coplanar gate was used as a control to verify that the device performance was preserved during the experiments. **Figure S3** shows the electrical characteristics of an EGOFET measured before and after performing a set of the aggregation tests described below, demonstrating that devices remain stable over the entire experiment.

2.2. Preparation and characterization of the transducing platforms

A gold disk electrode was used as the top gate (TG) for performing the aggregation experiments (Figure 1a). For this purpose, the electrode was modified with A11 anti-oligomer antibodies (A11 Ab), which are specific for $A\beta_{1-40}$ oligomeric species. That is, this antibody recognises soluble amyloid oligomers but does not interact with the monomers or the mature fibrils.

First, a monolayer of a recombinant Protein G cysteine-tagged (cys-PG) was prepared. PG is an antibody-binding protein that targets the fragment crystallizable region (Fc region) and has been extensively used to immobilize different types of antibodies in immunoassays.[35] Additionally, the cysteine tag allows for the formation of a covalent bond between the thiol group and the gold surface giving well-oriented PG monolayers.[46,47] Subsequently, the electrodes were further modified with 6-Mercapto-1-Hexanol (MCH) to shield uncoated Au areas and, hence, to avoid undesirable adsorption of bio-molecules on the metal surface. Finally, the antibody was grafted on the PG by immersing the electrode in a solution of A11 Ab. **Figure 2a** depicts the functionalization steps carried out (see further details in **Experimental Section** and **Supporting Information**). The stability of the functionalized surfaces was confirmed by Electrochemical Impedance Spectroscopy (EIS) (**Figure S4**).

Cyclic Voltammetry (CV) and EIS were used to investigate the electrode successive layer modification using $[Fe(CN_6)]^{3-/4-}$ as redox probe. By CV a reduction of the peak current intensity accompanied with a separation of the reduction and oxidation peaks were observed upon increasing the number of functionalization steps (**Figure 3a**). This agrees with the fact that the electron transfer between the electrode and the redox probe is hindered by the molecular layers. In addition, the Nyquist plots obtained by EIS show that the diameter of the semicircle increases with the electrode functionalization steps, which also indicates an increase in the charge-transfer resistance (R_{ct}) (**Figure 3b**). These results are in accordance with the successful functionalization of the gold electrode.

Furthermore, the transfer characteristics of the EGOFET using as top gate electrode the bare and bio-modified Au disk were also studied (Figure 3c). A significant and progressive shift of the transfer curve towards negative gate voltages is found upon the modification of the electrode with cys-PG and MCH. In contrast, when the A11 Ab is added, the curve shifts towards positive gate voltage values. All these electrical changes are attributed to the potentiometric effects triggered by the dipole/charges of the (bio)-molecules grafted on the electrode gate surface. This results in tuning the device threshold voltage, that is, the voltage required for switching on the EGOFET. Similar findings have been previously reported.[35]

2.3. Study of $A\beta_{1-40}$ aggregation kinetics

Once the protocol for the immobilization of the A11 Ab on the Au surface was optimized, we proceeded to investigate its suitability to detect $A\beta_{1-40}$ oligomers employing the functionalized electrode as i) working electrode in EIS analysis and ii) top gate electrode in the EGOFET device. Since the electrode should only interact with the oligomers species, its response should be directly linked to the oligomer concentration. In these studies, to ensure that aggregation of monomers into oligomers and fibrils takes place,

the $A\beta_{1-40}$ concentration selected was above the critical aggregation concentration employed (i.e., 12 µM),[48] which is also in agreement with the concentration values employed in other kinetic aggregation studies.[2,4]

In order to gain insights into the $A\beta_{1-40}$ aggregation process, two different methodologies were employed (**Figure 2b**). The first approach consisted of using one single working/gate electrode for the study. Essentially, the same A11 Ab-modified electrode was immersed in a solution of $A\beta_{1-40}$ incubated at 37ºC at different ageing times. In such a case, it is expected that the electrode response would increase due to the progressively increasing amount of oligomeric species present in the solution, until saturation. In fact, this methodology is the one typically used in conventional EGOFET bio-sensing measurements.

For the second strategy, a separate freshly A11 Ab-modified electrode was employed for each selected incubation time. Here, it could be anticipated that the electrode response would initially increase due to the aggregation of the monomer amyloid species into small oligomers, and eventually, it would decline because fibrils would start forming, leading to a reduction of the number of oligomers present in the solution. Hence, both approaches provide similar information regarding the formation of oligomers, although in the second approach we can also monitor the diminishment of this species in the solution, since a fresh electrode is employed each time. Thus, after a certain ageing time, when oligomers will assemble into fibrils, the concentration of oligomers (*i.e.*, the species that can interact with the antibody) will decrease. This will be translated in a stabilization of the electrode response in Approach I, but in Approach II this will be visualized with a reduction of the electrode response with respect to blank electrode.

3.2.1. Approach I

Nyquist plots were recorded incubating an A11 Ab-coated electrode in the prepared $A\beta_{1-40}$ solution every 15 minutes for 5 minutes, over a total time period of 150 minutes (**Figure 4a**). The evolution with time of the relative R_{ct} changes with respect to the initial A11 Ab-modified electrode is represented in **Figure 4c** as: $\Delta R'_{ct} = (R_{ct,t} - R_{ct,Ab})/R_{ct,Ab}$, where $R_{ct,t}$ is the charge transfer resistance found for the Ab-coated electrode incubated in the $A\beta_{1-40}$ solution aged for a specific time period and $R_{ct,Ab}$ is the charge transfer resistance of the A11 Ab-coated electrode before being exposed to the $A\beta_{1-40}$ solution. The variation over time of $\Delta R'_{ct}$ is normalized with respect to the maximum value ($\Delta R'_{ct,max}$). It can be observed that the electrode response increases until it reaches a saturation value at around 45-60 minutes, which can be attributed to the progressive increment of bound oligomer species on the electrode surface. After this time, the electrode response is quite stable over time.

Similarly, in a parallel experiment, the A11 Ab-modified electrode, incubated in the $A\beta_{1-40}$ solution at various ageing times, was utilized as the top gate contact in the EGOFET (**Figure 4b**). A linear interpolation in the transfer characteristics of an EGOFET allows extraction of the product ($C\cdot\mu$), which is proportional to the slope of the curve $\sqrt{I_{DS}}$ (in saturation regime) or I_{DS} (in linear regime) versus $V_{SG,}$ while the threshold voltage (V_{th}) is the intercept with the abscissa. A binding event in a bio-modified EGOFET can cause different electrical changes depending on the main prevailing mechanism.[49] If the binding event is affecting the device mobility or capacitance, the slope of the curve should change. However, if the main impact is on the metal workfunction (potentiometric effect) the curves will be shifted (i.e., the Vth would change).[50] The latter tends to occur when the ligands that are binded are charged, so then V_{th} can effectively transduce the electrostatic component of the binding interaction. In our experiments, it can be observed that he electrical changes observed upon binding the

oligomer species on the gate electrode are again ascribed to potentiometric effects that lead to the modification of the EGOFET threshold voltage. **Figure S5** plots the transfer characteristics from Figure 4b versus (V_{GS}-V_{th}), that is correcting the shift caused by the binding interaction. Clearly, the curves are overlapping, meaning that the device mobility and electrical double-layer capacitance are not significantly affected. This is commonly observed in EGOFET transducers.[35]

Figure 4d displays the time evolution of $\Delta I'_{DS} = (I_{DS,t} - I_{DS,Ab})/I_{DS,Ab}$, extracted at $V_{TG,S}$ equal to -0.1 V, where $I_{DS,t}$ corresponds to the source-drain current using as top-gate the A11 Ab-coated electrode immersed in the $A\beta_{1-40}$ solution aged for a specific time period and $I_{DS,Ab}$ is the current of the reference A11 Ab-coated electrode. The variation over time of $\Delta I'_{DS}$ is also normalized with respect to the maximum value ($\Delta I'_{DS,max}$). A trend analogous to the one found with the EIS measurements is observed with the EGOFET. Indeed, with time the device current intensity increases caused by the shifting of the transfer curves. After 45 minutes, the device response remains relatively stable.

These findings agree with the fact that the aggregation of the monomeric species leading to the formation of small oligomers that can interact with the antibody, is predominantly and progressively occurring over the first 45 minutes. Subsequently, either the oligomer concentration stops increasing due to the formation of fibrils, or the electrode is saturated and hence, is not able to detect higher oligomer concentrations. It is a well-known fact that in such experiments, electrodes exhibit a specific concentration range within which they provide a reliable response. Typically, at higher concentrations, all available binding sites become occupied, resulting in the electrode response saturation.[35] Therefore, in order to further understand the aggregation process of $A\beta_{1-40}$, the second measurement approach was carried out.

3.2.2. Approach II

As mentioned above, the methodology deployed here is focused on using various A11 Ab-functionalized electrodes, one for each incubation time, to study the $A\beta_{1-40}$ aggregation process. It should be noted that here each electrode has its specific reference, which corresponds to its response prior to the incubation into the $A\beta_{1-40}$ solution.

Representative examples of measured Nyquist plots and transfer characteristics for an electrode before and after incubation in an $A\beta_{1-40}$ solution aged for 60 minutes are shown in **Figure 5a and 5b**, respectively. Analyzing all the data, the evolution of the electrodes' response to the presence of oligomer species over time can be plotted. **Figure 5c and 5d** show the variation over time of $\Delta R'_{ct}$ and $\Delta I'_{DS}$ normalized with respect to the maximum value ($\Delta R'_{ct,max}$ and $\Delta I'_{DS,max}$, respectively). A gradual rise in $\Delta R'_{ct}$ and $\Delta I'_{DS}$ was observed during the first hour, in agreement with the fact that the oligomer concentration is increasing. After this time, with both techniques, a drop in the electrode response is found, pointing out that the quantity of oligomeric species in the solution diminishes. This is attributed to the aggregation of oligomers to form larger fibrils, which cannot interact with the anti-oligomer antibody A11 used in this study.

These results are in line with the ones achieved following Approach I. However, in Approach I the electrode seems to be saturating close to 45 min, whereas in Approach II an increase of the oligomeric concentration species is still detected between 45 and 60 min. Further, it should be noticed that in all these experiments a noteworthy dispersion in the results is noted, which can be attributed to differences in the electrodes, devices, and also in the prepared amyloid solutions. However, the tendency is clear and reproducible. Further, it should also be mentioned that when fibrils start to form, it is reported that the aggregation process becomes more complex since parallel processes of aggregation and disaggregation are simultaneously occurring.[51] This explains the larger variability and even oscillating tendency in the data obtained in Approach II after 60 min.

Since in our devices we are detecting soluble amyloid oligomers and it is not possible to prepare solutions of known concentration of oligomers, we cannot use our device to quantify this species or define a limit of detection. However, we can state that, in the conditions used here, a 60% increase in the measured I_{SD} current (at $V_{TG,S}$ = -0.5 V) is achieved when the oligomers concentration is maximum. In addition, we have fitted the time evolution curve in the time range in which the oligomer concentration is increasing (0-60 min) to a polynomial fit, giving the following fit: $(\Delta I'_{DS} / \Delta I'_{DS,max}) = 2 \cdot 10^{-4} \cdot t^2 + 8 \cdot 10^{-4} \cdot t + 0.225$ (R^2= 0.98) (**Figure S6**).

The amyloid aggregation process is known to be influenced by the type of peptide but also by the experimental conditions used (temperature, stirring conditions, concentration, etc).[10] Thus, although our results agree well with the reported work,[2,4] a direct comparison of the data is not straightforward. Thus, to further validate these obtained results, we analyzed the samples using the benchtop technique DLS. This technique allows us to study the particle size distribution of the amyloid peptide during the aggregation process under the studied conditions.[2] The hydrodynamic size distribution by volume of the $A\beta_{1-40}$ species obtained over the incubation time is plotted in **Figure 6**. This representation is the most suitable one to obtain information of a sample composition composed of different particle sizes. The respective plot in terms of intensity distribution, which can be more accurate for the determination of particle size, is shown in **Figure S7**. However, it should be noticed that DLS analysis assume homogeneous and spherical particles, which it is not the case here, and, thus, the obtained results should be considered in a qualitative manner. $A\beta_{1-40}$ samples displayed a size distribution centered in the 1-10 nm range after the first 15 minutes of incubation, which is ascribable to monomeric species. After 30 minutes, the particle size increased to produce a size distribution centered at 25 nm, indicating the formation of dimeric species. Extending the

incubation duration to 45 and 60 minutes resulted in larger particles with a diameter of a few hundred nanometers, indicating the presence of oligomeric species. At 90 minutes of incubation, the particle size distribution was centered at around 1000 nm, in agreement with the formation of fibrils. These results are in accordance with previous DLS studies[2] and also with the data obtained in this work by EIS and with the EGOFET measurements.

Protein aggregation is known to be associated with a wide range of human diseases, such as Alzheimer's or Parkinson diseases, but also is linked to systemic amyloidosis, type 2 diabetes, cataract and cancer.[52,53] Additionally, protein aggregation poses challenges for biopharmaceutical manufacturing of therapeutic proteins and peptides, since the unintended formation of aggregates can induce potential adverse immune reactions.[54] Despite the importance of the problem and the intense research carried out for the last few decades, many questions still remain open and the aggregation mechanisms are poorly understood. Commonly, the studies of the macroscopic protein aggregation over time are performed using specific fluorescent dyes. The application of organic low-cost transistors to monitor the aggregation of amyloids, or other proteins, by using simply an electrical readout signal and without the need of labelling might permit to perform more systematic studies of the key parameters affecting the kinetics of these processes. Hence, it is expected that a screening of the influence of a spectrum of experimental parameters could be realised more easily in parallel experiments using an electrical output.

3. Conclusion

An EGOFET-based transducer platform to monitor Aβ1-40 low-weight oligomeric species, a hallmark of neurodegeneration in important pathologies like Alzheimer and Parkinson, has been demonstrated For this purpose, two strategies have been employed. The first one follows the more conventional and simple methodology used in

electrochemical sensors and is focused on using a single Ab-coated electrode which is progressively immersed into an aging Aβ1-40 solution. In contrast, in the second route different Ab-coated electrodes are used for each aging time measurement. Although both approaches lead to comparable and interesting results, the first one is more susceptible to electrode saturation and cannot provide information regarding the reduction of the oligomeric species concentration once fibrils start forming. Our results demonstrate that in the conditions used in this study, the maximum amount of $A\beta_{1\text{-}40}$ oligomers is found after 1 hour when a 60% increase in the IDS is observed. These findings are validated with measurements performed by EIS and DLS, as well as with data reported in the literature.[2,4]

EGOFETs are highly sensitive devices, enabling rapid testing and demonstrating significant potential for label-free sensing in diagnosis. Here, we showed that EGOFETs also show great perspectives as electrical transducers for studying aggregation processes of clinically relevant proteins, offering clear advantages over the most commonly employed techniques, such as low cost, fast testing time, high sensitivity, and electrical readout. In particular, the understanding of amyloid aggregation under different conditions, for instance in the presence of specific drugs and inhibitors, is critical for the development of medical treatments. Thus, in this work, we proved that EGOFETs can represent a promising and novel tool to characterize these systems and processes.

4. Experimental Section

Materials and techniques: Potassium chloride, sodium phosphate dibasic, iron(III) ferrocyanide, chlorobenzene, 2,3,4,5,6-pentafluorothiphenol (PFBT), dextran (from Leuconostoc Mesenteroides, MW= 64.000-76.000 g/mol), polystyrene (PS, MW= 10000 g/mol), Tris(2-carboxyethyl)phosphine hydrochloride (TCEP), phosphate-buffered saline (PBS) tablets, 6-Mercapto-1-Hexanol (MCH), Pt wire (Ø= 0.5 mm), 1,1,1,3,3,3-

Hexafluoropropan-2-ol (HFIP), CH_3CN, NaOH, Na_2CO_3, H_2SO_4, H_2O_2, NH_4OH were purchased from Sigma-Aldrich. Sodium chloride and glycerol were purchased from Panreac Quimica. Recombinant Cysteine-Protein G was obtained from Labospace S.R.L. Amyloid β-Protein (1-40) trifluoroacetate salt was obtained from Bachem AG**.** Gold disk electrodes (Ø= 2 mm) were purchased from PalmSens**.** The oligomer A11 Polyclonal Antibody was purchased from ThermoFisher. The organic semiconductor 2,8-Difluoro-5,11-bis(triethylsilylethynyl)anthradithiophene (diF-TES-ADT) was purchased from Lumtec, as a racemic mixture, and used as received (purity >99%). Acetone HPLC grade and isopropanol HPLC grade were purchased from Chem-Lab and used without further purification. Shipley Microposit S1813 photoresist and Shipley Microposit MF-319 developer were purchased from Shipley. The Ag/AgCl reference electrode was acquired from Allum. Kapton foils were bought from DuPont (Kapton HN, 75µm thick).

Qsil216 A/B (polydimethylsiloxane, PDMS) was purchased from Farnell Componentes. PDMS gasket production consisted of mixing the two components of the Qsil216 kit in a weight ratio of 10:1. The mixture was vigorously mixed for approximately two minutes in a Petri dish. Then, the Petri dish was put under a vacuum for 1 hour in order to remove bubbles of air. Afterward, the epoxy was cured in an oven at 70ºC overnight.

Electrochemical characterization of the transducer platform was realized with a potentiostat/galvanostat Autolab (PGSTAT128N). The measurements were carried out in a standard three-electrode configuration cell by using Ag/AgCl, Pt, and Au as the reference, counter, and working electrode, respectively. Electrochemical Impedance Spectroscopy (EIS) was recorded between 0.1 MHz and 0.1 Hz with an AC amplitude equal to 10 mV. The setpoint voltage, equal to 0.25 V, was the redox potential of the ferricyanide probe. The impedance response was fitted utilizing the Randles circuit,

whose components are the solution resistance (R_s) in series with the charge transfer resistance (R_{ct}), and the Warburg element (W), and in parallel the double-layer capacitance (C_{dl}). Cyclic voltammetry (CV) was measured at a scan rate of 0.1 $V \cdot s^{-1}$ sweeping the potential from -0.4 V to 0.6 V, approximately 10 cycles. Differential Pulse Voltammetry (DPV) was also used for the concentration and incubation times optimization of cys-PG and TCEP (**Figure S8 and S9**). DPV was recorded sweeping the potential from -0.1 V and 0.5 V, at a sweep rate equal to 10 $mV \cdot s^{-1,}$ and its modulation amplitude equal to 25 mV. All the electrochemical measurements were performed in an aqueous solution containing $K_3[Fe(CN)_6]$ 5 mM, KCl 100 mM, and 50 mM of sodium phosphate buffer (pH 7.4). The pH was adjusted by using small aliquots of NaOH or HCl 1 M.

Dynamic Light Scattering (DLS) technique (Zetasizer Nano ZS from Malvern Panalytical) was used to monitor the aggregation process and the hydrodynamic size of heterogeneous species formed over time, incubating $A\beta_{1-40}$ peptide in PBS at pH 7.4 and 37°C and following the same incubation protocol used for electrochemical and electrical characterization.[2]

EGOFET fabrication and characterization: The Source (S), Drain (D), and coplanar Gate (CG) electrodes required for EGOFETs were patterned on 75 µm thick Kapton substrate by positive photolithography. The coplanar gate whose area was equal to 2.25 mm^2 was used as the control gate, while the aggregation monitoring measurements were carried out with a top Au gate (TG), employing a gold disk electrode (ø=2 mm). The coplanar electrodes consisted of 5 nm of evaporated Cr as an adhesive layer and 40 nm of Au. The channel length (L) and width (W) were fixed to 50 µm and 16000 µm respectively (W/L ratio equal to 320, see **Figure S10**). After the metal evaporation, the lift-off was carried out by sonication in acetone and isopropanol. The devices were

sonicated with both acetone and IPA for 15 minutes and exposed in a UV Ozone cleaner for 25 minutes. Then, the CG electrode was passivated with a coating of dextran (10 mg/mL)[55] by drop casting, acting as a sacrificial layer. Immediately, the devices were immersed in a PFBT solution (2 µL/mL in isopropanol) for 15 minutes to functionalize the gold S/D electrodes, rinsed with isopropanol, and dried under N_2. Subsequently, the organic semiconductor layer was deposited. A blend of diF-TES-ADT:PS in a weight ratio of 4:1 was dissolved in chlorobenzene (CB) at 2% wt. The solution was deposited at 10 $mm \cdot s^{-1}$ and 105°C, employing the Bar-Assisted Meniscus Shearing (BAMS) technique, as previously reported.[44] Finally, the dextran sacrificial layer was removed by immersing the device in water.

Polarized optical microscopy (POM) images were taken with an Olympus BX51 microscope equipped with a polarizer and analyzer at 90º in reflection mode.

A PDMS pool was employed to confine the electrolyte on top of the CG and interdigitated S and D electrodes, ensuring the electrical connection between them (see Figure 1a). The electrical characterization was performed using a two-channel Keithley Source Meter 2400 and 2601 controlled with a homemade Matlab script, under ambient temperature. The device was conditioned by using Milli-Q water as an electrolyte and applying a coplanar gate-source voltage ($V_{CG,S}$) of -0.2 V and a drain-source voltage (V_{DS}) of -0.2 V for 90 minutes until the drain-source current (I_{DS}) reached a steady regime. For each functionalization step at least three transfers were measured in Milli-Q water (**Figure S11**).

Bio-functionalization of the Au surfaces for the top-gated EGOFETs and measurements carried out for monitoring the $A\beta_{1-40}$ *aggregation*: The optimized functionalization protocol consisted of the following steps, illustrated in Figure 2.

(i) The gold electrodes were cleaned by polishing the electrodes with 0.3 µm alumina and 0.05 µm alumina powder, sonicating with Milli-Q and EtOH, and drying with an N_2 flow.

(ii) The pre-treated electrodes were firstly incubated in a solution composed of phosphate-buffered saline solution (PBS, 10 mM), cysteine-tagged Protein G (cys-PG, 100 µg/mL)[56,57] and Tris(2-carboxyethyl)phosphine hydrochloride (TCEP, 10 mM) for 30 minutes at R.T. and pH 7 The TCEP was used to reduce the disulfide bonds of the cys-PG dimers formed by the self-reaction of the protein.[58–60] This step leads to the formation of cys-PG monolayer thanks to the formation of S-Au bonds. Subsequently, the gold electrodes were rinsed with PBS and dried with a N_2 flow.

(iii) The non-covered electrode surface areas were passivated with an MCH. For this purpose, the electrodes were immersed in a 0.1 mM MCH solution in Milli-Q water for 15 minutes at R.T.[61] and, successively, rinsed with PBS and dried with N_2.

(iv) The electrodes were then incubated in an A11 anti-oligomer antibody solution (1 µg/mL) in PBS for 1 hour at R.T.[3,62] After this time, the surfaces were gently rinsed with PBS and dried with an N_2 flow.

$A\beta_{1\text{-}40}$ lyophilized powder was first dissolved in Hexafluoropropan-2-ol (HFIP) to monomerize pre-existing aggregates following the protocol previously reported by Bartolini et al.[5] $A\beta_{1\text{-}40}$ was dissolved in HFIP by brief sonication and vortexing and kept overnight at ambient temperature (25°C). The next day, the resulting clear solution was partitioned and cooled in ice in 100 µL aliquots, and the HFIP was left to evaporate overnight at 25°C. The resulting film was stored at -20°C and used when necessary.

For the aggregation monitoring experiments, the $A\beta_{1-40}$ film was re-dissolved (0.5 mg/mL) in a freshly prepared mixture that consisted of CH_3CN:Na_2CO_3:NaOH (300 µM:300 µM:250 mM) (48.3:48.3:3.4, v:v:v, respectively, resulting a total volume of 100 µL) by vortexing for 1 minute. The resulting alkaline $A\beta_{(1-40)}$ solution was then diluted by adding PBS, resulting in a final concentration of 0.05 µg/mL. Samples were incubated at 37°C and 200 r.p.m., and a 100 µL aliquot was taken every 15 minutes during the time course of the peptide aggregation study. The A11-functionalised Au surfaces were immersed for 5 min at R.T. in the $A\beta_{1-40}$ solutions and, finally, abundantly rinsed with PBS and dried with an N_2 flow. At each measurement time point, the electrodes were applied as working electrodes in Cyclic Voltammetry and Electrochemical Impedance Spectroscopy measurements, or as top gate contacts in the fabricated EGOFETs.

Two methods have been used to study the amyloid peptide aggregation process:

i) Approach I: In the first method, the amyloid peptide solution is incubated over time, and the same A11-Ab coated electrode is used for all measurements performed at varying incubation times. The response is analyzed with respect to the electrode response before exposing it to the amyloid solution.

ii) Approach II: The second strategy consists of using different A11 Ab-coated electrodes for each incubation time period investigated. In this case, the response of each electrode is analyzed with respect to its initial reference response.

Acknowledgements

This work was funded by MCIN/AEI/10.13039/501100011033/ERDF,UE with project SENSATION PID2022-141393OB-I00, and through the “Severo Ochoa” Programme for Centers of Excellence in R&D (FUNFUTURECEX2019-000917-S) and the Generalitat de Catalunya (2021-SGR-00443). S. R. is enrolled in the UAB Chemistry Ph.D.

References

[1] G.-F. Chen, T.-H. Xu, Y. Yan, Y. Jiang, K. Melcher, H. E. Xu, Acta Pharmacol Sin. 2017, 38, 1205-1235.

[2] S. Kalita, S. Kalita, A. Paul, A. Sarkar, B. Mandal. Chem. Sci. 2020, 11, 4171-4179.

[3] R. Sarroukh, E. Cerf, S. Derclaye, Y. F. Dufrêne, E. Goormaghtigh, J.-M. Ruysschaert, V. Raussens. Cell. Mol. Life Sci. CMLS. 2011, 68, 1429-1438.

[4] A. J. Veloso, A. M. Chow, H. V. S. Ganesh, N. Li, D. Dhar, D. C. H. Wu, S. Mikhaylichenko, I. R. Brown, K. Kerman. Anal. Chem. 2014, 86, 4901-4909.

[5] M. Bartolini, C. Bertucci, M. L. Bolognesi, A. Cavalli, C. Melchiorre, V. Andrisano. Chembiochem Eur. J. Chem. Biol. 2007, 8, 2152-2161.

[6] K. A. Bruggnik, M. Müller, H. B. Kuiperij, M. M. Verbeek. J. Alzheimers Dis. JAD. 2012, 28, 735-758.

[7] V. L. Anderson, W. W. Webb. BMC Biotechnology. 2011, 11, 125.

[8] O. N. Antzutkin. Magn. Reason. Chem. MRC. 2004, 42, 231-246.

[9] B. A. Chromy, R. J. Nowak, M. P. Lambert, K. L. Viola, L. Chang, P. T. Velasco, B. W. Jones, S. J. Fernandez, P. N. Lacor, P. Horowitz, C. E. Finch, G. A. Krafft, W. L. Klein. Biochemistry. 2003, 42, 12749-12760.

[10] W. B. Stine, K. N. Dahlgren, G. A. Krafft, M. J. LaDu. J. Biol. Chem. 2003, 278, 11612-11622.

[11] M. Bokvist, F. Lindström, A. Watts, G. Gröbner. J. Mol. Biol. 2004, 335, 1039-1049.

[12] Y. Fezoui, D. B. Teplow. J. Biol. Chem. 2002, 277, 36948-36954.

[13] R. W. Hepler, K. M. Grimm, D. D. Nahas, R. Breese, E. C. Dodson, P. Acton, P. M. Keller, M. Yeager, H. Wang, P. Shughrue, G. Kinney, J. G. Joyce. Biochemistry. 2006, 45, 15157-15167.

[14] G. Bitan, E. A. Fradinger, S. M. Spring, D. B. Teplow. Amyloid Int. J. Exp. Clin. Investig. Off. J. Int. Soc. Amyloidosis. 2005, 12, 88-95.

[15] H. Fukumoto, T. Tokuda, T. Kasai, N. Ishigami, H. Hidaka, M. Kondo, D. Allsop, M. Nakagawa. FASEB J. Off. Publ. Fed. Am. Soc. Exp. Biol. 2010, 24, 2716-2726.

[16] S. Lesné, M. T. Koh, L. Kotilinek, R. Kayed, C. G. Glabe, A. Yang, M. Gallagher, K. H. Ashe. Nature. 2006, 440, 352-357.

[17] R. Carrotta, M. Manno, D. Bulone, V. Martorana, P. L. San Biagio. J. Biol. Chem. 2005, 280, 30001-30008.

[18] I. Santa-María, F. Hernández, F. J. Moreno, J. Avila. Neurosci. Lett. 2007, 429, 91-94.

[19] J. T. Jarrett, P. T. Lansbury. Cell. 1993, 73, 1055-1058.

[20] K. C. Evans, E. P. Berger, C. G. Cho, K. H. Weisgraber, P. T. Lansbury. Proc. Natl. Acad. Sci. U. S. A. 1995, 92, 763-767.

[21] R. Khurana, V. N. Uversky, L. Nielsen, A. L. Fink. J. Biol. Chem. 2001, 276, 22715-22721.

[22] A. C. Klaver, L. M. Patrias, J. M. Finke, D. A. Loeffer. J Neurosci Methods. 2011, 195, 249-54.

[23] S. D. Meyer, J. M. Schaeverbeke, I. M. W. Verberk, B. Guille, M. D. Schaepdryver, E. S. Luckett, S. Gabel, R. Bruffaerts, K. Mauroo, E. H. Thijssen, E. Stoops, H. M. Vanderstichele, C. E. Teunisse, R. Vanderberghe, K. Poesen. Alzheimer's Research & Therapy. 2020, 12, 162.

[24] D. G. Georganopoulou, L. Chang, J.-M. Nam, C. S. Thaxton, E. J. Mufson, W. L. Klein, C. A. Mirkin. Proc. Natl. Acad. Sci. U. S. A. 2005, 102, 2273-2276.

[25] R. V. Nair, P. Padmanabhan, B. Gulýas, M. V. Matham. Plasmonics. 2021, 16, 863-872.

[26] A. Ruiz-Arias, R. Jurado, F. F. González, R. Herranz. Sensors and Actuators B Chemical. 2021, 350, 130882.

[27] S. Matsumura, K. Shinoda, M. Yamada, S. Yokojima, M. Inoue, T. Ohnishi, T. Shimada, K. Kikuchi, D. Masui, S. Hashimoto, M. Sato, A. Ito, M. Akioka, S. Takagi, Y. Nakamura, K. Nemoto, Y. Hasegawa, H. Takamoto, H. Inoue, S. Nakamura, Y. Nabeshima, D. B. Teplow, M. Kinjo, M. Hoshi. J. Biol. Chem. 2001, 286, 11555-11562.

[28] M. Bartolini, M. Naldi, J. Fiori, F. Valle, F. Biscarini, D. V. Nicolau, V. Andrisano. Anal. Biochem. 2011, 414, 215-225.

[29] S. Casalini, F. Leonardi, T. Cramer, F. Biscarini. Org. Electron. 2013, 14, 156.

[30] M. Magliulo, D. De Tullio, I. Vikholm-Lundin, W. M. Albers, T. Munter, K. Manoli, G. Palazzo, L. Torsi. Anal. Bioanal. Chem. 2016, 408, 3943-3952.

[31] M. Sensi, M. Berto, S. Gentile, M. Pinti, A. Conti, G. Pellacani, C. Salvarani, A. Cossarizza, C. A. Bortolotti, F. Biscarini. Chem. Commun. 2021, 57, 367-370.

[32] E. Macchia, K. Manoli, C. Di Franco, R. A. Picca, R. Österbacka, G. Palazzo, F. Torricelli, G. Scamarcio, L. Torsi. ACS Sens. 2020, 5, 1822-1830.

[33] N. Wang, A. Yang, Y. Li, F. Yan. Acc. Chem. Res. 2019, 52, 277-287.

[34] M. Magliulo, A. Mallardi, M. Y. Mulla, S. Cotrone, B. R. Pistillo, P. Favia, I. Vikholm-Lundin, G. Palazzo, L. Torsi. Adv. Mater. 2013, 25, 2090-2094.

[35] S. Ricci, S. Casalini, V. Parkula, M. Selvaraj, G. D. Saygin, P. Greco, F. Biscarini, M. Mas-Torrent. Biosens. Bioelectron. 2020, 167, 112433.

[36] B. Burtscher, P. A. M. Urbina, C. Diacci, S. Borghi, M. Pinti, A. Cossarizza, C. Salvarani, M. Berggren, F. Biscarini, D. T. Simon. Adv. Healthc. Mater. 2021, 10, 2100955.

[37] A. Kyndiah, F. Leonardi, C. Tarantino, T. Cramer, R. Millan-Solsona, E. Garreta, N. Montserrat, M. Mas-Torrent, G. Gomila. Biosens. Bioelectron. 2020, 150, 111844.

[38] P. A. Shaposhnik, S. A. Zapunidi, M. V. Shestakov, E. V. Agina, S. A. Ponomarenko. Russ. Chem. Rev. 2020, 89, 1483.

[39] Q. Zhang, A. Tamayo, F. Leonardi, M. Mas-Torrent. ACS Appl. Mater. Interfaces. 2021, 13, 30902-30909.

[40] L. Fillaud, T. Petenzi, J. Pallu, B. Piro, G. Mattana, V. Noel. Langmuir. 2018, 34, 3686-3693.

[41] F. G. del Pozo, S. Fabiano, R. Pfattner, S. Georgakopoulos, S. Galindo, X. Liu, S. Braun, M. Fahlman, J. Veciana, C. Rovira, X. Crispin, M. Berggren, M. Mas-Torrent. Adv. Funct. Mater. 2016, 26, 2379-2386.

[42] I. Temiño, F. G. del Pozo, M. R. Ajayakumar, S. Galindo, J. Puigdollers, M. Mas-Torrent. Adv. Mater. Technol. 2016, 1, 1600090.

[43] T. Salzillo, A. Campos, A. Babuji, R. Santiago, S. T. Bromley, C. Ocal, E. Barrena, R. Jouclas, C. Ruzie, G. Schweicher, Y. H. Geerts, M. Mas-Torrent. Adv. Funct. Mater. 2020, 30, 2006115.

[44] Q. Zhang, F. Leonardi, S. Casalini, I. Temiño, M. Mas-Torrent. Sci. Rep. 2016, 6, 39623.

[45] M. Di Lauro, M. Berto, M. Giordani, S. Benaglia, G. Schweicher, D. Vuillaume, C. A. Bortolotti, Y. H. Geerts, F. Biscarini. Adv. Electron. Mater. 2017, 3, 1700159.

[46] J. M. Lee, H. K. Park, Y. Jung, J. K. Kim, S. O. Jung, B. H. Chung. Anal. Chem. 2007, 79, 2680-2687.

[47] S. Casalini, A. C. Dumitru, F. Leonardi, C. A. Bortolotti, E. T. Herruzo, A. Campana, R. F. De Oliveira, T. Cramer, R. Garcia, F. Biscarini. ACS Nano. 2015, 9, 5051-5062.

[48] M. Iljina, G. A. Garcia, A. J. Dear, J. Flint, P. Narayan, T. C. T. Michaels, C. M. Dobson, D. Frenkel, T. P. J. Knowles, D. Klenerman. Sci. Rep. 2016, 6, 28658.

[49] K. Manoli, M. Magliulo, M. Y. Mulla, M. Singh, L. Sabbatini, G. Palazzo, L. Torsi. Angew Chem Int Ed Engl. 2015, 54, 12562-12576.

[50] L. Kergoat, L. Herlogsson, B. Piro, M. C. Pham, G. Horowitz, X. Crispin, M. Berggren. PNAS. 2012, 109, 8394-8399.

[51] T. C. T. Michaels, A. Šaric, S. Curk, K. Bernfur, P. Aroiso, G. Meisl, A. J. Dear, S. I. A. Cohen, C. M. Dobson, M. Vendruscolo, S. Linse, T. P. J. Knowles. Nat. Chem. 2020, 12, 445-451.

[52] J. A. J. Housmans, G. Wu, J. Schymkowitz, F. Rousseau. FEBS J. 2023, 290, 554-583.

[53] A. M. Morris, M. A. Watzky, R. G. Finke. Biochim Biophys Acta. 2009, 1794, 375-397.

[54] C. J. Roberts. Curr Opin Biotechnol. 2014, 30, 211-217.

[55] F. Leonardi, A. Tamayo, S. Casalini, M. Mas-Torrent. RSC Adv. 2018, 8, 27509-27515.

[56] Y. M. Bae, B.-K. Oh, W. Lee, W. H. Lee, J.-W. Choi. Biosens. Bioelectron. 2005, 21, 103-110.

[57] B. N. Johnson, R. Mutharasan. Langmuir. 2012, 28, 6928-6934.

[58] P. Liu, B. W. O'Mara, B. M. Warrack, W. Wu, Y. Huang, Y. Zhang, R. Zhao, M. Lin, M. S. Ackerman, P. K. Hocknell, G. Chen, L. Tao, S. Rieble, J. Wang, D. B. Wang-Iverson, A. A. Tymiak, M. J. Grace, R. J. Russell. J. Am. Soc. Mass Spectrom. 2010, 21, 837-844.

[59] D. L. Melnikova, V. D. Skirda, I. V. Nesmelova. J. Phys. Chem. B. 2019, 123, 2305-2315.

[60] J. A. Burns, J. C. Butler, J. Moran, G. M. Whitesides. J. Org. Chem. 1991, 56, 2648-2650.

[61] R.-G. Cao, B. Zhu, J. Li, D. Xu. Electrochem. Commun. 2009, 11, 1815-1818.

[62] H. Chunhui, X. Dilin, Z. Ke, S. Jieyi, Y. Sicheng, W. Dapeng, W. Qinwen, C. Wei. J. Vis. Exp. 2018, 135, 57592.

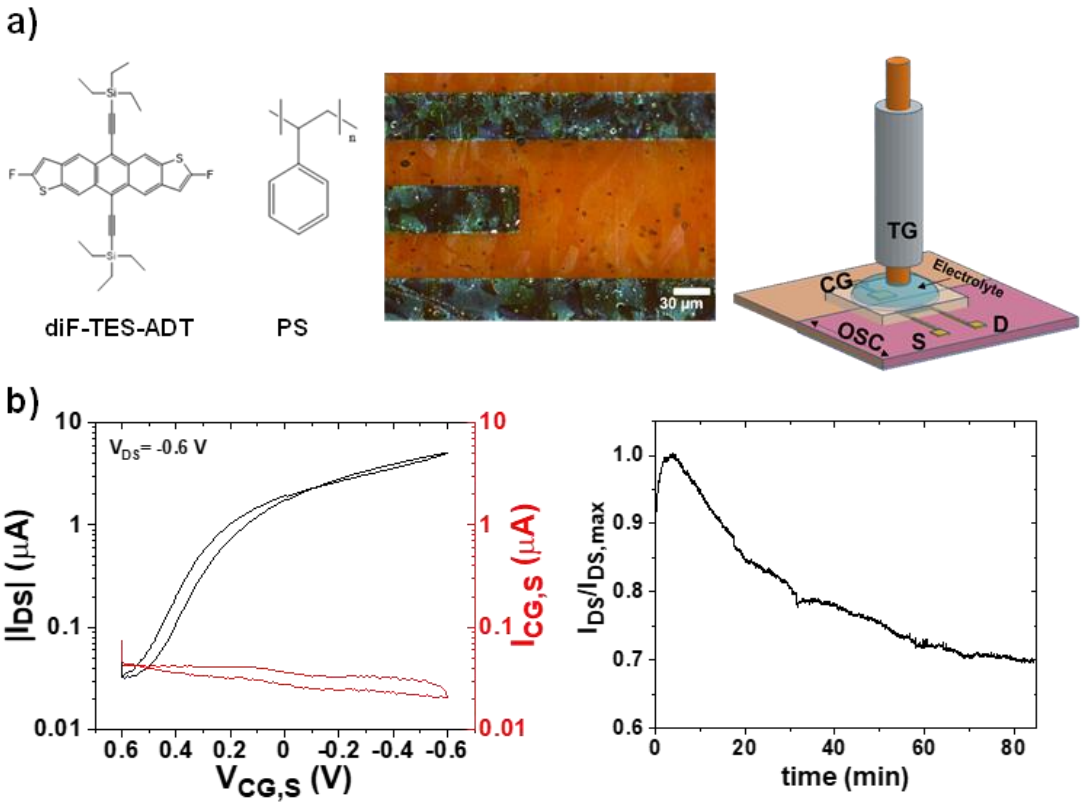

Figure 1. a) Molecular structure of diF-TES-ADT and PS, polarized optical microscopy image of the blended film, and schematic representation of the device configuration (CG: coplanar gate, TG: top gate, S: source, D: drain and OSC: organic semiconductor). b) Left: EGOFET transfer characteristics (CG) applying V_{DS}= -0.6 V (black curve) and $I_{CG,S}$ (red curve). Right: Real-time I_{DS} current monitoring of diF-TES-ADT:PS EGOFET in Milli-Q water applying $V_{CG,S}$= -0.2 V and V_{DS}= -0.2 V during 85 minutes.

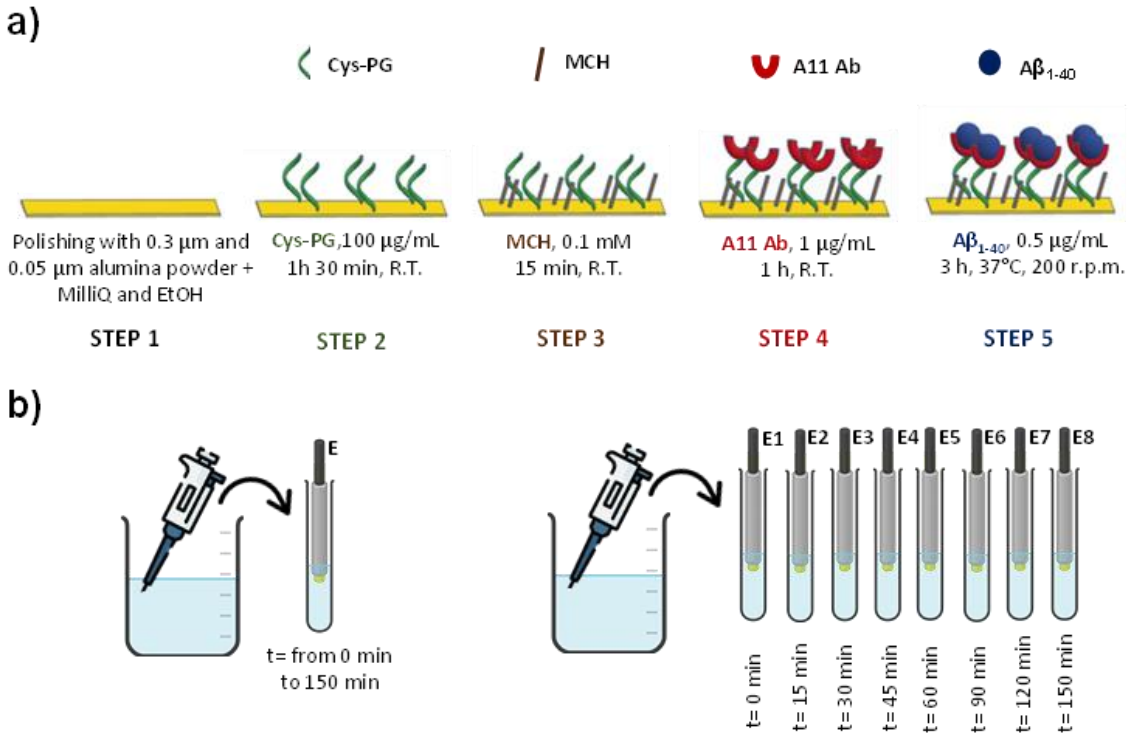

Figure 2. a) Scheme of the Au top gate functionalization and sensing protocol: Step 1: gold surface cleaning; Step 2: immobilization of cysteine-Protein G; Step 3: MCH to cover uncoated gold regions; Step 4: immobilization of A11 antibody; Step 5: incubation with $A\beta_{1-40}$ peptide. b) Schematic representation of the two methodologies followed for monitoring $A\beta_{1-40}$ aggregation. Left: Approach 1. Right: Approach 2.

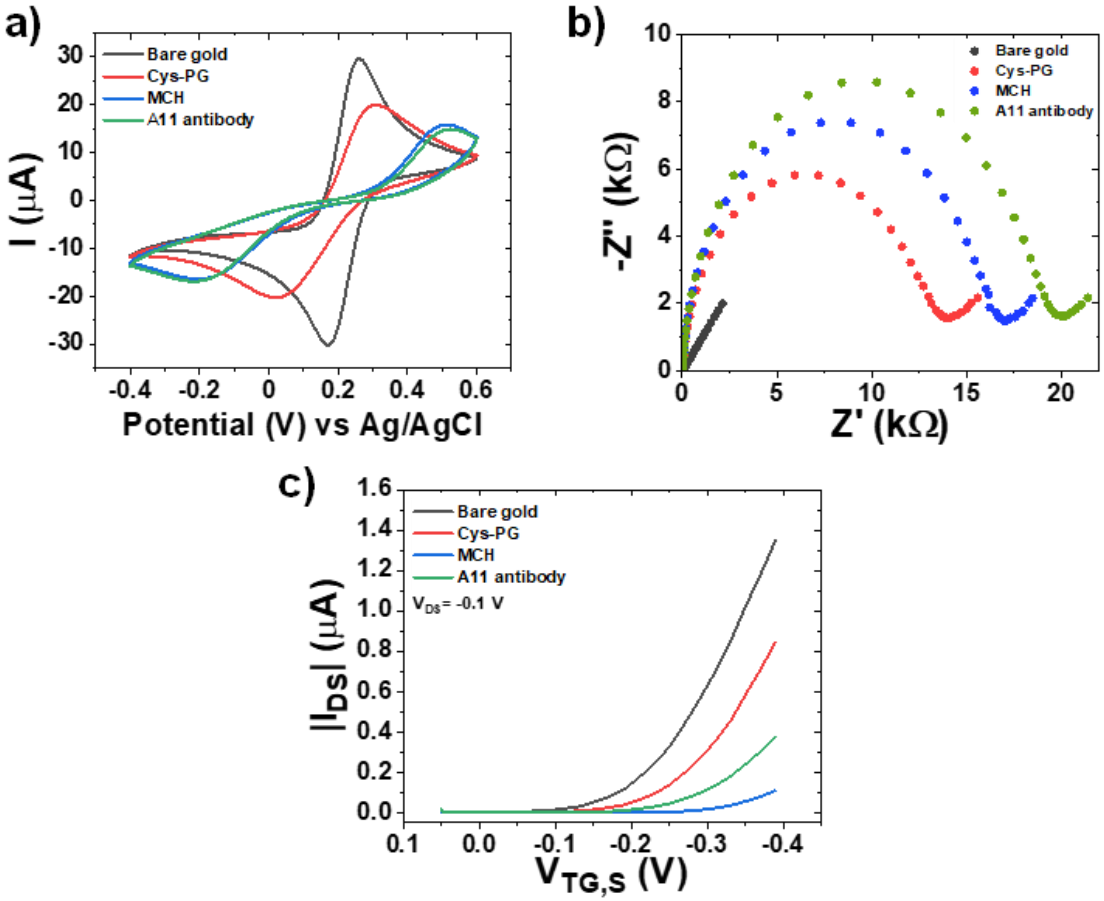

Figure 3. a) Cyclic voltammograms, b) Nyquist plots, and c) transfer characteristics using the bare and functionalized gold electrode as working electrode or top-gate: bare gold (black curves), cys-PG (red curves), MCH (blue curves), and A11 antibody (green curves).

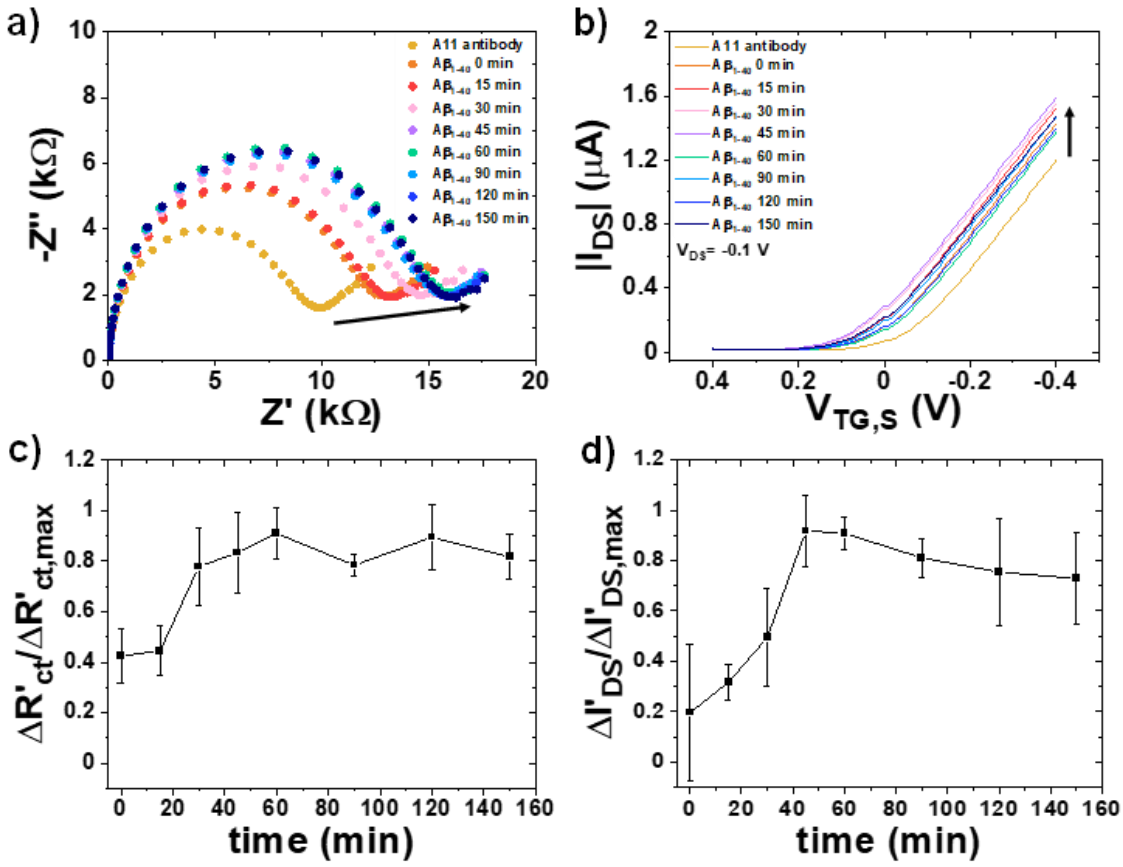

Figure 4. Electrical response in Approach I. a) Nyquist plots and b) transfer characteristics at V_{DS}= -0.1 V using as working electrode or top gate contact, respectively, an A11 Ab coated-electrode incubated in an $A\beta_{1\text{-}40}$ solution aged during a time period ranging from 0 to 150 min. c) Evolution of the relative $\Delta R'_{ct}/\Delta R'_{ct,max}$ with the aging time of the $A\beta_{1\text{-}40}$ solution extracted from the EIS measurements. d) Relative $\Delta I'_{DS}/\Delta I'_{DS,max}$ (at $V_{TG,S}$ = -0.1 V) extracted from the EGOFET characteristics at different aging times of the $A\beta_{1\text{-}40}$ solution. The data reported corresponds to the values extracted from three different experiments.

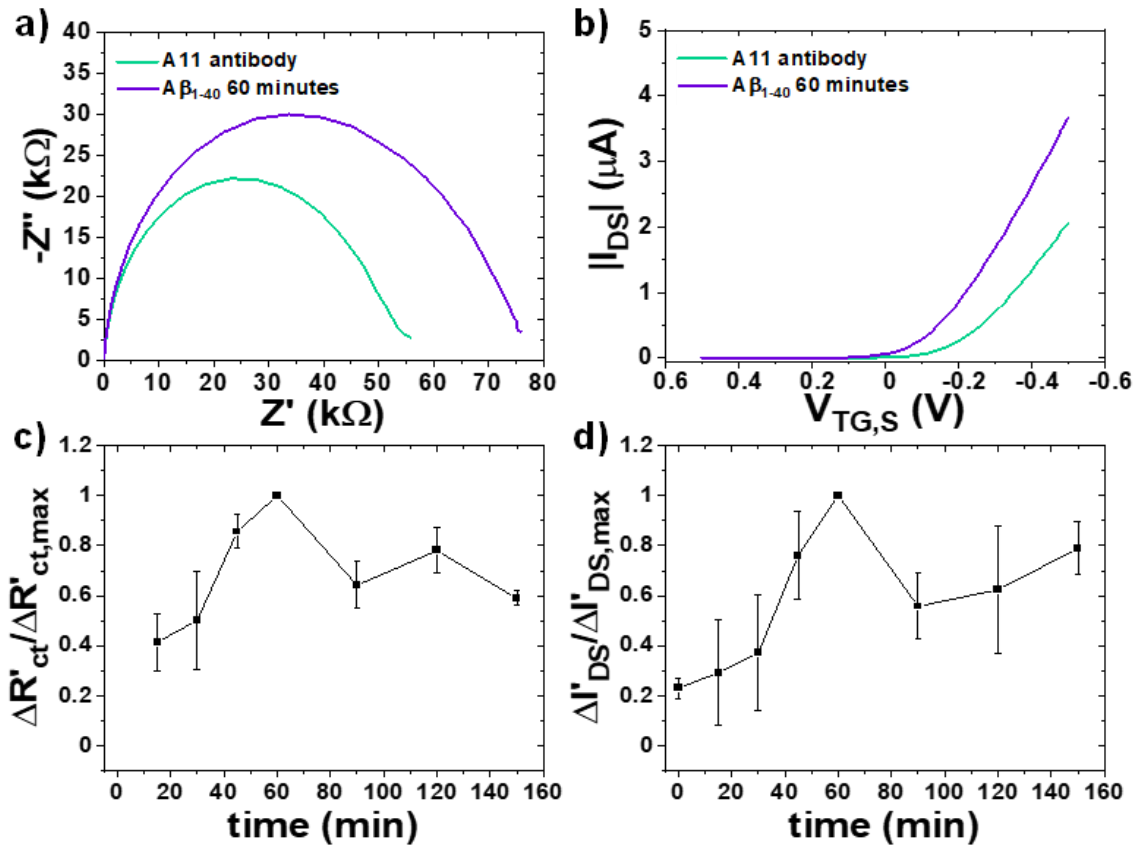

Figure 5. Electrical response in Approach II. Representative a) Nyquist plot and b) transfer characteristics (V_{DS}= -0.1 V) before (green) and after (purple) incubating an A11 Ab-modified electrode in an $A\beta_{1\text{-}40}$ solution aged during 60 min. Evolution with time of c) $\Delta R'_{ct}/\Delta R'_{ct,max}$ and d) $\Delta I'_{DS}/\Delta I'_{DS,max}$ (at $V_{TG,S}$ = -0.1 V). The data in c) and d) are averaged from three different series of measurements and normalised to the maximum response, which takes place in all the cases at 60 min.

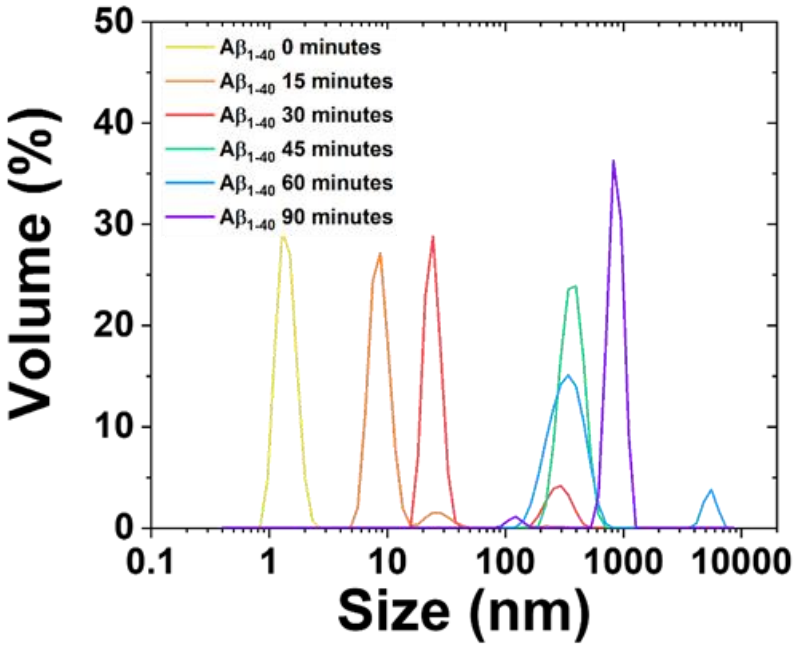

Figure 6. Hydrodynamic size distribution (diameter in nm) by volume of the $A\beta_{1-40}$ species characterized by Dynamic Light Scattering measured at different solution aging times: after 5 minutes (yellow line), 15 minutes (orange line), 30 minutes (red line), 45 minutes (green line), 60 minutes (blue line) and 90 minutes (purple line).

Supporting Information

Electrolyte-Gated Organic Field-Effect Transistor for monitoring amyloid aggregation

Sara Ruiz-Molina, Carme Martinez-Domingo, Simona Ricci, Stefano Casalini, Marta Mas-Torrent[1*]

	Techniques	Sample volume	Concentration used	Species detected	Expensive	Label-free	Sensitivity
Morphology and structural conformation	Transmission Electron Microscopy (TEM)[1–3]	10-100 µL	10-200 µM	Protofibrils and fibrils	Yes	Yes	Low
	Atomic Force Microscopy (AFM)[4,5]	10-20 µL	5-50 µM	Oligomers up to fibrils	Yes	Yes	Good
	Circular Dichroism (CD)[6–8]	100 µL	50-100 µM	Monomers up to fibrils	Yes	Yes	Good
Aggregation studies	Polyacrylamide Gel Electrophoresis (SDS-PAGE)[9,10]	20 µL	5 µM – 50 µM	Monomers up to oligomers	No	Yes	Good
	Size Exclusion Chromatography (SEC)[2,8,11]	100-300 µL	50 µM-0.5 mM	Oligomers and protofibrils	Yes	Yes	Good
	Dynamic Light Scattering (DLS)[2,12]	70 µL- 1 mL	50 µM	Oligomers	No	Yes	Good
	Thioflavin-T (ThT) assay[8,12,13]	10-100 µL	0.5 – 50 µM	HMW oligomers up to fibrils	Yes	No	Low
	Fluorescence Correlation Spectroscopy(FCS)[15 16]	20 µL-120 µL	10 µM – 50 µM	LMW oligomers	Yes	No	Good
	EGOFET (this work)	**20-100 µL**	**12 µM**	**LMW oligomers**	**No**	**Yes**	**Good**
Quantification	Sandwich ELISAs[17,18]	100 µL	50 µM	Oligomers	No	No	High
	Surface-Immobilized Bio-Barcode Assay (SI-BCA)[19,20]	10-20 µL	1 – 10 pM	Oligomers	Yes	Yes	High
	Fluorescence Resonance Energy Transfer (FRET)[21,22]	20 µL	5 µM	Oligomers	Yes	No	Good

Table S1. Comparative table of techniques employed to study amyloids.[23]

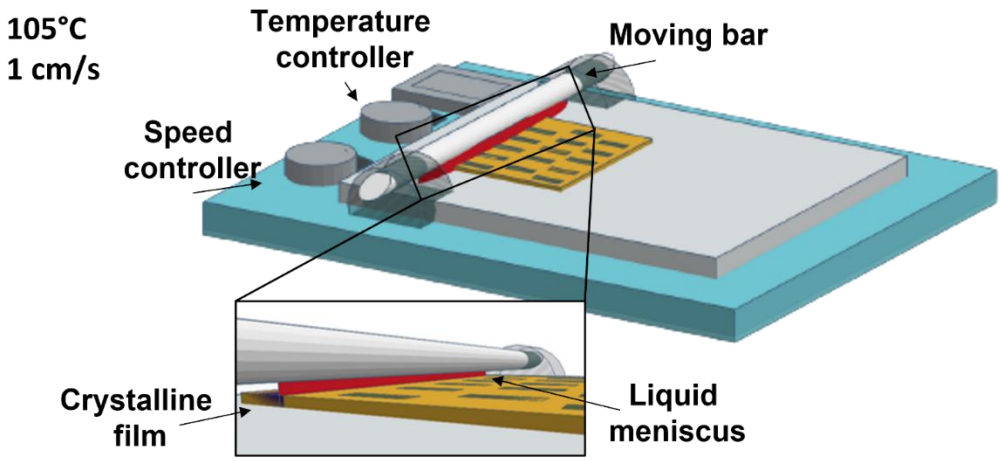

Figure S1. Scheme of the Bar-Assisted Meniscus Shearing (BAMS) technique.

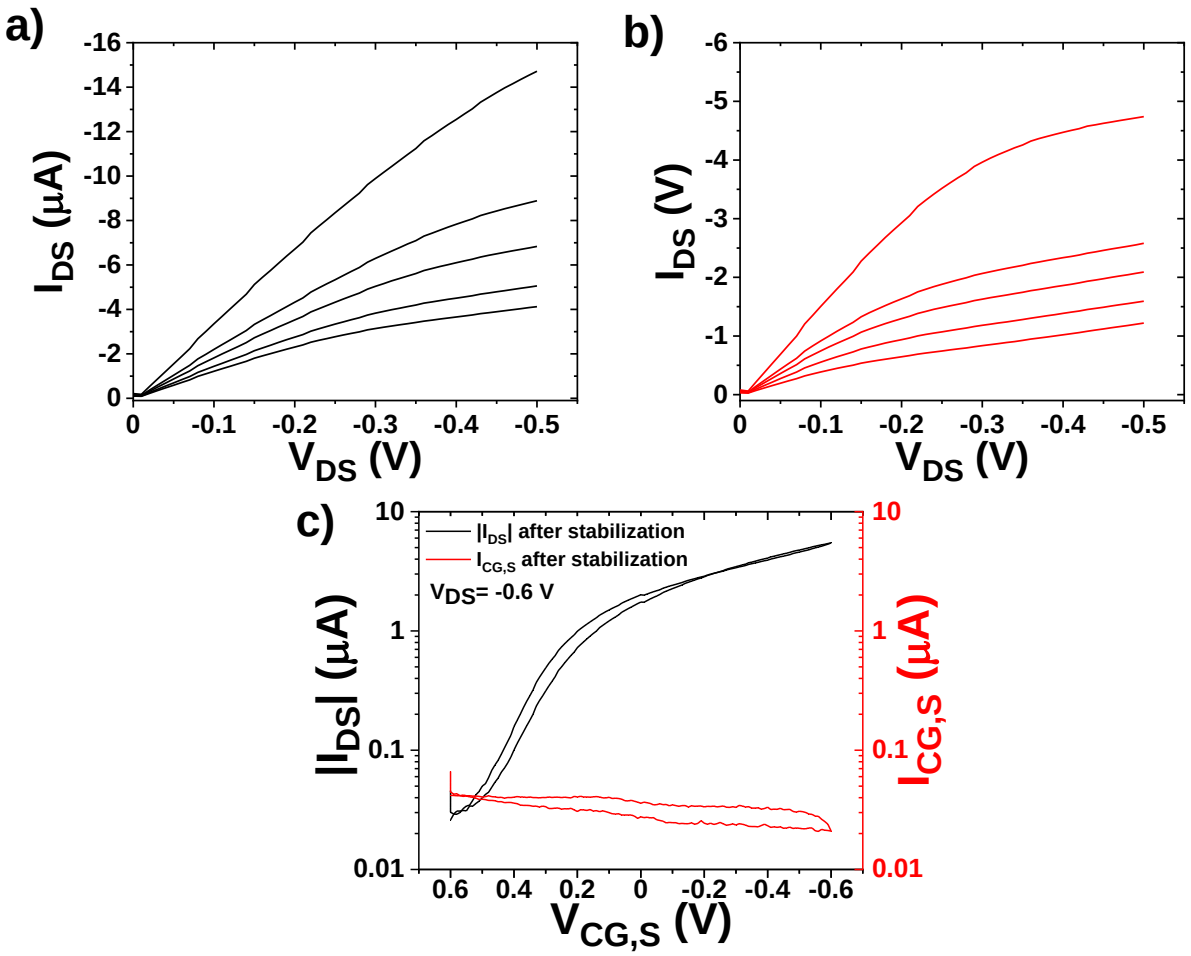

Figure S2. Output characteristics of diF-TES-ADT:PS using Milli-Q water as electrolyte (a) before the device stabilization and (b) after the device stabilization ($V_{CG,S}$= 0.05, 0, -0.1, -0.2, and -0.6 V). (c) EGOFET transfer characteristics after device stabilization employing Milli-Q water as electrolyte (I_{DS}: black line; $I_{CG,S}$: red line).

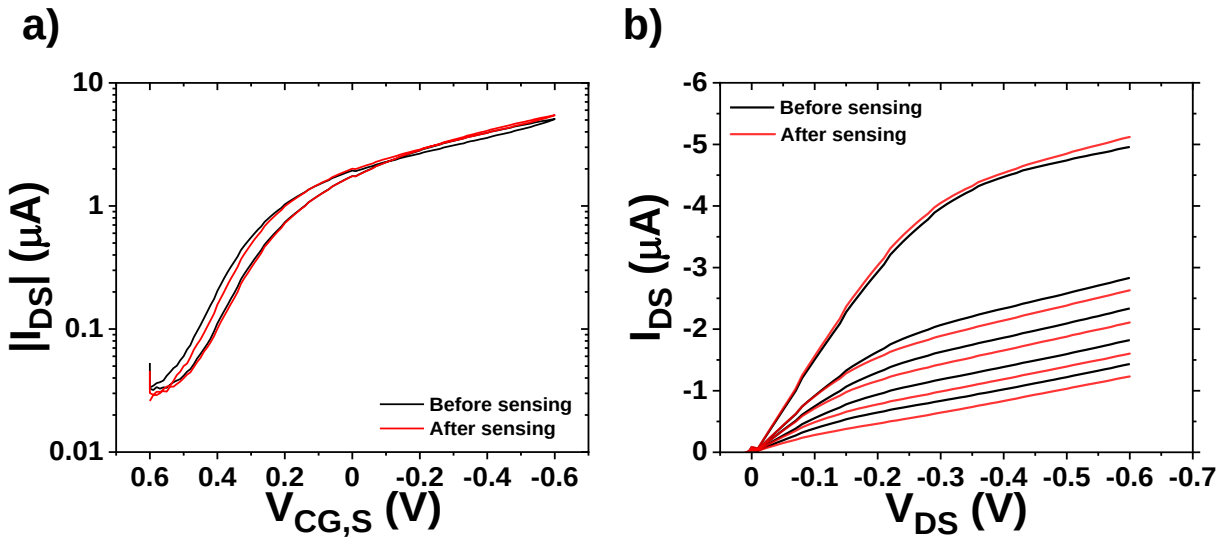

Figure S3. (a) Transfer characteristics (V_{DS}= -0.6 V) with the coplanar gate as control before (black curves) and after the sensing experiments (red curves), and (b) corresponding output characteristics ($V_{CG,S}$= 0.05, 0, -0.1, -0.2, -0.6 V). Milli-Q water was employed as electrolyte.

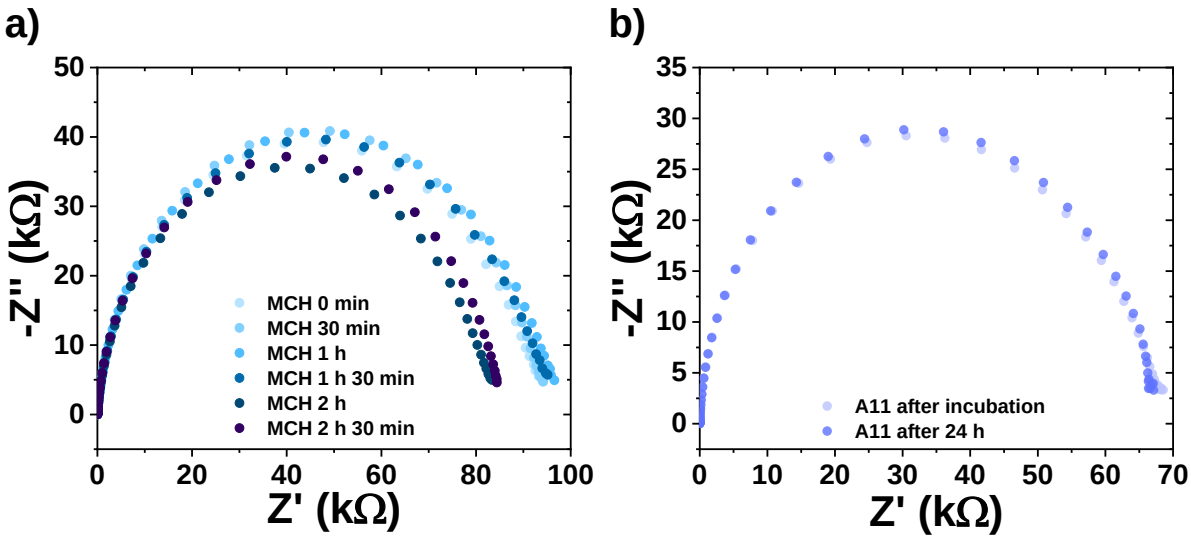

Figure S4. Monitoring of the MCH and A11 Ab SAMs over time employing Electrochemical Impedance Spectroscopy (EIS), showing that the functionalized surfaces are stable over time. The measurements were carried out in a standard three-electrode configuration cell by using Ag/AgCl, Pt, and Au as the reference, counter, and working electrode, respectively. Measurements were recorded between 0.1 MHz and 0.1 Hz with an AC amplitude equal to 10 mV and a setpoint voltage equal to 0.25 V. All the measurements were performed in an aqueous solution containing $K_3[Fe(CN)_6]$ 5 mM, KCl 100 mM, and 50 mM of sodium phosphate buffer (pH 7.4).

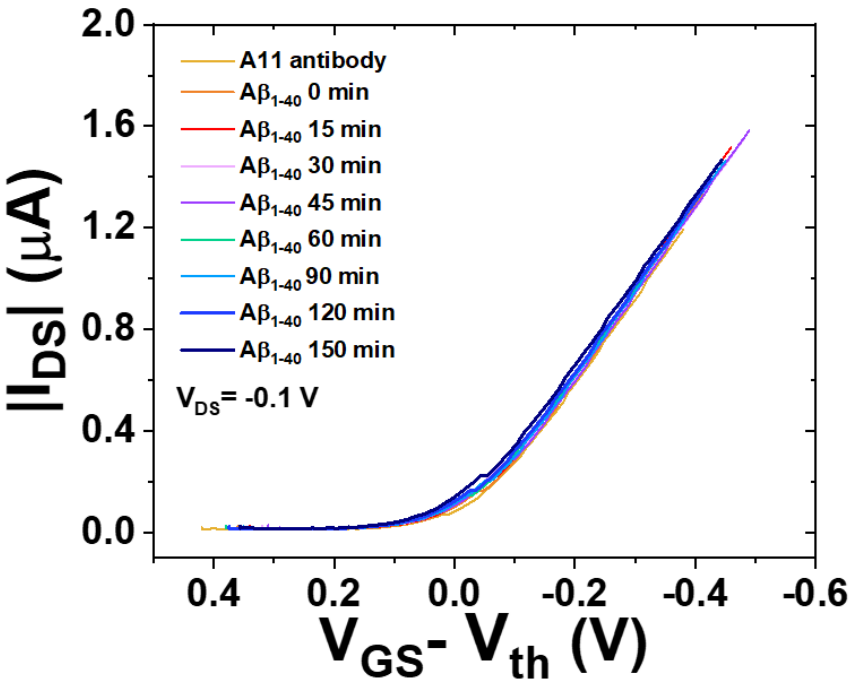

Figure S5. Corresponding transfer curves from Figure 4b, plotted against (V_{GS}-V_{th}).

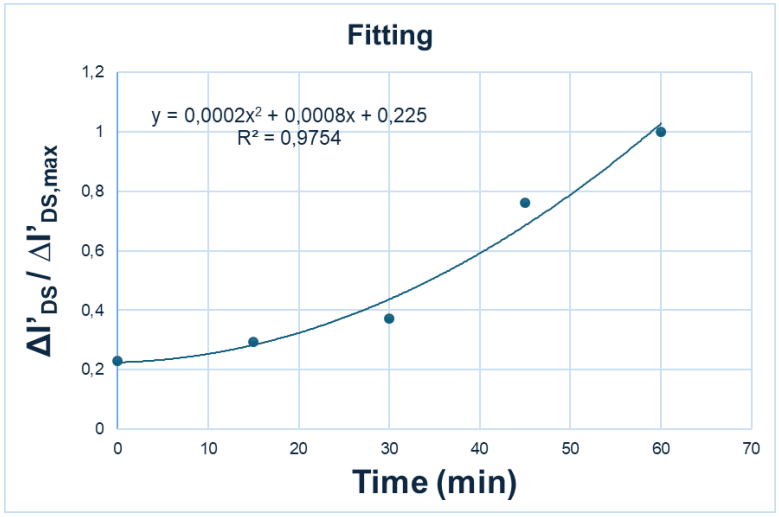

Figure S6. Fitting of the time evolution curve obtained with the EGOFET devices in the time period 0-60 min in which the oligomer concentration is increasing.

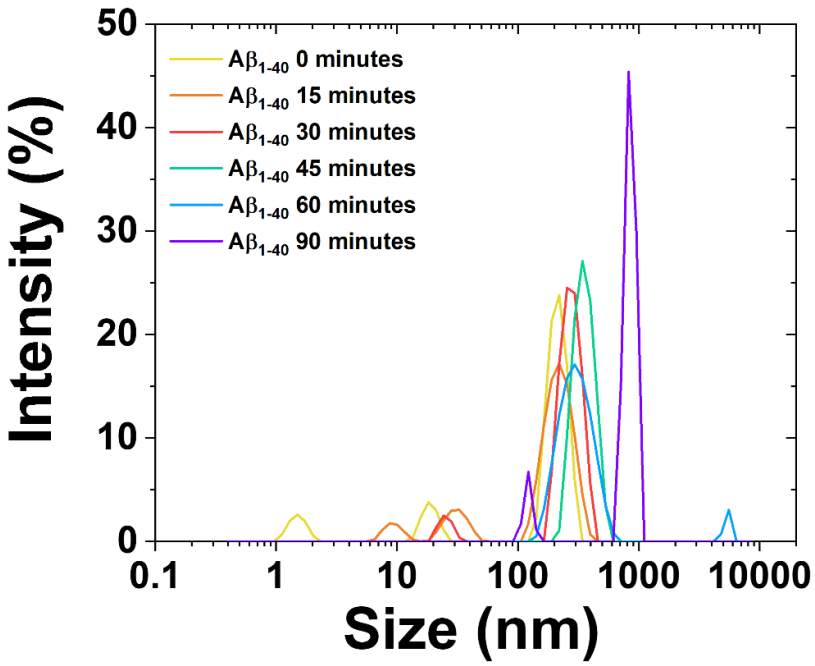

Figure S7. Hydrodynamic size distribution (diameter in nm) by the intensity of the $A\beta_{1\text{-}40}$ species characterized by Dynamic Light Scattering measured at different incubation times: after 5 minutes (yellow line), 15 minutes (orange line), 30 minutes (red line), 45 minutes (green line), 60 minutes (blue line) and 90 minutes (purple line).

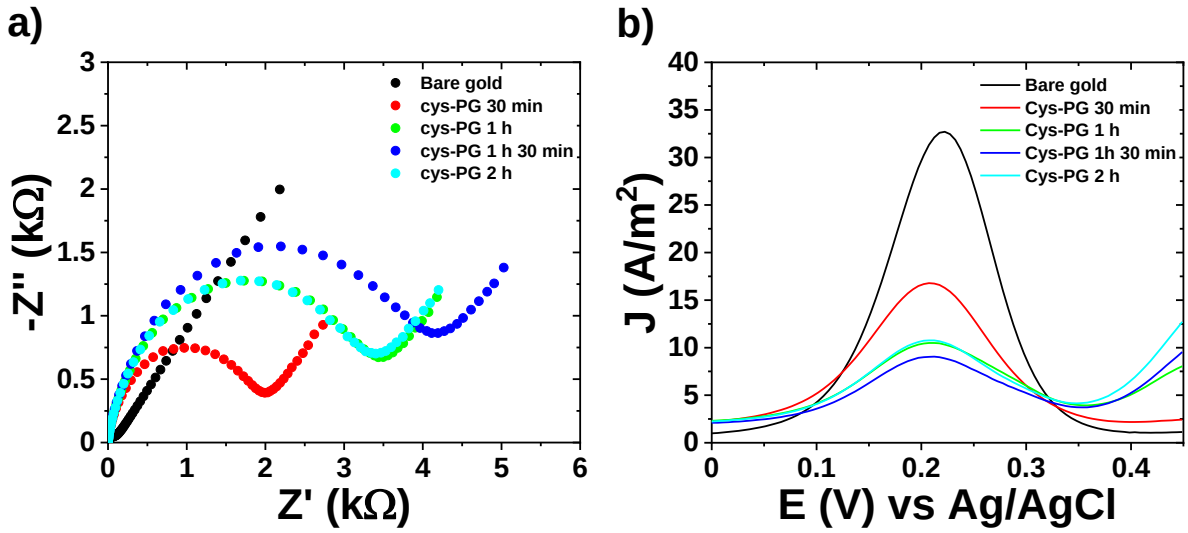

Figure S8. Optimization process for the Protein G layer formation. (a) EIS and (b) DPV characterization of the bare gold electrode (black) and after incubating it in a Protein G solution for 30 minutes (red), 1 hour (green), 1 h 30 min (dark blue), and 2 h (light blue). The measurements were carried out in a standard three-electrode configuration cell by using Ag/AgCl, Pt, and Au as the reference, counter, and working electrode, respectively. EIS was recorded in the same conditions as **Figure S4**. DPV measurements were recorded sweeping the potential from -0.1 V and 0.5 V, at a sweep rate equal to 10 $mV \cdot s^{-1}$, and a modulation amplitude equal to 25 mV. All the electrochemical measurements were performed in an aqueous solution containing $K_3[Fe(CN)_6]$ 5 mM, KCl 100 mM, and 50 mM of sodium phosphate buffer (pH 7.4).

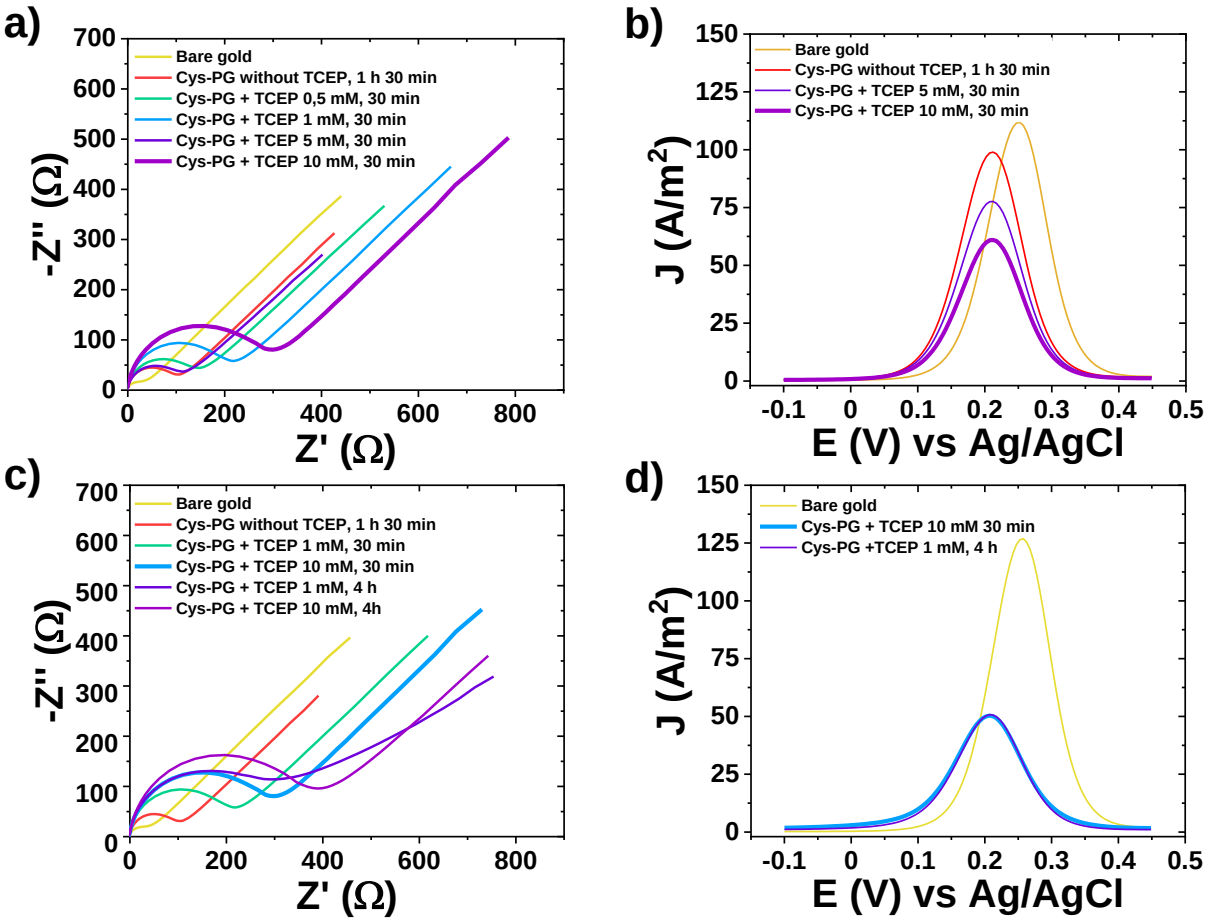

Figure S9. Optimization of the TCEP (reducing agent) concentration and incubation time employed to prepare the Protein G SAM monitored by EIS (a,c) and DPV (b,d). The EIS and DPV measurements were recorded employing the same conditions as **Figure S7**. All the electrochemical measurements were performed in an aqueous solution containing $K_3[Fe(CN)_6]$ 5 mM, KCl 100 mM, and 50 mM of sodium phosphate buffer (pH 7.4).

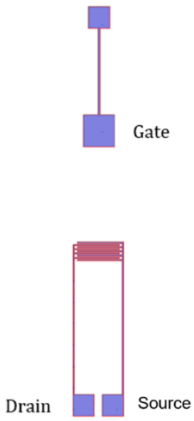

Figure S10. Device layout. W= 16000 µm L= 50 µm, W/L= 320 The coplanar gate electrode's area is equal to 2.25 mm^2.

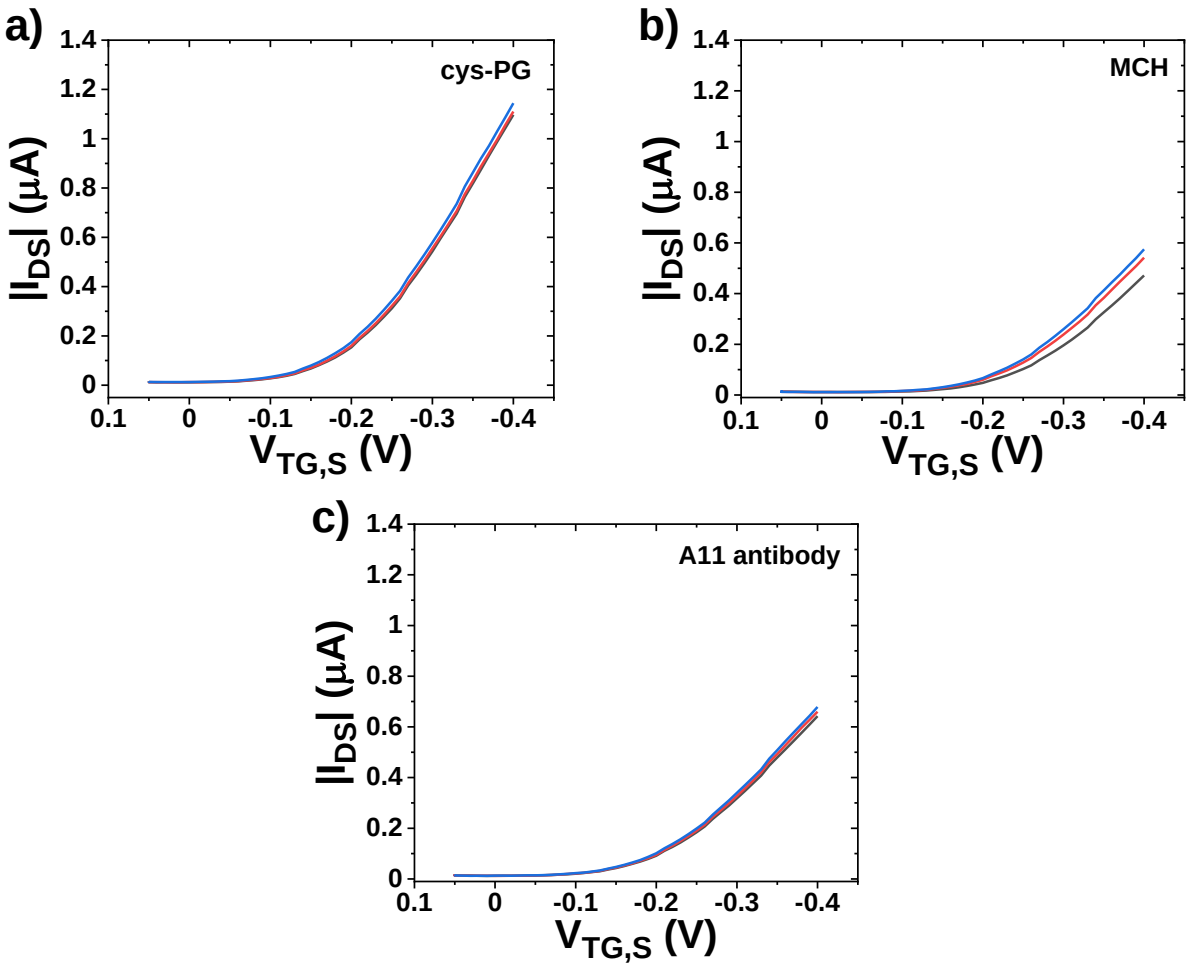

Figure S11. Three consecutive transfer characteristics employing Milli-Q water as electrolyte were performed in each functionalization step to study the electrode stability. (a) cys-PG, (b) PG with a self-assembled monolayer of MCH, and (c) immobilization of A11 Ab.

References:

[1] D. M. Walsh, A. Lomakin, G. B. Benedek, M. M. Condron, D. B. Teplow. *J. Biol. Chem*. **1997**, *272*, 22364-22372.

[2] D. M. Walsh, D. M. Hartley, Y. Kusumoto, Y. Fezoui, M. M. Condron, A. Lomakin, G. B. Benedek, D. J. Selkoe, D. B. Teplow. *J. Biol. Chem*. **1999**, *274*, 25945-25952.

[3] V. L. Anderson, W. W. Webb. *BMC Biotechnol*. **2011**, *11*, 125.

[4] O. N. Antzutkin. *Magn. Reason. Chem. MRC*. **2004**, *42*, 231-246.

[5] P. N. Nirmalraj, J. List, S. Battacharya, G. howe, L. Xu, D. Thompson, M. Mayer. *Sci. Adv.* **2020**, *6*, eaaz6014.

[6] S. M. Kelly, N. C. Price. *Curr. Protoc. Protein Sci.* **2006**, *46*, 20101-201018.

[7] M. Bokvist, F. Lindström, A. Watts, G. Gröbner. *J. Mol. Biol.* **2004**, *335*, 1039-1049.

[8] T. Okada, M. Wakabayashi, K. Ikeda, K. Matsuzaki. *J. Mol. Biol*. **2007**, *371*, 481-489.

[9] R. W. Hepler, K. M. Grimm, D. D. Nahas, R. Breese, E. C. Dodson, P. Acton, P. M. Keller, M. Yeager, H. Wang, P. Shughrue, G. Kinney, J. G. Joyce. *Biochemistry*. **2006**, *45*, 15157-15167.

[10] R. Pujol-Pina, S. Vilaprinyó-Pascual, R. Mazzucato, A. Arcella, M. Vilaseca, M. Orozco, N. Carulla. *Sci. Rep.* **2015**, *5*, 14809.

[11] Y.-M. Kuo, T. A. Kokjohn, M. D. Watson, A. S. Woods, R. J. Cotter, L. I. Sue, W. M. Kalback, M. R. Emmerling, T. G. Beach, A. E. Roher. *Am. J. Pathol.* **2000**, *156*, 797-805.

[12] S. Kalita, S. Kalita, A. Paul, A. Sarkar, B. Mandal. *Chem. Sci.* **2020**, *11*, 4171-4179.

[13] M. G. Dickens, K. J. Franz. ChemBioChem. 2010, 11, 59-62.

[14] M. Necula, R. Kayed, S. Milton, C. G. Glabe. *J. Biol. Chem*. **2007**, *282*, 10311-10324.

[15] S. Matsumura, K. Shinoda, M. Yamada, S. Yokojima, M. Inoue, T. Ohnishi, T. Shimada, K. Kikuchi, D. Masui, S. Hashimoto, M. Sato, A. Ito, M. Akioka, S. Takagi, Y. Nakamura, K. Nemoto, Y. Hasegawa, H. Takamoto, H. Inoue, S. Nakamura, Y. Nabeshima, D. B. Teplow, M. Kinjo, M. Hoshi. *J. Biol. Chem*. **2011**, *286*, 11555-11562.

[16] Y. Guan, K. J. Cao, A. Cantlon, K. Elbel, E. A. Theodorakis, D. M. Walsh, J. Yang, J. V. Shah. *ACS Chem. Neurosci*. **2015**, *6*, 1503-1508.

[17] H. Englund, D. Sehlin, A.-S. Johansson, L. N. G. Nilsson, P. Gellerfors, S. Paulie, L. Lannfelt, F. E. Pettersson. *J. Neurochem.* **2007**, *103*, 334-345.

[18] A. C. Klaver, L. M. Patrias, J. M. Finke, D. A. Loeffler. *J. Neurosci. Methods.* **2011**, *195*, 249-254.

[19] D. G. Georganopoulou, L. Chang, J.-M. Nam, C. S. Thaxton, E. J. Mufson, W. L. Klein, C. A. Mirkin. *Proc. Natl. Acad. Sci. U. S. A.* **2005**, *102*, 2273-2276.

[20] E. D. Goluch, S. I. Stoeva, J.-S. Lee, K. A. Shaikh, C. A. Mirkin, C. Liu. *Biosens. Bioelectron.* **2009**, *24*, 2397-2403.

[21] A. N. Santos, S. Torkler, D. Nowak, C. Schlitting, M. Goerdes, T. Lauber, L. Trischmann, M. Shaupp, M. Penz, F.-W. Tiller, G. Böhm. *J. Alzheimers Dis. JAD.* **2007**, *11*, 117-125.

[22] A. Ruiz-Arias, R. Jurado, F. Fueyo-González, R. Herranz, N. Gálvez, J. A. González-Vera, A. Orte. *Results. Chem.* **2022**, *4*, 100275.

[23] K. A. Bruggnik, M. Müller, H. B. Kuiperij, M. M. Verbeek. *J. Alzheimers Dis. JAD.* **2012**, *28*, 735-758.

CHAPTER 3

Hydrogel-Gated Organic Field-Effect Transistors

Abstract:

Flexible electronics increasingly impact many novel applications, including wearable healthcare sensors, in-vivo monitoring, and synthetic skin. Electrolyte-Gated Organic Field-Effect Transistors (EGOFETs) represent a significant focus of current research due to their advantages in miniaturization, low power consumption, direct transduction, and label-free detection of events in aqueous media. Hydrogels, which are hydrophilic and capable of swelling significantly in water, can serve as effective solid electrolyte media.[1] Over the last decade, these materials have earned widespread recognition for their integration in sensors and diagnostic tools. This chapter introduces a novel EGOFET in which the liquid electrolyte has been replaced by a water-based gel, namely agarose gel. The manufacturing method enables the production of a flexible device with high electrical performance and long-term stability if the hydrogel is preserved hydrated. In addition, we show that these devices can respond to pH changes and can be applied for the development of sensors when they are functionalized with suitable bio-receptors. This was demonstrated using an agarose modified with avidin as electrolyte to detect biotin.

1. Introduction

1.1. Flexible electronics

Flexible electronics represent a technological revolution, with applications ranging from foldable displays and implantable medical devices to wearable energy storage systems and touch panels. Unlike typical rigid electronics, flexible devices should maintain their function even when bent, stretched, or twisted, creating new possibilities for adaptive device designs. This innovation is based on the integration of materials that achieve a balance between mechanical flexibility, excellent electrical performance, biocompatibility, and environmental stability.[2–4]

Because of their flexibility, biocompatibility, and low cost, organic field-effect transistors (OFETs)[5] based on new organic semiconductors and fabrication methods, such as three-dimensional printing[6] or meniscus coating,[7] are expected to open up new possibilities for creating flexible displays,[8] foldable electronics,[9] and electronic skins.[10] Additionally, electrolyte-gated organic field-effect transistors (EGOFETs)[11,12] are compatible with flexible electronics and, further, due to their high electrolyte capacitance are operated at low voltages.[13,14] However, traditional liquid electrolytes are not easy to implement in flexible electronics due to their volatility and mechanical properties. Hence, solid electrolytes (i.e., ion gels, polyelectrolytes, or hydrogels) represent a promising alternative that has attracted great interest in recent years.[15]

1.2. Hydrogels in EGOFETs

Hydrogels can store and hold large amounts of fluid within their structure through swelling, giving them unique features like great flexibility, variable mechanical strength, and exceptional biocompatibility. This swelling is due to the chemical or physical crosslinking of polymer chains that support the network structure. Hydrogels have variable electrical and mechanical characteristics, making them suitable for flexible electronic devices like sensors, touch panels, and energy storage systems. They can act as substrates or as electrolytes in the form of a gel, overcoming the limitations of liquid water-based media by being produced as solid sheets.

As described in **Figure 3.1**, hydrogels are classified based on their **material source** (natural, synthetic, or hybrid), **type of crosslinking** (chemical or physical), **preparation method, and ionic charge.** This classification allows for tailored properties to meet specific requirements in flexible electronics.

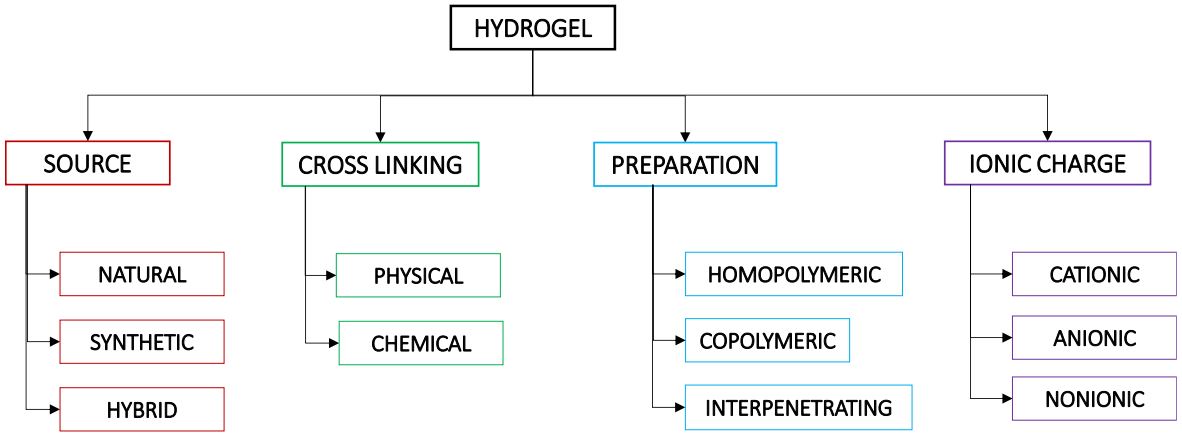

Figure 3.15. Possible classifications of hydrogels based on different criteria.[16]

Hydrogels have received significant attention over the last decade due to their valuable applications in drug delivery,[17] heavy metal ion removal,[18] contact lenses,[19] and tissue engineering scaffolds.[20] In the field of sensing, hydrogels can change volume in response to external stimuli, releasing and absorbing various fluids. These transformations are often reversible, allowing the hydrogel to return to its original state once the stimuli are removed, earning them the designation of 'intelligent' or 'smart' materials.

Stimulus-sensitive hydrogels can serve as active sensing materials due to their ability to respond to minor environmental changes. These gels are reactive to various physical stimuli (temperature, light, pressure, electric field, ionic strength, and magnetic field),[21,22] chemical

stimuli (pH, ions),[23] or biological stimuli (glucose, enzyme, and antigen)[24,25] through volume changes (**Figure 3.2**).[26–29] The rate of response is influenced by factors such as hydrogel composition, shape, and pore size, which can be adjusted by modifying the cross-linking density or the content of ionic groups. In the presence of these stimuli, the hydrogels modify their swelling properties, translating the physical/chemical/biological stimuli into macroscopic events. The change of the hydrogel swelling can be measured using various techniques like light transmission, conductimetry, or by measuring the mechanical properties changes.

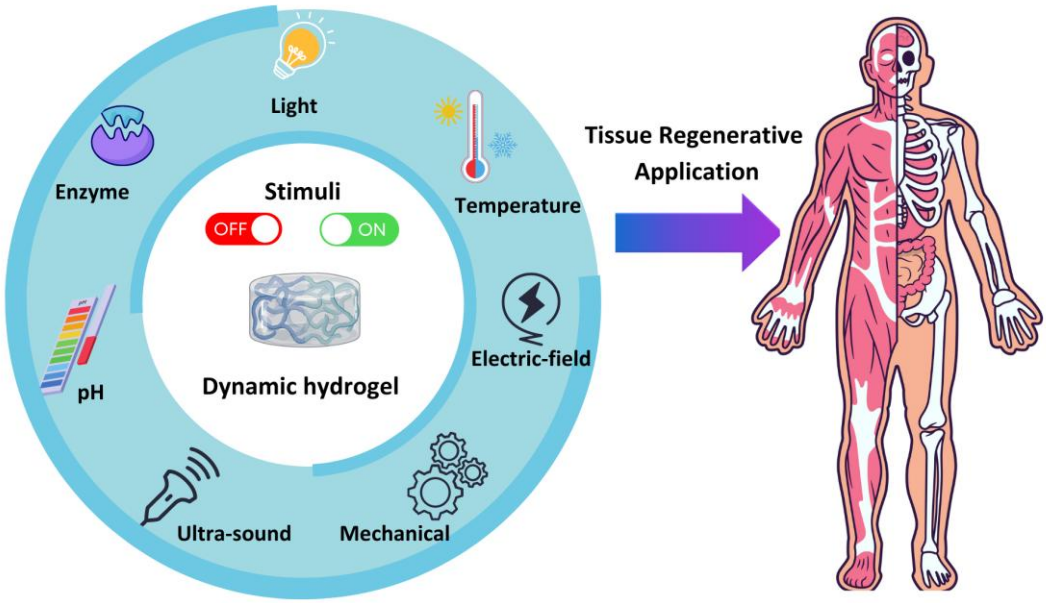

Figure 3.2. Schematic illustrations of various responsive stimuli for hydrogels that can be used for tissue regenerative applications. Adapted from ref[26].

Given these qualities, hydrogels are promising as innovative electrolytes for Hydrogel-Gated Organic Field-Effect Transistors (**HYGOFETs**). This opens up new possibilities for their use in sensors and ultra-sensitive transducers.

An example of a semisolid or solid hydrogel electrolyte is gelatin, which is a widely utilized natural, protein-based hydrogel known for its excellent biocompatibility, biodegradability, and non-toxicity.[30] Additionally, gelatin hydrogels can be readily applied using solution processing methods for the fabrication of electronic devices. A key feature of gelatin is its sol-gel transition; the hydrogen bonds between its molecules can be readily disrupted at temperatures above 40°C, when it is solubilized. Gelatin hydrogels are also sensitive to physical (e.g., temperature, pressure, and surface tension) and chemical effects (e.g., salt, enzymatic

degradation, and interaction with surfactants) from external environments.[31–33] Stretchable Organic Electrochemical Transistors (OECTs) based on gelatin hydrogels have been proved in neuromorphic devices and for developing glucose and pH sensors.[5,34]

Other polymeric materials, including microcrystalline cellulose hydrogel, acrylamide- and poly(vinylphosphonic acid-co-acrylic acid) based hydrogels, and poly(sodium-4-styrenesulfonate) combined with glycerol and D-sorbitol, have also been utilized in the development of liquid electrolyte-based transistors.[35] Nevertheless, fabricating devices with these electrolytes is generally more complex than with gelatin hydrogels, as they often involve extra synthetic steps.[36]

In this chapter, we have focused on agarose gels as electrolytes in HYGOFET devices. Agarose is a natural hydrogel derived from red seaweeds. Agarose is a linear polymer with the repeating unit shown in **Figure 3.3** and jellifies as a result of intermolecular physical cross-linking.[37] Due to its biocompatibility and affordability, this natural substance finds extensive use in various applications such as the food industry, electrophoresis, protein purification, separation techniques, and 3D cell culture or tissue engineering.[38,39] Typically, agarose is insoluble in cold water but dissolves readily in hot water. When the agarose solution cools below 34-35°C, it solidifies into a stable and robust gel. Previous studies have shown that an agarose-based HYGOFET can achieve high performance and is also highly sensitive to pressure stimuli (**Figure 3.4**).[40]

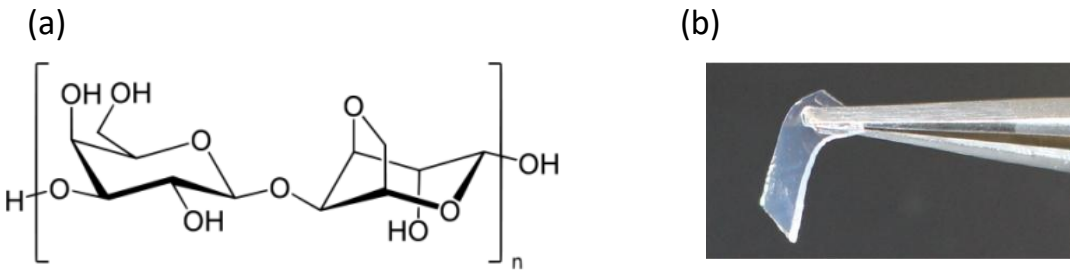

Figure 3.3. (a) Structure of an agarose polymer and **(b)** photography of an agarose hydrogel.

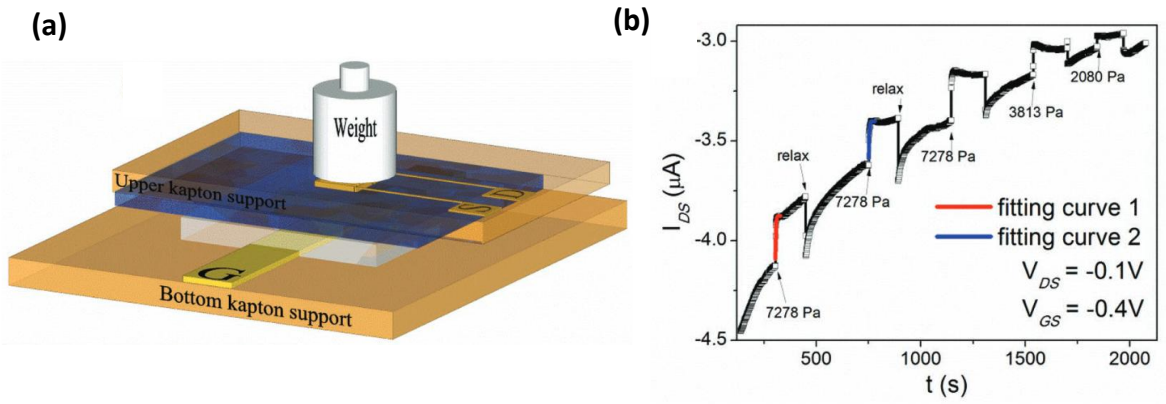

Figure 3.4. (a) Schematic diagram illustrates the HYGOFET based on agarose and the device configuration used for the pressure-sensing measurements. **(b)** I-t plot of the device operated with loaded pressure and relaxed with constant V_{GS}= -0.4 V and V_{DS}= -0.1 V. The base current demonstrates an initial drift during the first hour of operation but stabilizes to a constant value thereafter. The red and blue lines represent exponential fits highlighting the response speed toward pressure. Extracted from ref[40].

Hydrogels can serve as effective immobilization matrices for biosensing elements.[41] By embedding specific receptors in their native conformation within the hydrogel, it is possible to create biosensors with high selectivity and sensitivity. This ensures that the support material is resistant to nonspecific adsorption, enabling specific interactions with analytes. The interaction between the analyte and the sensing element can induce volumetric changes in the hydrogel, providing a novel sensing mechanism that differs from traditional biosensors and electrochemical biosensors.[42,43] Moreover, the quality of sensing and the level of sensitivity largely depend on the accessibility and activity of the immobilized sensing molecules.

Furthermore, hydrogels create favorable environments for enzymes and other biomolecules, aiding in the preservation of their active and functional structures.[44] Additionally, cells are often immobilized within hydrogel matrices for various applications.[45] In summary, since hydrogels may be easily tailored in their properties and can be extensively bio-modified, they are considered an ideal platform for a wide range of bio-applications.[46,47]

This chapter focuses on the production of agarose hydrogels to be used in HYGOFETs. Further, the HYGOFET electrical properties due to changes in pH in the agarose hydrogel were investigated. Next, we investigated the use of HYGOFETs as a potential biosensing platform. For this purpose, and as a model system, we used avidin-modified agarose as electrolyte of the HYGOFET to detect biotin, since avidin-biotin forms a well-known supramolecular complex with high affinity and specificity. This work aims to demonstrate the feasibility and efficiency

of agarose-based hydrogels in developing reliable and efficient point-of-care diagnostics tools and sensors.

2. Experimental procedures

2.1. Materials

- Materials for device fabrication

- **Kapton HN foils** were purchased from DuPont, 75 µm thick.
- Shipley Microposit **S1813** photoresist and Shipley Microposit **MF-319** developer were purchased from Shipley.
- 2,8-difluoro-5,11-bis(triethylsilylethynyl)anthradithiophene (**diF-TES-ADT**) was obtained from Lumtec and used as received (purity>99%), racemic mixture.
- **Polystyrene (PS)** (MW: 10000 g/mol) was purchased from Sigma-Aldrich and used without any further purification.
- 2,3,4,5,6-pentafluorothiophenol (**PFBT**) was purchased from Sigma-Aldrich.
- **Dextran** was purchased from *Leuconostoc spp.* (Mr <450000-650000> g/mol) was procured from Sigma-Aldrich.
- **Lateral-Flow system system**:
    - FFHP membrane: thin, backed membrane with reduced surfactant purchased from Cytiva.
    - Whatman CF4 dipstick pad. CF4 is a medium-weight, 100% cotton linter material (482 µm thickness at 53 kPA), suitable for use as a sample and absorption pad for lateral flow and flow-through assays. Purchased from Cytiva.

- Biological materials

- **Agarose powder** (Type I-B, low EEO) was obtained from Sigma-Aldrich.
- **Avidin-Agarose** from egg white – aqueous glycerol suspension was purchased from Sigma-Aldrich.
- **Biotin** (≥ 99 %, HPLC) lyophilized powder was obtained from Sigma-Aldrich.

- General products

- Polydimethylsiloxane (**PDMS**): The *Qsil216 A/B* components were obtained from Farnell Componentes.
- **Organic solvents**: Anhydrous chlorobenzene (CB) was sourced from Sigma-Aldrich. Acetone and isopropanol were acquired from Teknocroma Analítica S.A.
- Phosphate Buffer Saline (**PBS**): Prepared using NaCl 0.137 M, KCl 0.00027 M, Na_2HPO_4 0.01 M, KH_2PO_4 0.0018 M. The pH was adjusted using HCl 1 M or NaOH 1 M.
- **PDMS gasket production**: The components of the *Qsil216* kit were weighed in a 10:1 ratio. They were mixed thoroughly for about two minutes. The mixture was placed on a Petri dish and subjected to vacuum for 1 hour to remove air bubbles. The Petri dish was then cured at 70°C overnight to set the gasket.

2.2. Device fabrication procedures

The devices were fabricated on 75 µm thick Kapton substrates employing the following protocol:

- Au electrode design and Au evaporation

The fabrication of Au electrodes was performed using a photolithography technique in the 10.000-class Clean Room facility at ICMAB-CSIC (**Figure 3.5**). The design of the electrode pattern was created with CleWin4 software. Initially, the substrate underwent a cleaning process involving acetone and isopropanol, followed by drying with an N_2 stream. A positive photoresist (Shipley 1813) was applied using a Laurell Technologies WS-650SZ-6NPP/LITE spin-coater at 5000 rpm for 25 seconds. The coated substrate was then baked on a hotplate at 90°C for 1 minute before being placed in the Durham Magneto Optics LTD laser micro-writer system (MLTM) for exposure to a 405 nm laser to write the pattern. The substrate was subsequently developed in a Shipley Microposit MF-319 solution with gentle agitation for about 1 minute, during which the exposed photoresist dissolved, revealing the Source, Drain, and Gate electrode areas. After development, the substrate was rinsed with distilled water and dried with a N2 stream. The next step involved positioning the substrate in an Evaporation System Auto 306 from Boc Edwards, where a thin layer of gold was deposited under high vacuum conditions for optimal film quality. Following the Au deposition, a lift-off process was

conducted to remove the remaining photoresist and any excess metal, leaving a defined pattern of Au electrodes for the Source, Drain, and Gate.

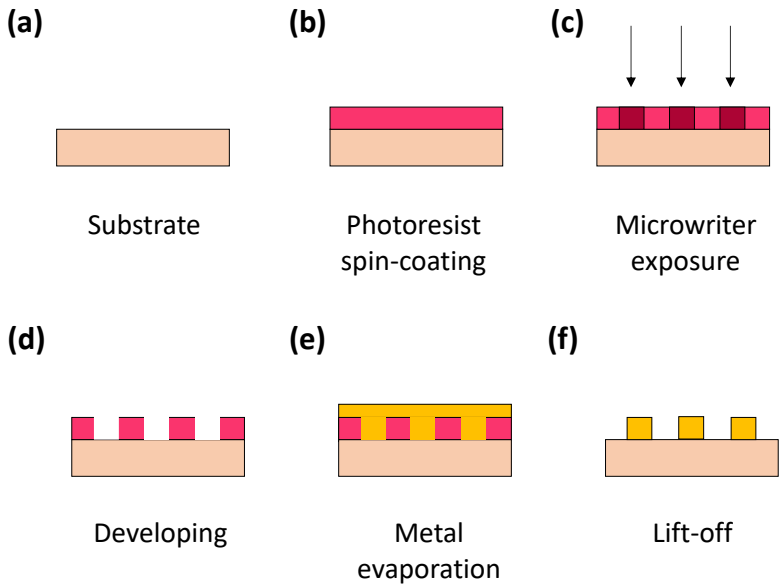

Figure 3.5. Gold interdigitated electrode patterning process using photolithography. **(a)** Kapton substrate; **(b)** spin-coating of the positive photoresist; **(c)** exposure of the photoresist-coated substrate to the micro-writer laser; **(d)** developing step; **(e)** metal evaporation, depositing 40 nm of gold atop a 5 nm of chromium adhesive layer; **(f)** lift-off in acetone removes the residual photoresist.

Concerning the electrode arrangement, **Figure 3.6** depicts the overall design of the interdigitated electrodes. The devices were produced in a 75 µm thick Kapton substrate and consisted of 8 interdigitated electrodes with the following characteristics: channel length (L) 50 µm, channel width (W) 16000 µm, and W/L= 320. The area of the coplanar gate was 25 mm^2.

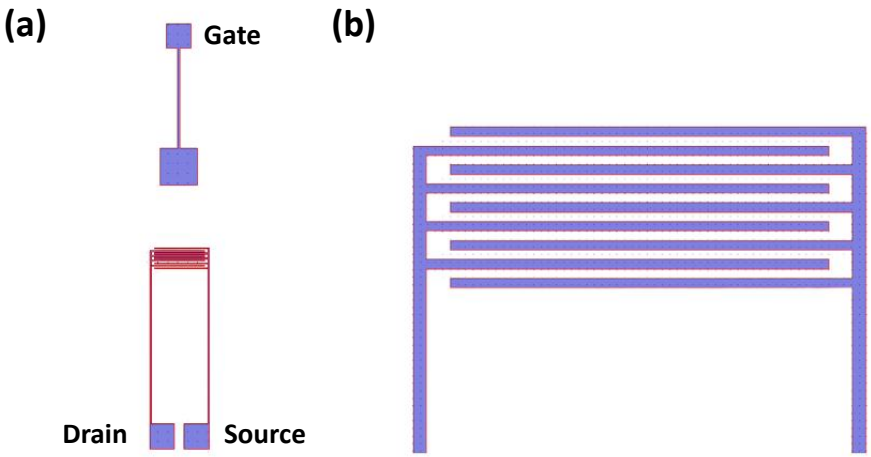

Figure 3.6. Device layout. W= 16000 µm, L= 50 µm, W/L= 320. The coplanar gate electrode's area is equal to 2.25 mm^2.

- Organic semiconductor (OSC) deposition

The OSC thin film was prepared by following a protocol well-established in our group.[11,48,49] As OSC, diF-TES-ADT was selected. Solutions of diF-TES-ADT and PS in CB at a concentration of 2% weight were prepared and mixed in a volume ratio diF-TES-ADT:PS 4:1. Before OSC deposition, the substrate was cleaned with acetone and isopropanol and then subjected to a UV Ozone cleaner for 25 minutes. Then, the gold Source and Drain contacts were functionalized with a self-assembled monolayer (SAM) of PFBT by immersing the substrates in a 2 µL/mL solution in isopropanol for 15 minutes. The formation of SAMs on gold is known to modify its work function, which can effectively reduce the gap between the gold work function and the HOMO level of the OSC.[50] In solution-processing techniques, SAMs can also influence the crystallization of the film by acting as nucleation sites.[51] Following the SAM formation, the substrate is thoroughly cleaned with isopropanol to remove any physisorbed thiol molecules and is subsequently dried under N_2 flow. To prevent SAM formation on the gate electrode and ensure it remains covered with the OSC, a sacrificial layer of dextran (10 mg/mL in water) is applied to the gate electrode before the substrate is immersed in the PFBT solution.[52] Dextran is insoluble in isopropanol but soluble in water, allowing it to be washed away with distilled water after the functionalization of the source-drain PFBT functionalization and OSC deposition (Figure 3.7).

The OSC ink solution was deposited on the substrate using the bar-assisted meniscus shearing technique (BAMS) with a custom-made bar coater (see Figure 3.7).[53,54] The hot plate in the BAMS setup was kept at 105°C. A droplet of the OSC ink, typically between 25-50 µL depending on the substrate size, was positioned between the bar and the substrate to create a stable meniscus. The bar was then moved at a controlled speed of 10 mm·s^{-1} allowing for a uniform and precise deposition of the ink across the substrate.

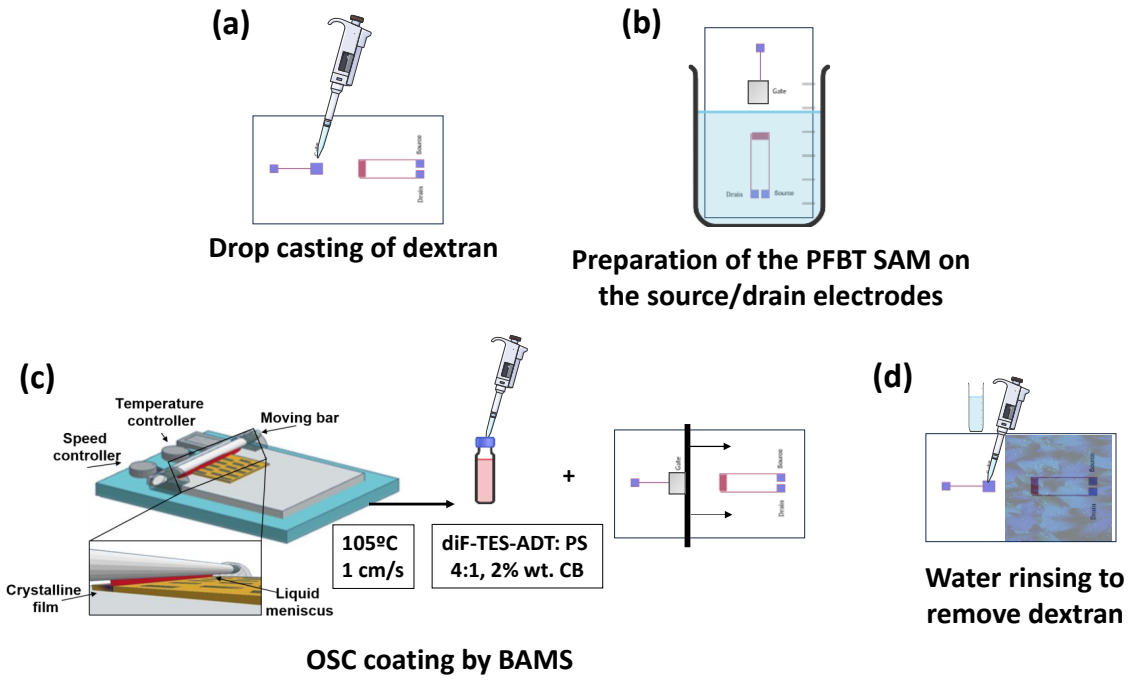

Figure 3.7. Schematic representation of diF-TES-ADT:PS coating protocol by BAMS. **(a)** Drop-casting of a sacrificial layer of dextran on top of the gate electrode; **(b)** dipping the interdigitated electrodes in a PFBT solution for SAM preparation; **(c)** OSC coating by BAMS and **(d)** removal of the sacrificial layer by water rinsing.

2.3.HYGOFET device assembly

- Hydrogel solutions preparation.

- **Agarose solution:** The agarose solution was prepared at a concentration of 2% wt. by dissolving agarose powder in MilliQ water (resistivity: 18.2 MΩ·cm at 25°C). The mixture was stirred continuously at 800 rpm while heated to 150°C for 5-10 minutes. Once the solution became transparent, it was promptly utilized for film preparation. This procedure was previously reported in our group.[40]
- **Avidin-Agarose solution**: Commercial agarose conjugated with avidin was acquired and suspended in a glycerol-containing solution. Firstly, to eliminate the glycerol of this commercialized product, 1 mL of the agarose-avidin suspension was subjected to washing with phosphate-buffered saline (PBS) solution 1X in an Eppendorf tube, followed by centrifugation at 2000xg. The supernatant obtained after this process was carefully removed to eliminate undesired glycerol. Subsequently, the gel was washed again three times with 0.5 mL of the PBS solution, following the same procedure (**Figure 3.8**). For each 1 mL of initial agarose suspension, 0.5 mL of packed hydrogel was obtained.

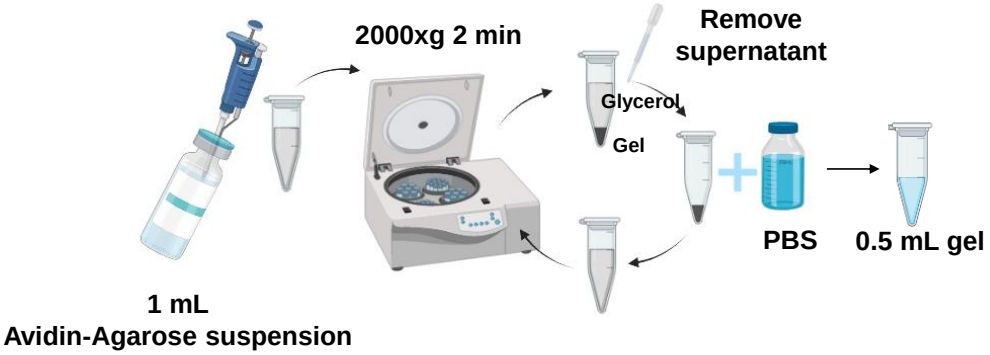

Figure 3.8. Avidin-Agarose gel obtaining process. From the marketed suspension to the ready-to-use gel. 1 mL of suspension yields 0.5 mL of packed gel.

Because gels containing Avidin-Agarose are difficult to manipulate, it was decided to mix it with agarose. Therefore, 1 mL of the obtained packed avidin-agarose hydrogel was mixed with different volumes (0.5, 1, 1.5, and 2 mL) of the agarose 2% wt. solution at 60°C, a temperature lower than the denaturation temperature of avidin, while stirring to ensure a homogeneous mixture. For clarity, these mixtures are named after Avidin-Agarose:Agarose 2% wt. 1:1, 1:2, 1:3, and 1:4 (v:v), respectively (**Figure 3.9).**

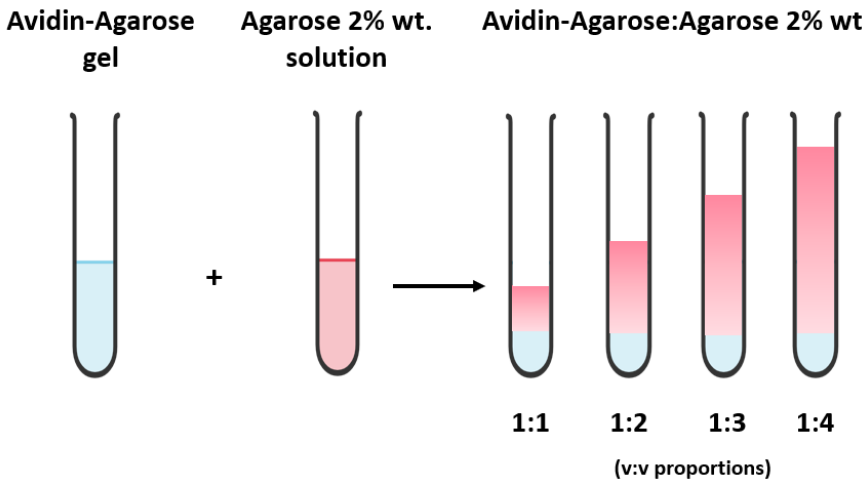

Figure 3.9. Schematic representation of the Avidin-Agarose:Agarose 2% wt. (v:v) ratios manufacture.

- Gel deposition procedures

For the deposition of solutions to create a gel film, the BAMS technique was used, with a coating speed of 1 $cm \cdot s^{-1}$ and a plate temperature maintained at 30°C, as the gelling temperature of this type of agarose is around 35°C.[55] Prior to the deposition, the tip of the micropipette was immersed in the hot agarose solution (150°C) for 30 seconds to prevent the solution from gelling inside the plastic pipette. After the hot agarose solution (60°C) deposition on the Kapton substrate, a solid hydrogel film was formed upon cooling down to room temperature. The resulting agarose film was then cut into square pieces (around 1 cm^2) and immediately used as the electrolyte in the transistors by sandwiching it on top of the prepared devices (**Figure 3.10**).

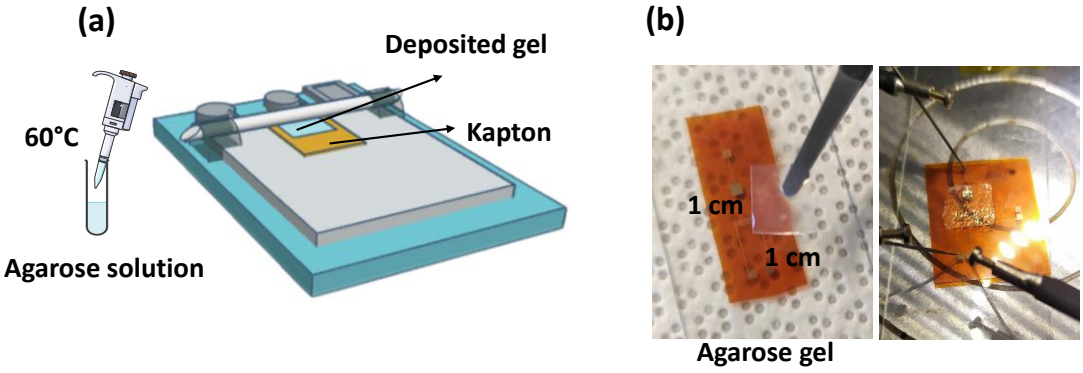

Figure 3.10. Agarose gel manufacturing scheme using BAMS. **(a)** Agarose 2% wt. deposition of the gel on a Kapton substrate using the BAMS technique (substrate temperature 30°C, coating speed 1 $cm \cdot s^{-1}$), **(b)** cutting the gel into pieces of 1 cm^2 and sandwiching it on top of the devices.

Alternatively, to obtain a thicker gel and avoid its rapid dehydration, for the manufacture of Avidin-agarose:Agarose 2% wt. gels, a polydimethylsiloxane (PDMS) gasket was employed for the formation of a gel with a specific area (**Figure 3. 11**). In this case, the hot agarose solution (i.e., 60°C) was deposited on a square PDMS pool of 1 cm^2 and let to cool down at room temperature. The use of the PDMS gasket results in a more homogeneous and thicker gel, which allows for a slower dehydration rate of the film. To prevent dehydration of the gels, all the prepared hydrogels were stored in a refrigerator at 5°C.

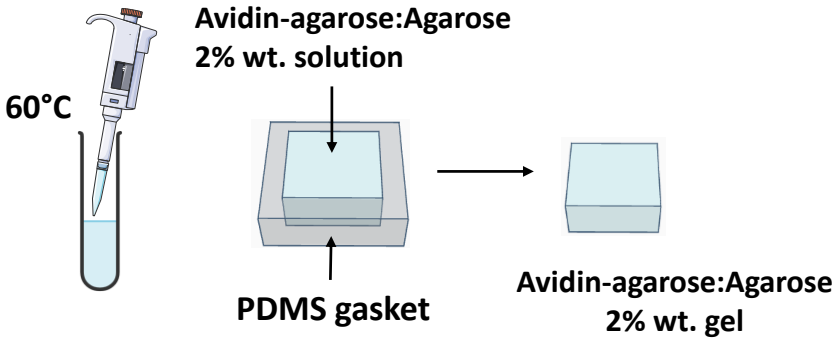

Figure 3.11. Avidin-agarose:Agarose 2% wt. manufacturing scheme using a PDMS gasket.

2.4. HYGOFET device characterization

- Electrically characterization of the HYGOFETs

The HYGOFETs were electrically characterized under ambient conditions using an Agilent 5100A SMU interfaced with the Easy Expert software. First, the devices were conditioned by applying a source-gate voltage V_{GS}= -0.1 V and a source-drain voltage V_{DS}= -0.1 V until the source-drain current (I_{DS}) reached a steady regime, employing Milli-Q water as the electrolyte, during approximately 30 minutes. Once a stable condition was reached, the first I_{DS}-V_{GS} curve was defined as a reference to evaluate the performance of the devices, by applying V_{DS}= -0.1 and -0.4 V. Output curves were also measured at V_{GS}= 0, -0.1, -0.2, and -0.4 V. After that, the liquid electrolyte was replaced by the agarose gel, and a transfer and output characteristic employing the same conditions were performed to compare the device's response employing both electrolyte media.

To study the dehydration of the hydrogel over time, which is a problem from the point of view of device stability, transfer characteristics were performed every 5 minutes, leaving the gel at ambient conditions. In addition, in a parallel experiment, a nitrocellulose system was designed to provide a continuous flow of the aqueous solution and avoid dehydration of the gel. Transfer characteristics were performed every 5 minutes applying V_{DS}= -0.5 V and V_{GS}= -0.1 V to -0.5 V.

- pH sensing measurements performed with the HYGOFETs

The HYGOFETs response was investigated at different pH. To perform the electrical measurements at different pH, the agarose hydrogels were immersed in phosphate-buffered saline (PBS) solutions of varying pH levels, ranging from acidic to basic, for 20 minutes, and, subsequently, the gels were placed on the device. Before measurements, the gel was left in contact with the device for 5 minutes and between each consecutive measurement, a waiting time of one minute was left. The gel was then removed from the device and the device was washed with the PBS solution corresponding to the next pH value to be tested. This process was replicated three times for each pH value (Figure 3.12). As a control test, the devices were also measured using the PBS solutions at different pHs as electrolytes of the transistors.

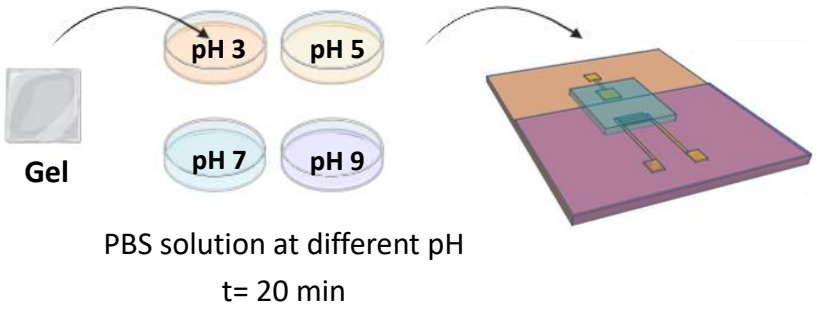

Figure 3.12. Study of the HYGOFET response at different pH. The agarose hydrogel was immersed in different PBS solutions at different pH for 20 minutes and subsequently placed on the device for electrical characterization. The same procedure was repeated for each pH studied.

The stability of the 2% wt. agarose hydrogel HYGOFET at different pH (i.e. pH 3 and 7) was also studied by measuring transfer characteristics (V_{DS}= -0.1 V, and -0.4 V, V_{GS} from 0.4 V to -0.4 V) every half an hour.

- Continuous sensing measurements (pH and biotin) using a lateral flow

Removing the hydrogel from the device for performing each measurement during the sensing measurements, can partially damage the OSC thin film. To avoid this, both sensing measurements (pH and biotin sensing) were carried out by using one single ensemble HYGOFET device and employing a lateral flow system composed of nitrocellulose as a membrane to circulate the different solutions.[56,57] Over the past few decades, lateral flow assay (LFA) has found widespread applications in point-of-care diagnostics.[57] These tests typically feature a 'strip' made up of four interconnected porous components arranged linearly: (i) a sample pad, (ii) a conjugate pad that contains dried, antibodies specific to the target analyte, (iii) a nitrocellulose membrane with immobilized capture agents located at both control and test lines, and (iv) a wicking pad designed to draw the sample through the device.[57] The user adds a microliter-volume sample (e.g., blood, urine, saliva) to the sample pad to initiate the test. The device's simplicity allows for easy manufacturing, and the dried reagents eliminate the need for refrigeration and extend shelf life.[58] In this case, the lateral flow was used to measure the HYGOFET response in a continuous operation, without assembling and dissembling it. The configuration employed was composed of the sample and the absorption pad connected to the nitrocellulose membrane, which was in direct contact with agarose hydrogel (Figure 3.13). Further, with this layout, the dehydration of the agarose gel can also be avoided.

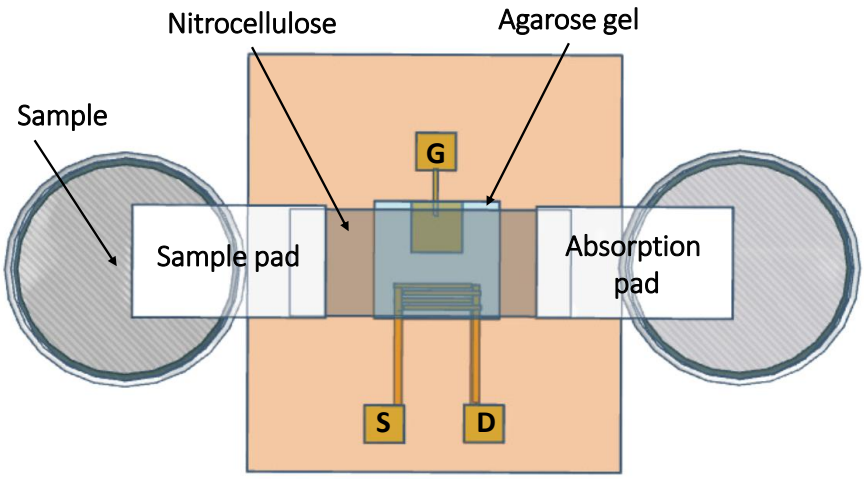

Figure 3.13. Schematic representation of nitrocellulose device assembling.

The experimental procedure used for the biotin sensing using the nitrocellulose system consisted of **(i)** the device was wetted and stabilized with the configuration presented in **Figure 3.13**, passing only PBS through the nitrocellulose to keep the hydrogel well-hydrated, **(ii)** once the device reached a steady state, 200 µL of the biotin solutions were injected in the absorption pads in ascending concentration order (from 10^{-17} M to 10^{-10} M) and **(iii)** after a 15-min wait to ensure that the entire sample had been in contact with the hydrogel, the electrical measurements were performed. Subsequently, the nitrocellulose was washed with PBS 1X, before adding the following biotin concentration.

The same procedure was followed for the pH measurements, but in this case, the washing step between sampling was not required.

3. Experimental results

3.1. HYGOFETs based on agarose 2% wt. hydrogel

To compare the performance of the devices using Milli-Q water (EGOFET) and the agarose hydrogel as an electrolyte (HYGOFET), transfer (in the linear and saturation regime) and output characteristics were measured and are plotted together in **Figure 3.14**. It is observed that there is no significant hysteresis and good saturation in the output characteristics is achieved. **Table 1** shows the product $\mu \cdot C_{dl}$ and the V_{th} values for both electrolytes studied, calculated in the saturation regime. It is observed that in the case of the HYGOFET, the $\mu \cdot C_{dl}$ is lower and also the V_{th} value is more negative than that obtained with Milli-Q water. This may be due to the lower quantity and mobility of the ions inside the hydrogel, which leads to a lower capacitance of the electrolyte and also to a larger voltage required to 'turn on' the device.

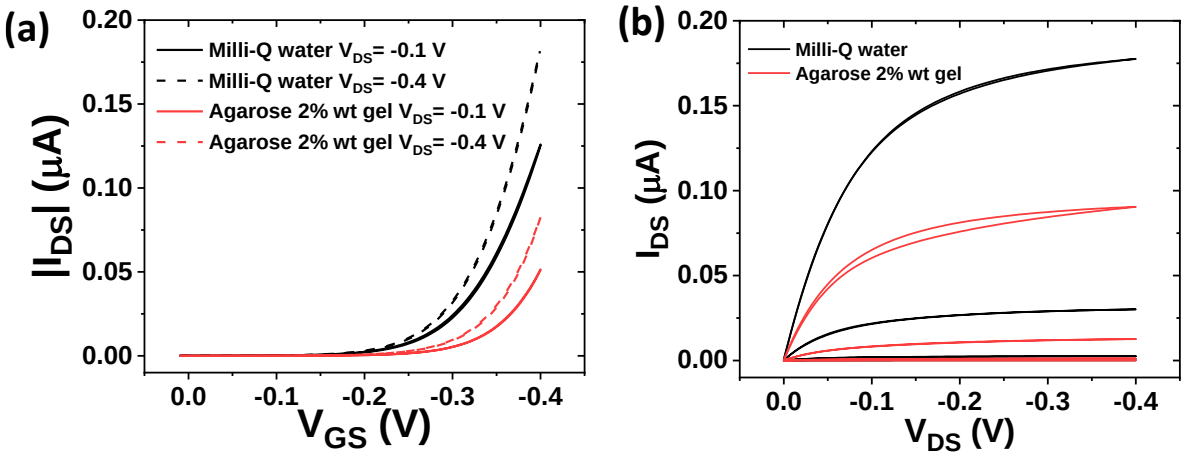

Figure 3.14. (a) Transfer (V_{DS}= -0.1 V and -0.4 V) and **(b)** output characteristics (V_{GS}= 0 V, -0.1 V, -0.2 V, and -0.4 V) comparison between EGOFETs measured in Milli-Q water **(black curves)** and HYGOFETs based on a hydrogel of agarose 2% wt. **(red curves)**.

Table 1. Comparison of μ^*C_{dl} and V_{th} extracted from EGOFETs and HYGOFETs using Milli-Q water and agarose gel 2% wt. as electrolyte, respectively.

Electrolyte	$\mu \cdot C_{dl}$ ($\mu S \cdot V^{-1}$)	V_{th} (V)
Milli-Q water	0.058 ± 0.001	-0.21 ± 0.01
Agarose gel 2% wt.	0.032 ± 0.020	-0.24 ± 0.04

The dehydration of hydrogels with time is known to be a problem from the point of view of the stability of the measurements. Therefore, it was decided to study the dehydration of the agarose hydrogel over time by performing continuous transfer characteristics every 5 minutes. In Figure 3.15 it can be observed that the device works correctly for approximately one hour, and afterward, signs of dehydration of the hydrogel are noticed. Then, the device's performance begins to worsen, until 170 minutes when it stops working.

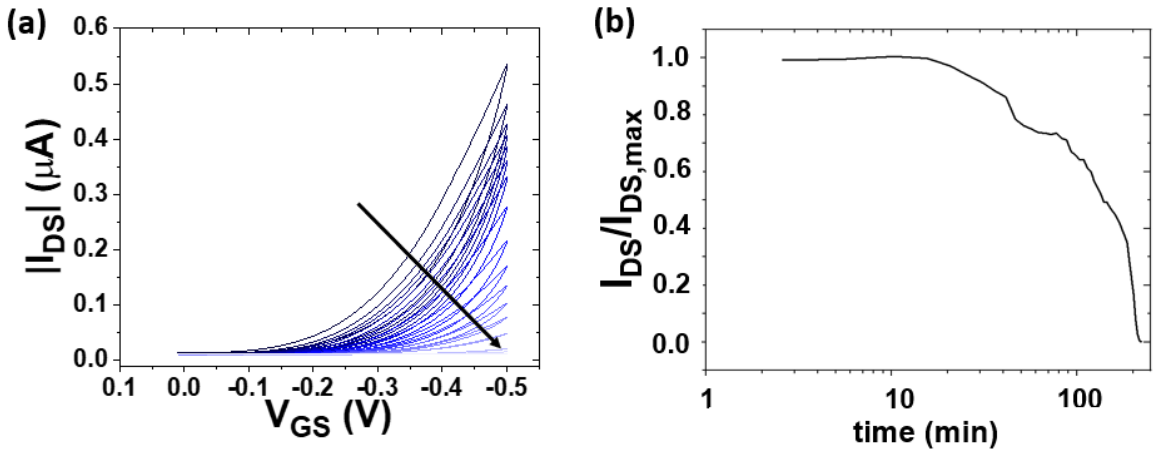

Figure 3.15. Time stability of the HYGOFET which is affected by the dehydration of the agarose hydrogel. **(a)** Continuous transfer characteristics of the HYGOFET (V_{DS}= -0.5 V). **(b)** Change in the normalized I_{DS} (at V_{GS}= -0.5 V) over time on a logarithmic scale.

3.2.HYGOFETS based on avidin-agarose hydrogels

Once the manufacture of HYGOFETs based on non-modified agarose hydrogels had been optimized, we proceeded to manufacture the avidin-agarose hydrogel. Due to the difficulties in forming stable hydrogels using only the avidin-modified agarose, we mixed it with non-modified agarose in the proportions Avidin-Agarose packed gel:Agarose 2% wt. aqueous solution 1:2, 1:3, 1:4 v:v, as explained in the experimental section.

In Figure 3.16 a,b, the transfer characteristics of the resultant HYGOFETs are shown. Table 2 presents a comparison of the $\mu \cdot C_{dl}$ and V_{th} parameters employing the different ratios, calculated in saturation regime. The devices corresponding to the ratio 1:4 exhibited the lowest current and $\mu \cdot C_{dl}$. The 1:2 ratio was selected as the optimal hydrogel to perform the following measurements since, in addition to exhibiting the best electrical performance, it has a lower proportion of the non-modified agarose, providing a higher concentration of avidin moieties in the hydrogel. Noticeably, mixtures containing a lower proportion of non-modified agarose did not lead to robust hydrogels easy to handle.

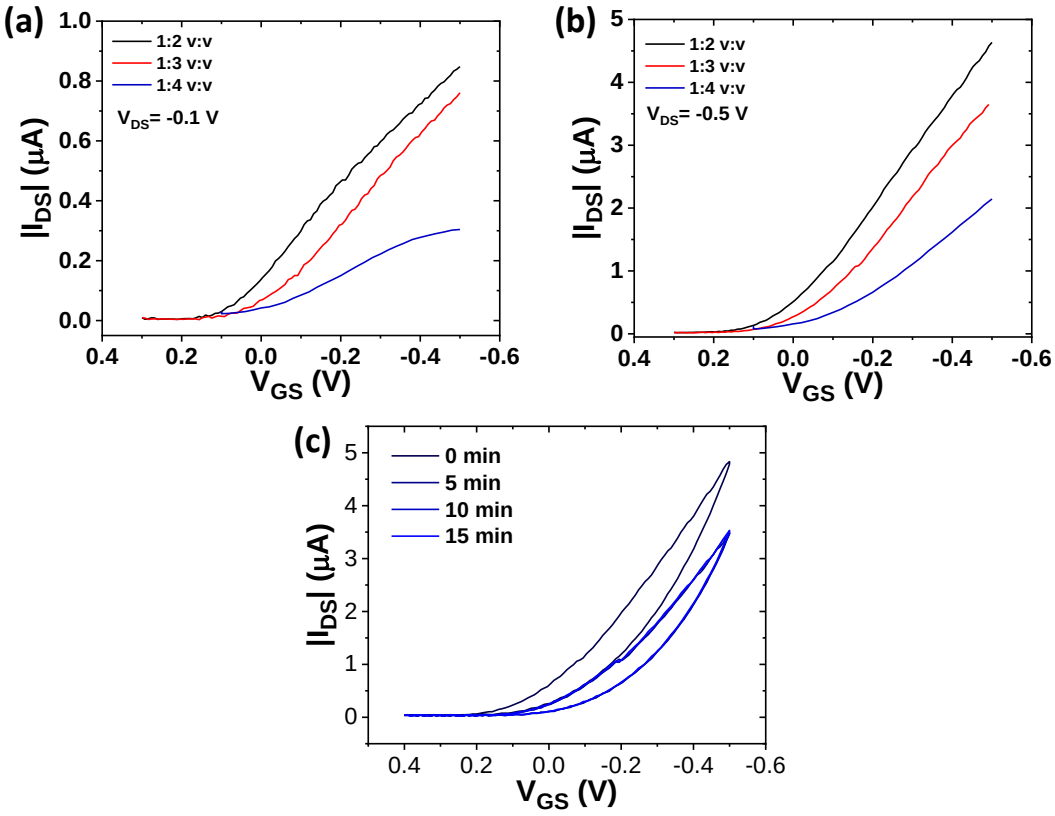

Figure 3.16. Comparison between the ratios 1:2, 1:3, and 1:4 (v:v) Avidin-Agarose:Agarose 2% wt. hydrogels. Transfer characteristics of the HYGOFETs using the 1:2, 1:3, 1:4 (v:v) ratios **(a)** in linear regime (V_{DS}= -0.1 V) and **(b)** in saturation regime (V_{DS}= -0.5 V). **(c)** Study of the time stability of the HYGOFET based on the hydrogel Avidina-Agarose:Agarose 2% wt 1:2 ratio. Transfer characteristics performed during 15 minutes and applying a V_{DS} equal to -0.5 V.

Table 2. Comparison of $\mu \cdot C_{dl}$ and V_{th} extracted from HYGOFETs using different Avidin-Agarose:Agarose 2% wt. ratios.

Electrolyte (v:v ratio)	$\mu \cdot C_{dl}$ ($\mu S \cdot V^{-1}$)	V_{th} (V)
Avidin-Agarose:Agarose 2% wt. ratio 1:2	0.058 ± 0.003	0.19 ± 0.06
Avidin-Agarose:Agarose 2% wt. ratio 1:3	0.054 ± 0.001	0.17 ± 0.01
Avidin-Agarose:Agarose 2% wt. ratio 1:4	0.029 ± 0.004	0.14 ± 0.003

The stability of the devices based on the selected Avidin-Agarose: Agarose 2% wt. 1:2 (v:v) ratio was studied with time as previously performed with the HYGOFETs based on non-modified agarose (**Figure 3.16 c**). It is observed that during the first minutes, the electrical response of the devices diminishes, but afterward remains stable for a time period before dehydration starts, similar to what was observed for the agarose hydrogel.

3.3. Study of the dependence of the electrical response of the HYGOFET devices on the pH

- EGOFET as a reference sample

To understand the influence of pH in our devices, we studied first a reference EGOFET device using PBS solutions at different pH as electrolytes going from acidic to basic conditions. **Figure 3.17** shows the transfer characteristics (V_{DS}= -0.4 V, V_{GS}= from 0.1 V to -0.4 V) of the devices. As can be observed, as the pH increases, the device current and $\mu \cdot C_{dl}$ decreases, and the V_{th} shifts towards negative gate voltage values. An increase in the off current is also noticed at acid pH. A linear dependence of the source-drain current on pH was found, and a sensitivity of 27.35 µA/pH (**Figure 3.17b**). In the case of V_{th}, although the linear correlation with pH is not so good in all the pH range, a linear fit in the measurements performed between pH= 5 and 9, results in a slope of 51 mV/pH, which is slightly lower than the Nernst limit of 59 mV/pH. However, no linear correlation was found with $\mu \cdot C_{dl}$, which tends to decrease at basic pH.

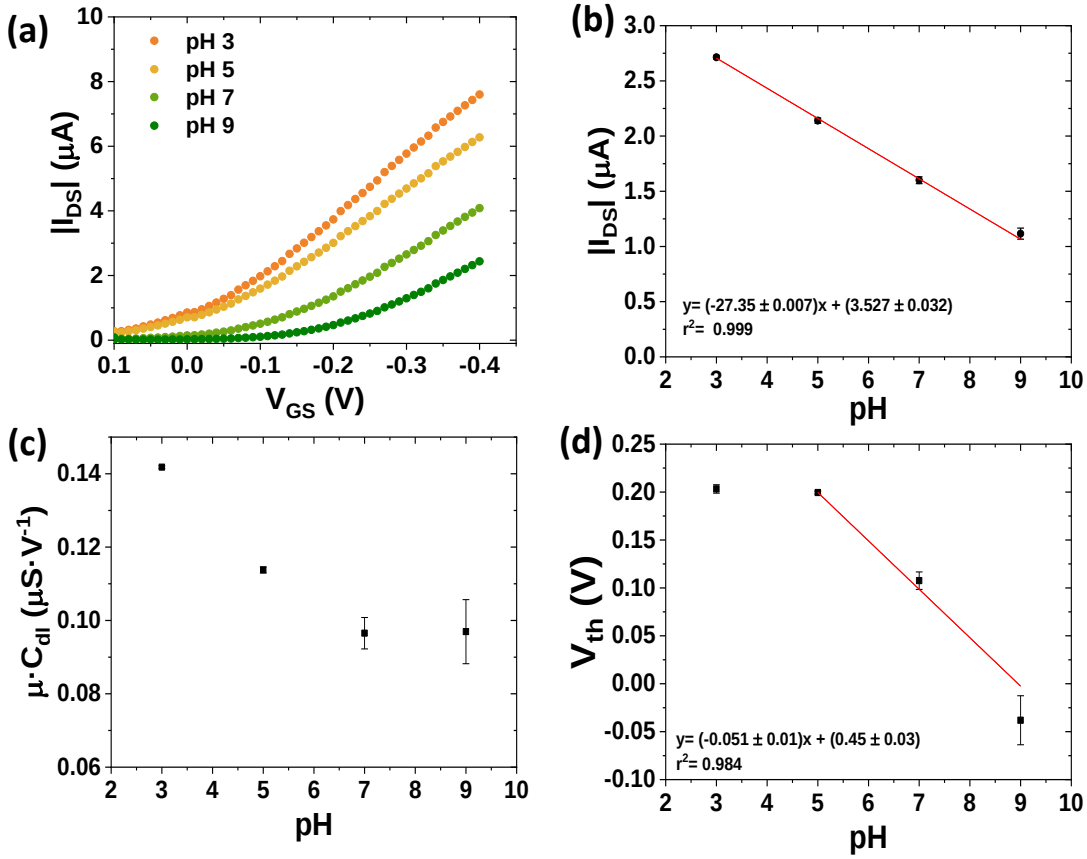

Figure 3.17. (a) EGOFET transfer characteristics (V_{DS}= -0.4 V, V_{GS}= from 0.1 V to -0.4 V) employing PBS solutions at different pH as the electrolyte, **(b)** I_{DS} at V_{GS}= 0.4 V of the EGOFETs measured at different pH (from 3 to 9) **(c)** $\mu \cdot C_{dl}$ vs pH and **(d)** V_{th} vs pH. Error bars correspond to the average of 3 replicates.

The stability of the devices at each pH was studied by performing 3 consecutive measurements for each pH (i.e., pH 3, 5, 7, and 9) and waiting for 1 minute between each transfer characteristic. As a result, it was observed that the stability of the devices at basic pH is lower (**Figure 3.18**).

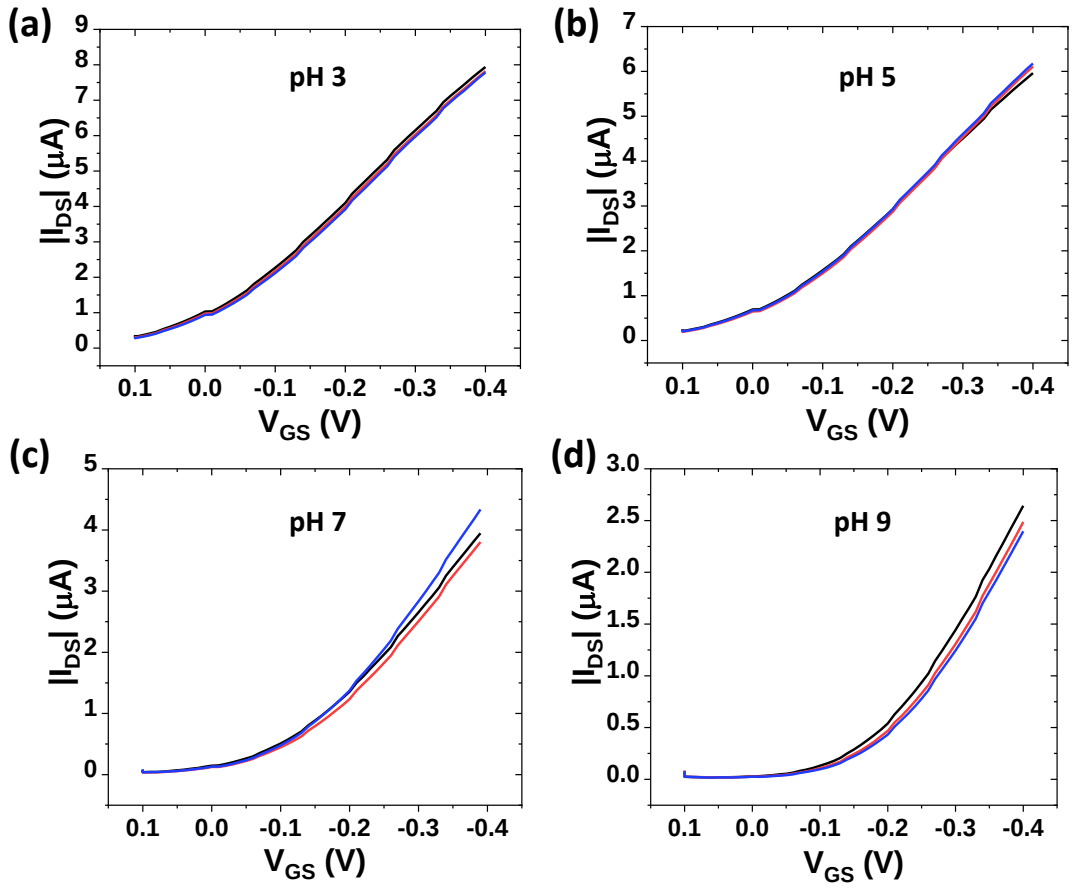

Figure 3.18. Study of the stability of the EGOFET at different pH realized by performing 3 consecutive transfer characteristics (V_{DS}= -0.4 V, V_{GS}= from 0.1 V to -0.4 V): **(a)** pH 3, **(b)** pH 5, **(c)** pH 7, and **(d)** pH 9. It is observed that there is a greater variability in the measurements when working in basic pH.

Previous works with OFETs and EGOFETs have also observed a dependency on the performance of the device with pH values ranging from 3 to 12.[59,60] Shaposhnik et al.[60] described EGOFETs that exhibited a positive shift in V_{th} when operating in acidic solutions, without impairing mobility. The authors suggested that protons from the electrolyte were chemically doping the OSC. This effect was only noticeable in the acidic pH range, while in neutral or slightly basic solutions no significant changes were observed. Chemical doping might occur because protons are associated with free electron pairs of the sulfur atoms of the OSC. This would cause the formation of charges that could act as 'healers' of deep traps, which would be reflected in the positive shift of V_{th} without significantly affecting the mobility of the charge carriers. We believe that a similar doping phenomena might be occurring here since at acid pH the device turns on at much lower gate voltages and the off current is higher.

Next, we performed studies of the influence of pH on the HYGOFETs based on agarose 2% wt. Although it was expected to observe a similar trend with changes in pH, it had to be taken into account here that the hydrogel itself can also change with pH.

- HYGOFETs based on Agarose 2% wt. hydrogel

Studies have shown that changes in pH can slightly alter the mechanical and stability properties of the gel, affecting the formation of hydrogen bonds and, therefore, its physical conformation and elasticity. However, Kunkel and Asuri[61] highlighted that agarose is relatively stable over a wide pH range, but under extreme conditions, it may lose rigidity.

As mentioned in the experimental section, we measured the electrical response of a HYGOFET using different Agarose 2% wt. hydrogel pieces incubated in different solutions with adjusted pH from acidic to basic pH (**Figure 3.19)**. The same tendency observed with the liquid electrolyte (PBS) was found here. At basic pH, the device current decreases significantly as well as $\mu \cdot C_{dl}$, and, V_{th} shifts to more negative values of V_{GS}.

Analyzing the dependency of the source-drain current with pH, a linear dependence of the source-drain current on pH was found, and a sensitivity of 21.45 µA/pH (**Figure 3.19b**), which is of a similar order to the one found with the liquid electroyte. In the case of V_{th}, a linear fit in the range of pH= 6-9 results in a slope of 35 mV/pH, lower than the Nernst limit (**Figure 3.19d**).

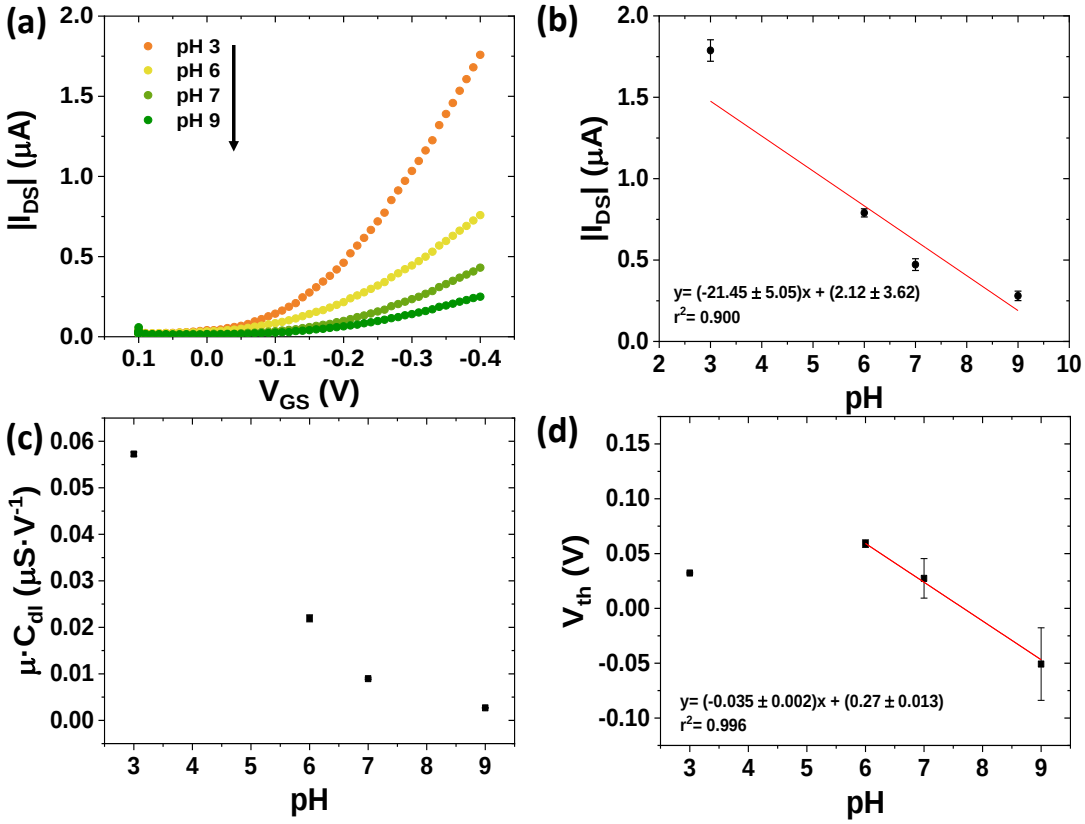

Figure 3.19. Figures of merit of agarose 2% wt. HYGOFET. **(a)** Transfer characteristics (V_{DS}= -0.4 V, V_{GS}= 0.1 V to -0.4 V) from pH 3 to pH 9. **(b)** I_{DS} current vs pH at V_{GS}= -0.4 V, **(c)** $\mu \cdot C_{dl}$ vs pH, and **(d)** V_{th} vs pH. From acidic to basic pH. The arrow in (a) indicates the order of pH used. The error bars correspond to 3 replicates.

To study the HYGOFETs' stability with time, transfer characteristics were measured for 3 hours for two HYGOFETs at two different pHs (i.e., pH 3 and 7). For these experiments, the devices were encapsulated with a Kapton foil to prevent dehydration over time. As observed in Figure 3.20, the devices show high stability during this time period.

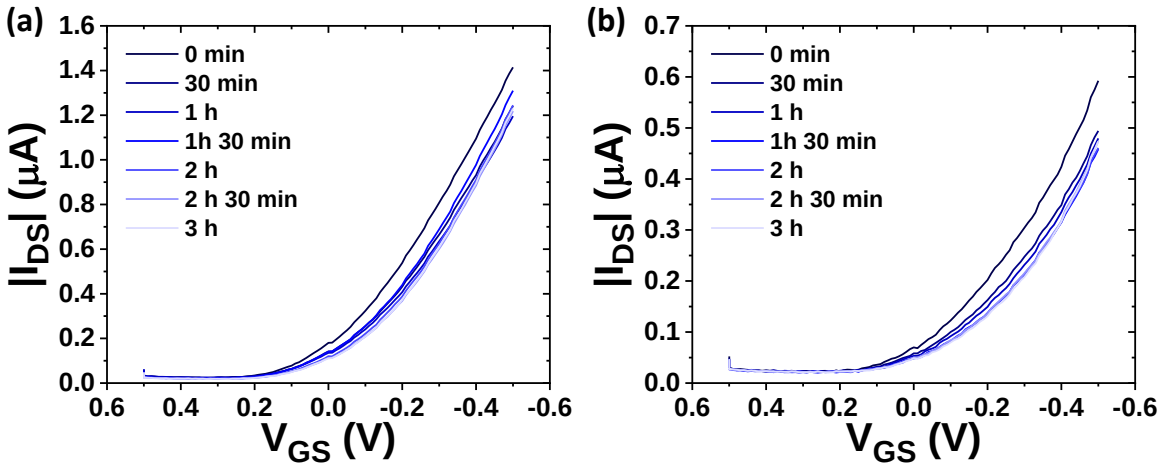

Figure 3.20. Study of the HYGOFET stability using agarose 2% wt. hydrogels at **(a)** pH 3 and **(b)** pH 7. Transfers characteristics applying a V_{DS}= -0.4 V and V_{GS}= from 0.5 V to -0.5 V, measured over 3 hours.

It is hypothesized that the device's performance may degrade due to the removal and placement of the hydrogel, as well as the manipulation of the device. This could influence the observed electrical changes and cause a lower reproducibility. Such effects are key when the HYGOFETs are going to be applied as biosensor platforms. To solve this problem, it was decided to work with a lateral flow system using nitrocellulose. This avoids having to remove the hydrogel for testing each condition since the lateral flow can transport the target aqueous solution through the hydrogel.

In a preliminary test, the effect of changing the pH in the hydrogel was studied, following the procedure described in Section 2.4 (**Figure 3.21**). The same trend observed in the previous experiments was found here, that is, the device current decreased at basic pH. Therefore, we concluded that the nitrocellulose system functions correctly and can be suitable for performing continuous sensing experiments without the need to disrupt the assembled HYGOFET.

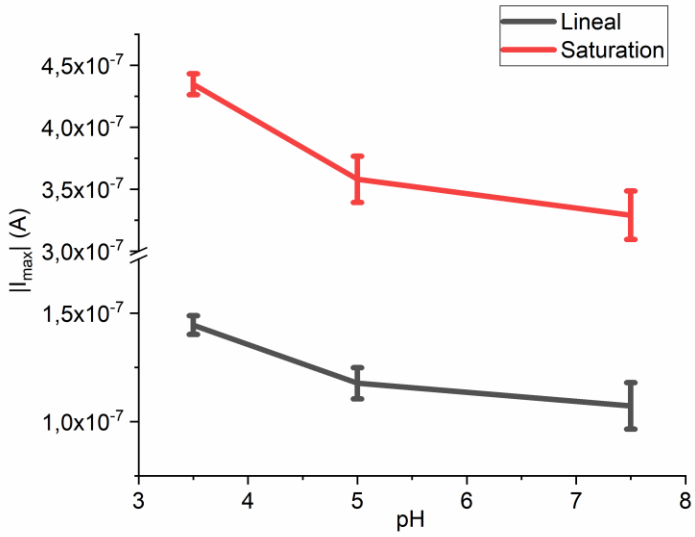

Figure 3.21. I_{DS} current (at V_{GS}= -0.4 V) vs pH of an HYGOFET based on agarose 2% wt. and employing a nitrocellulose paper for transporting the PBS solutions at different pH on the device without removing the hydrogel from the EGOFET.

3.4. Sensing response of the HYGOFET to biotin

The HYGOFETs based on the Avidin-Agarose:Agarose 2% wt. 1:2 ratio hydrogel were explored as a sensing platform to detect biotin. Biotin is known that form a supramolecular complex with avidin with a high affinity.

The devices were embedded with the lateral flow assay and biotin solutions of different concentrations in ascending concentration order were flowed. The measurements were performed on three different devices. **Figure 3.22a** shows the transfer characteristics obtained, where it can be observed that I_{DS} current decreases while increasing biotin concentration. A linear dependence of the relative change of I_{DS} on the biotin concentration can be observed (**Figure 3.22b**), accompanied by a shift of the V_{th} towards negative gate values (**Figure 3.22d**). On the other hand, no appreciable changes were observed in the product $\mu \cdot C_{dl}$, indicating that the OSC layer remains intact (**Figure 3.22c**).

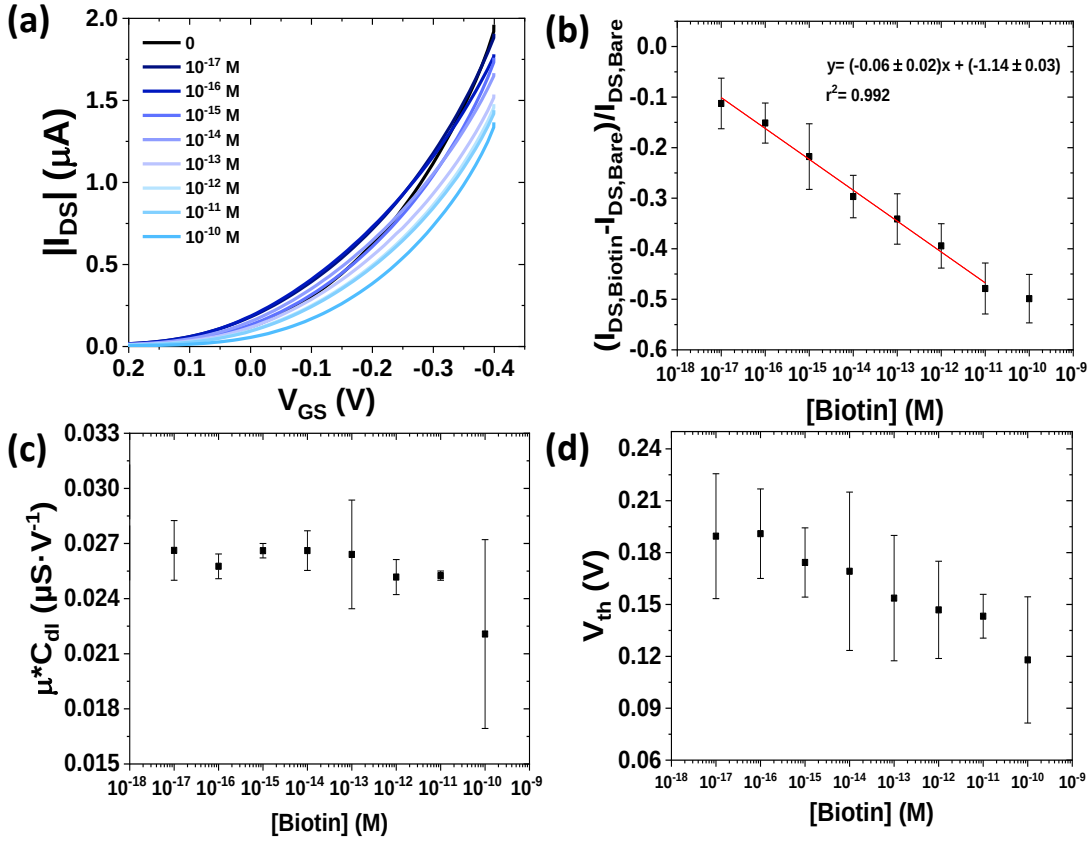

Figure 3.22. (a) Transfer characteristics of HYGOFETs based on avidin-modified agarose embedded in the lateral flow assay system and exposed at increasing concentrations of biotin (V_{DS}=-0.4 V and V_{GS} = from 0.2 V to -0.4 V). **(b)** Representation of $(I_{DS}-I_{DS,Bare})/I_{DS,Bare}$ extracted from the transfer characteristics at V_{GS}= -0.4 V. **(c)** $\mu \cdot C_{dl}$ vs biotin concentration and **(d)** V_{th} vs biotin concentration. 'Bare' in (a) and (b) means the reference, that is, the initial measurements performed in nitrocellulose with PBS 1X.

As the hydrogel is exposed to a higher concentration of biotin, more avidin binding sites from the hydrogel become occupied, forming avidin-biotin complexes. This can introduce conformational changes in the structure of the agarose hydrogel, affecting its porosity and density, as well as it can alter the charge distribution within the gel. Avidin is a charged protein and biotin-binding can modify the net charge and ionic distribution within the gel and affect the properties of the electrical double layers at the hydrogel-gate electrode and hydrogel-OSC interfaces of the HYGOFET. An excellent linear tendency was observed by increasing biotin concentrations in the range of 10^{-17} M- 10^{-11} M (r^2= 0.992), reaching a limit of detection (LOD) of 10^{-17} M, and a high sensitivity of 0.06 ± 0.02 M^{-1}.

The tendency observed agrees well with a previous work carried out in our group where the interaction avidin-biotin was also studied in an EGOFET operating in liquid electrolyte.[62] In that work, magnetic gold nanoparticles were functionalized with biotin and then incubated in avidin solutions. Subsequently, the nanoparticles were trapped on the surface of a magnetic carbon electrode, which was then implemented as gate contact in the EGOFET. High sensitivities and low limits of detection of the order of fM were then achieved. The devices here reported exhibit a slightly higher sensitivity, a much lower LOD (i.e., two orders of magnitude lower), and a lower variability and, in addition, are simpler and easier to implement in applications.

4. Conclusions

In this chapter we used hydrogels, semi-solid electrolytes, as an alternative to liquid electrolytes in EGOFETs, giving rise to the Hydrogel-Gated Organic Field-Effect Transistor (HYGOFET) devices. For this, agarose was selected as hydrogel due to its low cost, ready availability, and easy gelling procedure.

The potential of the fabricated HYGOFETs for high-performance biosensing applications has been thoroughly demonstrated. The devices exhibited excellent performance, showing stable operation over time, provided that the hydrogel dehydration is effectively controlled. This finding underscores the importance of managing the hydrogel environment to maintain long-term stability, making these devices more reliable for continuous monitoring and practical use. Additionally, it has been shown that the properties of the hydrogel can be modulated by adjusting the pH, which introduces a valuable tunable element for various applications, including sensing .

Furthermore, a key achievement of this chapter has been the introduction of receptor units in the hydrogel for the development of sensors together with the design and implementation of a HYGOFET device integrated with a lateral flow system, enabling continuous sensing measurements. As a proof of concept, the system was successfully applied to detect avidin-biotin interactions, yielding highly promising results. This application serves as a demonstration of the potential of HYGOFETs in real-time biosensing scenarios, where continuous and reliable detection is crucial.

In conclusion, HYGOFETs present a promising advancement in the field of biosensing. They retain the key advantages of EGOFETs, such as low operating voltage and operation in an aqueous environment, while offering enhanced manageability. Importantly, the hydrogels employed can be made biocompatible, further extending the range of potential bio-applications. These characteristics make HYGOFETs a versatile and powerful tool in the development of the next generation of biosensors, especially when continuous monitoring and biocompatibility are required.

5. References

[1] Buenger, D., Topuz, F. and Groll, J. Hydrogels in sensing applications. *Prog. Polym. Sci.* 2012, 12, 1678–1719.

[2] Hu, L., Chee, P. L., Sugiarto, S., Yu, Y., Shi, C., Yan, R., Yao, Z., Shi, X., Zhi, J., Kai, D., Yu, H.-D. and Huang, W. Hydrogel-based flexible electronics. *Adv. Mater.* 2023, 35, 2205326.

[3] Rong, Q., Lei, W. and Liu, M. Conductive hydrogels as smart materials for flexible electronic devices. *Chem. – Eur. J.* 2018, 24, 16930–16943.

[4] Song, J., Chan, S. Y., Du, Z. D., Yan, Y., Wang, T., Li, P. and Huang, W. Hydrogel-based flexible materials for diabetes diagnosis, treatment, and management. *Npj Flex. Electron.* 2021, 5, 1–17.

[5] Jo, Y. J., Kwon, K. Y., Khan, Z. U., Crispin, X. and Kim, T. Gelatin hydrogel-based organic electrochemical transistors and their integrated logic circuits. *ACS Appl. Mater. Interfaces* 2018, 10, 39083–39090.

[6] Kwak, D., Choi, H. H., Kang, B., Kim, D. H., Lee, W. H. and Cho, K. Tailoring morphology and structure of inkjet-printed liquid-crystalline semiconductor/insulating polymer blends for high-stability organic transistors. *Adv. Funct. Mater.* 2016, 26, 3003–3011.

[7] Gu, X., Shaw, L., Gu, K., Toney, M. F. and Bao, Z. The meniscus-guided deposition of semiconducting polymers. *Nat. Commun.* 2018, 9, 534.

[8] Kim, S., Kwon, H. J., Lee, S., Shim, H., Chun, Y., Choi, W., Kwack, J., Han, D., Song, M., Kim, S., Mohammadi, S., Kee, I. and Lee, S. Y. Low-power flexible organic light-emitting diode display device. *Adv. Mater.* 2011, 23, 3511–3516.

[9] Lee, S., Seong, H., Im, S. G., Moon, H. and Yoo, S. Organic flash memory on various flexible substrates for foldable and disposable electronics. Nature Communications. 2017, 8, 725.

[10] Miyamoto, A., Lee, S., Cooray, N. F., Lee, S., Mori, M., Matsuhisa, N., Jin, H., Yoda, L., Yokota, T., Itoh, A., Sekino, M., Kawasaki, H., Ebihara, T., Amagai, M. and Someya, T. Inflammation-free, gas-permeable, lightweight, stretchable on-skin electronics with nanomeshes. *Nat. Nanotechnol.* 2017, 12, 907–913.

[11] Leonardi, F., Casalini, S., Zhang, Q., Galindo, S., Gutiérrez, D. and Mas-Torrent, M. Electrolyte-gated organic field-effect transistor based on a solution sheared organic semiconductor blend. *Adv. Mater.* 2016, 28, 10311–10316.

[12] Choi, Y., Kang, J., Jariwala, D., Kang, M. S., Marks, T. J., Hersam, M. C. and Cho, J. H. Low-voltage complementary electronics from ion-gel-gated vertical van der Waals heterostructures. *Adv. Mater.* 2016, 28, 3742–3748.

[13] Lee, K. H., Zhang, S., Lodge, T. P. and Frisbie, C. D. Electrical impedance of spin-coatable ion gel films. *J. Phys. Chem. B.* 2011, 115, 3315–3321.

[14] Lee, J., Kaake, L. G., Cho, J. H., Zhu, X.-Y., Lodge, T. P. and Frisbie, C. D. Ion gel-gated polymer thin-film transistors: operating mechanism and characterization of gate dielectric capacitance, switching speed, and stability. *The Journal of Physical Chemistry C.* 2009, 113, 8972-8981.

[15] Ma, X. and Maimaitiyiming, X. Highly stretchable, self-healing, and low temperature resistant double network hydrogel ionic conductor as flexible sensor and quasi-solid electrolyte. *Macromol. Rapid Commun.* 2023, 44, 2200685.

[16] Bahram, M., Mohseni, N. and Moghtader, M. An introduction to hydrogels and some recent applications. *Emerging Concepts in Analysis and Applications of Hydrogels*. 2015.

[17] Far, B. F., Safaei, M., Nahavandi, R., Gholami, A., Naimi-Jamal, M. R., Tamang, S., Ahn, J. E., Farani, M. R. and Huh, Y. S. Hydrogel encapsulation techniques and its clinical applications in drug delivery and regenerative medicine: a systematic review. *ACS Omega.* 2024, 2, 29139-29158.

[18] Zhu, H., Chen, S. and Luo, Y. Adsorption mechanisms of hydrogels for heavy metal and organic dyes removal: a short review. *Journal of Agriculture and Food Research.* 2023, 12, 100552.

[19] Childs, A., Li, H., Lewittes, D. M., Dong, B., Liu, W., Shu, X., Sun, C. and Zhang, H. F. Fabricating customized hydrogel contact lens. *Scientific Reports*. 2016, 6, 34905.

[20] Drury, J. L. and Mooney, D. J. Hydrogels for tissue engineering: scaffold design variables and applications. *Biomaterials*. 2003, 24, 4337-4351.

[21] Pourbadiei, B., Monghari, M. A. A., Khorasani, H. M. and Pourjavadi, A. A light-responsive wound dressing hydrogel: Gelatin based self-healing interpenetrated network with metal-ligand interaction by ferric citrate. *J. Photochem. Photobiol. B.* 2023, 245, 112750.

[22] He, W., Guo, X., Xia, P., Lu, S., Zhang, Y. and Fan, H. Temperature and pressure sensitive ionic conductive triple-network hydrogel for high-durability dual signal sensors. *J. Colloid Interface Sci.* 2023, 647, 456–466.

[23] Zhou, P., Zhang, Z., Mo, F. and Wang, Y. A review of functional hydrogels for flexible chemical sensors. *Adv. Sens. Res.* 2024, 3, 2300021.

[24] Lin, X., Wang, Z., Jia, X., Chen, R., Qin, Y., Bian, Y., Sheng, W., Li, S. and Gao, Z. Stimulus-responsive hydrogels: A potent tool for biosensing in food safety. *Trends Food Sci. Technol.* 2023, 131, 91–103.

[25] Barhoum, A., Sadak, O., Ramirez, I. A. and Iverson, N. Stimuli-bioresponsive hydrogels as new generation materials for implantable, wearable, and disposable biosensors for medical diagnostics: Principles, opportunities, and challenges. *Adv. Colloid Interface Sci.* 2023, 317, 102920.

[26] Amirthalingam, S., Kumar Rajendran, A., Gi Moon, Y. and S. Hwang, N. Stimuli-responsive dynamic hydrogels: design, properties and tissue engineering applications. *Mater. Horiz.* 2023, 10, 3325–3350.

[27] Bhaladhare, S. and Bhattacharjee, S. Chemical, physical, and biological stimuli responsive nanogels for biomedical applications (mechanisms, concepts, and advancements): A review. *Int. J. Biol. Macromol.* 2023, 226, 535–553.

[28] Wang, X., Behl, M., Lendlein, A. and Balk, M. Responses to single and multiple temperature-, medium-, and pH-stimuli triggering reversible shape shifts in hydrogel actuators. *Mater. Des.* 2023, 225, 111511.

[29] Zhao, C.-X., Guo, M., Mao, J., Li, Y.-T., Wu, Y.-P., Guo, H., Xiang, D. and Li, H. Self-healing, stretchable, temperature-sensitive and strain-sensitive hydrogel-based flexible sensors. *Chin. J. Polym. Sci.* 2023, 41, 334–344.

[30] Guan, Y., Huang, Y. and Li, T. Applications of gelatin in biosensors: Recent trends and progress. *Biosensors.* 2022, 12, 670.

[31] Jaipan, P., Nguyen, A. and Narayan, R. J. Gelatin-based hydrogels for biomedical applications. *MRS Commun.* 2017, 7, 416–426.

[32] Salahuddin, B., Wang, S., Sangian, D., Aziz, S. and Gu, Q. Hybrid gelatin hydrogels in nanomedicine applications. *ACS Appl. Bio Mater.* 2021, 4, 2886–2906.

[33] Petros, S., Tesfaye, T. and Ayele, M. A review on gelatin based hydrogels for medical textile applications. *J. Eng.* 2020, 8866582.

[34] Wang, W., Li, Z., Li, M., Fang, L., Chen, F., Han, S., Lan, L., Chen, J., Chen, Q., Wang, H., Liu, C., Yang, Y., Yue, W. and Xie, Z. High-transconductance, highly elastic, durable and

recyclable all-polymer electrochemical transistors with 3D micro-engineered interfaces. *Nano-Micro Lett.* 2022, 14, 184.

[35] Kim, C.-H., Azimi, M., Fan, J., Nagarajan, H., Wang, M. and Cicoira, F. All-printed and stretchable organic electrochemical transistors using a hydrogel electrolyte. *Nanoscale.* 2023, 15, 3263–3272.

[36] Zhong, Y., Lopez-Larrea, N., Alvarez-Tirado, M., Casado, N., Koklu, A., Marks, A., Moser, M., McCulloch, I., Mecerreyes, D. and Inal, S. Eutectogels as a Semisolid electrolyte for organic electrochemical transistors. *Chem. Mater.* 2024, 36, 1841–1854.

[37] Ghebremedhin, M., Seiffert, S. and Vilgis, T. A. Physics of agarose fluid gels: Rheological properties and microstructure. *Curr. Res. Food Sci.* 2021, 4, 436–448.

[38] López-Marcial, G. R., Zeng, A. Y., Osuna, C., Dennis, J., García, J. M. and O'Connell, D. O. Agarose-based hydrogels as suitable bioprinting materials for tissue engineering. *ACS Biomaterials Science & Engineering*. 2018, 4, 3610-3616.

[39] Jiang, F., Xu, X.-W., Chen, F.-Q., Weng, H.-F., Chen, J., Ru, Y., Xiao, Q. and Xiao, A.-F. Extraction, modification and biomedical application of agarose hydrogels: a review. *Mar Drugs.* 2023, 21, 299.

[40] Zhang, Q., Leonardi, F., Pfattner, R. and Mas-Torrent, M. A solid-state aqueous electrolyte-gated field-effect transistor as a low-voltage operation pressure-sensitive platform. *Adv. Mater. Interfaces.* 2019, 6, 1900719.

[41] Kandimalla, V. B., Tripathi, V. S. and Ju, H. Immobilization of biomolecules in Sol-Gel: biological and analytical applications. *Critical Reviews in Analytical Chemistry.* 2006, 36, 73-106.

[42] Kaniewska, K., Nowakowski, J., Bacal, P. and Karbarz, M. Reversible change in volume of thin hydrogel layer deposited on electrode surface using Cu(II)↔Cu(I) process. *Sens. Actuators B Chem.* 2021, 344, 130114.

[43] Ehrenhofer, A., Elstner, M. and Wallmersperger, T. Normalization of hydrogel swelling behavior for sensoric and actuatoric applications. *Sens. Actuators B Chem.* 2018, 255, 1343-1353.

[44] Meyer, J., Meyer, L. and Kara, S. Enzyme immobilization in hydrogels: A perfect liaison for efficient and sustainable biocatalysis. *Eng. Life Sci.* 2021, 22, 165–177.

[45] Jen, A. C., Wake, M. C. and Mikos, A. G. Review: Hydrogels for cell immobilization. *Biotechnol. Bioeng.* 1996, 50, 357–364.

[46] Lee, K. Z., Jeon, J., Jiang, B., Subramani, S. V., Li, J. and Zhang, F. Protein-based hydrogels and their biomedical applications. *Molecules* 2023, 28, 4988.

[47] Zhong, R., Talebian, S., Mendes, B. B., Wallace, G., Langer, R., Conde, J. and Shi, J. Hydrogels for RNA delivery. *Nature Materials.* 2023, 22, 818-831.

[48] Perez-Rodriguez, A., Temiño, I., Ocal, C., Mas-Torrent, M. and Barrena, E. Decoding the vertical phase separation and its impact on C8-BTBT/PS transistor properties. *ACS Appl. Mater. Interfaces* 2018, 10, 7296-7303.

[49] Zhang, Q., Leonardi, F., Casalini, S., Temiño, I. and Mas-Torrent, M. High performing solution-coated electrolyte-gated organic field-effect transistors for aqueous media operation. *Sci. Rep.* 2016, 6, 39623.

[50] Casalini, S., Bortolotti, C. A., Leonardi, F. and Biscarini, F. Self-assembled monolayers in organic electronics. *Chem. Soc. Rev.* 2017, 46, 40–71.

[51] Niazi, M. R., Li, R., Abdelsamie, M., Zhao, K., Anjum, D. H., Payne, M. M., Anthony, J., Smilgies, D. M. and Amassian, A. Contact-induced nucleation in high-performance bottom-contact organic thin film transistors manufactured by large-area compatible solution processing. *Adv. Funct. Mater.* 2016, 26, 2371–2378.

[52] Leonardi, F., Tamayo, A., Casalini, S. and Mas-Torrent, M. Modification of the gate electrode by self-assembled monolayers in flexible electrolyte-gated organic field effect transistors: work function vs. capacitance effects. *RSC Adv.* 2018, 8, 27509–27515.

[53] Del Pozo, F., Fabiano, S., Pfattner, R., Georgakopoulos, S., Galindo, S., Liu, X., Braun S., Fahlman, M., Veciana, J., Rovira, C., Crispin, X., Berggren, M. and Mas-Torrent, M. Single crystal-like performance in solution-coated thin-film organic field-effect transistors. *Adv. Funct. Mater.* 2016, 26, 2379–2386.

[54] Temiño, I., Del Pozo, F. G., Ajayakumar, M. R., Galindo, S., Puigdollers, J. and Mas-Torrent, M. A rapid, low-cost, and scalable technique for printing state-of-the-art organic field-effect transistors. *Adv. Mater. Technol.* 2016, 1, 1600090.

[55] Normand, V., Lootens, D. L., Amici, E., Plucknett, K. P. and Aymard, P. New insight into agarose gel Mechanical properties. *Biomacromolecules.* 2000, 1, 730-738.

[56] Fridley, G. E., Holstein, C. A., Oza, S. B. and Yager, P. The evolution of nitrocellulose as a material for bioassays. *MRS Bull.* 2013, 38, 326–330.

[57] Jia, P., Li, Z., Wang, X., Xu, F., You, M. and Feng, S. Performance improvement of lateral flow assay using heterogeneous nitrocellulose membrane with nonuniform pore size. *Int. Commun. Heat Mass Transf.* 2023, 143, 106729.

[58] Posthuma-Trumpie, G. A., Korf, J. and van Amerongen, A. Lateral flow (immuno)assay: its strengths, weaknesses, opportunities and threats. A literature survey. *Anal. Bioanal. Chem.* 2009, 393, 569–582.

[59] Sagar, S. and Das, B. C. Highly-sensitive full-scale organic pH sensor using thin-film transistor topology. *Org. Electron.* 2022, 111, 106654.

[60] Shaposhnik, P. A., Poimanova, E. Y., Abramov, A. A., Trul, A. A., Anisimov, D. S., Kretova, E. A., Agina, E. V. and Ponomarenko, S. E. Applying of C8-BTBT-based EGOFETs at different pH values of the electrolyte. *Chemosensors.* 2023, 11, 74.

[61] Kunkel, J. and Asuri, P. Function, structure, and stability of enzymes confined in agarose gels. *PLoS ONE.* 2014, 9, e86785.

[62] Tamayo, A., Muñoz, J., Martínez-Domingo, C. and Mas-Torrent, M. Magnetic carbon gate electrodes for the development of electrolyte-gated organic field effect transistor bio-sensing platforms. *J. Mater. Chem. C.* 2023, 11, 11912–11919.

CHAPTER 4

Influence of Mechanical Stress on Flexible Electrolyte-Gated Organic Field-Effect Transistors

This chapter investigates how Electrolyte-Gated Organic Field-Effect Transistor (EGOFET) devices respond to mechanical (tensile and compressive) stress. The devices showed a current increase when a compressive deformation was applied, and the opposite behavior when subjected to a tensile stress. Large gauge factors were found, which were hypothetically ascribed to alterations in the electrical double layer. This work emphasizes the need to control the impact of mechanical deformation in flexible EGOFET-based sensors to achieve consistent performance.

1. Introduction

The use of Organic Field-Effect Transistors (OFETs) to sense mechanical stress has received a lot of interest during the last two decades.[1–3] Flexible and stretchy OFET-based sensors use variations in the electrical performance of the devices caused by deformation of the crystalline cell or the film morphology of the organic semiconductor (OSC) layer to create strain sensors for wearable electronics applications[4,5] such as human activity monitoring[6], robotics[7], and biomedicine.[8]

A key parameter to evaluate the sensitivity of an OSC material under stress is the so-called **gauge factor**, ***k***, which is defined as:

$$k = \frac{\frac{\Delta I}{I_0}}{\frac{\Delta L}{L_0}} = \left(\frac{\Delta I}{I_0}\right) \cdot \left(\frac{1}{\varepsilon}\right) Eq.\,4.1$$

where I_0 is the initial current of the device without the application of strain, ΔI is the current change induced by the external strain, L_0 is the length of the layer without stress and ΔL is the variation of the length after the application of the stress. From this equation, the applied stress, ε, can be defined. Hence, a high gauge factor means high sensitivity to deformations, in the sense that a minimal strain can produce a high change in the output current.[9]

Wang et al.[10] demonstrated that strain in single crystals of OSCs can adjust intermolecular distances, thereby influencing the material's electrical characteristics. For their strain sensor, they selected a rubrene single crystal due to its long-range order and well-defined molecular packing, which lacks grain boundaries. Applying compressive strain resulted in an increased current through the device, whereas tensile strain led to a decrease in current. This behavior was explained by the reduction in intermolecular distance caused by compression, which enhances electronic coupling and boots current flow. The opposite effect is occurring under tension.[11] This phenomenon was exploited to develop a human motion detector(**Figure 4.1**).[11] The device was secured to an index finger to monitor its motion by detecting changes in current. The authors reported high sensitivity (gauge factor = 279), wide detection range and excellent cycle stability.

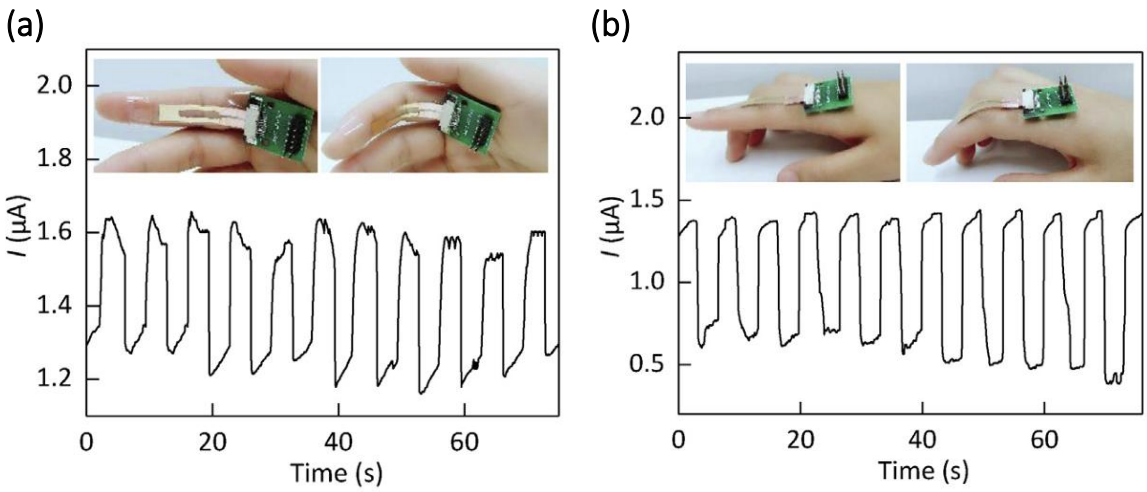

Figure 4.1. Real-time current response of a rubrene single-crystal strain sensor when the index finger is in motion, showing the effects of applied **(a)** compressive and **(b)** tensile strains. The insets provide photographs of the device at different strain levels. Throughout the current monitoring process, the voltage was fixed at 10 V. Extracted from ref[10].

In OSC thin films, the electrical reactions to film elongation/compression might be caused by crystallite deformation or it can be also related to the morphological characteristics of the OSC film.[12] One example is the work of Scenev et al.[13] that revealed bending strain-induced variations in charge carrier mobility in pentacene organic thin-film transistors and rationalized them using a comprehensive analysis of morphological, structural, and electrical aspects. Scanning force microscopy and specular synchrotron X-ray diffraction were used to investigate the morphology and structure of the active pentacene layer, revealing that bending stress caused morphological rather than structural changes, primarily modifying the lateral spacing between individual pentacene crystallites. Furthermore, source and drain gold electrodes shatter at deformations greater than 2%. In contrast to metal electrodes, the change of the organic layer was found to be reversible for deformations up to 10% (**Figure 4.2**).

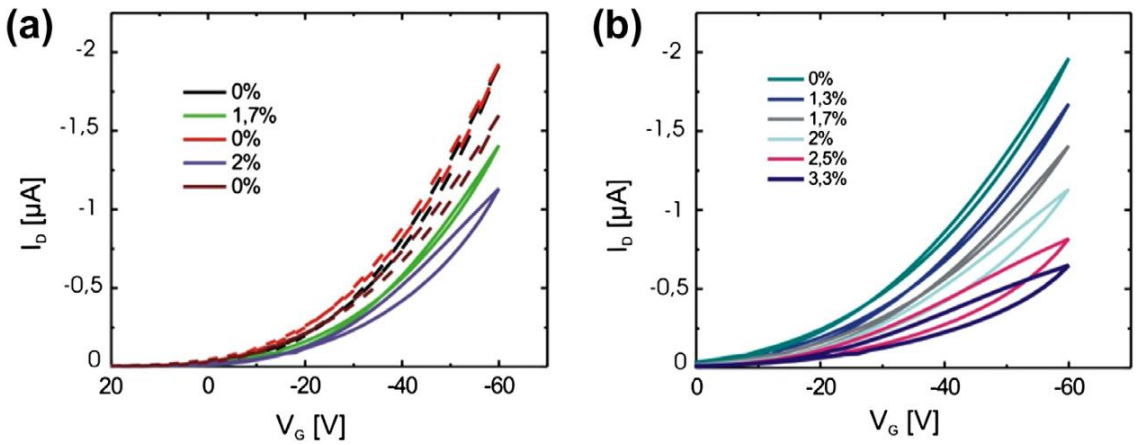

Figure 4.2. Electrical characteristics of a representative thin film pentacene OFET device. **(a)** Transfer curves recorded during successive bending of the device, along with the relief of bending stress indicated by ε= 0% after each deformation, with V_{DS}= -60 V. **(b)** Transfer curves demonstrating the increase in the area of the hysteresis loop as deformation increases, also with V_{DS}= -60 V. Extracted from ref[13].

Previously in our group, it was studied the application of compression and elongation stress on TIPS-pentacene thin films prepared by the bar-assisted meniscus shearing (BAMS) technique.[2] The crystalline size domains changed depending on the deposition direction (i.e. orthogonal or parallel to the channel length). Interestingly, the morphological alterations in the OSC thin films were found to affect the mechanical response of the flexible OFETs. Specifically, it was observed that elongation imposed greater stress on the devices compared to compression, particularly for those utilizing films with larger crystallites achieved through orthogonal coating. Conversely, films featuring smaller crystals produced by parallel coating demonstrated increased sensitivity to compression relative to their orthogonally coated counterparts (**Figure 4.3**). The formation of cracks in the OSC films was observed in both cases; however, the cracks were more interconnected in the films with larger crystallites, indicating that mechanical stress has a more significant impact in this scenario. These results demonstrate that the response to bending can be tuned based on the morphological properties of the films.

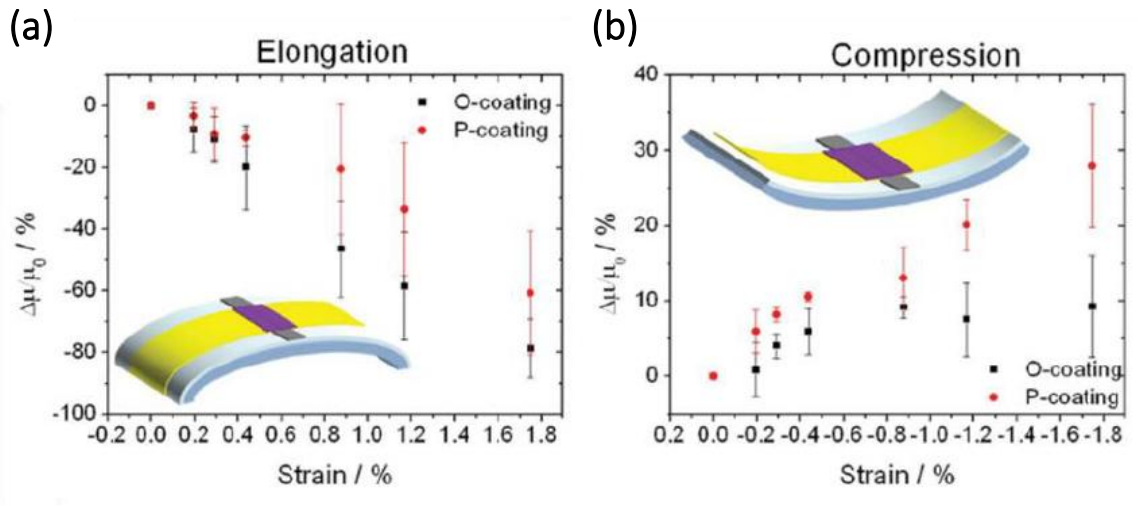

Figure 4.3. Average percentage mobility variation ($\Delta\mu/\mu_0$) as a function of the applied strain, including both elongation and compression, for devices featuring orthogonal-coated and parallel-coated OSC. Extracted from ref[2].

EGOFETs have high potential in flexible applications, however research on EGOFET performance under bending is extremely restricted. This chapter explores the electrical response of flexible EGOFETs prepared by BAMS under bending strain, considering two bending directions: **(i)** concave side, resulting in tensile strain, and **(ii)** convex side, resulting in compressive strain.

2. Summary of the results

In this work, flexible EGOFETs with two different organic semiconductor layers deposited by BAMS (*i.e.,* diF-TES-ADT:PS and C_8O-BTBT-OC_8:PS) were fabricated on Kapton substrates. Both materials were implemented as active layers in EGOFETs exhibiting state-of-the-art performance. Next, their electrical response to tensile and compressive stresses was measured in real-time. Both devices showed a source-drain current increase under compressive strain and a decrease in current under tensile stress (**Figure 4.4**). These real-time measurements showed that the devices responded quickly and reversibly.

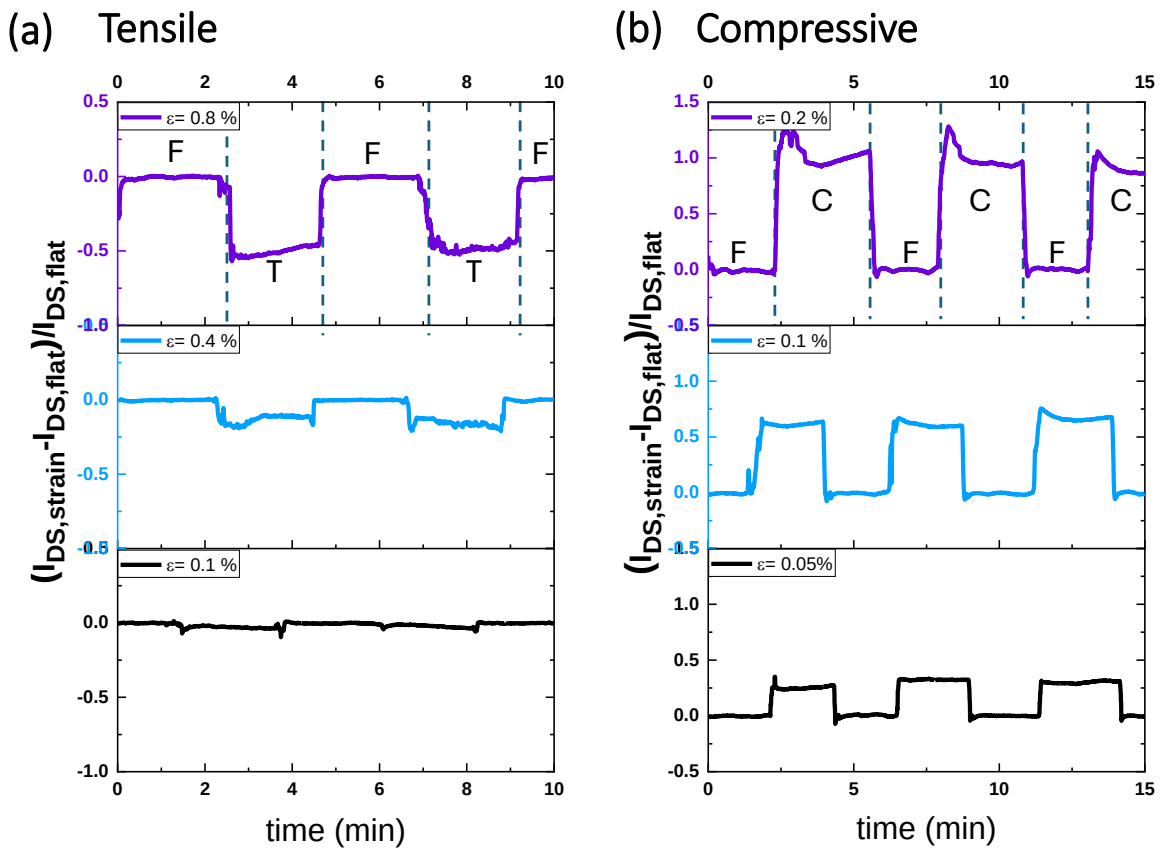

Figure 4.4. Comparison of real-time I_{DS} current monitoring of a diF-TES-ADT:PS EGOFET employing Milli-Q water as electrolyte and fixing at V_{DS}= -0.2 V and V_{GS}= -0.2 V, applying **(a)** cyclic tensile strain equal to 0.1, 0.4 and 0.8 %, and **(b)** cyclic compressive strain equal to 0.05, 0.1 and 0.2 %. F stands for flat, C for compression, and T for tension.

We measured the percentage difference in current for each applied strain relative to the flat position and analyzed the resulting gauge factors to quantify the findings. Both semiconductors had similar tendencies. For tensile stress, the greatest gauge factor was -68±5 at 0.8 % strain for diF-TES-ADT:PS and -110±25 at 0.1 % strain for C_8O-BTBT-OC_8:PS. For compressive stress, the greatest gauge factor was 600±39 at 0.05 % strain for diF-TES-ADT:PS and 453±36 at 0.1 % strain for C_8O-BTBT-OC_8:PS. These values, notably for compression, are greater than those commonly reported for traditional thin film OFETs with solid dielectrics, and they are equivalent to or surpass those recorded for single crystals.

As previously mentioned, changes in current under compression or tensile stress in OFETs are mainly related to changes in thin film morphology or OSC crystal structure. A similar process may explain the strain response found in our EGOFETs, although the large gauge factors obtained indicate that other mechanisms may be involved. Given that EGOFETs are particularly sensitive to changes occurring at the electrical double-layer interfaces (electrolyte/OSC and electrolyte/gate interfaces), it is hypothesized that strain-induced deformations may influence also these interfaces affecting the device's electrical properties. In particular, we believe that changes in the dipole orientation in the electrical double-layers can have an impact on the EGOFET characteristics.

3. Conclusions

This chapter described the fabrication and electrical characterization of flexible EGOFETs made using diF-TES-ADT and C_8O-BTBT-OC_8 blended with PS. Both OSCs displayed excellent performance in EGOFETs. The devices' response to tensile and compressive strain led to a source-drain current decrease and increase, respectively. Both EGOFETs exhibited high gauge factors, especially under compressive strain. This high sensitivity is tentatively attributed to changes at the electrical double-layer interfaces. This work emphasizes the importance of understanding mechanical deformation effects in flexible EGOFET-based sensors to ensure reliable performance.

4. References

[1] Temiño, I., Basiricò, L., Fratelli, I., Tamayo, A., Ciavatti, A., Mas-Torrent, M. and Fraboni, B. Morphology and mobility as tools to control and unprecedentedly enhance X-ray sensitivity in organic thin-films. *Nat. Commun.* 2020, 11, 2136.

[2] Lai, S., Temiño, I., Cramer, T., Del Pozo, F. G., Fraboni, B., Cosseddu, P., Bonfiglio, A. and Mas-Torrent, M. Morphology influence on the mechanical stress response in bendable organic field-effect transistors with solution-processed semiconductors. *Advanced Electronic Materials*. 2017, 4, 1700271.

[3] Zeidell, A. M., Ren, T., Filston, D. S., Iqbal, H. F., Holland, E., Bourland, J. D., Anthony, J. E. and Jurchescu, O. D. Organic field-effect transistors as flexible, tissue-equivalent radiation dosimeters in medical applications. Advanced Science. 2020, 7, 2001522.

[4] Gualandi, I., Marzocchi, M., Achilli, A., Cavedale, D., Bonfiglio, A. and Fraboni, B. Textile organic electrochemical transistors as a platform for wearable biosensors. Sci. Rep. 2016, 6, 33637.

[5] Mattana, G., Cosseddu, P., Fraboni, B., Malliaras, G. G., Hinestroza, J. P. and Bonfiglio, A. Organic electronics on natural cotton fibres. Org. Electron. 2011, 12, 2033–2039.

[6] Yadav, A., Yadav, N., Wu, Y., RamaKrishna, S. and Hongyu, Z. Wearable strain sensors: state-of-the-art and future applications. Mater. Adv. 2023, 4, 1444–1459.

[7] Liu, Z., Qi, D., Guo, P., Liu, Y., Zhu, B., Yang, H., Liu, Y., Li, B., Zhang, C., Yu, J., Liedberg, B. and Chen, X. Thickness-gradient films for high gauge factor stretchable strain sensors. Adv. Mater. 2015, 27, 6230–6237.

[8] Schwartz, G., Tee, B. C.-K., Mei, J., Appleton, A. L., Kim, D. H., Wang, D. H. and Bao, Z. Flexible polymer transistors with high pressure sensitivity for application in electronic skin and health monitoring. Nat. Commun. 2013, 4, 1859.

[9] Liu, Z., Qi, D., Guo, P., Liu, Y., Zhu, B., Yang, H., Liu, Y., Li, B., Zhang, C., Yu, J., Liedberg, B. and Chen, X. Thickness-gradient films for high gauge factor stretchable strain sensors. Adv. Mater. 2015, 27, 6230–6237.

[10] Wang, H., Tong, Y., Zhao, X., Tang, Q. and Liu, Y. Flexible, high-sensitive, and wearable strain sensor based on organic crystal for human motion detection. Org. Electron. 2018, 61, 304–311.

[11] Wang, H., Deng, L., Tang, Q., Tong, Y. and Liu, Y. Flexible organic single-crystal field-effect transistor for ultra-sensitivity strain sensing. IEEE Electron Device Lett. 2017, 38, 1598–1601.

[12] Liu, K., Ouyang, B., Guo, X., Guo, Y. and Liu, Y. Advances in flexible organic field-effect transistors and their applications for flexible electronics. Npj Flex. Electron. 2022, 6, 1–19.

[13] Scenev, V., Cosseddu, P., Bonfiglio, A., Salzmann, I., Severin, N., Oehzelt, M., Koch, N. and Rabe, J. P. Origin of mechanical strain sensitivity of pentacene thin-film transistors. Org. Electron. 2013, 14, 1323–1329.

Article 2

Influence of Mechanical Stress on Flexible Electrolyte-Gated Organic Field-Effect Transistors

Sara Ruiz-Molina, Simona Ricci, Carme Martínez-Domingo, María Jesús Ortiz, Raphael Pfattner, Y. H. Geerts, Tommaso Salzillo, Marta Mas-Torrent

*Submitted

Influence of mechanical stress on flexible electrolyte-gated organic field-effect transistors

Sara Ruiz-Molina,[1,⊥] Simona Ricci,[1,⊥] Carme Martínez-Domingo,[1] María Jesús Ortiz-Aguayo,[1] Raphael Pfattner,[1] G. Schweicher,[2] Y. H. Geerts,[2,3] Tommaso Salzillo,[1,Ω] Marta Mas-Torrent[1,*]

[1]Institut de Ciència de Materials de Barcelona, ICMAB-CSIC, Campus UAB, 08193 Bellaterra, Spain.
[2]Laboratoire de Chimie des Polymères, CP 206/01Faculté des Sciences Université libre de Bruxelles (ULB), Boulevard du Triomphe 1050 Brussels (Belgium).
[3]International Solvay Institutes of Physics and Chemistry, Boulevard du Triomphe, CP 231, 1050 Bruxelles, Belgium

[⊥]Equally contributed

Keywords: electrolyte-gated organic field-effect transistor, flexible electronics, mechanical stress response

Abstract

Electrolyte-gated organic field-effect transistors (EGOFETs) are attracting great attention for the development of low-cost and flexible sensors. However, in order to progress towards such applications, it is key to understand the stability of these devices in aqueous media and under mechanical deformation. Here, we have fabricated flexible EGOFETs based on two small molecule organic semiconductors blended with polystyrene. These materials have been printed employing a low-cost solution-based technique, obtaining large area crystalline films. The EGOFET performance of the devices exhibited state-of-the-art performance. Finally, the devices were operated under tensile and compressive strain, observing a current increase (decrease) when a compressive (tensile) deformation was applied, revealing large gauge factors. Thus, this work shows the importance of assessing the device response under mechanical deformation when flexible EGOFET-based sensors are developed, in order to achieve a reliable response.

1. Introduction

Electrolyte-gated organic transistors have gained a lot of interest over the last few years due to their relevance in different areas, such as in biosensing,[1] neuromorphic devices,[2] and implantable[3] or wearable sensors.[4] They can be divided into two main categories: organic electrochemical transistors (OECTs)[5] and electrolyte-gated organic field-effect transistors (EGOFETs). Both are three-terminal devices, in which the active organic semiconducting layer is contacted between the source (S) and drain (D) contacts and separated from the gate (G) electrode by an electrolyte. In OECTs, the active layer is made of a conducting polymer that is permeable to ions. The operational mechanism of OECTs relies on the doping and de-doping of the active layer driven by the gate-modulated ion penetration.[5] The most employed conducting polymer in OECTs up to now is poly(3,4-ethylenedioxythiophene) polystyrene sulfonate (PEDOT:PSS). In contrast, EGOFETs are based on an organic semiconductor (OSC) film impermeable to ions that is capacitively coupled to the gate electrode.[6,7] In EGOFETs, the non-desired water or ion penetration into the OSC layer as well as that unwanted electrochemical reactions, hampers the device's performance mainly due to doping or damaging the OSC layer.[8,9] This results in devices showing hysteretic curves and/or a lack of current modulation by the gate voltage. In order to achieve OSC layers stable in aqueous media and more impermeable to ions, it is key to prepare highly crystalline and homogenous films, which are less prone to ion penetration than amorphous films or films containing more defects.[9,10] Thus, soluble semi-crystalline polymers, such as poly-3-hexylthiophene (P3HT), have been widely used for this purpose.[8,11] Alternatively, small conjugated molecule thin films are also appealing since they more easily form polycrystalline films.[12]

The benchmark small conjugated molecule OSC 2,8-difluoro-5,11-bis(trithylsilylethynyl)anthradithiophene (diF-TES-ADT) and the family of [1]benzothieno[3,2-b]benzothiophene (BTBT) have been thoroughly investigated as active layer in organic field-effect transistors (OFETs) and EGOFETs giving excellent performance.[13–18] Recently, it was also proved that blending the OSC with polystyrene (PS) is helpful to realize more crystalline films and also to boost the device's performance and stability.[10] This is partly due to the vertical phase separation that takes place during deposition, where the OSC crystallises on top of a PS layer reducing the interfacial charge traps.[19,20]

In addition, flexibility is a key aspect of organic electronic devices for a broad range of domains, including biomedicine,[21] robotics,[22] and wearable electronics.[23,24] Depending on the type of application, tolerance to one-time strain or to small but repetitive strain cycles must be

realised. Further, the device response to deformation can also be exploited in sensing.[25] Thus, understanding the correlation between mechanical stress and the electrical properties of the active layer is fundamental. Despite a fully comprehensive model has not already been found, a few works have been devoted to gaining insights into the driving mechanisms affecting the electrical response of OFETs when they are exposed to mechanical stress.[25–28] However, to our knowledge, although OECTs and EGOFETs also often require flexible substrates for their applications and many of these devices are commonly fabricated on plastics,[29–31] studies of the electrical response changes of these devices upon bending are very scarce, and all of them have been performed using solid electrolytes.[32]

Here, the fabrication and electrical characterization of flexible EGOFETs based on blends of diF-TES-ADT and 2,7-bis(octyloxy)[1]benzothieno[3,2-b]-benzothiophene (C_8O-BTBT-OC_8) with PS are reported. Thin films of C_8O-BTBT-OC_8:PS blends were previously reported to exhibit high OFET mobility and stability thanks to the stabilization of the surface-induced polymorph achieved with the blend film, but their application in an EGOFET device has not been previously reported.[33] Highly homogeneous and crystalline films of these blended OSCs were prepared by the Bar-Assisted Meniscus Shearing (BAMS) technique.[32] Both materials were implemented as active layer in EGOFETs exhibiting state-of-the-art performance. Subsequently, the response of the devices under tensile and compressive strain was monitored. Both materials exhibited a current increase when a compression strain was applied and a decrease when the devices were subjected to a tension stress. The high sensitivity found was tentatively attributed to changes occurring at the electrical double layer interfaces. This work sheds light on the importance of controlling the effects of mechanical deformation in flexible EGOFET-based sensors to avoid interference with the sensing response.

2. Experimental section

2.1.Materials

Polystyrene (PS) (MW: 10000 g/mol and MW:100000 g/mol), Dextran (from Leuconostoc spp. M_w <450000-650000> g/mol), 2,3,4,5,6-pentafluorothiophenol (PFBT) and anhydrous chlorobenzene were purchased from Sigma Aldrich and used without further purification. Acetone HPLC grade and isopropanol HPLC grade were purchased from Teknokroma Analítica S.A. The substrates employed consisted of Kapton® foils (25 μm thick) from DuPont. Si/SiO_x substrates purchased from Si-Mat, (p^+ doped, σ= 0.005-0.02 Ω·cm, 200 nm of thermally-grown SiO_2) were also tested. The OSC 2,7-dioctyloxy[1]benzothieno[3,2-

b]benzo-thiophene (C_8O-BTBT-OC_8) was synthesized according to a previously reported procedure,[34] while 2,8-difluoro-5,11-bis(trithylsilylethynyl)anthradithiophene (diF-TES-ADT) was obtained from Lumtec and used as received (purity>99%), a racemic mixture.
Poly(dimethylsiloxane) (PDMS) Qsil216 A/B was purchased from Farnell Components. The procedure to prepare a PDMS gasket consisted of: the two components of the Qsil216 kit were mixed in a weight ratio 10:1 and mixed strongly for approximately two minutes in a Petri dish. Then, the Petri dish was placed under vacuum for 1 hour to remove air bubbles. Afterward, the resin was cured in an oven at 70 °C overnight.

2.2.Device fabrication and electrical measurements

The devices were fabricated on 25 µm thick Kapton and on Si/SiO_x substrates. Interdigitated Source (S) and Drain (D) electrodes and the coplanar Gate (G) electrode were patterned by positive photolithography (Micro-Writer ML2 from Durham Magneto Optics Ltd.) with a lateral resolution of 5 µm. A thin film of Au was evaporated (40 nm) on top of an adhesive layer of Cr (5 nm). Afterward, the substrates were cleaned in acetone and isopropanol (15 minutes each, repeating this process three times). The device featured the following geometry: L= 50 µm, W = 18000 µm, W/L= 360 (see **Supporting Information, Figure S1**). The coplanar gold gate (G) electrode was designed to have an area equal to 2.25 mm^2.

Following, the electrodes were exposed to UV-ozone cleaner for 25 minutes. Then, the coplanar gate electrode was passivated with a coating layer of dextran (10 $mg \cdot mL^{-1}$ in water) by drop casting and, subsequently, the substrates were dipped in a solution of PFBT (2 $\mu L \cdot mL^{-1}$ in isopropanol) for 15 min to modify the S and D electrodes. [35]

The OSC inks were deposited using the BAMS technique as previously reported,[36] heating the hot plate at 105 °C and moving the bar at a speed rate of 10 $mm \cdot s^{-1}$. For this purpose, 2 % wt. blend solutions of diF-TES-ADT and PS (M_W:10000 $g \cdot mol^{-1}$) and C_8O-BTBT-OC_8 and PS (M_W: 100000 $g \cdot mol^{-1}$) were prepared in chlorobenzene in a OSC:PS ratio 4:1.[33,37,38] After the OSC deposition, the dextran sacrificial layer was removed by immersing the gate electrode in water.

Polarized optical microscopy (POM) images were taken with an Olympus BX51 microscope equipped with a polarizer and analyzer at 90° in reflection mode.

A PDMS pool was employed to confine the electrolyte on top of the G and the interdigitated S and D electrodes. The electrical characterization was carried out using an Agilent B1500A. Measurements under strain were performed with a Keithley 2612A Source Meter controlled by a homemade MATLAB script, under ambient temperature. The devices

were conditioned by applying a source-gate voltage V_{GS}= -0.2 V and a source-drain voltage V_{DS}= -0.2 V until the source-drain current (I_{SD}) reached a steady regime. Once the I_{SD} reached a steady state, devices were tested under mechanical stress under real-time monitoring, applying the stress in the direction parallel to the conducting channel.

From the equation of standard MOSFETs, the product C_{dl}·μ can be extracted in the saturation regime as follows:

$$\mu \cdot C_{dl} = \frac{2L}{W} \cdot \left(\frac{\partial \sqrt{I_{DS,sat}}}{\partial V_{GS}} \right)^2_{V_{DS}} = \frac{2L}{W} \cdot S^2$$

where, *L* and *W* are the channel length and width, respectively, I_{DS} is the source-drain voltage and V_{GS} is the applied source-gate voltage. By performing a linear fit of the plot of the square root of the absolute source-drain current *vs* source-gate voltage in the saturation regime, we can extract the slope (*S*).

Gauge factors were calculated employing Eq. 3. Both tensile and compressive strains from 0.05 % to 0.8 % were applied for both OSCs. The manual adjustment of the radius of curvature during real-time monitoring made it impossible to achieve a perfectly linear increase in curvature. Likewise, there is a slight variation between the compression strains applied to the two semiconductors. Finally, the device was returned to the flat position, and a transfer was recorded to assess the recovery of its performance.

2.3.Bending measurement setup

For carrying out the bending measurements, a homemade apparatus was conceived by assembling different components (**Figure S2**). The substrate was fixed by its extremities into a holder. The holder incorporates a pusher block which can be leaned forward by a pivot, connected to a spring. The movement of the pusher block promotes the bending of the substrate in the upward or downward direction. To facilitate and control achieving the different strains (calculated by Eq. 2), different polymethylmethacrylate (PMMA) pieces with known radii were used to force the bending of the substrate at specific radius in tensile strains.

3. Results and discussion

Blends of the OSCs diF-TES-ADT with PS of molecular weight of 10 KDa and blends of C_8O-BTBT-OC_8 with PS of 100 KDa were selected because of their excellent performance in conventional OFET configuration (**Figure 1a**).[13,33,37] As previously mentioned, diF-TES-ADT:PS films have also shown to exhibit a high performance in EGOFETs.[10] Both OSCs were

deposited using the BAMS technique on top of pre-patterned S and D electrodes on flexible Kapton substrates, which also contained a lateral G contact (see Experimental section).[13,36] As can be observed in the cross-polarised optical microscope images of **Figures 1b and 1c**, highly crystalline and homogeneous thin films were obtained for both materials.[33]

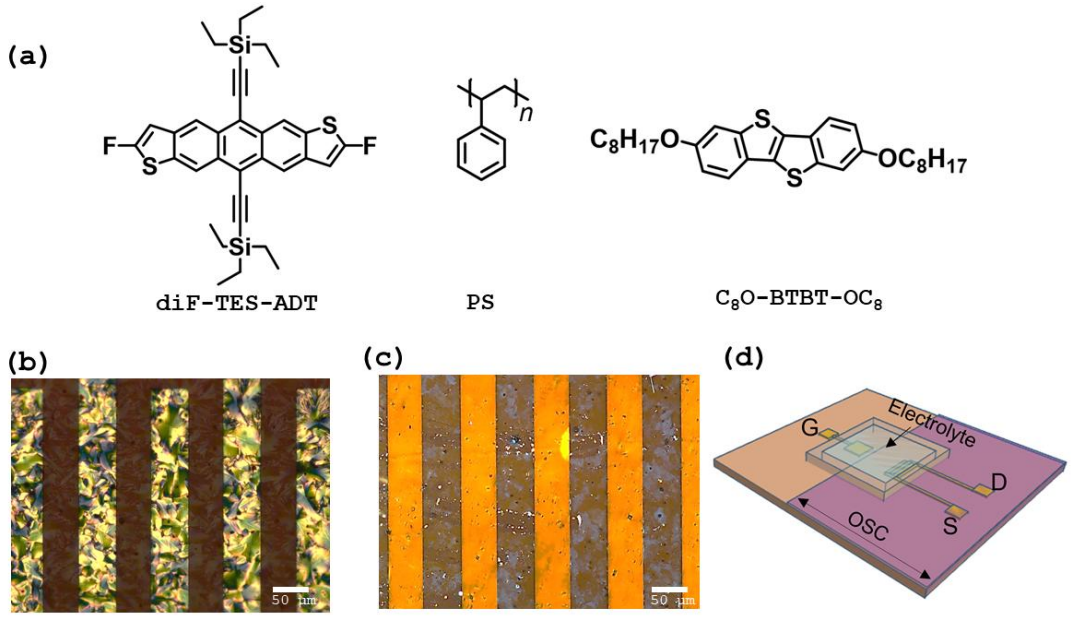

Figure 1. (a) Molecular structure of diF-TES-ADT, polystyrene, and C_8O-BTBT-OC_8. Polarized optical microscopy images of (b) diF-TES-ADT:PS, and (c) C_8O-BTBT-OC_8:PS thin films coated on Kapton substrates. The scale bar of POM images is 50 µm. (d) Schematic representation of the EGOFET device configuration employed.

The as-prepared devices were characterized by recording the transfer and output characteristics employing Milli-Q water as electrolyte (**Figure 1d**). Aqueous solutions are appealing for detecting physiological chemical and electrical signals, bio-interfacing, and health monitoring because its excellent biocompatibility.[39] Water has been shown to work as an efficient electrolyte in EGOFETs and is a less harsh media than buffer solution electrolytes.[6,10] In **Figure 2a**, the transfer characteristics of diF-TES-ADT:PS and C_8O-BTBT-OC_8:PS thin films are shown together with the gate-source current (I_{GS}). In the case of EGOFETs, it is common to report the product of the mobility (µ) and the double-layer capacitance (C_{dl}) to evaluate the performance of the device. This value can be extracted directly from the slope of the transfer characteristics. A C_{dl}·µ= 0.11(±0.02) µS·V^{-1} and 0.13 (±0.05) µS·V^{-1} were estimated for diF-TES-ADT:PS and C_8O-BTBT-OC_8:PS, respectively, in the linear regime, which is in line with state-of-the-art EGOFET devices found in the literature.[17] It should be noticed that these values

are lower than the ones obtained when SiO_2 substrates are used instead of Kapton, which is ascribed to the rougher surface of the flexible substrates that might affect the thin film crystallization and the density of charge traps (**Figure S3**).[16] The $I_{on/off}$ ratio was found to be around 10^2-10^3 for both OSCs. **Figure 2b** and **Figure S4** display the output characteristics of diF-TES-ADT:PS and C_8O-BTBT-OC_8:PS EGOFETs, respectively, showing typical p-type behavior and low hysteresis.

Electrical stability is still an issue for organic transistors, especially for liquid-gated transistors in which the OSC is in direct contact with the aqueous electrolyte. As previously mentioned, the limited stability in aqueous media restricts the number of OSCs that can be applied in EGOFETs and is surely the main bottleneck that hampers the implementation of these devices for practical applications. In order to gain insights into the stability of our devices in operation, current monitoring tests were performed by continuously applying a source-drain voltage (V_{DS}) and source-gate voltage (V_{GS}) of -0.2 V, whilst recording the source-drain current (I_{DS}). As illustrated in **Figures 2c and 2d**, a quite similar overall behavior for both OSCs is found: an initial current increase is observed followed by a decrease. In the diF-TES-ADT:PS EGOFET, I_{DS} increases during the first 2 minutes until a quasi-steady state is reached. From this time onwards, a slow but constant decrease in current is noticed reaching a value close to the initial one after around 9 minutes. This tendency was also demonstrated by Zhang Q et al.[10] In **Figure S5a**, the transfer curves recorded for the as-prepared device and after the application of the bias stress are reported, where a slight shift of the threshold voltage (V_{th}) towards more negative values and an increase of the hysteresis are noted. This behavior could be ascribed to an increase in surface defects at the OSC/electrolyte interface due to the long exposition of the OSC to water under electrical stress. On the other hand, C_8O-BTBT-OC_8:PS exhibits a similar behavior but with a faster current decrease (Figure 2d). After less than two minutes of measurement, the current starts progressively decreasing reaching around 15% of current decrease with respect to the initial current value after 9 minutes of measurement. In the transfer characteristics recorded before and after the current monitoring (**Figure S5b**) a large shift of the V_{th} is observed. Thus, C_8O-BTBT-OC_8:PS suffer more in water environment under operation than the films based on diF-TES-ADT:PS, which shows state-of-the art performance compared to previous reported EGOFETs.[10,40,41] This difference in stability between the two materials cannot be ascribed to difference in energy levels, since C_8O-BTBT-OC_8 has a lower-lying highest occupied molecular orbital (HOMO) and, thus, is less prone to oxidation than diF-TES-ADT.[33,34] Thus, the origin might come from differences in thin film morphology,

such as a less efficient vertical phase separation between the OSC and the PS, a higher level of charge traps or the presence of more defects in the film.[19,42] Following, the influence of mechanical stress on the device electrical characteristics during operation were explored for both materials.

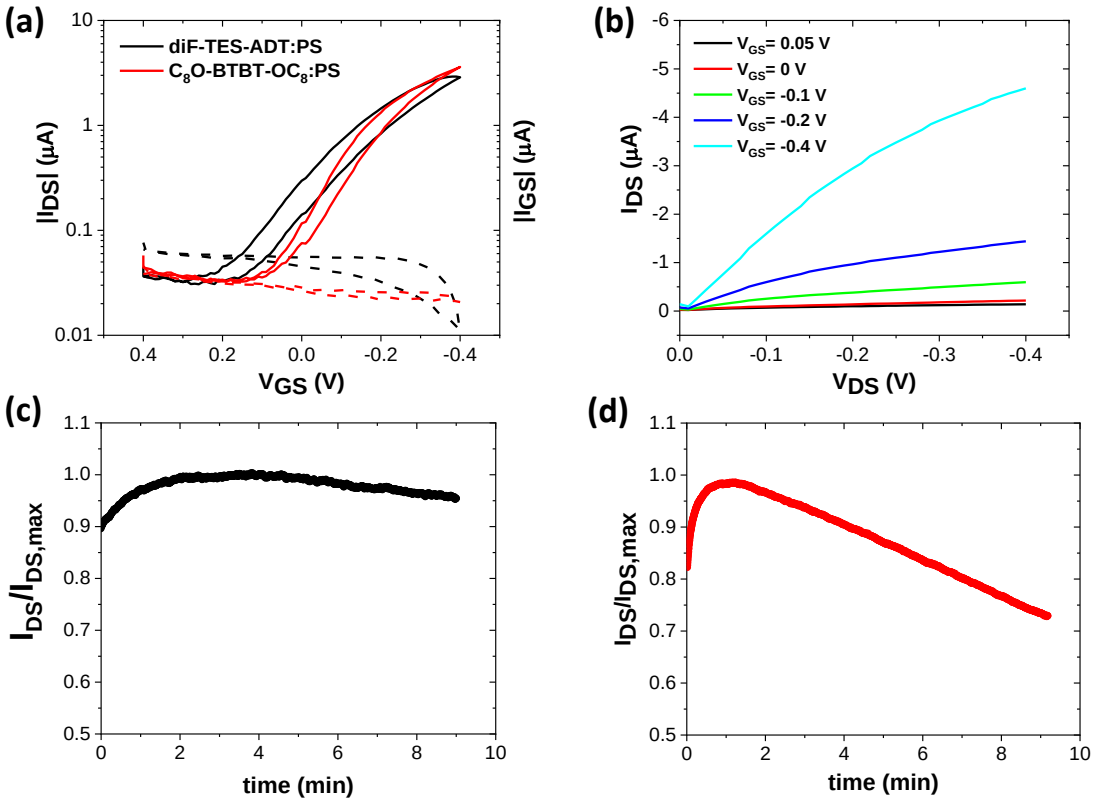

Figure 2. (a) Transfer characteristics (V_{DS}= -0.1 V) and their corresponding source-gate current (dashed lines) for diF-TES-ADT:PS (black curves) and C_8O-BTBT-OC_8 (red curves) EGOFETs. (b) Output characteristics (V_{GS}= 0.05, 0, -0.1, -0.2, -0.4 V) of diF-TES-ADT:PS EGOFETs. Real-time I_{DS} monitoring of a diF-TES-ADT:PS EGOFET (c) and C_8O-BTBT-OC_8:PS EGOFET (d) fixing V_{DS} =V_{GS}= -0.2 V.

Flexibility is a key requirement in sensing and/or wearable applications.[4] Considerable literature is dedicated to all-flexible OFETs and the mechanism driving the electrical response under mechanical strain.[28,43] Surface strain induced on the OFETs active layer can influence the morphology/structure of the OSC films and modify the hopping energy barrier for charge transport and the intermolecular electronic coupling.[27,43–46] Typically, this results in an increase or decrease in the mobility of the thin film when the films are compressed or elongated, respectively. However, the effect of strain in liquid-gated transistors has hardly been explored. Thus, we proceed to explore the electrical response of our EGOFETs under bending strain.

There are two different directions in which bending can be addressed, (i) on the concave side of the flexible sheet, resulting in a tensile strain, and (ii) on the convex side, resulting in a compressive strain. To quantitatively estimate the applied strain (ε), a simple relation is used:[47]

$$\varepsilon = \frac{\Delta L}{L_{flat}} \qquad \text{Eq. 1}$$

where L_{flat} is the length of the layer without stress and ΔL is the variation of the length after the application of the stress.

In the case of thin-film devices, where the overall thickness of the active layer is negligible with respect to the one of the substrate (t_{sub}), ε can be obtained by bending the substrate with a certain bending radius (r):

$$\varepsilon = t_{sub}/2r \qquad \text{Eq. 2}$$

Hence, by changing the radius of curvature it is possible to apply different strains and evaluate the electric response of the devices under mechanical stress.

A key parameter to analyze the sensitivity of a material under stress is the so-called gauge factor, *k*, which can be defined as follows:

$$k = \frac{\frac{\Delta I}{I_{flat}}}{\frac{\Delta L}{L_{flat}}} = \frac{\Delta I}{I_{flat}} \cdot \frac{1}{\varepsilon} \qquad \text{Eq. 3}$$

where I_{flat} corresponds to the I_{SD} in a flat position (considered as reference), ΔI corresponds to the difference between the I_{DS} when the strain is applied and when no strain is applied (*i.e.*, I_{flat}). A high gauge factor means high sensitivity, in the sense that a very small strain can produce a high change in the output current.[48]

The electrical response applying tensile and compressive strains was evaluated in real-time in EGOFETs previously electrically stabilized (see Experimental Section). The device current was stabilized by applying a V_{DS}= -0.2 V and V_{GS}= -0.2 V. Then, a strain was induced for 2 minutes until a new steady state was reached. At this point, the device was placed again in the flat position. Compressive and tensile strains from 0.05 % to 0.2 % and from 0.1 % to 0.8 % were applied, respectively. **Figure 3a** shows the bending response for diF-TES-ADT:PS under tensile stress, while **Figure 3b** displays the bending response when compressive strain is applied. **Figure S6** shows the results obtained for C_8O-BTBT-OC_8:PS EGOFETs**.** Compressive and tensile strains foster opposite behaviors. When tensile strain is applied, a decrease in the I_{SD} is induced, which is further noticed when larger strains are applied. On the contrary, the application of a compressive strain, leads to an increase in the I_{SD}, which is also proportionally to the strain value applied. In all the cases, after removing the strain and

recovering the flat position, the initial current value was achieved. This behavior is coherent with the results observed in other works using conventional OFETs[28,44,46,49,50].

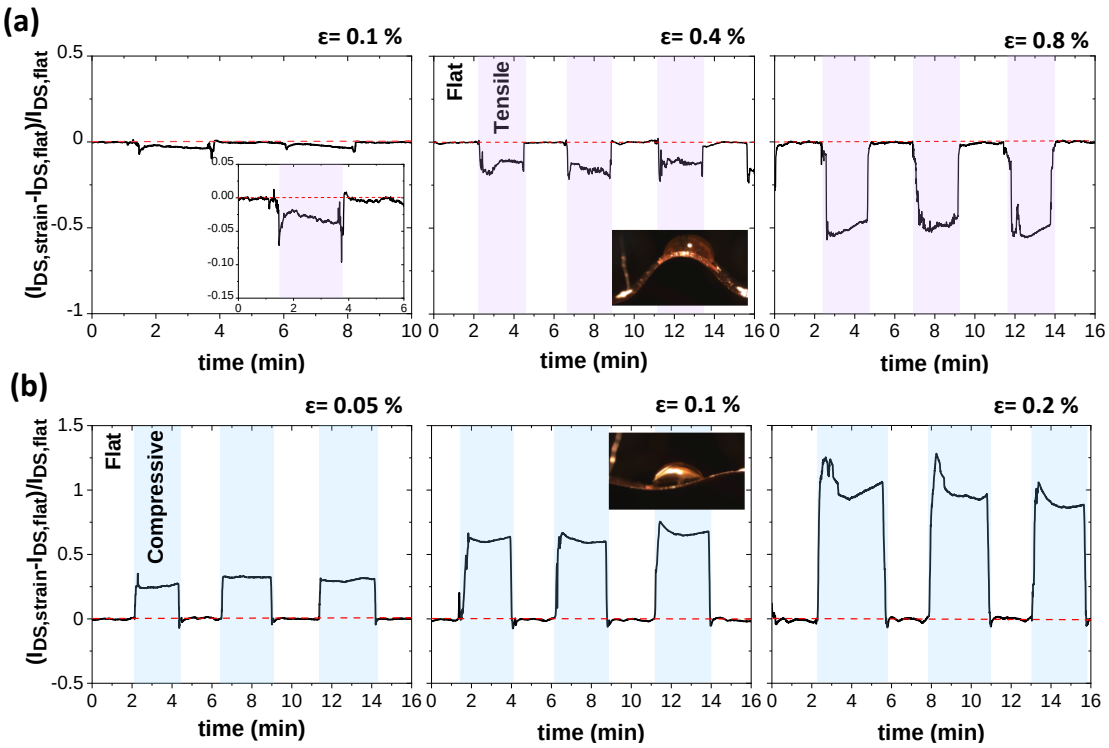

Figure 3. Real-time I_{DS} current monitoring (baseline corrected) of a diF-TES-ADT:PS EGOFET employing Milli-Q water as electrolyte and fixing V_{DS}= -0.2 V and V_{GS}= -0.2 V, applying (a) cyclic tensile strain (purple regions) equal to 0.1, 0.4 and 0.8 %, and (b) cyclic compressive strain (blue regions) equal to 0.05, 0.1 and 0.2 %.

In order to quantify the results, **Figure 4** plots the average percentage of current difference for each applied strain with respect to the flat position for three different devices. In the same plot the values calculated of their corresponding gauge factors are shown. Both semiconductors exhibit a similar tendency. The maximum gauge factor for tensile stress is found at a strain value of 0.8 for diF-TES-ADT:PS and 0.1 for C_8O-BTBT-OC_8:PS, giving gauge factors of -17±2 and -58±9, respectively. On the other hand, the maximum gauge factor for compressive stress is found at a strain value of 0.05 for diF-TES-ADT:PS and 0.1 for C_8O-BTBT-OC_8:PS, giving gauge factor of 429±90 and 210±32, respectively. Noticeably, these values, especially the ones related to compression, are higher than the values typically reported for conventional thin film OFETs with solid dielectric, and they are of the same order of the values reported for single crystals.[51–54]

In OFETs, typically the current increase or decrease observed when a compression or tensile stress is applied, respectively, is attributed to changes in the thin film morphology or in the OSC crystal structure.[55,25] Here, a similar effect might be playing a key role in the strain response observed in the EGOFETs. However, the high values of the estimated gauge factors seem to point that other mechanisms might also be involved.

Previously, a solid electrolyte OECT was reported to exhibit high pressure sensitivity due to the fact that pressure adjusted the ion injection into the polymer semiconductor.[56] In EGOFETs, ions are not expected to be injected in the OSC, but they are highly sensitive to changes occurring at the electrical double layers (EDLs) formed at both the electrolyte/OSC and electrolyte/gate interfaces. Hence, the movement of ions with the applied deformation could also affect these EDLs.

In addition, it was reported that a hydrogel-gated OFET operated as pressure sensor at low pressures (in the range of several hundred Pa to 9 kPa).[57] This device response was ascribed to changes in the water dipole orientation within the OSC film induced by the applied pressure. In fact, several works have pointed out that the water orientation can be modulated by an electric field of by pressue.[58–60] Further, in a recent publication Ota et al. also reported a pressure sensor based on an ion gel-gated transistor. This was rationalised by the fact that quantity of ions at the EDLs was modified with pressure, which was demonstrated measuring the capacitance of the ion gel sandwiched between two electrodes, and was further corroborated by performing theoretical calculations.[61] Another recent work based on EGOFETs using hydrogels or ion gels also showed that the application of tensile stress led to changes in the electrical characteristics, which were dependant on the nature of the solid electrolyte.[62] Remarkably, higher electrical changes were observed when using hydrogels as electrolyte, which show higher ionic mobility than ion gels.

Considering all above, we believe that the deformations induced by strain might be also affecting here the EDLs formed at the EGOFET interfaces under the application of an electric field. Further, the high mobility of the ions in the liquid electrolyte might result in a large effect. In order to gain insights into the sensing mechanism, we also proceed in measuring transfer characteristics of the EGOFETs bended at different radius of curvature, since it is known that variations in the curve slopes could be indicative of alterations in the device capacitance. Unfortunately, the data obtained was not conclusive enough and the changes observed were more attributable to bias stress or to effects caused by the ion diffusion towards the OSC. We believe that when we do continuous current measurements at fixed gate-source and drain-

source voltages, a stable EDL is formed. In these conditions, applying a strain causes a small change in the EDL, which is translated into a change in the measured current. However, when we measure the transfer characteristics, the EDL is continuously changing as a result of the different applied gate voltages, and the small changes occurring at the EDL are no easily detected. Further studies should be conducted for gaining further insights into the mechanisms involved.

This work shows that the application of strain has an influence on the electrical properties of EGOFETs, which should be kept in mind particularly when these devices are applied in flexible sensors. On the other hand, this work also points out that highly strain sensitive devices could be potentially fabricated using EGOFETs based on solid electrolytes.

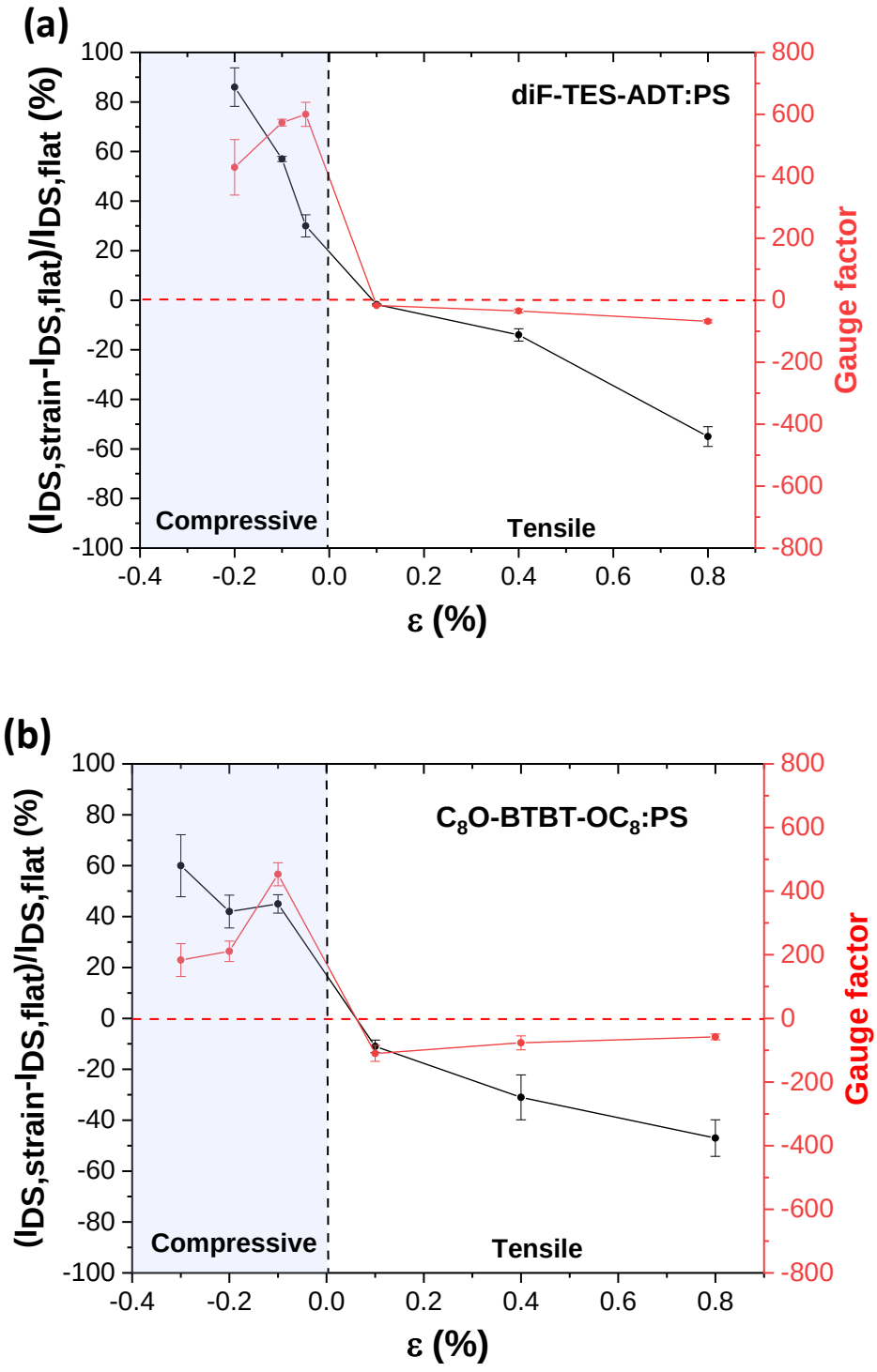

Figure 4. Changes in current (black line) and gauge factor (red line) while applying compressive and tensile strain for (a) diF-TES-ADT:PS and (b) C_8O-BTBT-OC_8:PS EGOFET employing Milli-Q water as electrolyte in real-time current monitoring.

4. Conclusion

In conclusion, we have studied the electrical performances of two small molecule OSCs, namely diF-TES-ADT and C_8O-BTBT-OC_8 blended with polystyrene as active materials in EGOFETs. Thin films have been prepared by solution shearing (*i.e.*, BAMS) giving homogeneous films with high crystallinity. Both materials exhibit a high EGOFET performance, although the films based on diF-TES-ADT show a higher stability under continuous water operation.

Following, the electrical response of the EGOFETs were studied under the application of tensile and compressive strain. The devices showed a source-drain current increase when compressed and the opposite behavior when a tensile deformation was applied. Remarkably, both EGOFETs exhibited a very high gauge factor, especially when they are compressed. This has been tentatively attributed to be partly due to changes occurring at the electrical double layers. Overall, this work points out the importance of assessing the device performance of EGOFETS when they are mechanically deformed, which is particularly relevant for the development of flexible sensors.

5. Acknowledgments

This work was funded by MCIN/AEI/10.13039/501100011033/ERDF,UE with project SENSATION PID2022-141393OB-I00, and through the “Severo Ochoa” Programme for Centers of Excellence in R&D (CEX2023-001263-S) and the Generalitat de Catalunya (2021-SGR-00443). This work was also funded by European Union’s Horizon 2020 research and innovation programme under the Marie Skłodowska-Curie grant agreement No 811284 (UHMob). S. R.-M. is enrolled in the UAB Chemistry Ph.D. program. C. M. acknowledges her Juan de la Cierva fellowship. T.S. thanks the Programma per Giovani Ricercatori “Rita Levi Montalcini” year 2020 (grant PGR20QN52R) of the Italian Ministry of University and Research (MUR) for the financial support. Project funded under the National Recovery and Resilience Plan (NRRP), Mission 04 Component 2 Investment 1.5─NextGenerationEU, call for tender no. 3277 dated 30/12/2021 (award number: 0001052 dated 23/06/2022). Y.G. thanks the Belgian National Fund for Scientific Research (FNRS) for financial support through research projects: PDR T.0058.14, Pi-Fast PDR T.0072.18, PICHIR PDR T.0094.22, DIFFRA GEQ U.G001.19, POLYP EQP U.N032.21F, POLYP2 EQP U.N03323F, CHIRI CDR J. 0088.24. G.S. thanks the **FNRS** for financial support through research project COHERENCE2 N° F.4536.23. G.S. is a FNRS Research Associate. G.S. acknowledges financial support from

the Francqui Foundation (Francqui Start-Up Grant) and Wiener-Anspach Foundation (FWA, ZT1 research project).

7. References

1. Rosaria Anna Picca, Kyriaki Manoli, Eleonora Macchia, Lucia Sarcina, Cinzia Di Franco, Nicola Cioffi, Davide Blasi, Ronald Österbacka, Fabrizio Torricelli, Gaetano Scamarcio and Luisa Torsi. *Advanced Functional Materials*, 2019, **30**, 1904513.
2. Yoeri van de Burgt, Armantas Melianas, Scott Tom Keene, George Malliaras and Alberto Salleo. *Nature Electronics*, 2018, **1**, 386-397.
3. Dion Khodagholy, Thomas Doublet, Pascale Quilichini, Moshe Gurfinkel, Pierre Leleux, Antoinde Ghestem, Esma Ismailova, Thierry Hervé, Sébastien Sanaur, Christophe Bernard and George G Malliaras. *Nature Comunications*, 2013, **4**, 1575.
4. Wei Gao, Hiroki Ota, Daisuke Kiriya, Kuniharu Takei and Ali Javey. *Accounts of Chemical Research*, 2019, **52**, 523-533.
5. Jonathan Rivnay, Pierre Leleux, Michele Sessolo, Dion Khodagholy, Thierry Hervé, Michel Fiocchi and George G Malliaras. *Advanced Materials*, 2013, **25**, 7010.
6. Loig Kergoat, Lars Herlogsson, Daniele Braga, Benoit Piro, Minh-Chau Pham, Xavier Crispin, Magnus Berggren and Gilles Horowitz. *Advanced Materials*, 2010, **18**, 2565-9.
7. Najmeh Delavari, Klas Tybrandt, Magnus Berggren, Benoît Piro, Vincent Noël, Giorgio Mattana and Igor Zozoulenko. *Journal of Physics D: Applied Physics*, 2021, **54**, 415101.
8. Rosaria Anna Picca, Kyriaki Manoli, Eleonora Macchia, Angelo Tricase, Cinzia Di Franco, Gaetano Scamarcio, Nicola Cioffi and Luisa Torsi. *Frontiers in Chemistry*, 2019, **7**, 667.
9. Fabrizio Torricelli, Demetra Z. Adrahtas, Zhenan Bao, Magnus Berggren, Fabio Biscarini, Annalisa Bonfiglio, Carlo A. Bortolotti, C. Daniel Frisbie, Eleonora Macchia, George G, Malliaras, Iain McCulloch, Maximilian Moser, Thuc-Quyen Nguyen, Róisín M. Owens, Alberto Salleo, Andrea Spanu and Luisa Torsi. *Nature Reviews Methods Primers*, 2021, **1**, 66.
10. Qiaoming Zhang. Francesca Leonardi, Stefano Casalini, Inés Temiño and Marta Mas-Torrent. *Scientific Reports*, 2016, **6,** 39623.

11. Matteo Parmeggiani, Alessio Verna, Alberto Ballesio, Matteo Cocuzza, Erik Piatti, Vittorio Fra, Candido Fabrizio Pirri and Simone Luigi Marasso. *Sensors*, 2019, **19,** 4497.
12. Sergi Galindo, Adrián Tamayo, Francesca Leonardi and Marta Mas-Torrent. *Advanced Functional Materials*, 2017, **27**, 1700526.
13. Inés Temiño, Freddy G Del Pozo, M R. Ajayakumar, Sergi Galindo, Joaquim Puigdollers and Marta Mas-Torrent. *Advanced Material Technologies*, 2016, **1**, 1600090.
14. Oana D. Jurchescu, Sankar Subramanian, R. Joseph Kline, Steven D. Hudson, John E. Anthony, Thomas N. Jackson and David J. Gundlach. *Chemistry of Materials*, 2008, **21**, 20.
15. Pengshan Xie, Tianjiao Liu, Jia Sun and Junliang Yang. *Advanced Functional Materials*, 2022, **32**, 2200843.
16. Polina A. Shaposhnik, Elena Y. Poimanova, Anton A, Abramov, Askold A. Trul, Daniil S. Anisimov, Elena A. Kretova, Elena V. Agina and Sergey A. Ponomarenko. *Chemosensors*, 2023, **11**, 74.
17. Michele Di Lauro, Marcello Berto, Martina Giordani, Simone Benaglia, Guillaume Schweicher, Dominique Vuillaume, Carlo Augusto Bortolotti, Yves Henri Geerts and Fabio Biscarini. *Advanced Electronic Materials*, 2017, **3**, 9.
18. Elena Yu. Poimanova, Polina A. Shaposhnik, Daniil S. Anisimov, Elena G. Zavyalova, Askold A. Trul, Maxim S. Skorotetcky, Oleg V. Borshchev, Dmitry Z. Vinnitskiy, Marina S. Polinskaya, Vadim B. Krylov, Nikolay E. Nifantiev, Elena V. Agina and Sergey A. Ponomarenko. *ACS Applied Materials & Interfaces*, 2022, **14**, 16462-16476.
19. Antonio Campos, Sergi Riera-Galindo, Joaquim Puigdollers and Marta Mas-Torrent. *ACS Applied Materials & Interfaces*, 2018, **10**, 15952-15961.
20. Francesca Leonardi, Stefano Casalini, Qiaoming Zhang, Sergi Galindo, Diego Gutiérrez and Marta Mas-Torrent. *Advanced Materials*, 2016, **28,** 10311-10316.
21. Gregor Schwartz, Benjamin C.-K. Tee, Jianguo Mei, Anthony L. Appleton, Do Hwan Kim, Huiliang Wang and Zhenan Bao. *Nature Communications*, 2013, **4**, 1859.
22. Nanshu Lu and Dae-Hyeong Kim. *Soft Robotics*, 2014, **1**, 53-62.
23. Isacco Gualandi, Marco Marzocchi, Andrea Achili, D. Cavedale, Annalisa Bonfiglio and Beatrice Fraboni. *Scientific Reports*, 2016, **6**, 33637.
24. Giorgio Mattana, Piero Cosseddu, Beatrice Fraboni, George G Malliaras, Juan P Hinestroza and Annalisa Bonfiglio. *Organic Electronics*, 2011, **12**, 2033-2039.

25. Stefano Lai, Inés Temiño, Tobias Cramer, Freddy G del Pozo, Beatrice Fraboni, Piero Cosseddu, Annalisa Bonfiglio and Marta Mas-Torrent. *Advanced Electronic Materials*, 2018, **4**, 1700271.
26. Kenjiro Fukuda, Kenta Hikichi, Tomohito Sekine, Yasunori Takeda, Tsukuru Minamiki, Daisuke Kumaki and Shizuo Tokito. *Scientific Reports*, 2013, **3**, 2048.
27. Piero Cosseddu, Silvia Milita and Annalisa Bonfiglio. *IEEE Electron Device Letters*, 2012, **33**, 113-115.
28. Hyun Ho Choi, Hee Take Yi, Junto Tsurumi, Jae Joon Kim, Alejandro L Briseno, Shun Watanabe, Jun Takeya, Kilwon Cho and Vitaly Podzorov. *Advanced Science*, 2020, **7**, 1901824.
29. Jiajun Song, Hong Liu, Zeyu Zhao, Peng Lin and Feng Yan. *Advanced Materials*, 2024, **36**, 2300034.
30. Zeyu Zhao, Zhiyuan Tian and Feng Yan. *Cell Reports Physical Science*, 2023, **4**, 101673.
31. Shiming Zhang, Yang Li, Gaia Tomasello, Maddy Anthonisen, Xinda Li, Marco Mazzeo, Armando Genco, P. Grutter, Fabio Cicoira. *Advanced Electronic Materials*, 2019, **5**, 1900191.
32. Freddy G. del Pozo, Simone Fabiano, Raphael Pfattner, Stamatis Georgakopoulos, Sergi Galindo, Xianjie Liu, Slawomir Braun, Mats Fahlman, Jaume Veciana, Concepció Rovira, Xavier Crispin, Magnus Berggren and Marta Mas-Torrent. *Advanced Functional Materials*, 2015, **26**, 2379-2386.
33. Tommaso Salzillo, Antonio Campos, Adara Babuji, Raul Santiago, Stefan T Bromley, Carmen Ocal, Esther Barrena, Rémy Jouclas, Christian Ruzié, Guillaume Schweicher, Yves Henri Geerts and Marta Mas-Torrent. *Advanced Functional Materials*, 2020, **30**, 2006115.
34. Christian Ruzié, Jolanta Karpinska, Anne Laurent, Lionel Sanguinet, Simon Hunter, Thomas D Anthopoulos, Vincent Lemaur, Jérome Cornil, Alan R Kennedy, Oliver Fenwick, Paolo Samorì, Guillaume Schweicher, Basab Chattopadhyay and Yves Henri Geerts. *Journal of Materials Chemistry C.*, 2016, **4**, 4863-4879.
35. Jeremy W Ward, Marsha A Loth, R Joseph Kline, Mariona Coll, Carmen Ocal, John E Anthony and Oacan D Jurchescu. *Journal of Materials Chemistry*, 2012, **22**, 19047-19053.

36. Freddy G del Pozo, Simone Fabiano, Rphael Pfattner, Stamatis Georgakopoulos, Sergi Galindo, Xianjie Liu, Slawomir, Mats Fahlman, Jaume Veciana, Concepció Rovira, Xavier Crispin, Magnus Berggren and Marta Mas-Torrent. *Advanced Functional Materials*, 2015, **26**, 2379-2386.
37. Tommaso Salzillo, Nieves Montes, Raphael Pfattner and Marta Mas-Torrent. *Journal of Materials Chemistry C.*, 2020, **8**, 15361-15367.
38. Tommaso Salzillo, Francesco D'Amico, Nieves Montes, Raphael Pfattner and Marta Mas-Torrent. *CrystEngComm*, 2021, **23**, 1043-1051.
39. Wei Huang, Jianhua Chen, Gang Wang, Yao Yao, Xinming Zhuang, Robert M. Pankow, Yuhua Cheng, Tobin J. Marks and Antonio Facchetti. *Journal of Materials Chemistry C*, 2021, **9,** 9348-9376.
40. Nicolò Lago, Marco Buonomo, Sara Ruiz-Molina, Andrea Pollesel, Rafael Cintra Hensel, Francesco Sedona, Mauro Sambi, Marta Mas-Torrent, Stefano Casalini and Andrea Cester. *Organic Electronics*, 2022, **106**, 106531.
41. Xingyu Jiang, Cheng Shi, Zi Wang, Lizhen Huang and Lifeng Chi. *Advanced Materials*, 2023, **36**, 2308952.
42. Adrian Tamayo, Ilaria Fratelli, Andrea Ciavatti, Carme Martínez-Domingo, Paolo Branchini, Elisabetta Colantoni, Luca Tortora, Adriano Contillo, Raul Santiago, Stefan T. Bromley, Beatrice Fraboni, Marta Mas-Torrent and Laura Basiricò. *Advanced Electronic Materials*, 2022, **8,** 2200293.
43. Piero Cosseddu, Gianmarco Tiddia, Silvia Milita and Annalisa Bonfiglio. *Organic Electronics*, 2013, **14**, 206-211.
44. Tsuyoshi Sekitani, Yusaku Kato, Shingo Iba, Hiroshi Shinaoka, Takao Someya, Takayasu Sakurai and Shinichi Takagi. *Applied Physics Letters*, 2005, **86**, 073511.
45. Tsuyoshi Sekitani, Shingo Iba, Yusaku Kato and Takao Someya. *Japanese Journal of Applied Physics*, 2005, **44**, 2841-2843.
46. V. Scenev, Piero Cosseddu, Annalisa Bonfiglio, Ingo Salzmann, N. Severin, Martin Oehzelt, Norbert Koch and Jürgen P Rabe. *Organic Electronics*, 2013, **14,** 1323-1329.
47. Jay Lewis. Materials Today, 2006, 9, 38-45.
48. Zhiyuan Liu, Dianpeng Qi, Peizhi Guo, Yan Liu, Bowen Zhu, Hui Yang, Yaquing Liu, Bin Li, Chenguang Zhang, Jiancan Yu, Bo Liedberg and Xiaodong Chen. *Advanced Materials*, 2015, **27,** 6230-6237.

49. Anatoliy N Sokolov, Yadong Cao, Olasupo B Johnson and Zhenan Bao. *Advanced Functional Materials*, 2012, **22**, 175-183.
50. Haiting Wang, Liangliang Deng, Q. Tang, Y. Tong, and Yichun Liu. *IEEE Electron Device Letters*, 2017, **38**, 1598-1601.
51. Haiting Wang, Yanhong Tong, Xiaoli Zhao, Qingxin Tang, Yichun Liu. *Organic Electronics*, 2018, **61**, 304-311.
52. A. L. Briseno, Ricky J Tseng, M. M. Ling, E.H.L. Falcao, Yang Yang, F. Wudl and Zhenan Bao. *Advanced Materials*, 2006, **18**, 2320-2324.
53. Takayoshi Kubo, Roger Häusermann, Junto Tsumuri, Junshi Soeda, Yugo Okada, Yu Yamashita, Norihisa Akamatsu, Atsushi Shishido, Chikahiko Mitsui, Toshihiro Okamoto, Susumu Yanagisawa, Hiroyuki Matsui and Jun Takeya. *Nature Communications*, 2016, **7**, 11156.
54. Qingxin Tang, Yanhong Tong, Yongmei Zheng, Yudong He, Yajie Zhang, Huanli Dong, Wenping Hu, Tue Hassenkam and Thomas Bjornholm. *Small*, 2011, **7**, 189-193.
55. Damien Thuau, Katherine Begley, Rishat Dilmurat, Abduleziz Ablat, Guillaume Wantz, Cédric Ayela and Mamatimin Abbas. *Materials*, 2020, **13**, 1583.
56. Shuai Chen, Abhijith Surendran, Xihu Wu, Wei Lin Leong. *Advanced Functional Materials*, 2020, **30**, 2006186.
57. Qiaoming Zhang, Francesca Leonardi, Raphael Pfattner and Marta Mas-Torrent. *Advanced Materials Interfaces*, 2019, **6**, 1900719.
58. Gaurav Chopra and Michael Levitt. *Proceeding of the National Academy of Sciences*, 2011, **108**, 14455-14460.
59. Yuchi He, Gang Sun, Kenichiro Koga and Limei Xu. *Scientific Reports*, 2014, **4**, 6596.
60. Belisa R. H. de Aquino, H. Ghorbanfekr-Kalashami, M. Neek-Amal, and F. M. Peeters. *Physical Review B.*, 2018, **97**, 144111.
61. Kota Inoue, Kazumoto Miwa, Sunao Shimizu, Kazuhide Ueno, Junichiro Ohe, Shimpei Ono, Kiroki Ota. *IEEE 37TH International Conference on Micro Electro Mechanical Systems (MEMS)*, 2024, 604-605.
62. Mona Azimi, Arunprabaharan Subramanian, Jiaxin Fan, Francesca Soavi and Fabio Cicoira. *Journal of Materials Chemistry C.* 2023, **11**, 4623.

Supporting Information

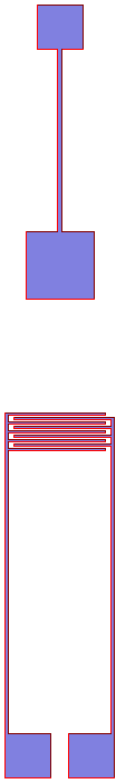

Figure S1. Device layout. W=18000 µm, L= 50 µm, W/L=360. The coplanar gate electrode's area is equal to 2.25 mm^2.

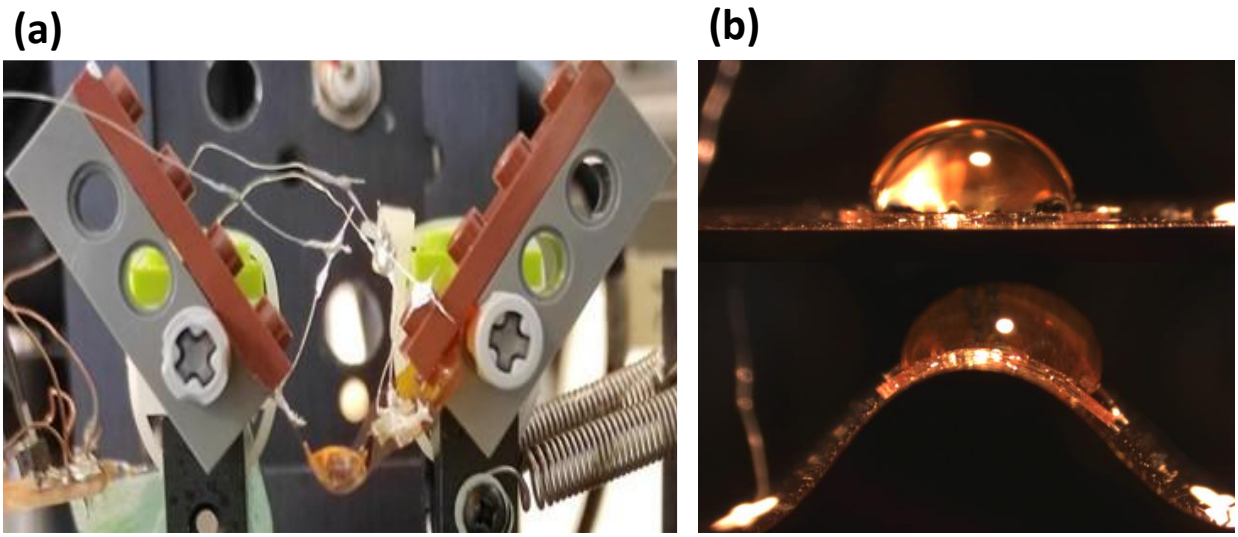

Figure S2. (a) Setup for mechanical stress and (b) photography of devices with Milli-Q water in flat configuration and during the application of stress.

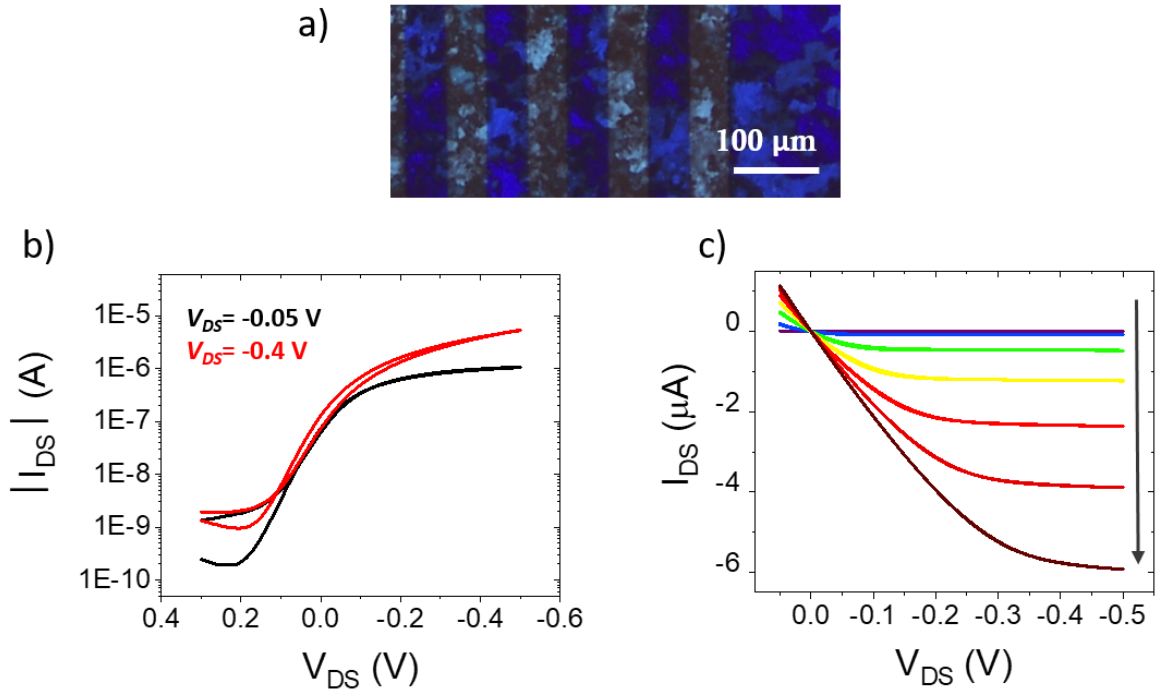

Figure S3. Electrical characterization of EGOFETs based on C_8O-BTBT-OC_8:PS films fabricated on Si/SiO_2 substrates and using Milli-Q water as electrolyte. (a) POM image of the film. (b) Transfer characteristics (V_{DS}= -0.05 V (black line) and V_{DS}= -0.4 V (red line)). (c) output characteristics recorded at V_{GS} = 0.35 V, 0.20 V, 0.05 V, -0.1 V, -0.25 V, 0.40 V and -0.55 V (in the direction of the arrow).

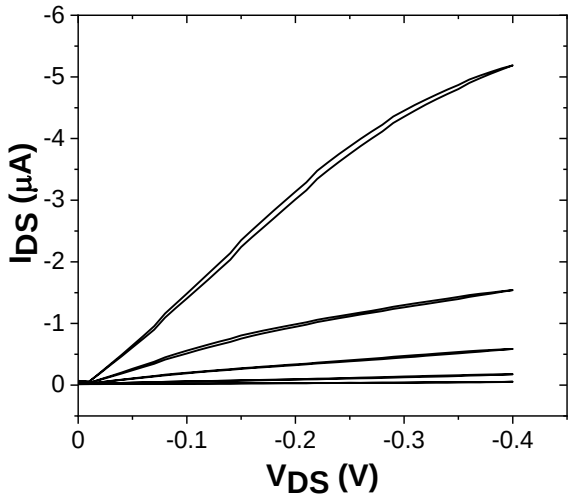

Figure S4. Output characteristics (V_{GS}= 0.05, 0, -0.1, -0.2, and -0.4 V) of C_8O-BTBT-OC_8:PS-based thin film on Kapton using Milli-Q water as electrolyte.

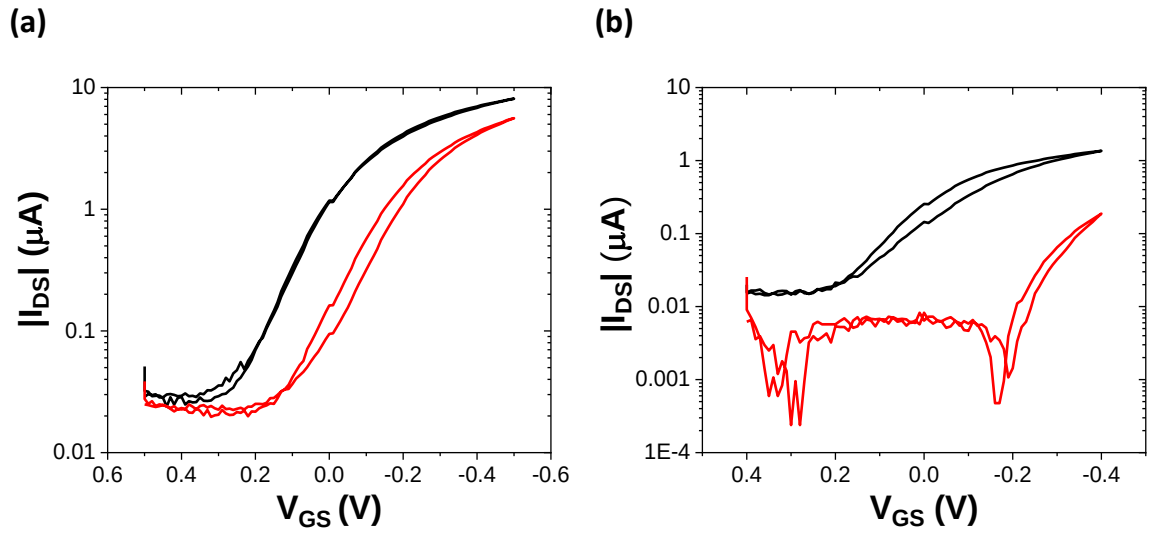

Figure S5. Transfers characteristics (V_{DS}= -0.1 V) of (a) diF-TES-ADT:PS and (b) C_8O-BTBT-OC_8:PS EGOFETs before (black curves) and after (red curves) performing a bias stress test that consisted of applying a source-drain voltage (V_{DS}) and source-gate voltage (V_{GS}) of -0.2 V for 9 minutes.

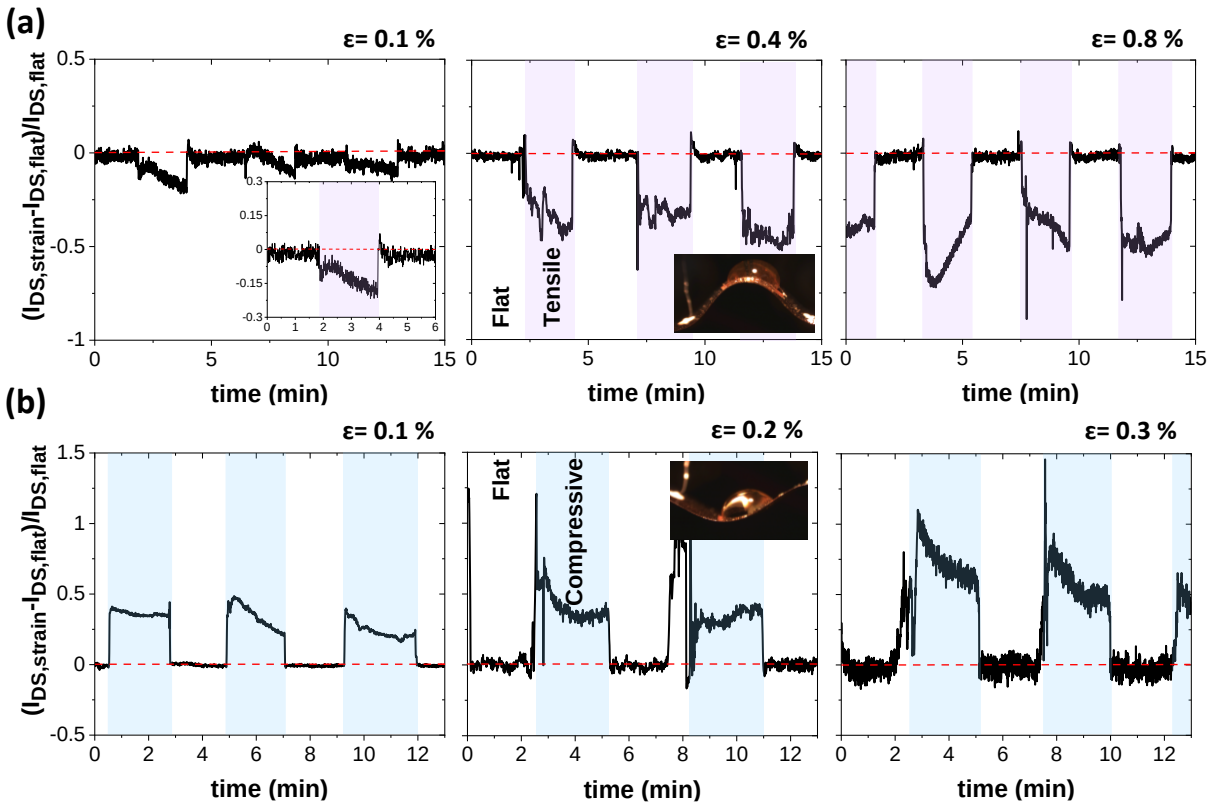

Figure S6. Real-time I_{DS} current monitoring of C_8O-BTBT-OC_8:PS_{100k} employing Milli-Q water fixing V_{DS}= -0.2 V and V_{GS}= -0.2 V, applying (a) cyclic tensile strain (purple regions) equal to 0.1, 0.4 and 0.8 %, respectively; and (b) cyclic compressive strain (blue regions) equal to 0.1, 0.2 and 0.3 %, respectively.

CHAPTER 5

Electrolyte-Gated Organic Field-Effect Transistors for Cell Stimulation and Recording

Electrolyte-Gated Organic Field-Effect Transistors (EGOFETs) not only offer the potential for low-cost, low-power electronics in applications like sensors and point-of-care tests but they can also be used for cell stimulation and recording. However, EGOFETs face stability challenges, like drift in their operative point, leading to signal distortion. In this chapter, we applied a methodology to compensate for the threshold voltage drift by using a dual-gate EGOFET. This route improves the reliability of the devices for applications in medical and sensing devices. Further, we demonstrated extracellular voltage stimulation and single-cell membrane potential recording using our fabricated EGOFETs, emphasizing the importance of device design and measurement accuracy for developing EGOFET-based bio-sensing.

Article 3*: Real-time threshold voltage compensation on dual-gate electrolyte-gated organic field-effect transistors.

Article 4*: Single-cell membrane potential stimulation and recording by an electrolyte-gated organic field-effect transistor.

*In collaboration with the Department of Information Engineering, Department of Physics and Astronomy 'G. Galilei' and Department of Chemical Sciences of University of Padova, Italy; Veneto Institute of Molecular Medicine (VIMM), Padova, Italy; Policlinico Agostino Gemelli IRCCS, Roma; and Institute of Endocrinology and Oncology 'Gaetano Salvatore' (IEOS-CNR), Napoli, Italy.

1. Introduction

Electrolyte-Gated Organic Field-Effect Transistors (EGOFETs) offer significant advantages for interfacing with biological systems, including improved signal-to-noise ratio and compatibility with flexible substrates. This makes them ideal candidates for bio-sensing applications, such as recording and stimulating neural activity at the single-cell level. Indeed, living cells, such as neurons, communicate via transient changes in membrane potential, known as action potentials.[1] The ability to stimulate and record electrical activity in neurons is a key milestone for applications in neural interfaces, which aim to control and monitor brain activity with high precision.

However, the use of EGOFETs in aqueous environments, such as those found in biological tissues, presents challenges. Traditional EGOFETs suffer from degradation and instability when water and other electrolytes are exposed. The drift of the threshold voltage over time is one of the most significant technological issues connected with EGOFETS.[2,3] In long-term biological monitoring, the drift of the device's operating point can lead to signal distortion and the loss of critical information. Hence, if this issue cannot be solved, the implementation of EGOFETs would require the development of compensation circuitries that can compensate the transistor gate voltage to drive a constant current.

Organic-based transistors have already been used for extracellular recording.[4] Thanks to their large current density and high volumetric capacitance, Organic Electrochemical Transistors (OECTs) have been explored extensively as a tool for in vitro and in vivo recording of cellular electrical signals.[5,6]

Bonafè et al.[7] provided a quantitative examination of OECT's performance as single-cell impedance sensors. They designed optimized sensors to perform in vitro single-cell detection tests and they discovered that PEDOT:PSS based OECTs can monitor the cell adhesion process and regain their previous function following cell detachment using trypsin. Yao et al.[8] presented the design of an OECT-based cell monitoring system in which a monolayer of epithelial cells was cultivated on the PEDOT:PSS semiconductor surface of OECTs. The activity of the cells, that is the opening and shutting of cystic fibrosis transmembrane conductance regulators (CFTR), is known to affect the sodium flow and,

more specifically, the sodium concentration at the basolateral side near the PEDOT:PSS. This variation in ionic strength altered the electrical properties of the transistor.

Despite all these achievements with OECTs, the larger cut-off frequency of EGOFETs would suggest that EGOFETs should be more suitable than OECTs for the recording of fast action potentials lasting just a few milliseconds, thereby making the EGOFET technology very attractive for bioelectronics applications. Regarding previous works on EGOFET devices for cell recording, Desvief et al.[9] demonstrated an electrolyte-gated hybrid nanoparticle/organic synapse (synapse-transistor, or EGOS) with short-term plasticity similar to biological synapses. The reaction of EGOS was suited for interaction with neurons: short-term plasticity was exhibited at spike voltages as low as 50 mV (equivalent to the magnitude of an action potential in neurons) and response times in the tens of milliseconds. When human neuroblastoma stem cells were cultured on the EGOS and differentiated into neurons, it was found that their presence did not interfere with the device's short-term plasticity. Further, Kyndiah et al.[10] used an EGOFET as a bioelectronic recording platform, demonstrating that EGOFETs can record the extracellular action potentials of human pluripotent stem cell-derived cardiomyocyte cells (hPSCs-CMs) (**Figure 5.1**). The authors showed that the electrical activity of grown cells plated on an EGOFET array can be recorded over many days with high stability and as well as with the presence of drugs that inhibited or accelerated their activity. This work demonstrates that EGOFETs can be a promising and powerful tool in cardiac biology for cardiac disease modeling.

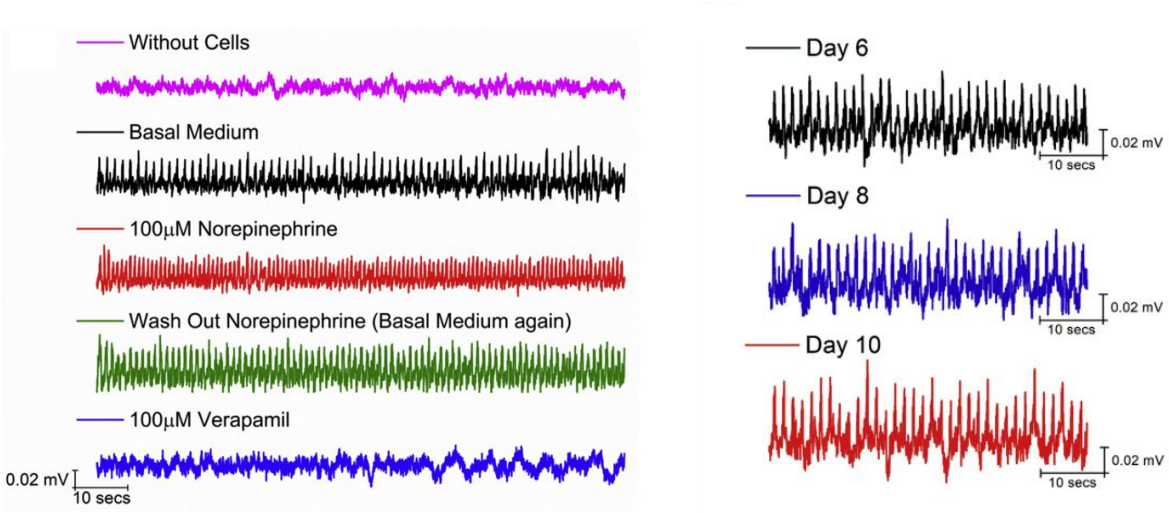

Figure 5.1. (a) Electrical recordings from the EGOFET device using hPSC-derived cardiac cells under various conditions. The time traces illustrate equivalent gate voltage variations derived from source-drain current, represented as $\Delta V_{GS} = \Delta I_{DS}/g_m$. The dark pink curve indicates the electrical response of the EGOFET without cells, while the black curve corresponds to the basal medium. The red curve reflects the basal medium with the addition of 100 µM of Norepinephrine, the green curve shows the response of the basal medium after washing out the drug, and the blue curve corresponds to the basal medium when 100 µM of Verapamil drug is added. **(b)** Electrical recordings taken on different days highlight the device's stability over time. Extracted from ref[10].

This chapter includes two different works. The first one has been focused on the development of a methodology to compensate for the characteristic threshold voltage shift found in EGOFETs working under continuous operation by the application of a back gate voltage. In the second study, we have designed EGOFETs suitable to be applied in single-cell recording and stimulating using a double gate configuration.

2. Summary of the results

- Article 3:

As previously mentioned, EGOFET devices exhibit unwanted current drift during operation, resulting in signal distortion and information loss. Here, we fabricated dual-gated EGOFETs on SiO_2 substrates based on blends of diF-TES-ADT:PS. In this way, a top-gate electrode has been applied to modulate the EGOFET, whilst the Si back gate has been used for implementing digital feedback to compensate dynamically for the transistor threshold voltage. This permitted us to fix its operative point. As a consequence, it has been proven that the current drift can be eliminated while maintaining electrical stability throughout extensive experiments with powerful electrolytes (>10 h). Further, this device also preserved the EGOFETs sensing capability for the detection of action potentials (AP) whose time constant is faster than the drift of the device, that is signals with frequencies larger than 0.1 Hz. A proof-of-concept was established by superposing AP signals to the Top-Gate DC bias, proving that the compensation system described in this publication may offer a stable operating point while detecting signals with characteristic frequencies greater than 1 Hz.

- Article 4:

Here, the ability of EGOFETs to trigger and record single-cell membrane potentials employing a dual-gate architecture was developed. For this purpose, also dual-gate EGOFETs on SiO_2 substrates were fabricated using active material blends of diF-TES-ADT:PS. However, in this case, to obtain a sufficiently small transistor footprint to allow bidirectional communication at the single cell level, the EGOFET technology was scaled down implementing a Corbino layout, with a channel length of 20 mm (Figure 5.2). The circular-shaped Source and Drain electrodes of this configuration allow for a uniform distribution of the electric field, also, the higher electric field in proximity to the Source electrode (inner electrode) facilitates carrier injection.

Figure 5.2. Corbino layout with a channel length equal to 20 mm.

With these devices, it was possible to record single-cell (i.e., HeLa cells) membrane potentials. In addition, the application of a back gate voltage was exploited to stimulate the cells. The application of stimulating voltages between 0.1 to 1 V resulted in the modulation of the intracellular voltage variation.

3. Conclusions

In conclusion, the two studies described here represent major steps forward toward the development of EGOFET technology for applications in cell activity recording:

Article 3 provides a solution to the problem of threshold voltage drift occurring during EGOFET operation, ensuring that the devices can maintain their sensitivity and accuracy in the long term. The development of a real-time threshold voltage compensation system addresses one of the major barriers to the practical implementation of EGOFETs in long-term biological monitoring. This breakthrough could lead to the creation of more reliable and sensitive biosensors for detecting a wide range of biological events.

Article 4 shows how, with a suitable device design, EGOFETs can both capture single-cell activity and stimulate them, paving the way toward novel bidirectional electrocorticography devices with a high spatial resolution. Indeed, since, EGOFETs might allow for accurate stimulation and recording at the cellular level, they are promising for the development of new advanced neural implants that can monitor brain activity while also administering specific electrical impulses.

4. References

[1] Cramer, T. *et al.* Organic ultra-thin film transistors with a liquid gate for extracellular stimulation and recording of electric activity of stem cell-derived neuronal networks. *Phys. Chem. Chem. Phys.* 2013, 15, 3897–3905.

[2] Zhang, Q., Leonardi, F., Casalini, S., Temiño, I. and Mas-Torrent, M. High performing solution-coated electrolyte-gated organic field-effect transistors for aqueous media operation. *Sci. Rep.* 2016, 6, 39623.

[3] Zhang, Q., Tamayo, A., Leonardi, F. and Mas-Torrent, M. Interplay between Electrolyte-Gated Organic Field-Effect Transistors and Surfactants: A Surface Aggregation Tool and Protecting Semiconducting Layer. *ACS Appl. Mater. Interfaces.* 2021, 13, 30902–30909.

[4] Piro, B., Mattana, G. and Reisberg, S. Transistors for chemical monitoring of living cells. *Biosensors.* 2018, 8, 65.

[5] Go, G.-T., Lee, Y., Seo, D.-G. and Lee, T.-W. Organic neuroelectronics: From neural interfaces to neuroprosthetics. *Adv. Mater.* 2022, 34, 2201864.

[6] Abarkan, M., Pirog, A., Mafilaza, D., Pathak, G., N'Kaoua, G., Puginier, E., O'Connor, R., Raoux, M., Donahue, M. J., Renaud, S. and Lang, J. Vertical organic electrochemical transistors and electronics for low amplitude micro-organ signals. *Adv. Sci.* 2022, 9, 2105211.

[7] Bonafè, F., Decataldo, F., Zironi, I., Remondini, D., Cramer, T. and Fraboni, B. AC amplification gain in organic electrochemical transistors for impedance-based single cell sensors. *Nat. Commun.* 2022, 13, 5423.

[8] Yao, C., Xie, C., Lin, P., Yan, F., Huang, P. and Hsing, I-Ming. Organic electrochemical transistor array for recording transepithelial ion transport of human airway epithelial cells. *Advanced Materials*. 2013, 25, 6575-6580.

[9] Desbief, S., di Lauro, M., Casalini, S., Guerin, D., Tortorella, S., Barbalinardo, M., Kyndiah, A., Murgia, M., Cramer, T., Biscarini, F. and Vuillaume, D. Electrolyte-gated organic synapse transistor interfaced with neurons. Organic Electronics. 2016, 38, 21–28.

[10] Kyndiah, A., Leonardi, F., Tarantino, C., Cramer, T., Millan-Solsona, R., Garreta, E., Montserrat, N., Mas-Torrent, M. and Gomila, G. Bioelectronic recordings of cardiomyocytes with accumulation mode electrolyte gated organic field effect transistors. Biosens. Bioelectron. 2020, 150, 111844.

Article 3

Real-time threshold voltage compensation on dual-gate electrolyte-gated organic field-effect transistors

Nicolò Lago, Marco Buonomo, Sara Ruiz-Molina, Andrea Pollesel, Rafael Cintra Hensel, Francesco Sedona, Mauro Sambi, Marta-Mas Torrent, Stefano Casalini, Andrea Cester

Organic Electronics, 2022, 106, 106531

.

DOI: 10.1016/j.orgel.2022.106531

Article 4

Single-cell membrane potential stimulation and recording by an electrolyte-gated organic field-effect transistor

Nicolò Lago, Alessandra Galli, Sarah Tonello, Sara Ruiz-Molina, Saralea Marino, Stefano Casalini, Marco Buonomo, Simona Pisu, Marta Mas-Torrent, Giada Giorgi, Morten Gram Pedersen, Mario Bortolozzi, Andrea Cester

Advanced Electronic Materials, 2024, 2400134

DOI: 10.1002/aelm.202400134

CHAPTER 6.

Conclusions

This thesis focused on the use of Electrolyte-Gated Organic Field-Effect Transistors (EGOFETs) for their application in various bioelectronic applications. The primary goals were to design transducers for monitoring biomolecule aggregation and cellular activity, as well as to produce flexible, low-power devices. Remarkably, all the devices were fabricated using a low-cost printing technique to deposit the organic semiconductor, named after the Bar-Assisted Meniscus Shearing (BAMS).

One of the most remarkable accomplishments was the demonstration that EGOFETs are not only suitable platforms to detect relevant proteins for diagnosis, but they can also be successfully exploited to study the aggregation of proteins. In particular, we fabricated an EGOFET-based transducer for measuring amyloid peptide aggregation, which is important in neurodegenerative illnesses such as Alzheimer's and Parkinson's. EGOFETs can detect peak concentrations of $A\beta_{1\text{-}40}$ oligomers, in early phases of aggregation, providing a quick, sensitive, and cost-effective response. Furthermore, the ability of EGOFETs to operate as label-free electrical transducers without the need of using fluorescent tags or markers, makes them highly promising for performing systematic studies. For instance, they can be employed to explore parameters or drugs affecting the protein aggregation processes, which is crucial for the development of treatments for these illnesses.

Furthermore, Hydrogel-Gated Organic Field-Effect Transistors (HYGOFETs) that employ hydrogels as solid electrolytes instead of liquid ones, offer the benefits of EGOFETs, such as low operating voltage and compatibility with an aqueous environment, together with improved stability and robustness. In this respect, agarose hydrogel is an appealing material due to its availability, water-swelling qualities, facile gelling procedure, and bio-compatibility. Agarose-based HYGOFETs were demonstrated to work effectively in a constant humidity environment, which can be realized by assembling them in a lateral flow assay where nitrocellulose paper can be used to transport the aqueous fluid on the device. This enables to reach a reliable and efficient operation, which is required in biosensing applications. Moreover,

we proved that the modification of agarose with suitable receptors can be a promising route for the development of biosensors as an alternative to the more used approaches where the bio-receptor is incorporated on the gate electrode. As a proof of principle, we have developed a highly sensitive sensor to detect biotin with a very low limit of detection of 0.01 fM.

For the development of flexible biosensors based on EGOFETs, it is key to understand how the deformation of the devices affects their electrical response. Our investigations on flexible EGOFETs based on two different organic semiconductors, diF-TES-ADT and C_8O-BTBT-OC_8, showed that tensile and compressive stresses applied during continuous device operation cause considerable variations in the drain current. The large gauge factors measured indicated that the origin of this high sensitivity relies on changes in the electrical double-layers caused by these deformations. These findings are critical for designing flexible sensors capable of operating reliably under a variety of mechanical conditions, as when they are incorporated into wearable or implantable systems. Additionally, these results also point out that EGOFETs could be applied as sensitive strain sensors. In this case, the liquid electrolyte should be replaced with more mechanically robust solid electrolytes.

The EGOFET devices are also promising for cell activity recording. However, one of the main bottlenecks is the device voltage drift during operation, which should be compensated with external circuitry in potential applications. In this thesis, we have shown that by using a double-gate EGOFET it is possible to overcome such threshold voltage drift, assuring long-term sensitivity and accuracy in biological monitoring. This innovation has immediate implications for the development of sensitive biosensors that can detect a wide range of biological processes in real time. Furthermore, we have also demonstrated that, with a suitable device design, dual gate EGOFETs can be implemented to record single-cell (i.e., HeLa cells) membrane potentials using the top-gate and, additionally, to stimulate the cells by the application of a back gate voltage. The development of devices capable of capturing single-cell activity opens new perspectives for the creation of sophisticated neural implants that not only monitor brain activity but also give focused electrical impulses for therapy.

As a general conclusion, the research described in this thesis demonstrated the enormous potential of EGOFETs and HYGOFETs for bioelectronic applications. The findings not only improve our understanding of how these devices work and operate but also pave the way for future studies into their application in biological sensing and for the development of next-generation flexible devices for monitoring and managing cellular and molecular activity.

[Annex 1] Nanoscale Operando Characterization of Electrolyte-Gated Organic Field-Effect Transistors Reveals Charge Transport Bottlenecks. Shubham Tanwar, Ruben Millan-Solsona, Sara Ruiz-Molina, Marta Mas-Torrent, Adrica Kyndiah and Gabriel Gomila. *Advanced Materials,* 2024, 36, 2309767.

DOI: 10.1002/adma.202309767

[Annex 2] Automated Scanning Dielectric Microscopy Toolbox for Operando Nanoscale Electrical Characterization of Electrolyte-Gated Organic Transistors. Shubham Tanwar, Ruben Millan-Solsona, Sara Ruiz-Molina, Marta Mas-Torrent, Adrica Kyndiah and Gabriel Gomila. *Advanced Electronic Materials,* 2024, 2400222.

DOI: 10.1002/aelm.202400222